DISSERTATION

SUBMITTED TO THE
COMBINED FACULTIES FOR THE NATURAL SCIENCES AND FOR
MATHEMATICS
OF THE RUPERTO-CAROLA UNIVERSITY OF HEIDELBERG, GERMANY
FOR THE DEGREE OF
DOCTOR OF NATURAL SCIENCES

PUT FORWARD BY

DIPLOM-PHYSICIST BENJAMIN PHILIPP MOSTER
BORN IN PFORZHEIM

ORAL EXAMINATION: NOVEMBER 2nd, 2010

HYDRODYNAMIC SIMULATIONS OF COSMOLOGICAL GALAXY MERGER TREES

Mich dünkt, man könne hier in gewissem Verstande ohne Vermessenheit sagen:
Gebet mir Materie, ich will eine Welt daraus bauen!

Allgemeine Naturgeschichte und Theorie des Himmels
Immanuel Kant

Hydrodynamic Simulations of Cosmological Galaxy Merger Trees

Abstract   In this thesis we use cosmological merger trees and semi-analytic models of galaxy formation to provide the initial conditions for multi-merger hydrodynamic simulations. In this way we exploit the advantages of merger simulations (high resolution and detailed treatment of the gas physics) and semi-analytic models (cosmological background and low computational cost), and integrate them to create a novel tool. This approach allows us to study the evolution of various galaxy properties with an improved treatment of the gas components, including, for the first time, the hot gaseous halo from which gas cools and accretes onto the central disc. Using a suite of minor merger simulations we find that disc thickening is reduced relative to the collisionless case through the absorption of kinetic impact energy by the gas. In a following series of major merger simulations, we show that adding the hot gas component is a key ingredient in order to reproduce several observed properties of elliptical galaxies, like the abundance of fast rotators. Moreover, the presence of a gaseous halo reduces the starburst efficiency. We then focus on the effects of multiple concurrent mergers, which we found to be cosmologically more common than sequences of isolated binary mergers. For this, we investigate, whether accreted satellite stars can be distinguished kinematically from stars formed 'in situ' in the central galaxy, and find that this is only possible for a fraction of the disrupted satellites. Our simulations to date indicate that the combination of a detailed treatment of gas physics, high resolution, and a cosmological background, brings numerical simulations in better agreement with observations. Overall, the novel tool developed in this thesis will be very useful for pursuing a number of questions pertaining to the transformation of galaxy internal structure by mergers and accretion.

Hydrodynamische Simulationen kosmologischer Galaxienvermelzungsbäume

Zusammenfassung   In der vorliegenden Arbeit werden kosmologische Verschmelzungsbäume und semi-analytische Galaxienentstehungsmodelle benutzt, um Anfangsbedingungen für hydro-dynamische Simulationen von mehrfachen Galaxienverschmelzungen zu erstellen. Somit werden die Vorteile von Simulationen (hohe Auflösung und detaillierte Behandlung der Gasphysik) und semi-analytischen Modellen (kosmologischer Hintergrund und geringer Rechenaufwand) in einem neuen Instrument vereinigt. Dieser Ansatz ermöglicht es, die Entwicklung von verschiedenen Galaxieneigenschaften mit einer detaillierten Behandlung der Gaskomponenten zu untersuchen, wobei erstmals der heiße Gashalo berücksichtigt wird, von dem aus Gas kühlt und auf die zentrale Scheibe akkretiert wird. Mittels einer Reihe von kleineren Verschmelzungssimulationen wird gezeigt, dass im Vergleich zum stoßfreien Fall das Verdicken von Scheibengalaxien reduziert wird, da das Gas kinetische Stoßenergie absorbiert. In einer Serie großer Verschmelzungssimulationen wird demonstriert, dass der Gashalo ein Schlüsselelement ist, um beobachte Eigenschaften von Ellipsengalaxien zu reproduzieren wie die Häufigkeit schneller Rotatoren. Zudem reduziert der Gashalo die Sternentstehungseffizienz von Galaxienkollisionen. Im Weiteren wird der Schwer-punkt auf Simulationen von Mehrfachverschmelzungen gelegt, welche kosmologisch häufiger sind, als eine Sequenz isolierter Verschmelzungen. Hierzu wird untersucht, ob akkretierte Satel-litensterne kinematisch von der Zentralgalaxie unterschieden werden können, und gezeigt, dass dies nur für einen Teil der Satelliten möglich ist. Unsere bisherigen Simulationen verdeutlichen, dass die Kombination einer detaillierten Behandlung der Gasphysik, hoher Auflösung und eines kosmologischen Hintergrundes Simulationen in eine bessere Übereinstimmung mit Beobachtun-gen bringt. Die hier entwickelte Methode wird für eine Reihe von Fragen von Nutzen sein, die sich mit der Transformation der inneren Struktur von Galaxien durch Kollisionen und Akkretion beschäftigen.

Contents

List of Figures

List of Tables

Chapter 1

Introduction

Since the dawn of mankind, the celestial bodies of the night sky have exerted a mystical attraction. The human mind was always wondering about the origin of planets, stars, galaxies and the Universe itself. In particular the majesty and variety of galaxies has inspired scientists to explore what has shaped these systems and how they will evolve in the future. Only in the last century, however, has it become possible to address extragalactic phenomena in an empirical manner. Modern scientific cosmology is usually considered to have begun in 1917 with Albert Einstein's publication of the cosmological implications of general relativity (Einstein 1917), which prompted astronomers such as Willem de Sitter, Karl Schwarzschild and Arthur Eddington to explore the astronomical consequences of the theory. In parallel to this, a debate was unfolding regarding the nature of the cosmos itself. On the one hand, Harlow Shapley (1919) favoured the model of a cosmos made up of the Milky Way (MW) star system only. On the other hand, Heber Curtis (1920) suggested that spiral nebulae were star systems in their own right: island universes. This became known as the Great Debate. The resolution of this debate on the structure of the cosmos came with the detection of cepheids in NGC 6822 and the Andromeda galaxy by Edwin Hubble (1925, 1929b). Their distance established spiral nebulae well beyond the edge of the MW and as galaxies of their own.

At this time, the Universe was still assumed to be static by many scientists, including Albert Einstein who included a cosmological constant in his field equation in order to prevent the Universe from rapid collapse through gravity. However, when Hubble (1929a) discovered that most of the extragalactic nebulae were moving away from the observer, it was noticed that the Universe is not static at all, but expanding. Subsequent modelling of the Universe explored the possibility that the cosmological constant may result in an expanding universe, depending on its value. Recent observations of the microwave background radiation made by the *COBE* (Smoot *et al.* 1992) and *WMAP* (Spergel *et al.* 2003) satellites have effectively transformed cosmology from a highly speculative science into a predictive science, as the fundamental cosmological parameters are measured to decimal places, rather than orders of magnitude. This has led many to refer to modern times as the 'Golden age of cosmology'. This cosmological framework has direct implications on the formation of structures in the Universe and can be understood as the stage on which galaxy formation and evolution take place.

1.1   Cosmology and galaxies

Cosmology is based on two fundamental assumptions: on sufficiently large scales the Universe is uniform in all directions and our position in the Universe is not preferred over any other. From these assumptions the cosmological principle follows, which states that the Universe is spatially homogeneous and isotropic. Since gravity, which is specified by general relativity, is the only force relevant on cosmological scales, one can describe the evolution of the Universe with the Einstein equation and a proper metric. For a homogeneous and isotropic universe this is the Robertson-Walker metric. Evaluating the Einstein equation, one can derive the Friedmann equation

$$H^2(t) = \left[\frac{\dot{a}(t)}{a(t)}\right]^2 = H_0^2 \left(\frac{\Omega_r}{a^4} + \frac{\Omega_m}{a^3} + \frac{\Omega_K}{a^2} + \Omega_\Lambda\right), \qquad (1.1)$$

where $H(t)$ is the Hubble function and $a(t)$ is the scale factor which describes the expansion of the Universe and is explicitly time dependent. The constituents of the Universe at the present time are specified by the density parameters Ω_r for radiation, Ω_m for matter, Ω_K for the curvature and Ω_Λ for the cosmological constant which represents one possibility for the elusive 'dark energy'. As our Universe is observed to be flat, Ω_K is equal to zero. The luminous matter, commonly called the 'baryonic matter', is only a fraction of the total matter $\Omega_b = f_b \cdot \Omega_m$. The remaining 'dark matter' does not interact electromagnetically and has not been directly observed yet.

Most of the energy content of the Universe at the present epoch is dark and the dominant components dark energy and dark matter account for over 95 per cent of the energy density of the Universe. The origin and the nature of both the dark components is still unknown and the evidence for their presence is purely astrophysical. Dark matter was postulated as a result of its gravitational interaction (Zwicky 1933; Rubin *et al.* 1982) while dark energy drives the accelerated expansion of the Universe (Riess *et al.* 1998; Perlmutter *et al.* 1999; Kowalski *et al.* 2008). The theoretical motivations for both components are still untested: while the presence of dark matter is assumed to be an implication of supersymmetric particle physics (Blumenthal *et al.* 1982; Ellis *et al.* 1984), the presence of dark energy is suspected to be related to the vacuum energy in quantum field theory or a self-interacting scalar field (dynamical dark energy; Wetterich 1988). In the simplest picture the dark energy is assumed to be an ubiquitous, non-clustering form of energy, whereas dark matter is supposed to be dynamically cold, collisionless, and able to cluster due to its gravitation. Together, dark energy, which can be described by a cosmological constant Λ, and cold dark matter (CDM) form the foundation of the ΛCDM theory.

In this framework the Universe was a dense hot compound of elementary particles at the time it was created. When the early Universe went through a phase of rapid expansion (called inflation) possibly driven by a scalar field, density perturbations generated by quantum fluctuations were stretched to cosmologically large scales. These fluctuations were thus imprinted onto the initial density field of the particles. The dark matter component was then able to form structures in the
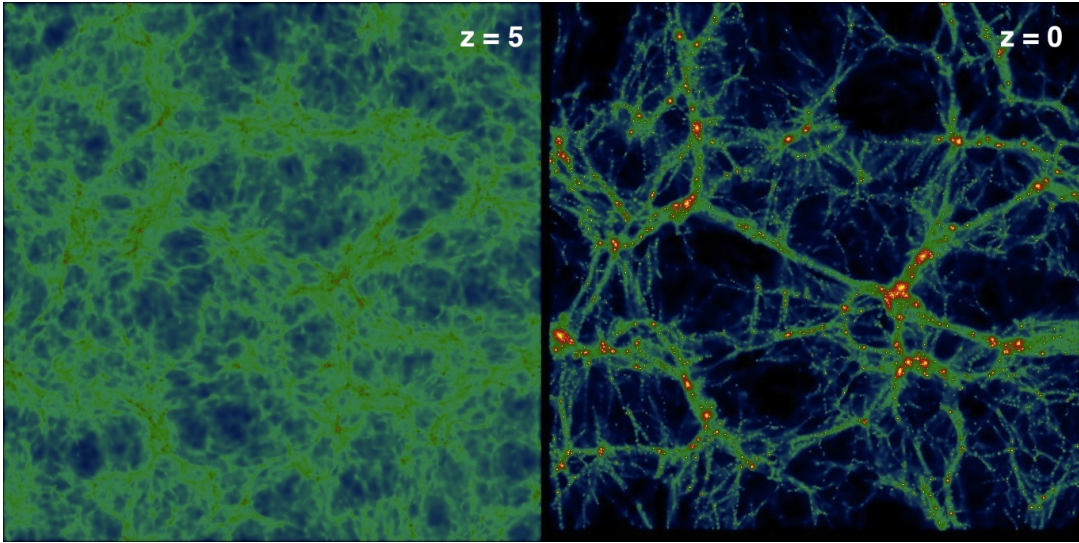
Figure 1.1 The Universe on large scales as found in N-body simulations. The comoving side length of the simulation box is 90 Mpc. Dark colours represent regions of low density while bright colours represent regions of high density.

Universe due to its gravitational collapse. The small initial perturbations of the density field grew in time through gravity and formed bound objects, called dark matter haloes. In the ΛCDM scenario structure formation is hierarchical, i.e. small haloes grow first while larger haloes are formed by the coalescence of smaller progenitors. After the time of recombination, when the temperature of the Universe became low enough that neutral atoms could form from protons and electrons, the baryonic matter fell into the potential wells created by the dark matter haloes. Undergoing a series of complex physical processes, the baryons were able to form the galaxies that we can observe today. As a result, galaxies trace the dark matter on large scales and can be thought of as lighthouses with which we can study the large scale structure in the Universe.

Using the linear relationship between recessional velocity and the distance of galaxies discovered by Hubble (1929a), one can define the observable redshift as $z = (\lambda_0 - \lambda_e)/\lambda_e$, where λ_0 is the observed and λ_e is the emitted wavelength. The redshift increases with the distance of the observed galaxy due to the expansion of the Universe and can be related to the scale factor $a(t)$: $z + 1 = a^{-1}$. We can thus associate a certain age of the Universe, also called the 'cosmic time', to a certain redshift. Large galaxy redshift surveys, such as the Two Degree Field Galaxy Redshift Survey (2dFGRS; Folkes *et al.* 1999) and the Sloan Digital Sky Survey (SDSS; e.g. Stoughton *et al.* 2002) have provided large data sets of the large scale structure of the Universe. On the other side, the ΛCDM theory is able to make predictions of the large scale structure, e.g. employing numerical simulations. Figure 1.1 shows the structures that are found at scales of 90 Mpc in such a simulation. The left panel presents the total mass distribution at an early epoch ($z = 5$), where the Universe is still relatively smooth, while the right panel shows the Universe today ($z = 0$),

where many different structures can be found. The small bright structures are dark matter haloes and their distribution agrees very well with the observed distribution of galaxies found in surveys. Thus on large scales, we are able to explain the observed structures extremely well.

On small scales however, it is much more difficult to explain and predict structures as this requires the understanding of the physical processes that drive the formation of galaxies, once the baryons have entered a dark matter halo. The standard picture of hierarchical galaxy formation was introduced by White & Rees (1978) and has been subsequently extended. In this picture, the small initial density fluctuations grow with time due to gravitational instability. While the dark matter collapses into haloes with a quasi-equilibrium state through violent relaxation, the baryonic matter falls into the potential wells of these haloes creating shocks that raise the entropy of the material. The baryonic matter relaxes to hydrostatic equilibrium and forms a hot gaseous halo for which the self-gravity is balanced by pressure gradients. The gas of this halo is able to cool through various physical processes (e.g. bremsstrahlung) which reduces the pressure support and causes the accretion of cold gas from the halo onto a central object. As the gas in the halo typically has an initial nonzero angular momentum, the gas will spin up as it flows inward, settling in a cold disc at the centre of the halo. As the gas in the disc further cools, its self-gravity will eventually dominate leading to a collapse and the fragmentation into small, dense cores that form stars. The efficiency of this star formation process depends on the density of the gas and happens on a characteristic time-scale. The result is a rotating stellar disc in centrifugal equilibrium. A fraction of the newly created stars, however, is short-lived and explodes in supernovae (SNe) producing enormous amounts of energy. The radiation from these explosions can heat the surrounding gas, blowing it out of the galaxy in a galactic wind. This reduces the efficiency of star formation, especially in haloes of low mass where these winds are able to escape the potential well. Another source of feedback is provided by the accretion of gas onto a supermassive black hole (BH) in the centre of the galaxy, called active galactic nuclei (AGN).

Due to the hierarchical nature of the ΛCDM scenario, a dark matter halo constantly accretes new material and eventually other galactic systems merge with it. When a smaller halo containing a central galaxy enters a larger halo with its own central galaxy, the entering halo becomes a subhalo of the larger or main halo, and the galaxy in the subhalo becomes a satellite galaxy of the main system. The subhalo and the satellite subsequently lose orbital energy and angular momentum due to dynamical friction and, eventually, the satellite merges with the central galaxy at the centre of the main halo. Such a merger may be accompanied by a strong burst of star formation if the merging galaxies have a similar mass and contained significant amounts of cold gas. At the same time, angular momentum is transferred to the stars in the disc. For a merger of nearly equal mass, or major merger, the orbits of the disc stars are randomised, resulting in the destruction of the discs and the creation of an elliptical galaxy. This process is called the 'merger hypothesis'. After such a merger a new gas disc can be created and a new stellar disc formed, producing an early-type spiral galaxy. In mergers with a large mass ratio, or minor mergers, the disc of the
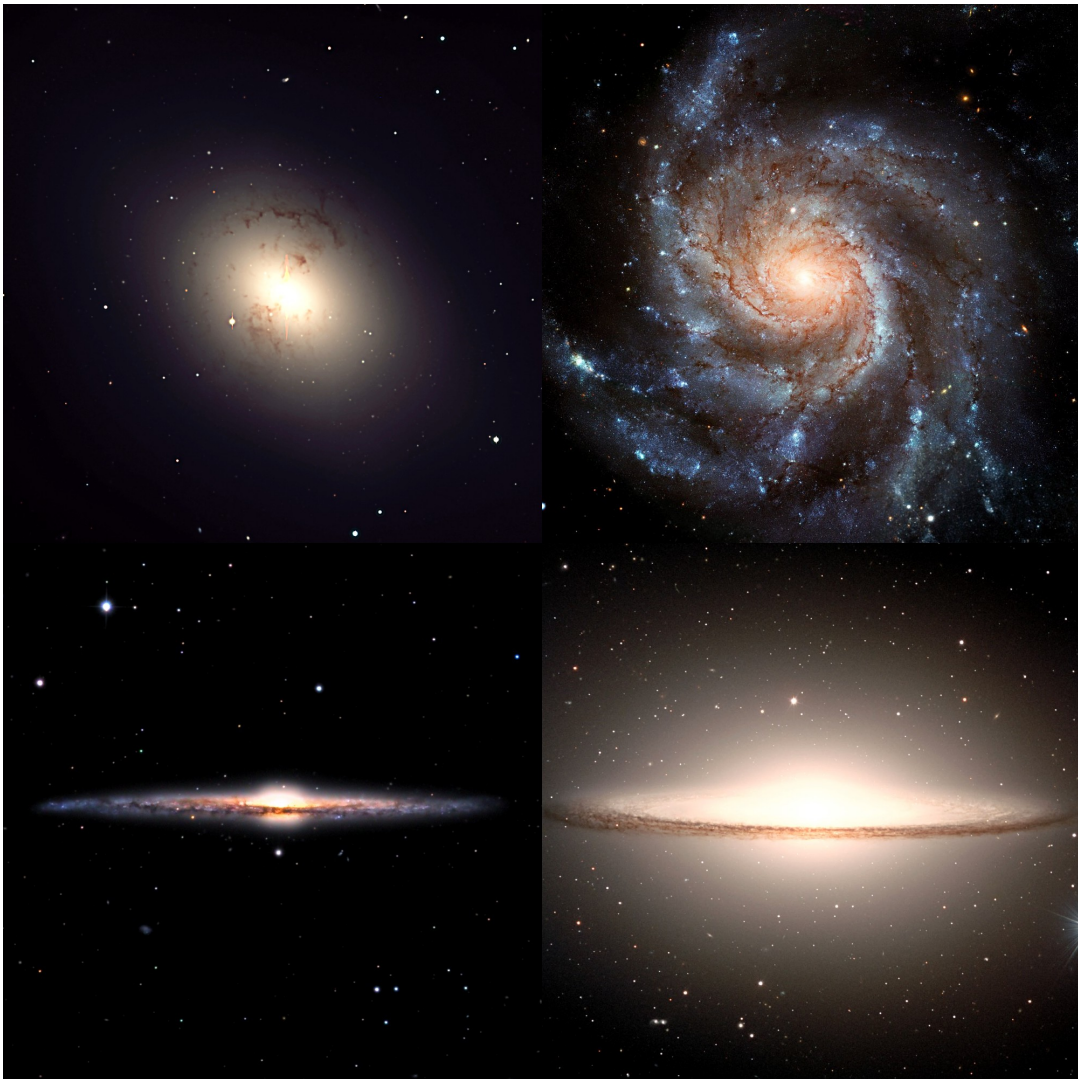
Figure 1.2 Images of observed galaxies. The upper left panels shows the elliptical galaxy NGC1316. In the upper right the typical face-on spiral galaxy M101 (the 'Pinwheel' galaxy) is shown while the lower left panel shows NGC4565 (the 'Needle' galaxy), a spiral galaxy seen edge-on. Finally the lower right panel shows the typical early-type spiral M104 (the 'Sombrero' galaxy). Credit: ESO and ESA/NASA.

central galaxy typically survives, although it may be thickened and some of the stars can be removed from the disc and transferred to a spherical component (called bulge) while the satellite is completely destroyed. In this way, galaxy mergers affect the morphology of galaxies and shape their properties. Finally, we receive the light from a galaxy in different bands emitted by its stars depending on their age and their mass distribution.

On the observational side, one finds galaxies with a large variety of structures: e.g. discs, spiral arms, bulges and bars. However, these components are very similar in all galaxies and can

be described with few parameters. In this sense, galaxies show a large amount of regularity on small scales, i.e. galactic scales of several kpc. As a consequence, galaxies can be arranged into a continuous sequence of types, as originally introduced by Hubble (1926) and revised several times (e.g. Kormendy & Bender 1996). This Hubble sequence classifies galaxies into four classes. Elliptical galaxies show little internal structure and have smooth, almost elliptical isophotes. Depending on their ellipticity they are divided into the subclasses E0 to E7. Spiral galaxies have thin discs with spiral arm structures and are divided into two branches, normal spirals and barred spirals, according to whether a bar-like structure is present. They are further divided into three classes a, b and c, according to their bulge fraction. Lenticular (S0) galaxies are the intermediate class between ellipticals and spirals. They have a disc and a bulge, but the bulge is more prominent than in spiral galaxies. Finally irregular galaxies have neither a dominant bulge nor a rotationally symmetric disc. Many of these systems have been perturbed due to a merger event. Ellipticals and lenticulars are often referred to as early-type galaxies, while spirals and irregulars form the class of late-type galaxies. In order to illustrate these types, we show four typical galaxies in Figure 1.2. As we can see, an elliptical galaxy shows little internal structure, while spiral galaxies have many substructures. From the image of a spiral galaxy as seen edge-on, we see that the luminosity decreases with increasing radius, and height above the disc plane. This can be expressed with specific scale parameters, the scalelength and scaleheight.

Observed galaxies not only show a large amount of regularity with respect to their morphology, but they also obey a number of tight scaling relations. Elliptical galaxies, for example, populate a so-called 'fundamental plane' (FP), which is a relationship between the average surface brightness, the effective radius and the central velocity dispersion. The origin of the FP is usually interpreted in terms of the virial theorem, which leads to specific slope parameters for the FP. The deviation of the observed slopes from the virial predictions is called the 'tilt' of the FP. The physical reasons for this tilt and for the small thickness of the FP, however, are still poorly understood. Another open issue is, how the FP plane evolves with redshift, e.g. why elliptical galaxies are more compact at high redshift. Similarly, disc galaxies obey a number of scaling relations, i.e. correlations between luminosity, the scalelength and the rotation velocity. The relation between luminosity and the scalelength indicates that the details of the gas accretion process depend on the size of the system, while the relation between luminosity and rotation velocity (the so-called 'Tully-Fisher relation') states a connection between the dynamical and the luminous mass, and is influenced by feedback mechanisms. However, the details of the physical processes that determine these relations, are so far not well understood, and it is hard to model all scaling relations simultaneously.

In the light of the large amount of regularity on small scales, we can specify the three requirements that are needed for a successful galaxy formation model that attempts to reproduce and explain observed galaxies and tries to make useful predictions. The first prerequisite is the inclusion of gas and the processes it is subject to in the model. While this seems trivial, there are many studies that neglect the gaseous component and use initial conditions that employ only the

collisionless components stars and dark matter. However, not only does the gas form stars, subsequently altering the density and gravitational potential, but the gas is also able to radiate energy away through cooling. By this mechanism, the total energy content of a system can be reduced, which is not possible in pure collisionless studies. The next requirement is the achievement of a high resolution by the model, in order to be able to capture all effects that shape the morphology of the galaxy. The regularity of the various components (e.g. scalelengths and scaleheights of the discs and bulge sizes) can only be modelled correctly if the smallest scales that can be resolved within the model are much smaller than the typical scales of the system. Finally, the last requirement that any galaxy formation model must provide is the inclusion of the cosmological background. As we have outlined above, the cosmological framework has a large impact on the evolution of a galaxy. It specifies when a halo and a galaxy form and how much mass they accrete during their evolution. Furthermore, the cosmology determines the merger histories of the galaxies, i.e. when and how often a galaxy undergoes a merger event. This is very important to determine the morphological transformation a galaxy is subject and is thus directly reflected in the scale parameters. As a consequence, a successful galaxy formation model has to incorporate all three requirements. In addition, although not an absolute requirement, methods are preferred that are able to model the formation and evolution of galaxies within a short amount of time, or for a large number of systems, or even both.

1.2 Numerical simulations

The most popular tool used to study galaxy formation and evolution are numerical simulations. These can be divided into two categories: collisionless N-body simulations, that evolve an initial distribution of point masses according to the laws of gravity, and hydrodynamical simulations that additionally incorporate gas physics, i.e. pressure forces and the formation of stars from gas. N-body methods, which only include two of the three necessary requirements for galaxy formation models – high resolution and a cosmological background – have been employed for a long time. For dark matter haloes, they have yielded a wealth of informations, such as the progenitor mass distribution (Bond *et al.* 1991), merger histories (Lacey & Cole 1993), spatial clustering (Mo & White 1996), density profiles (Navarro *et al.* 1997), substructure (Moore *et al.* 1998; Klypin *et al.* 1999) and angular momentum distributions (Bullock *et al.* 2001). State-of-the-art N-body simulations such as the 'Millennium' simulation (Springel *et al.* 2005b), the 'Via Lactea' simulation (Diemand *et al.* 2007), the 'Aquarius' project (Springel *et al.* 2008) and the 'GHALO' simulations (Stadel *et al.* 2009) have established a coherent picture of the properties of dark matter haloes.

The first hydrodynamical simulations of galaxy formation including dark matter focused on the collapse of a homogeneous uniformly rotating sphere (Katz & Gunn 1991; Katz 1992). In this simplified scenario the gas physics could be included reaching a good resolution. However,

the cosmological background was not considered. Similarly, studies of the evolution of galaxies in binary galaxy (i.e. the isolated merger of two galaxies) were able to study galaxy evolution at a very high resolution employing gas physics (Noguchi 1988; Combes *et al.* 1990; Mihos & Hernquist 1996; Cox *et al.* 2006a; Naab *et al.* 2006) while the initial conditions for the merger were not cosmologically motivated. Instead, pre-formed model galaxies have been employed, where their properties and those of the merger orbits are drawn from multidimensional grids. The first hydrodynamical simulations of galaxy formation and evolution by hierarchical clustering from proper cosmological initial conditions were performed by Navarro & Benz (1991) and Navarro & White (1994). This method, also called a 'full cosmological simulation', samples the cosmological initial conditions at high redshift in a large box, and evolves the density distribution using the laws of gravity and hydrodynamics, including the various astrophysical processes that transform the baryons into luminous galaxies. While in this way many systems can be modelled, the problem is that the resolution that can be obtained is very low. As a consequence the small scales at which the important physical processes happen cannot be resolved and the properties of the resulting galaxies do not agree with observations.

In order to overcome this problem and include all three necessary requirements, a new method was introduced by Katz & White (1993) and has been improved to date. This 'renormalisation' or 'zoom-in' technique is similar to a cosmological simulation, but increases the resolution in a selected region within a large cosmological volume. This volume includes regions with varying mass and spatial resolution which decreases with the distance from a selected object, e.g. a single galaxy-sized system. In this way most of the particles are placed in the region of interest, optimising the use of computer time. Simulations with millions of baryonic and dark matter particles are thus able to produce stellar disks whose size is comparable with that of real galaxies (Governato *et al.* 2004; Robertson *et al.* 2004; Okamoto *et al.* 2005; Governato *et al.* 2010). The drawback of this approach, however, is the still enormous computational expense, even if the resolution is only very high in the regions of interest. As a consequence, a single galactic system can only be simulated within several months, such that is not possible to obtain a statistical sample of highly resolved model galaxies.

1.3   Semi-analytic models

In order to overcome the limitations of numerical simulations, a semi-analytic approach was developed by White & Frenk (1991), based on the two-stage theory by White & Rees (1978) that separates the evolution of the dark matter and baryonic components. This method, which was only considering isolated systems and could only predict average quantities, was later extended to model the full merger history as predicted by the CDM scenario. This was done independently by the 'Munich' group at the Max-Planck-Institute for Astrophysics in Munich (Kauffmann *et al.* 1993) and the 'Durham' group at the University of Durham (Cole *et al.* 1994) and has been

adopted by other groups, such as the 'Santa Cruz' group (Somerville & Primack 1999) and the 'Trieste' group (Monaco *et al.* 2007). In a semi-analytic model (SAM) one starts with specifying a cosmological model and then traces the merger histories for a series of dark matter haloes using either an N-body simulation or the analytic extended Press-Schechter (EPS) formalism. The evolution of the baryonic component in the haloes, which consists of the components hot gas, cold gas and stars, is followed by using simple, yet physical analytic recipes for gas cooling and accretion, star formation and feedback. Cooling converts hot gas into cold gas, star formation converts cold gas into stars, and feedback converts cold gas into hot gas, or reheats the hot gas directly. When two haloes merge, the less massive progenitor galaxy becomes a satellite, while the more massive one becomes the central galaxy. It is then assumed that a satellite can merge with the central object on a time scale set by dynamical friction, possibly altering the properties of both systems. In a minor merger the satellite is assumed to be destroyed without major impact on the central galaxy, while in a major merger the discs of both progenitors are likely to be destroyed, resulting in an elliptical remnant. A sample of model galaxies that represents the galaxy population in the present-day Universe can then be built by modelling a large number of haloes that sample the halo mass function and applying a stellar synthesis model that converts the star formation history and metallicity into luminosity and colour.

Thus, in a SAM the complicated astrophysical processes that are responsible for the formation and evolution of galaxies are modelled as a set of recipes which carry a number of free model parameters. As the current understanding of many of these processes is limited, the model parameters cannot be derived from first principles. Instead, the model is normalised with a set of observational constraints, and with the help of more detailed hydrodynamical simulations (e.g. the evolution during a merger). The advantage of SAMs is their flexibility, as it is possible to run many realisations in a short amount of time. It is very simple to test the effects of the various assumptions and model parameters, which highlights the importance of certain specific model ingredients. By failing to reproduce the faint-end slope of the luminosity function in early models, it was discovered that SN feedback and re-ionisation are important requirements (Kauffmann *et al.* 1994; Heyl *et al.* 1995; Baugh *et al.* 1996). As later models predicted a colour-magnitude relation that was inverted with respect to the observations, it became clear that chemical evolution and a treatment for dust extinction had to be included (Kauffmann & Charlot 1998; Cole *et al.* 2000). Finally, the overprediction of massive galaxies seemed to require a process that can suppress cooling in massive haloes, such as AGN feedback (Bower *et al.* 2006; Croton *et al.* 2006; Somerville *et al.* 2008a; Kang *et al.* 2006), thermal conduction (Benson *et al.* 2003; Voigt & Fabian 2004), or multi-phase cooling (Maller & Bullock 2004). This shows that SAMs have been able to yield many insights into the process of galaxy formation. The drawback of this method is that by construction any back reactions of the baryons on the dark matter haloes are neglected and have to be included a posteriori. Furthermore, SAMs yield little or no spatial information: most SAMs do not predict the spatial location of the galaxies. Some morphological parameters are computed

only with a simple recipe (such as the scalelength of the disc), while others are completely ne-glected (such as the disc scaleheight). As a consequence, one can consider a SAM as a galaxy formation model with a low resolution, that is able to predict many statistical properties within a short amount of time.

1.4 Combining simulations and semi-analytic models

Existing galaxy formation models have led to numerous insights, however, none of them is capable of incorporating all three requirements together without the need for a large computational time. The goal of this thesis is to develop a method that includes gas physics, a cosmological background and offers the best resolution while being able to model a sample of galaxies within a short amount of time. In particular, hydrodynamical merger simulations can achieve a very high resolution and have a short run time, as the system is only modelled in the regions of interest, but they lack a cosmological background. On the other hand, SAMs are able to predict the merger histories that follow from a specific cosmological model for a large amount of galaxies within a short amount of time. This information is given in galaxy merger trees, which specify for a certain system at $z = 0$ when each satellite galaxy entered the halo and what were the properties of these satellites. Consequently we combine this prediction of SAMs with hydrodynamical merger simulations by using the semi-analytic merger trees as initial conditions for a multiple merger simulation. Specifically, we evolve the galaxy in the main branch in a simulation and include the satellite galaxies in this simulation at the time when the satellite enters the larger halo using the satellite properties predicted by the SAM. In this way we gain the advantages of the merger simulations (high resolution and correct treatment of gas physics) and the SAM (cosmological background). Simultaneously, the computational cost is comparably low (a few days using 32 processors), so that a meaningful sample can be modelled in a short amount of time.

Since with this method the small scales can be resolved, that are important for the evolution of galaxies and their resulting morphology, it is particularly well suited for studies that focus on the evolution of the stellar components of galaxies and their scale parameters, such as the disc scalelength and height and the bulge radius. In particular, we are able to investigate how the stellar disc evolves during mergers and how the stellar bulge is formed. Furthermore, we want to study how the stellar mass grows for various galaxies and which processes are most important for its evolution. While many applications of our model focus on the evolution of the central galaxy, we can also address the evolution of the satellite population at a high resolution and investigate whether satellites are able to gain mass while they orbit the central galaxy and how much of their mass is stripped due to tidal forces. Specific questions we plan to address with our new method include: How does the morphology of a galaxy transform in mergers? How does the bulge fraction change in a major merger and what happens to the disc in minor mergers (thickening, warping and bar formation)? What is the efficiency of starbursts in mergers? How efficient is gas cooling and

accretion after a merger? How does the stellar mass of a galaxy grow – are gas accretion and star formation more important or the accretion of satellite stars? How is mass stripped from orbiting satellites and with which efficiency? How do stellar streams form? Finally, we are able to develop generalised semi-analytic prescriptions (e.g. to predict spheroid sizes and velocity dispersions) based on the results of our simulations. In this way, also existing semi-analytic recipes can be improved.

1.5 Structure of the thesis

In this thesis we aim to develop a novel method to study galaxy formation and evolution by combining semi-analytic predictions with high resolution hydrodynamical merger simulations. In order to do this, we extend the initial conditions used in the simulations to include accretion from the halo (i.e. smooth accretion of dark matter and cooling of the hot gaseous halo for the baryonic component). Using our method in a set of simulations, we study the evolution of the stellar mass and the morphology, as well as the contamination of a MW-like galaxy with satellite stars.

This thesis is structured as follows: chapter 2 discusses the foundation of our method, numerical simulations. First an introduction to N-body and hydrodynamical techniques is presented, followed by the cooling, star formation and feedback models employed in the hydrodynamical code GADGET-2 (Springel 2005), which is used in this thesis. We then explain the code that creates the initial conditions for merger simulations, i.e. pre-formed galaxies consisting of a dark matter halo a stellar and gaseous disc and a stellar bulge. We apply these codes in a suite of minor merger simulations to study the heating and thickening of a thin disc, like that of the MW. In particular, we focus on the difference between dissipational and dissipationless simulations and compare our results with observations.

In chapter 3 we outline the techniques used in SAMs. For this we demonstrate how halo merger trees can be obtained from the analytic Press-Schechter formalism and from N-body simulations. Furthermore, we explain how the baryonic components are evolved, which includes gas cooling, star formation and feedback, galaxy mergers and chemical evolution. We show how these processes are modelled in the *Santa Cruz* SAM (Somerville *et al.* 2008a), which is employed in this thesis. Applying the SAM to a large sample of merger trees, we study the merger histories of MW-like galaxies. We determine the number of mergers as a function of the halo mass and compute the probability for multiple mergers, i.e. a second satellite entering the halo before the first satellite has merged with the central galaxy. Moreover, we study the dependence of the merger rate on the merger ratio, the initial gas fraction and the morphology.

The initial conditions generator is extended in chapter 4 in order to include accretion from the halo. For the dark matter component, the smooth accretion is modelled with many small overdensities, called blobs, which have a three-dimensional Gaussian density profile. Each blob is then placed around the dark matter halo, such that it enters at a specified time, chosen to reproduce the

mass accretion history of the halo. For the baryonic component, we include a slowly rotating hot gaseous halo that is in hydrostatic equilibrium with the dark matter halo. We apply this modification in a suite of major merger simulations and study how the starburst efficiency and the structural and kinematic properties of the remnants change when a gaseous halo is included. In addition, we run a minor merger simulation and study how the disc thickening is changed when a hot halo is included.

In chapter 5 we combine semi-analytic merger trees with hydrodynamical simulations using the galaxies in semi-analytic merger trees as the initial conditions for multiple merger simulations. We first illustrate the general procedure and then demonstrate how we create particle representations of semi-analytic galaxies and how these model galaxies are included in the merger simulations. We apply our new method in a set of ten merger trees that yield central galaxies comparable to the MW. The evolution of both the central and the satellite galaxies are analysed, with the results compared to the predictions by the SAM. This includes the total stellar mass, the bulge fraction and the scale parameters. In a last study, we address the question of whether it is possible to distinguish stars that formed in the central galaxy from stars that originated in a satellite employing a pure kinematic analysis.

Finally, in chapter 6 we summarise the methods that have been used in this thesis and the results we have obtained. We also give an outlook on future projects utilising our new model, including a study focusing on the origin and the evolution of the galaxy FP, and a study about stellar stripping and the morphological transformation of satellites in a MW-like halo. In appendix A we summarise all conventions and acronyms and in appendix B we include a DVD containing additional visualisation material, i.e. rendered movies of the simulations.

Chapter 2

Numerical Simulations

Numerical simulations have become a very useful tool in theoretical studies of the structure formation process in the Universe. This is because direct simulation is often the only method to predict the fully non-linear outcome of the well-specified initial conditions of the standard ΛCDM cosmology. Particularly for the hierarchical structure formation process, with its inherently complex three dimensional geometry (e.g. galactic discs and bulges), it is important to be able to model the astrophysical processes at the relevant scales. In fact, numerical simulations have played a vital role in establishing the viability of the standard cosmogony including fundamental results, such as density profiles of dark matter haloes (Navarro *et al.* 1997), the existence of dark matter substructure (Tormen 1997; Diemand *et al.* 2007), the abundance and clustering properties of dark matter haloes and galaxies (Jenkins *et al.* 1998, 2001; Moster *et al.* 2010), or the gas temperature and profiles of galaxy clusters (Evrard 1990).

2.1 N-body methods

When only collisionless dark matter and stars are considered, state-of-the-art cosmological codes have reached a high degree of accuracy and an impressive dynamical range. As the physical modelling of collisionless systems requires only integrating the $6N$ ordinary differential equations defining the particle motions in Newtonian gravity, there is little doubt about what is needed to achieve this high accuracy: First an accurate gravitational force calculation, second an accurate time integration and third the use of a large number of particles in order to resolve small scales.

The oldest and most simple approach employed for the gravitational N-body problem is the direct summation, or particle-particle (PP) method, where the gravitational forces are directly computed for every pair of particles. Obviously, this method is inefficient for large particle numbers as the cost of the computations scales with $\mathcal{O}(N^2)$. As a consequence, particle-mesh (PM) codes have been developed in which space is discretised on a mesh and, for the purposes of computing the density and the gravitational potential, particles are assumed to be divided between the nearby vertices of the mesh. The potential Φ can then be easily calculated from the Poisson Equation:

$$\Delta \Phi = 4\pi G \rho \,, \tag{2.1}$$

where G is the gravitational constant and ρ is the density. By using a Fourier transform one can go to the frequency domain, where the Poisson equation has the simple form

$$\hat{\Phi} = 4\pi G \frac{\hat{\rho}}{k^2} \,, \tag{2.2}$$

where k is the wavenumber and the hats denote Fourier transforms. The advantage of this method is that it is very fast, as it only depends on the number of grid cells and Fourier techniques. The disadvantage is, however, that for scales below one to two mesh cells, the force is heavily suppressed, thus greatly reducing the spatial resolution. In order to circumvent this problem, P^{3}M codes have been developed. They have two parts: a PM part which takes care of large-scale forces, and a PP part, which adds a small-scale particle-particle contribution. However, because of strong clustering at the late stages of evolution, the PP part becomes prohibitively expensive once large objects start to form in great numbers. A further improvement is achieved by the AP3M method, which uses additional Fourier meshes adaptively placed on areas of high density.

An alternative to these schemes are hierarchical tree algorithms, pioneered by Appel (1981, 1985) which have no intrinsic resolution limit. In tree methods, particles are arranged in a hierarchy of groups which can be achieved by dividing the volume into cubic cells or with nearest-neighbour pairings. Gravitational forces are then computed directly within a group while particles in distant groups can be either treated as a single large particle located at its centre of mass or as a low-order multipole expansion. In order to be treated as a distant group a tree node has to fulfil an opening criterion. The size of the opening angle θ determines the accuracy of the force calculation: for smaller values of θ the forces will become more accurate, but also more costly to compute. For an optimal opening angle the number of particle pair interactions that must be computed can be dramatically reduced so that the computational cost of a complete force evaluation scales as $\mathcal{O}(N \log N)$. While PM codes are generally much faster for near-homogeneous particle distributions, tree codes can adapt flexibly to clustering states and are more efficient than PM codes if a large dynamic range in density is needed. Furthermore, tree codes are free from any geometrical restrictions. A rather recent development is the combination of PM and tree solvers into hybrid TreePM codes. In this approach, the PM method is used for the computation of long-range forces, while a tree method is used for the short-range part. Thus, the direct summation in the P^{3}M method is replaced by a tree algorithm. This allows for reduced computational times in comparison to pure tree codes.

2.2 Hydrodynamics

Compared to gravity, much larger conceptual differences exist between the different hydrodynamical methods employed in current cosmological codes. The most prominent ones are Eulerian mesh-based hydrodynamics and Lagrangian smoothed particle hydrodynamics (SPH). The Eu-

lerian specification of the flow field is a way of looking at gas motion that focuses on specific locations in the space through which the gas flows as time passes. Eulerian methods discretise space and represent gas variables on a mesh. The Lagrangian specification of the flow field is a way of looking at gas motion where the observer follows an individual gas parcel as it moves through space and time. These parcels can be modelled with particles with discretised mass. Both methods have found widespread application in astrophysics.

The foundational axioms of gas dynamics are the conservation laws, specifically, conservation of mass, conservation of momentum (Newton's Second Law of Motion), and conservation of energy (First Law of Thermodynamics). These conservation laws can be written in the form of integral equations as well as in the form of partial differential equations. In the laboratory frame the hydrodynamical equations can be written in their Eulerian form:

$$\partial_t \rho + \nabla(\rho \boldsymbol{v}) = 0 \tag{2.3}$$

$$\partial_t(\rho \boldsymbol{v}) + \nabla(\rho \boldsymbol{v}\boldsymbol{v}) + \nabla P = -\rho \nabla \Phi \tag{2.4}$$

$$\partial_t(\rho e_{tot}) + \nabla[(\rho e_{tot} + P)\boldsymbol{v}] = 0. \tag{2.5}$$

Here, $\boldsymbol{v}$ is the velocity of the flow, P is the pressure, and e_{tot} is the total specific energy, consisting of thermal (internal) specific energy e and kinetic specific energy $e_{kin} = u^2/2$.

These hydrodynamic equations can also be written in the rest frame of the flow, where they take their Lagrangian form. The idea is to follow a gas element along its path and see how its density and pressure change along its way. For this we introduce the Lagrangian time derivative $\mathrm{d}/\mathrm{d}t$ as

$$\frac{\mathrm{d}}{\mathrm{d}t} = \frac{\partial}{\partial t} + \boldsymbol{v} \cdot \nabla. \tag{2.6}$$

With this, the hydrodynamical equations become:

$$\frac{\mathrm{d}\rho}{\mathrm{d}t} + \rho \nabla \boldsymbol{v} = 0 \tag{2.7}$$

$$\frac{\mathrm{d}\boldsymbol{v}}{\mathrm{d}t} + \frac{\nabla P}{\rho} = -\nabla \Phi \tag{2.8}$$

$$\frac{\mathrm{d}e}{\mathrm{d}t} + \frac{P}{\rho}\nabla \boldsymbol{v} = 0. \tag{2.9}$$

In this form the equation of momentum conservation has a physical interpretation: a gas parcel will be accelerated due to forces, which are the gradients of the pressure and the gravitational potential. The energy conservation equation can be interpreted as follows: the thermal energy of a gas parcel changes only as a result of adiabatic compression.

2.2.1 Eulerian method: mesh codes

In the traditional Eulerian methods space is discretised and gas variables are represented on a mesh: $x \to x_i$ and $t \to t^n$. The numerical solution is solved on these discrete mesh points. Thus functions as $q(x, t)$ are replaced by their discrete counterparts $q(x_i, t^n) = q_i^n$. The equations must be formulated in a way that q_i^{n+1} can be derived from q_i^n. The difficulty is then to formulate the discretised form of the differential equations such that the solutions for the q_i^{n+1} are numerically stable and as close as possible to the true $q(x, t)$. In practice, one can solve the system of hyperbolic equations by advecting them on the mesh. Of course, there is no ideal and universally good method and some problems require entirely different methods than others. Hydrodynamics of subsonic flows require high-order precision algorithms, for example, while for supersonic flows so-called shock-capturing methods are needed.

There are decades of experience with Eulerian methods and for various problems accurate schemes exist, which offer high-order spatial accuracy, have negligible post-shock oscillations, and low numerical diffusivity. Moreover, mesh codes offer superior resolving power for shocks, with some methods being able to capture shocks without artificial viscosity and with very low residual numerical viscosity. However, there are still several fundamental problems. The most serious issue is the lack of Galilean invariance, which makes the results depend on the presence of bulk motion. While this problem is less serious in studies of planet and star formation, it is rather substantial in studies of galaxy formation. Here, galaxies move with large velocities relative to each other. Those velocities are often orders of magnitude larger than the sound speed of the interstellar medium which is followed hydrodynamically.

Another problem of static meshes is that they are only poorly suited for the high dynamic range encountered in cosmology. Even for large meshes, individual galaxies are only poorly resolved, which makes resolving the internal structure (discs and bulges) even harder. A possible solution is given by the development of adaptive mesh refinement (AMR) codes. In this method, subgrids are adaptively positioned in regions of high density hence achieving a higher resolution and dynamic range. However, even for AMR codes, various problems remain. It is challenging to model systems with high relative velocities to the adopted reference frame, as it is hard to construct refinement criteria which are able to correctly anticipate the motion of the system on the mesh. Furthermore, AMR codes have difficulties with accurately treating structure formation driven by gravitational instability, as it is difficult to capture all the small density fluctuations that grow at high redshift through refinement.

2.2.2 Lagrangian method: smoothed particle hydrodynamics

In Lagrangian SPH, it is not space that is discretised, but mass. The particle-based SPH is extremely flexible in its ability to adept to any given geometry. As its Lagrangian nature allows a locally changing resolution that automatically follows the local mass density it is particularly well

suited to follow the gravitational growth of structure. Thus, computational time can be saved, by focusing the computational effort on the regions of the highest gas concentrations, which are the regions of primary interest in cosmology. Moreover, SPH ties naturally to the N-body approach for self-gravity and can be easily implemented in three dimensions. However, an important disadvantage of SPH is that the method has to rely on an artificial viscosity for supplying the necessary entropy injection in shocks. The shocks are unavoidably broadened over the smoothing scale and can no longer be resolved as discontinuities.

In SPH, a set of discrete tracer particles is used to describe the state of the gas. One can think of the particles with positions $\boldsymbol{x_i}$, velocities $\boldsymbol{v_i}$ and masses m_i as elements that sample the gas in a Lagrangian sense. Continuous gas quantities are defined by a kernel interpolation technique. This means that the hydrodynamical properties of each particle are smoothed with a kernel $W(\boldsymbol{x_i} - \boldsymbol{x_j}, h_i)$ over its smoothing length h_i, which is chosen such that a constant number of particles (~ 64) lies within a sphere of radius h_i. The density is then estimated as

$$\rho(\boldsymbol{x_i}) = \rho_i = \sum_{j=1}^{N} m_j W(\boldsymbol{x_i} - \boldsymbol{x_j}, h_i). \tag{2.10}$$

For each of the SPH particles the hydrodynamical equations are based on the Lagrangian form of the Euler equations. One can easily show that the equation of motion for SPH particles can be written in the form

$$\frac{\mathrm{d}\boldsymbol{v_i}}{\mathrm{d}t} = -\sum_{j=1}^{N} m_j \left[f_i \frac{P_i}{\rho_i^2} \nabla_i W(\boldsymbol{x_i} - \boldsymbol{x_j}, h_i) + f_j \frac{P_j}{\rho_j^2} \nabla_j W(\boldsymbol{x_i} - \boldsymbol{x_j}, h_j) \right], \tag{2.11}$$

where the coefficients f_i are given by

$$f_i = \left(1 + \frac{h_i}{3\rho_i} \frac{\partial \rho_i}{\partial h_i} \right)^{-1}. \tag{2.12}$$

The pressure for each particle is given by $P_i = A_i \rho_i^{\gamma}$, where A_i is a measure for the entropy of the particle and γ is the adiabatic index. If there are no shocks and no external sources of heat, it is simple to compute the change of velocity and position in one time step from the equation of motion. However, gas flows can easily develop discontinuities such that entropy is generated. In order to capture shocks, SPH employs an artificial viscous force

$$\left(\frac{\mathrm{d}\boldsymbol{v_i}}{\mathrm{d}t} \right)_{\mathrm{visc}} = -\sum_{j=1}^{N} m_j \Pi_{ij} \nabla_i W(\boldsymbol{x_i} - \boldsymbol{x_j}, h_i), \tag{2.13}$$

where Π_{ij} is non-zero only when particles approach each other.

Due to the many advantages of an SPH code when modelling the interactions of galaxies,

where a large dynamic range is needed, we use the GADGET-2 code (Springel 2005) for all numerical studies in this work.

2.3 **The SPH code** GADGET-2

The principal structure of GADGET-2 is that of a TreeSPH code. This means that gravitational forces are computed using a tree algorithm with a hierarchical multipole expansion while the gas dynamics are followed with SPH. Alternatively, GADGET-2 supports the use of the TreePM method. The code is massively parallel and has been used on up to 64 parallel CPUs in our studies. Two types of particles are employed: collisionless particles which represent dark matter and stars and respond only to gravitational forces and collisional particles which represent the gas and feel gravity and pressure. Gravitational forces are softened with the spline kernel used in SPH employing $W(x, 2.8\epsilon)$ which corresponds to a Plummer sphere with a smoothing length ϵ.

The smoothing kernel for the SPH calculations is given by:

$$W(x, h) = \frac{8}{\pi h^3} \begin{cases} 1 - 6\left(\frac{x}{h}\right)^2 + 6\left(\frac{x}{h}\right)^3, & \text{if } 0 \leq \frac{x}{h} \leq \frac{1}{2}, \\ 2\left(1 - \frac{x}{h}\right)^3, & \text{if } \frac{1}{2} < \frac{x}{h} \leq 1, \\ 0, & \text{if } \frac{x}{h} > 1. \end{cases} \tag{2.14}$$

The artificial viscosity implemented in GADGET-2 has the form

$$\Pi_{ij} = -\frac{\alpha}{2} \frac{(c_i + c_j - 3w_{ij})w_{ij}}{\rho_{ij}}, \tag{2.15}$$

where α is a free parameter (in the range 0.5-1.0), c_i and c_j are the sound speeds of the particles i and j, ρ_{ij} is the arithmetic mean of the density and $w_{ij} = (\boldsymbol{v_i} - \boldsymbol{v_j}) \cdot (\boldsymbol{x_i} - \boldsymbol{x_j})/|\boldsymbol{x_i} - \boldsymbol{x_j}|$ is the relative velocity projected on to the separation vector. This choice reduces the occurrence of very large viscous accelerations resulting in a more stable time integration.

Furthermore GADGET-2 uses an SPH formulation which conserves both energy and entropy in regions of free dissipation even when fully adaptive smoothing lengths are used. Traditional SPH methods violate entropy conservation in certain circumstances leading to problems as this accelerates cooling in dense regions.

Up to now, we have described how the code computes the gravitational and hydrodynamical forces that are responsible for the dynamics of the system. In this model, however, the gas can only cool adiabatically which means that radiative cooling is not considered so far. Furthermore, when the gas cools it can form new stars thereby releasing feedback energy into the surrounding gas. Thus in order to correctly model the formation and interaction of galaxies, it is important to consider these processes and implement them into the code. The problem here is that the relevant physical processes happen on scales which are smaller than those that can be resolved. Specifically, stars form from dense clouds consisting of molecular hydrogen with a spatial extension of

several parsecs. However, current spatial resolutions reached in SPH simulations are on the order of tens of parsecs. This means that in order to model star formation and feedback an effective subresolution model has to be used which can predict the average star formation and feedback rates at the resolved scales.

2.3.1 Cooling, star formation and feedback

In order to model the sub-grid physics, Springel & Hernquist (2003) have developed a multiphase model for the gas. In this model, the gas particles are treated as a two-phase medium, comprised of condensed clouds in pressure equilibrium with an ambient hot gas. The material available for star formation is supplied by the cold clouds. The local density of the hot medium is given by ρ_{h}, the density of cold clouds is ρ_{c}, the density of long-lived stars is ρ_*, and $\rho = \rho_{\mathrm{h}} + \rho_{\mathrm{c}}$ is the total gas density. As individual molecular clouds and stars cannot be resolved, ρ_{c} and ρ_* represent averages over small regions. The specific energy of the hot and cold components is e_{h} and e_{c}, respectively, and the thermal energy per unit volume of the gas is given by $\epsilon = \rho_{\mathrm{h}} e_{\mathrm{h}} + \rho_{\mathrm{c}} e_{\mathrm{c}}$. The three basic processes that are responsible for mass exchange between the components are star formation, cloud evaporation arising from SNe and cloud growth caused by radiative cooling. All these processes are only active when the density exceeds a threshold $\rho > \rho_{\mathrm{th}}$ which is motivated by the observed star formation threshold, otherwise only ordinary cooling is active.

For the star formation process, one assumes that cold clouds are converted to stars on a characteristic time-scale t_* and that a mass fraction β of these stars are short-lived and instantly explode as SNe:

$$\frac{\mathrm{d}\rho_*}{\mathrm{d}t} = \frac{\rho_{\mathrm{c}}}{t_*} - \beta \frac{\rho_{\mathrm{c}}}{t_*} = (1 - \beta)\frac{\rho_{\mathrm{c}}}{t_*} \, . \tag{2.16}$$

The reservoir of cold clouds is therefore depleted by star formation at the rate ρ_{c}/t_* while the mass in the hot phase is increased as $\beta\rho_{\mathrm{c}}/t_*$ through ejecta from SNe. The parameter β is the mass fraction of massive stars ($> 8M_\odot$) formed for each initial population of stars and thus depends on the initial mass function (IMF). For the Salpeter (1955) IMF

$$\xi(m) \propto m^{-1.35} \, , \tag{2.17}$$

with upper and lower limits of 40 and 0.1 $M_\odot$, respectively, it has the value $\beta = 0.1$. If a Kroupa (2001) IMF is adopted,

$$\xi(m) \propto \begin{cases} m^{-0.3}, & \text{for } 0.01 \leq \frac{m}{M_\odot} < 0.08, \\ m^{-1.3}, & \text{for } 0.08 \leq \frac{m}{M_\odot} < 0.5, \\ m^{-2.3}, & \text{for } 0.5 \ \ \leq \frac{m}{M_\odot} \end{cases} \tag{2.18}$$

it has the value $\beta = 0.16$.

In addition to returning mass to the hot phase, SNe also release energy. For the canonical value of 10^{51} erg per SN, an average return of $\epsilon_{\mathrm{SN}} = 4 \times 10^{48}$ erg $M_\odot^{-1}$ is expected for each solar mass and a Salpeter IMF, while for a Kroupa IMF we get $\epsilon_{\mathrm{SN}} = 9 \times 10^{48}$ erg $M_\odot^{-1}$. This energy can be expressed as an equivalent SN temperature

$$T_{SN} = \frac{2\mu}{3k} e_{SN} = \frac{2\mu}{3k} \frac{1-\beta}{\beta} \epsilon_{SN}, \tag{2.19}$$

where μ is the molecular weight and k is the Boltzmann constant. For a Salpeter IMF, $T_{SN} \approx 10^8$K, while for a Kroupa IMF, $T_{SN} \approx 1.25 \times 10^8$K.

The mass of the ambient gas is not only increased by exploding stars, but also by cloud evaporation. When cold clouds are evaporated inside the hot bubbles of SNe, material is moved from the cold clouds to the hot gas. The total mass of clouds that are evaporated is assumed to be proportional to the mass in SNe:

$$\left(\frac{\mathrm{d}\rho_c}{\mathrm{d}t} \right)_{\mathrm{EV}} = A\beta \frac{\rho_c}{t_*}, \tag{2.20}$$

where the efficiency A of the evaporation process is expected to be a function of the local environment.

Furthermore, a process by which cold clouds come into existence and grow has to be modelled. For this, one assumes that the radiated energy cools gas from the temperature of the hot phase to that of the cold phase and thus leads to a growth of the cold clouds:

$$\left(\frac{\mathrm{d}\rho_c}{\mathrm{d}t} \right)_{\mathrm{RC}} = - \left(\frac{\mathrm{d}\rho_h}{\mathrm{d}t} \right)_{\mathrm{RC}} = \frac{\Lambda_{\mathrm{net}}(\rho_h, e_h)}{e_h - e_c}. \tag{2.21}$$

The cooling function Λ_{net} is computed for a primordial mixture of hydrogen and helium as described by Katz *et al.* (1996). The abundances of the various ionisation states are computed explicitly in the presence of a spatially uniform time-independent local UV background field in the optically thin limit (Haardt & Madau 1996). The temperature of the cold clouds is typically assumed to be $T \approx 1000$K. In summary, the rates at which the masses of the hot and the cold phases evolve (when $\rho > \rho_{\mathrm{th}}$) can be written as

$$\frac{\mathrm{d}\rho_c}{\mathrm{d}t} = -\frac{\rho_c}{t_*} - A\beta \frac{\rho_c}{t_*} + \frac{\Lambda_{\mathrm{net}}(\rho_h, e_h)}{e_h - e_c} \tag{2.22}$$

$$\frac{\mathrm{d}\rho_h}{\mathrm{d}t} = \beta \frac{\rho_c}{t_*} + A\beta \frac{\rho_c}{t_*} - \frac{\Lambda_{\mathrm{net}}(\rho_h, e_h)}{e_h - e_c}. \tag{2.23}$$

Following McKee & Ostriker (1977), the density dependence of the evaporation parameter A is expressed as

$$A(\rho) = A_0 \left(\frac{\rho}{\rho_{\mathrm{th}}} \right)^{-4/5}. \tag{2.24}$$

Finally, the star formation time-scale t_* needs to be specified. Since a unique explanation for

the empirical Schmidt law is as of yet unknown, modelling star formation processes is largely aimed at reproducing this relationship. Any process in which the gas consumption time depends on the local average dynamical time ($\propto \rho^{-1/2}$) will produce a Schmidt-type relation (Kravtsov 2003). For this reason t_* is parametrized as:

$$t_*(\rho) = t_0^* \left(\frac{\rho}{\rho_{\mathrm{th}}} \right)^{-1/2} . \tag{2.25}$$

The free parameters of the model are thus β and T_{SN} (which have been fixed depending on the IMF) and the parameters that determine the regulation of the multiphase model, ρ_{th}, A_0, and t_0^*, which need to be fixed. A_0 can be constrained by requiring that the cooling of the hot phase happens at the onset of star formation ($\rho = \rho_{\mathrm{th}}$). Therefore the cooling function has to fall at this temperature, which is at $\sim 10^5$ K. Thus $T_{\mathrm{SN}}/A_0 = 10^5$ K which fixes A_0 to a value of $A_0 \approx 1000$ for a Salpeter IMF, and $A_0 \approx 1250$ for a Kroupa IMF. The threshold density ρ_{th} is determined self-consistently by demanding that the equation of state (EOS) is continuous at the onset of star formation. Thus the only free parameter remaining is the star formation time-scale t_0^*. As this parameter sets the overall gas consumption time-scale it can be constrained by observations of the efficiency of star formation.

Observationally, a tight correlation between disc-averaged measurements of the star formation rate (SFR) per unit area and the surface density of the gas is found, e.g. by Kennicutt (1998):

$$\Sigma_{\mathrm{SFR}} = 2.5 \times 10^{-4} \left(\frac{\Sigma_{\mathrm{gas}}}{M_\odot \ \mathrm{pc}^{-2}} \right)^{1.4} . \tag{2.26}$$

Note that this result is valid for a Salpeter IMF, while for a Kroupa IMF the normalisation factor needs to be divided by 2. This Kennicutt law is valid from typical disc-averaged surface densities of $10 M_\odot \ \mathrm{pc}^{-2}$ to very high densities of $10^5 \ M_\odot \ \mathrm{pc}^{-2}$ in central regions of starbursting galaxies. The star formation time-scale t_0^* can now be easily constrained by modelling individual galaxies and fitting for the Kennicutt law. This results in $t_0^* = 2.1$ Gyr for a Salpeter IMF, and $t_0^* = 3.5$ Gyr for a Kroupa IMF.

The SFR for long-lived stars of an SPH particle with mass m is given by $\dot{M}_* = (1-\beta)xm/t_*$, where $x = \rho_{\mathrm{c}}/\rho$ is the density fraction of cold clouds. In a given time step Δt a new long-lived stellar particle of mass $m_* = m/N_g$ is spawn provided that a random number uniformly drawn from the interval $[0, 1]$ falls below

$$p_* = \frac{m}{m_*} \left[1 - \exp\left(-\frac{(1-\beta)x\Delta t}{t_*} \right) \right] , \tag{2.27}$$

where N_g is an integer that gives the number of generations of stars that each gas particle can form. Typically a value of $N_g = 2$ is used meaning that the total number of particles in the simulation increases as a result of star formation.

An interesting consequence of this feedback model is that it leads to self-regulated star forma-
tion. Owing to evaporation, star formation reduces the density in cold clouds, lowering the SFR.
On the other hand, a higher density of hot gas leads to an increase of the cooling rate, and thus to
more rapid replenishment of the cold clouds, increasing the SFR. In this manner, a self-regulated
cycle of star formation is established where, in equilibrium the growth of cold clouds is balanced
by their evaporation arising from SN feedback. Thus, gas contained in dark matter haloes can
cool and settle in a rotationally supported disc, subsequently forming stars at a rate consistent with
observations. In this model, the thickness and the SFR of a disc are regulated by the SN feed-
back, which provides pressure support to the star forming ISM. In this way SN feedback prevents
the ISM from collapsing gravitationally to exceedingly high densities. Note that our version of
GADGET-2 does not include feedback from accreting BHs (AGN feedback) which will therefore
be neglected in this work.

2.3.2 Stellar winds

It has become increasingly clear that galactic winds and outflows play a crucial role in galaxy
formation studies. Being observed at both low and high redshifts, they are not only responsible for
chemically enriching and possibly heating the intergalactic medium, but may also be an important
mechanism in regulating the star formation on galactic scales. As winds can reheat and transport
collapsed gas from the centre of a galaxy back to its extended dark matter halo and even beyond,
they can help to reduce the overall cosmic SFR to a level consistent with observations.

The mechanism by which galactic winds originate is not yet well understood. It is possible
that not all of the hot gas in SN remnants will remain confined to the disc by being quickly used
up to evaporate clouds, but SN bubbles close to the surface of the star forming region may break
out of the disc and vent the hot gas into the halo, producing a galactic wind. Therefore, Springel
& Hernquist (2003) have developed a phenomenological approach which can easily be combined
with the two-phase model of star formation.

In this approach, the disc mass-loss rate that goes into the wind $\dot{M}_w$ is proportional to the SFR

$$\dot{M}_w = \eta \dot{M}_* \,, \tag{2.28}$$

where η is the mass loading factor and $\dot{M}_*$ is the SFR of long-lived stars. Whether this material
can escape from the halo depends on the velocity to which the gas is accelerated, the amount of
intervening gas, and the depth of the potential well, i.e. the mass of the halo. For small velocities
and a large halo mass, the wind material will remain bound to the halo and eventually fall back to
the disc, while in dwarf galaxies even slow winds may escape the halo, thus dramatically reducing
the SFR. The fiducial value for η adopted in the model is $\eta = 2$, consistent with observations
(Martin 1999).

It is further assumed that the wind carries a fixed fraction χ of the SN energy. If the energy input by SNe $\chi \epsilon_{\mathrm{SN}} \dot{M}_*$ is set equal to the kinetic energy of the wind $\dot{M}_w v_w^2/2$, one can obtain the velocity of the wind when it leaves the star forming region:

$$v_w = \sqrt{\frac{2\beta\chi e_{SN}}{\eta(1-\beta)}} \,. \tag{2.29}$$

The fraction χ, or equivalently the velocity v_w, are free parameters of the model and are assumed to be $\chi = 0.25$ and $v_w = 480\,\mathrm{km\,s^{-1}}$ which is typical for a MW-like galaxy at low redshift. Note that this is an energy-driven wind, with a constant wind speed for all haloes and redshifts. The deficiencies of this approximation are discusses in section 4.3.5.

In this model an SPH particle is added to the wind during a time step Δt if a uniformly distributed number in the interval $[0,1]$ falls below

$$p_w = 1 - \exp\left(-\frac{\eta(1-\beta)x\Delta t}{t_*}\right) \,. \tag{2.30}$$

In this case, the velocity of the particle $\boldsymbol{v}$ is modified according to $\boldsymbol{v}' = \boldsymbol{v} + v_w \boldsymbol{n}$. The unit vector $\boldsymbol{n}$ is either chosen in a random direction on the unit sphere (isotropic wind), or in a random direction along $\boldsymbol{v} \times \nabla\Phi$ (axial wind). In the latter scheme, the wind particles are preferentially ejected along the rotation axis of the disc. However, even for isotropic winds the presence of a disc will lead to a bipolar wind pattern, as the wind can propagate much more easily in the direction orthogonal to the disc. Therefore, we will use isotropic winds in this work.

2.4 Initial conditions

As we focus on the evolution of galaxies rather than their initial formation, we begin our simulations with pre-assembled galaxies consisting of a dark matter halo, a stellar and a gaseous disc, and a stellar bulge. Generating initial conditions to follow galaxy formation in a cosmological simulation is a well-defined task as particle coordinates are obtained from the cosmological perturbation spectrum and evolved according to linear theory. However, creating an already formed, stable galaxy in equilibrium is much more challenging, since the distribution functions for the positions and velocities must be determined.

Early attempts to create equilibrium galaxies used largely static potentials. However, this approximation does not allow for interactions between the components, which is problematic, as the angular momentum redistribution between the components is critical for the formation of structures that can be observed. Later methods created galaxies by starting with the spherical components and evolved them until they reached an equilibrium, after which the disc was added and the system had to relax again. The problem of this method is that forcing the galaxy to

equilibrium modifies the galaxy's input parameters such that control over the defining structure parameters is lost.

The initial conditions generator employed in our work has been developed by Springel *et al.* (2005a), improving an earlier version of the code (Springel & White 1999). It consists of a rotating dark matter halo with a cosmologically motivated profile, exponential stellar and gaseous discs and a spherical stellar bulge. The distribution function of all components is approximated using the moments of the collisionless Boltzmann equation.

2.4.1   Dark matter halo

The density distribution of the dark matter halo is modelled with a Hernquist (1990) profile

$$\rho_{\mathrm{dm}}(r) = \frac{M_{\mathrm{dm}}}{2\pi} \frac{a}{r(r+a)^3} \,, \tag{2.31}$$

with the cumulative mass profile $M(<r) = M_{\mathrm{dm}} \, r^2/(r+a)^2$. For the creation of pre-formed galaxies this profile has two advantages over the Navarro *et al.* (1997, NFW) profile: in its inner part it agrees with the NFW profile, but due to its faster decline in the outer parts, the total mass converges such that no truncation is needed. Furthermore, in contrast to the NFW profile the Hernquist profile has an analytic distribution function so that the positions and velocities can be easily modelled. Defining the radius r_{200} at which the mean enclosed dark matter density is 200 times the critical density ρ_{c} and which contains the mass $M_{200} = 200\rho_{\mathrm{c}} \, r_{200}^3 \, 4\pi/3$, the Hernquist profile can be associated with a corresponding NFW halo. In addition the inner density profiles are set equal ($\rho_{\mathrm{dm}} = \rho_{\mathrm{NFW}}$ for $r \ll r_{200}$) which implies a relation between a, the scalelength r_s, and the concentration parameter $c = r_{200}/r_s$ of the NFW profile:

$$a = r_s \sqrt{2[\ln(1+c) - c/(1+c)]}. \tag{2.32}$$

For a concentration parameter of $c = 10$, the mass M_{200} of a Hernquist halo is 75 per cent of the total mass M_{dm} and $a = 1.73r_s$. The total angular momentum of the halo is defined as

$$J = \lambda M_{200} \sqrt{\frac{2GM_{200}r_{200}}{f_c}} \,, \tag{2.33}$$

where λ is the spin parameter, G is the gravitational constant, and f_c is a factor depending on the concentration.

2.4.2 Discs and bulges

The stellar and cold gaseous discs are modelled with exponential surface density profiles

$$\Sigma_{\mathrm{cg}}(R) = \frac{M_{\mathrm{cg}}}{2\pi r_g^2} \exp\left(-\frac{R}{r_g}\right) \quad \text{and} \quad \Sigma_{*\mathrm{d}}(R) = \frac{M_{*\mathrm{d}}}{2\pi r_d^2} \exp\left(-\frac{R}{r_d}\right), \qquad (2.34)$$

so that the total mass in the disc is $M_d = M_{\mathrm{cg}} + M_{*\mathrm{d}}$. Following the model by Mo *et al.* (1998), the scalelength r_d is set by relating it to the angular momentum of the stellar disc, and one assumes $J_d = (M_{*d}/M_{200})J$, corresponding to conservation of specific angular momentum of the material that forms the disc. Assuming that the disc is centrifugally supported this implies a one-to-one relation between λ and r_d. The scalelength of the cold gaseous disc is then related to that of the stellar disc by $r_g = \chi r_d$. The vertical mass distribution of the disc stars is specified by the profile of an isothermal sheet with a radially constant scaleheight z_0 which is treated as a free parameter. The three dimensional density profile of the stellar disc is thus given by

$$\rho_{*d}(R, z) = \frac{M_{*d}}{2\pi r_d^2 z_0} \operatorname{sech}^2\left(\frac{z}{z_0}\right) \exp\left(-\frac{R}{r_d}\right). \qquad (2.35)$$

A similar freedom is not available for the gas: for a given surface density the vertical structure of the gas disc arises as a result of self-gravity and the pressure given by the EOS, such that the vertical profile cannot be chosen freely. Therefore it has to be computed self-consistently in the model. For this one assumes that the vertical structure of the gas disc is governed by hydrostatic equilibrium. The solution can then be determined by the constraint that the integral of the density over the spin dimension has to yield the surface density. In practice, this is solved on a logarithmic grid of points in the $R - z$ plane.

The bulge is taken to be spherical and also modelled with a Hernquist profile

$$\rho_{\mathrm{b}}(r) = \frac{M_{\mathrm{b}}}{2\pi} \frac{r_b}{r(r + r_b)^3}, \qquad (2.36)$$

where r_b is the scalelength of the bulge and treated as a free parameter.

2.4.3 Velocity structure

Once the full density distribution has been determined, the velocity structure of the components can be computed. For the halo and bulge particles the velocity distribution functions depends only on energy and the z-component of the angular momentum. It can then be approximated as a triaxial Gaussian and its second order moments follow from the Jeans equations:

$$\langle v_z^2 \rangle = \langle v_R^2 \rangle = \frac{1}{\rho} \int_z^\infty \rho(R, z') \frac{\partial \Phi}{\partial z'} \mathrm{d}z' \quad \text{and} \quad \langle v_\phi^2 \rangle = \langle v_R^2 \rangle + \frac{R}{\rho} \frac{\partial (\rho \langle v_R^2 \rangle)}{\partial R} + R \frac{\partial \Phi}{\partial R}. \qquad (2.37)$$

The first order moments in radial and vertical direction and all mixed second order moments vanish, but in the azimuthal direction there can be a mean streaming component $\langle v_\phi \rangle$ which is not determined by the Jeans equations. For the bulge this component is set equal to zero, meaning that the bulge is not rotating. For the dark matter halo it is set such that the angular momentum J is given by equation (2.33). The dispersion of the Gaussian velocity distribution is then given by $\sigma_\phi^2 = \langle v_\phi^2 \rangle - \langle v_\phi \rangle^2$.

The velocity structure of the stellar disc is in principe more complicated, but for simplicity it is also modelled with a triaxial Gaussian. As observationally there is good evidence that for the disc $\langle v_R^2 \rangle$ and $\langle v_z^2 \rangle$ are proportional, one sets $\langle v_R^2 \rangle = f_R \langle v_z^2 \rangle$ and typically assumes that $f_R = 1$. To specify the mean streaming the epicyclic approximation which relates the radial and azimuthal dispersions in the disc is employed (see e.g. Binney & Tremaine 1987). Then the streaming velocity can be computed using the Jeans equations. For the gas, only a single valued velocity field is considered, where only the azimuthal streaming velocity has to be specified. It is determined by the radial balance between gravity and centrifugal pressure such that

$$v_{\phi,\mathrm{gas}}^2 = R \left(\frac{\partial \Phi}{\partial R} + \frac{1}{\rho_{\mathrm{cg}}} \frac{\partial P}{\partial R} \right) . \tag{2.38}$$

All integrations over the force field needed in the Jeans equations are solved on a logarithmic grid of points in the $R - z$ plane. Values for the velocity structure at individual particle coordinates are obtained by bilinear interpolation of the grid.

2.5   Application: disc thickening

Having laid out the basic techniques used to create the initial conditions and to evolve these pre-formed galaxies according to the laws of gravitation and hydrodynamics, we can employ these methods in a first study of galaxy evolution. For this we focus on MW-like galaxies and study how their stellar discs evolve during minor mergers. Specifically we investigate the effects of the dissipative gas component on the stability of the thin stellar disc during these mergers.

The large population of merging satellites has raised the question of whether mergers are *too* common in the CDM scenario. Some studies have questioned whether CDM models can produce a large enough population of 'bulgeless' discs (or systems with very low bulge-to-total ratios, $B/T \lesssim 0.2$) (e.g. Graham & Worley 2008; Weinzirl *et al.* 2009) and whether thin, dynamically fragile discs such as the one observed in the MW can survive this bombardment by incoming satellites (e.g. Toth & Ostriker 1992; Quinn *et al.* 1993; Walker *et al.* 1996; Wyse 2001; Bournaud *et al.* 2007). Clearly, there are three main aspects to settling this question: first, we must understand the statistics of galaxy mass accretion and merger histories in a CDM universe; second, we need to understand the physics of how galaxies are transformed by mergers with various mass

ratios, orbits, and other parameters; and finally, we need accurate and unbiased statistics for the observed populations of the relevant objects (cf. Kormendy & Fisher 2008).

The availability of large, high-resolution N-body simulations has made progress possible on the first of these aspects. For example, Stewart *et al.* (2008) recently carried out a detailed study of statistics of merger events in galaxy-sized dark matter haloes. They confirmed previous results based on semi-analytic methods (Purcell *et al.* 2007; Zentner 2007), finding that the majority of the mass delivery into a dark matter halo of mass M_h is due to systems with masses $M_{\mathrm{sat}} = (0.03 - 0.3)M_h$. They also found that a large fraction (95 per cent) of MW-sized haloes have accreted a satellite with a virial mass comparable with the total mass of the MW disc and approximately 70 per cent have accreted an object with more than twice this mass since $z \sim 1$.

There have been numerous studies based on collisionless simulations that have tried to quantify the effects of these minor mergers on the thickness and stability of stellar discs (e.g. Velazquez & White 1999; Font *et al.* 2001; Benson *et al.* 2004; Gauthier *et al.* 2006; Kazantzidis *et al.* 2008, 2009; Villalobos & Helmi 2008). This work has demonstrated that the answer depends quite sensitively on the mass ratio of the satellite to the primary; there seems to be a consensus that the main danger to thin discs is not from the ubiquitous mergers with very small mass ratios (less than $\sim$ 1:10) but rather from the rarer, yet still frequent, events with larger mass ratio ($\gtrsim$1:10). For example Kazantzidis *et al.* (2008) studied the effects of mergers with $(0.2-1)M_{\mathrm{disc}}$ and concluded that thin discs could survive such mergers. Employing dissipationless simulations, Purcell *et al.* (2009, P09) studied the response of a fully formed MW-like stellar disc within a $\sim 10^{12} M_\odot$ DM halo to mergers involving satellites with a total mass $M_{\mathrm{sat}} \sim 10^{11} M_\odot \simeq 3\, M_{\mathrm{disc}}$. They came to the conclusion that regardless of the orbital configuration of the merger these events transform the discs into structures that are roughly three times thicker than the observed thin disc component of the MW.

On the observational side, there is a general consensus that $\sim$70 per cent of MW-mass ($\sim 10^{12} M_\odot$) haloes host a disc dominated, late-type galaxy (Weinmann *et al.* 2006; van den Bosch *et al.* 2007; Choi *et al.* 2007; Park *et al.* 2007). While it is also well known that the majority of the mass in the disc of our MW resides in a thin component (e.g. Jurić *et al.* 2008), how typical this situation is for other disc galaxies in the MW's mass range is less certain. Quantifying the vertical thickness of the discs of external galaxies has been attempted in a few studies (e.g. Schwarzkopf & Dettmar 2000; Yoachim & Dalcanton 2006), but is challenging because of small sample sizes, inclination effects and extinction.

P09 suggested two possible explanations for the existence of a thin disc in our Galaxy: one possibility is that the MW is not a representative case and that perhaps it has had an unusually quiet accretion history for a halo of its mass. A second explanation is related to the fact that all the numerical studies performed so far have only considered the dissipationless components in the galaxy (dark matter and stars), neglecting the presence of a dissipative gas component in the disc. However, the inclusion of gas physics is known to play an important role in stabilising

galactic discs. Numerical simulations have shown that gas is important for the survivability and the regrowth of stellar discs during major mergers (Barnes 2002; Springel & Hernquist 2005; Robertson *et al.* 2006b; Naab *et al.* 2006; Scannapieco *et al.* 2009; Governato *et al.* 2009), and that the presence of gas in disc-type merger progenitors greatly suppresses the formation of a post-merger spheroidal component Hopkins *et al.* (2009a,b). It is reasonable to expect that the presence of gas in the progenitor disc could also have an impact on the efficiency of the disc heating and thickening: gas may be able to absorb some of the kinetic impact energy of the merging satellite, and then radiate this energy away by cooling; or, gas may be able to cool and reform a new thin disc after the merger, forcing heated stars to contract again onto the disc plane.

Our main goal here is to study in detail how the presence of a dissipational gas component affects disc thickening in minor mergers. For the first time, we address this problem using a suite of high-resolution, fully hydrodynamical numerical merger simulations, run with the GADGET-2 code. We consider simulations with and without gas, with a variety of initial orbital parameters, and with different values of the star formation efficiency parameters. We then re-examine the issue of whether the cosmologically expected rate of minor mergers presents a problem for CDM in the light of our new results and the available observations.

2.5.1 Simulation parameters

In our 'fiducial' runs, we adopt the standard parameters for the multiphase feedback model in order to match the Kennicutt law as specified in Springel & Hernquist (2003). The star formation time-scale is set to $t_*^0 = 2.1$ Gyr, the cloud evaporation parameter to $A_0 = 1000$ and the SN 'temperature' to $T_{\mathrm{SN}} = 10^8$ K, corresponding to a Salpeter IMF. In order to test whether the values of these (uncertain) parameters affect our results, we reran two simulations with parameters that are a factor of 4 larger ($t_*^0 = 8.4$ Gyr, $A_0 = 4000$, $T_{\mathrm{SN}} = 4 \times 10^8$ K). As Springel *et al.* (2005a) noted, this choice of parameters results in a SFR of ~ 1 $M_\odot$ yr^{-1} for a MW-like galaxy and gives better agreement with the long gas consumption time-scale inferred for the MW. However, these parameters yield a SFR that lies slightly below the Kennicutt law.

The SPH properties of the gas particles are averaged over the standard GADGET-2 kernel using ~ 64 SPH particles. Additionally the minimum SPH smoothing length is required to be equal to the gravitational softening length in order to prevent artificial stabilisation of small gas clumps at low resolution (Bate & Burkert 1997). All simulations have been performed with a high force accuracy of $\alpha_{\mathrm{force}} = 0.005$ and a time integration accuracy of $\eta_{\mathrm{acc}} = 0.02$ (for further details see Springel 2005). Stellar winds are neglected in this study.

We construct a set of primary systems, each with a virial mass of $M_{\mathrm{vir}} = 10^{12} M_\odot$ containing a disc and a bulge, and a satellite system with a virial mass of $M_{\mathrm{vir}} = 10^{11} M_\odot$ containing only a bulge. We use the results of Macciò *et al.* (2008) to compute halo concentration as a function of virial mass. Since we wish to study a *typical* galaxy in a $M_{\mathrm{vir}} = 10^{12} M_\odot$ halo, rather than

Table 2.1 Parameters kept constant for all simulations. Masses are in units of $10^{10} M_\odot$; scale and softening lengths are in units of kpc and pc respectively.

System	$M_{\rm vir}$	$M_{\rm disc}$	$M_{\rm b}$	$r_{\rm d}$	$r_{\rm b}$	c	$N_{\rm halo}$	$N_{\rm disc}$	$N_{\rm bulge}$
Primary	100	2.4	0.600	3.0	0.5	9.65	4 000 000	1 000 000	500 000
Sat	10	0.0	0.063	0.0	0.3	11.98	900 000	0	100 000

use the specific parameters of the MW, we use the average stellar-to-halo mass ratio derived by Moster *et al.* (2010) to compute the stellar mass of every system (both primaries and satellites). The Moster *et al.* (2010) constraints were derived empirically by asking how the population of dark matter haloes and sub-haloes predicted by CDM must be populated with galaxies in order to reproduce the observed galaxy stellar mass function, and are in excellent agreement with constraints from other methods such as galaxy clustering, satellite kinematics and weak lensing. Note that the stellar mass we get for a typical galaxy in a $M_{\rm vir} = 10^{12} M_\odot$ halo is significantly less than what is found for the MW and M31 (cf. Klypin *et al.* 2002).

All primary systems have a concentration parameter of $c = 9.65$ and a stellar mass of $M_{*,\rm pri} = 3 \times 10^{10} M_\odot$. Distributing 80 per cent of this stellar mass into the exponential disc yields a stellar disc mass of $M_{\rm disc} = 2.4 \times 10^{10} M_\odot$ and a bulge mass of $M_{\rm b,pri} = 6 \times 10^9 M_\odot$. We assume a bulge scalelength of $r_{\rm b,pri} = 0.5$ kpc.

For models that also include a gaseous disc component we add $M_{\rm gas,20\%} = 0.6 \times 10^{10} M_\odot$ and $M_{\rm gas,40\%} = 1.6 \times 10^{10} M_\odot$ such that the gas fraction in the disc is 20 per cent and 40 per cent in the two cases (cf. Stewart *et al.* 2009). The total disc mass is then $M_{\rm d,0\%} = 2.4 \times 10^{10} M_\odot$, $M_{\rm d,20\%} = 3.0 \times 10^{10} M_\odot$ and $M_{\rm d,40\%} = 4.0 \times 10^{10} M_\odot$ for a gas fraction of 0, 20 and 40 per cent, respectively. We decided to keep the total stellar mass constant in order to have a more direct comparison between the dissipational and dissipationless cases. We fix the disc scaleradius at $r_{\rm d} = 3.0$ kpc for all primary galaxies; because in the Mo *et al.* (1998) model, $r_{\rm d}$ depends on the disc mass and on the halo spin parameter, we have chosen λ in each case such that this value of $r_{\rm d}$ is obtained in all primary systems. The corresponding spin parameters are $\lambda_{0\%} = 0.033$, $\lambda_{20\%} = 0.034$ and $\lambda_{40\%} = 0.036$. We consider two cases for the initial disc scaleheight: we adopt a 'fiducial' value of $z_0 = 0.4$ kpc for direct comparison with P09, and also consider an initially thinner disc with $z_0 = 0.25$ kpc for two values of the gas fraction (0 and 20 per cent). Edge-on surface brightness maps for the initial conditions of our primary galaxies are shown in the upper and lower left panels of Figure 2.1 for $z_0 = 0.4$ and 0.25 kpc, respectively.

The satellite systems consist only of a dark matter halo and a stellar bulge. The concentration parameter of the satellite halo is $c = 11.98$. Using the stellar-to-halo mass ratio we derive a stellar mass of $M_{\rm b,sat} = 6.3 \times 10^8 M_\odot$. We set the scalelength of the bulge to $r_{\rm b,sat} = 0.3$ kpc.

The primary systems always contain $N_{\rm dm} = 4 \times 10^6$ dark matter, $N_{\rm disc} = 10^6$ stellar disc

Table 2.2 Parameters for the different simulation runs. Masses are in units of $10^{10} M_\odot$, and scale-height and softening lengths are in units of kpc and pc respectively. The star formation time-scale (t_*^0) is expressed in Gyr. The first three entries are for isolated galaxies, and the remainder are for mergers.

Run	f_{gas}	M_{gas}	M_{d}	N_{gas}	ϵ_{gas}	λ	z_0	θ	t_*^0	A_0	T_{SN}
IA	0.0	0.0	2.4	0	0	0.033	0.40	-	2.1	1000	$1 \times 10^8\mathrm{K}$
IB	0.2	0.6	3.0	125 000	70	0.034	0.40	-	2.1	1000	$1 \times 10^8\mathrm{K}$
IC	0.4	1.6	4.0	333 333	70	0.036	0.40	-	2.1	1000	$1 \times 10^8\mathrm{K}$
MA60	0.0	0.0	2.4	0	0	0.033	0.40	60°	2.1	1000	$1 \times 10^8\mathrm{K}$
MB60	0.2	0.6	3.0	125 000	70	0.034	0.40	60°	2.1	1000	$1 \times 10^8\mathrm{K}$
MC60	0.4	1.6	4.0	333 333	70	0.036	0.40	60°	2.1	1000	$1 \times 10^8\mathrm{K}$
MA45	0.0	0.0	2.4	0	0	0.033	0.40	45°	2.1	1000	$1 \times 10^8\mathrm{K}$
MB45	0.2	0.6	3.0	125 000	70	0.034	0.40	45°	2.1	1000	$1 \times 10^8\mathrm{K}$
MA30	0.0	0.0	2.4	0	0	0.033	0.40	30°	2.1	1000	$1 \times 10^8\mathrm{K}$
MB30	0.2	0.6	3.0	125 000	70	0.034	0.40	30°	2.1	1000	$1 \times 10^8\mathrm{K}$
MA60T	0.0	0.0	2.4	0	0	0.033	0.25	60°	2.1	1000	$1 \times 10^8\mathrm{K}$
MB60T	0.2	0.6	3.0	125 000	70	0.034	0.25	60°	2.1	1000	$1 \times 10^8\mathrm{K}$
MB60S	0.2	0.6	3.0	125 000	70	0.034	0.40	60°	8.4	4000	$4 \times 10^8\mathrm{K}$
MB60TS	0.2	0.6	3.0	125 000	70	0.034	0.25	60°	8.4	4000	$4 \times 10^8\mathrm{K}$

and $N_{\mathrm{bulge}} = 5 \times 10^5$ bulge particles. Models with 20 and 40 per cent gas fractions contain $N_{\mathrm{gas},20\%} = 1.25 \times 10^5$ and $N_{\mathrm{gas},40\%} = 3.33 \times 10^5$ gas particles, respectively. The satellite system consists of $N_{\mathrm{dm}} = 9 \times 10^5$ dark matter and $N_{\mathrm{bulge}} = 10^5$ bulge particles. We set the gravitational softening lengths to $\epsilon = 50\,\mathrm{pc}$, $70\,\mathrm{pc}$ and $100\,\mathrm{pc}$ for stellar, gas and dark matter particles, respectively.

Following P09 we choose orbits which are motivated by studies of substructure accretion in cosmological N-body simulations. The most likely values of the radial and tangential velocity components (v_r and v_t) are found to be respectively at 90 and 60 per cent of the virial velocity of the primary halo (Benson 2005; Khochfar & Burkert 2006). For a halo of mass $M_{\mathrm{vir}} = 10^{12} M_\odot$ the virial velocity is $v_{\mathrm{vir}} = 129\,\mathrm{km\,s^{-1}}$ which results in an initial subhalo velocity with $v_r = 116\,\mathrm{km\,s^{-1}}$ and $v_t = 77\,\mathrm{km\,s^{-1}}$. The initial separation of the galaxies was chosen to be relatively large, $d_{\mathrm{start}} = 120\,\mathrm{kpc}$, in order to prevent significant perturbations of the disc due to the sudden presence of the satellite's gravitational pull. Once d_{start} is chosen, the orbital parameters are uniquely determined. This, of course, limits our study to a single cosmologically motivated orbit. Our combination of initial velocity and distance fixes the pericentric distance at $\sim 18\,\mathrm{kpc}$. We use a set of three orbital inclinations ($\theta = 60°$, $45°$ and $30°$, where θ is the angle between the spin axes of the disc and the orbit) to investigate the effect of the inclination on the rate of thickening of the disc. All orbits are prograde and all simulations were evolved for a total of 6 Gyr. Prograde orbits are expected to be more destructive to the disc than retrograde mergers (Velazquez & White
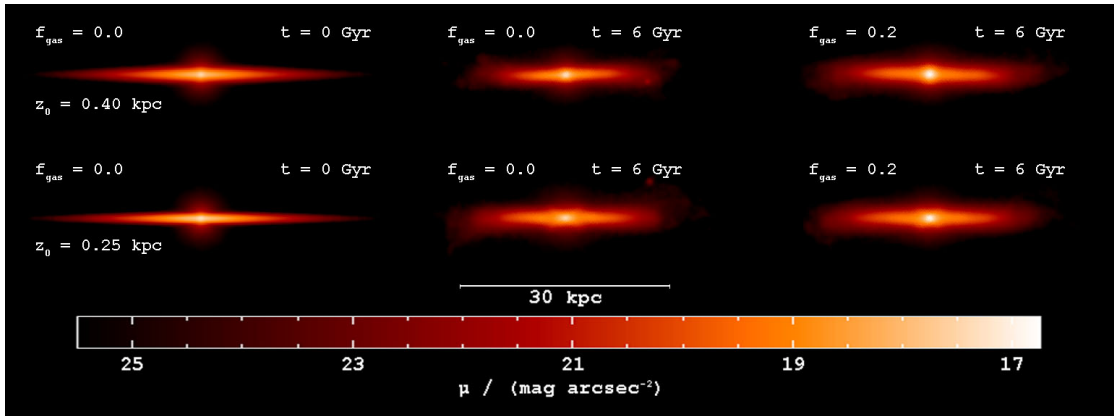
Figure 2.1 Edge-on surface brightness maps for galaxies with an initial scaleheight of $z_0 = 0.40\,\mathrm{kpc}$ (upper row) and $z_0 = 0.25\,\mathrm{kpc}$ (lower row). The left column shows the initial models while the centre and the right columns show the final galaxies (t=6 Gyr) for an initial gas fraction of 0 and 20 per cent, respectively. A mass-to-light ratio of 3 $(M/L)_\odot$ has been assumed, typical of the MW in the B-band.

1999).

We summarise the parameters that are kept constant for all simulations in Table 2.1, and parameters that differ for the various simulation runs are summarised in Table 2.2. We label the different simulations with the first letter I for isolated runs and an M for mergers. The second letter signifies the gas fraction of the disc followed by a number signifying the orbital inclination. We add a T for discs with an initial scaleheight of $z_0 = 0.25$ and an S for simulations with a lower star formation efficiency. We adopt a gas fraction-inclination combination of 20 per cent and $60°$ as our fiducial model.

2.5.2   Analysing the density profiles

In order to study the evolution of the disc we compute the stellar mass density as a function of the distance to the galactic plane at a distance of $R_\odot \sim 8\,\mathrm{kpc}$ from the disc spin axis. Figure 2.2 shows density profiles for a set of simulations that do not contain any gas. In the left panel, stellar mass density profiles of the initial disc (with $z_0 = 0.4\,\mathrm{kpc}$) and the final discs for an isolated galaxy and mergers with three inclination angles are plotted. To compare simulations to observations we also compute the edge-on projected surface brightness as a function of the distance to the galactic plane at a radius of $R_\odot$. This is done by taking a vertical slice at a distance of $R_\odot$ to the galactic centre and assuming a mass-to-light ratio of $M/L = 3(M/L)_\odot$, appropriate for the MW in the B-band (Zibetti *et al.* 2009). In the right panel of Figure 2.2, the edge-on surface brightness profiles are shown for the same simulations. As is clearly visible from both panels, the disc of the isolated galaxy is stable over the duration of the simulation, while during mergers the profiles clearly broaden, implying that the disc becomes thicker.
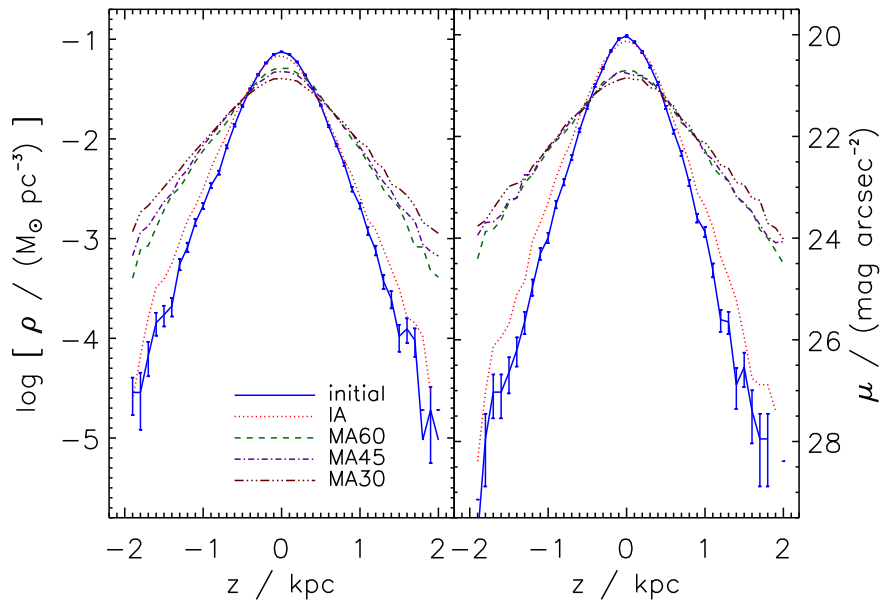
Figure 2.2 Density profiles for the initial ($z_0 = 0.4$ kpc) and final discs for an isolated galaxy and mergers with three inclination angles, for the simulations with no gas. The left panel shows the stellar mass density as a function of the distance to the galactic plane at a radius of 8 kpc. The right panel shows the edge-on projected surface brightness at a projected radius of 8 kpc.
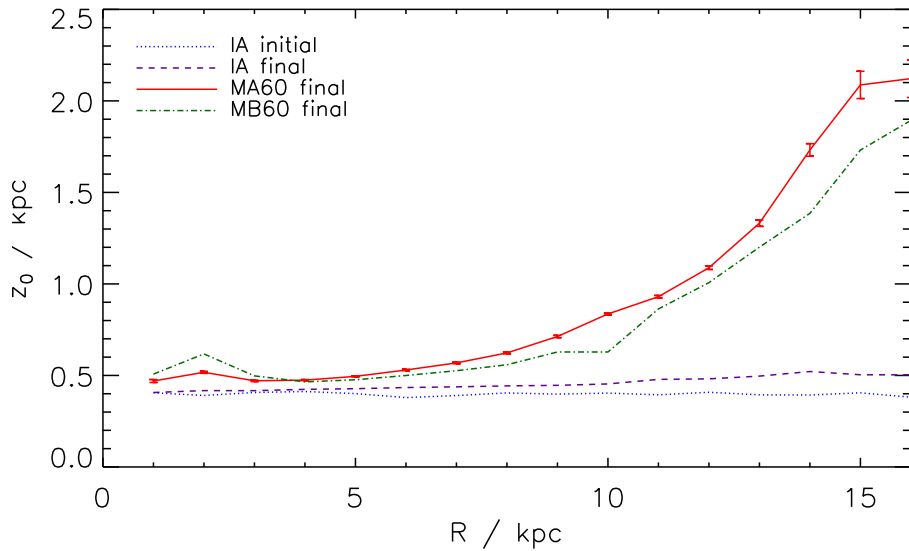
Figure 2.3 Disc scaleheight derived from fitting to the stellar mass density at different radii, for the initial (dotted line) and final states of a an isolated galaxy (IA; dashed line) and for a merger without gas (MA60, solid line) and with 20 per cent gas (MB60; dot-dashed line), both for an inclination of $60°$.
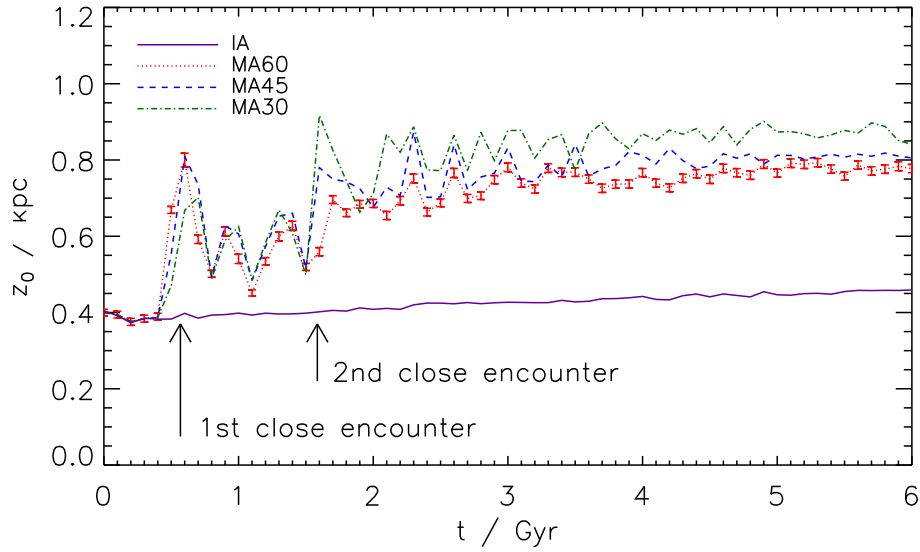
Figure 2.4 Evolution of the disc scaleheight for simulations with no gas. The solid line shows the scaleheight of an isolated galaxy while the other lines illustrate mergers with different inclinations.

We note that the projected edge-on surface density profiles are thicker than the 'slices' through the 3d mass density profiles. To understand this we plot the disc scaleheights derived by fitting to the 3d stellar mass density slices at different radii in Figure 2.3. This shows that z_0 increases with increasing distance from the galaxy centre. When computing the projected edge-on surface density profiles, stellar particles with a larger distance from the galactic centre than the specified radius are naturally included, since some of these particles happen to lie along the line of sight. These particles are on average also more distant from the galactic plane, as Figure 2.3 indicates. This results in an apparently thicker edge-on surface density profile and a larger projected disc scaleheight. In order to compare our results with observations we use the scaleheight obtained by fitting to the projected edge-on surface density profile in the following.

2.5.3   Stability of the initial conditions and evolution of the scaleheight

Galactic discs are fragile systems and there is always the possibility that purely numerical effects can modify their morphology, e.g. through bar formation or flaring. The stability of the initial disc is then a key point to be addressed before looking at the effects of satellite mergers. To quantify the amount of disc thickening we fit for the value of z_0 assuming a sech^2 profile. We always fit to the projected edge-on surface brightness profile at $R_\odot$ as discussed above.

The dotted and dashed lines in Figure 2.3 show the values of the disc scaleheight as a function of radius for an isolated galaxy (IA) at $t = 0$ and $t = 6$ Gyr, respectively. The final disc does not develop any appreciable flaring and the thickening at larger distances is negligible compared to the thickening due to satellite accretion events. In Figure 2.4 we show the resulting time evolution of

z_0 for an isolated galaxy and mergers with varying inclinations, all containing no gas. The isolated case (solid line) shows that in the absence of perturbations the thin disc is extremely stable during the 6 Gyr time-scale over which we run the simulations. This is also true for the isolated runs including a gas component (IB and IC) as the solid and dashed lines in Figure 2.5 show. This implies that any increase in z_0 is due to accretion events. We see that regardless of the inclination of the orbit, the disc thickens significantly in the merger simulations, with z_0 increasing by a factor of ~ 2.

We note that we also ran a simulation of an isolated galaxy using one fourth the number of particles of our fiducial case (in all species) and find that the scaleheight increases by 50 per cent. This demonstrates the importance of numerical resolution in determining the disc stability.

2.5.4 The effect of gas in the disc

All of the previous numerical experiments devoted to studying the heating and thickening of stellar discs by minor mergers have included only the dissipationless components of the galaxies: dark matter and stars. The presence of a gaseous component in the disc, which requires a hydrody-namical approach to the problem instead of a purely gravitational one, has been neglected so far. The presence of gas may suppress disc thickening in two ways. One possibility is that the gas may absorb some of the kinetic impact energy of the merging satellite, which can then be removed from the system by radiative cooling. In this way the impact energy that is transferred to the stars, causing heating and thickening, may be reduced. Another possible mechanism is that gas forms a new thin stellar disc after the merger. This disc could then cause the heated stars to contract towards the disc plane.

We analyse the surface brightness profiles of the merger simulations with gas, and show the resulting evolution of the scaleheight in Figure 2.5 for initial gas fractions of 0, 20 and 40 per cent, and an inclination of $60°$ (MA60, MB60 and MC60). This shows that the presence of gas does indeed suppress the thickening of the disc by a minor merger. The final scaleheight increases by a factor of ~ 1.75 for the 20 per cent gas case, and by only a factor of 1.5 for the 40 per cent gas case, in contrast to the factor of 2 increase in the gas-free case (corresponding to a decrease in the final scaleheight of 25 and 50 per cent, respectively).

One might wonder whether the reduced thickening is due to the additional potential of the gas particles. In order to investigate whether the gas physics or the greater potential have a larger impact on the suppression of the disc thickening, we ran two additional collisionless simulations. For the first simulation we use the initial conditions of MC60 and convert all gas particles to stellar particles at $t = 0 \, \text{Gyr}$ (MC60X). We thus get an additional stellar disc which has the same profile and potential as the previous gaseous disc, but behaves collisionlessly during the simulation. In a second simulation we create a galaxy like MA60 but increase the mass of the stellar disc to $M_{\text{disc}} = 4.0 \times 10^{10} M_{\odot}$ (MA60Y). This galaxy has the same disc mass as MC60
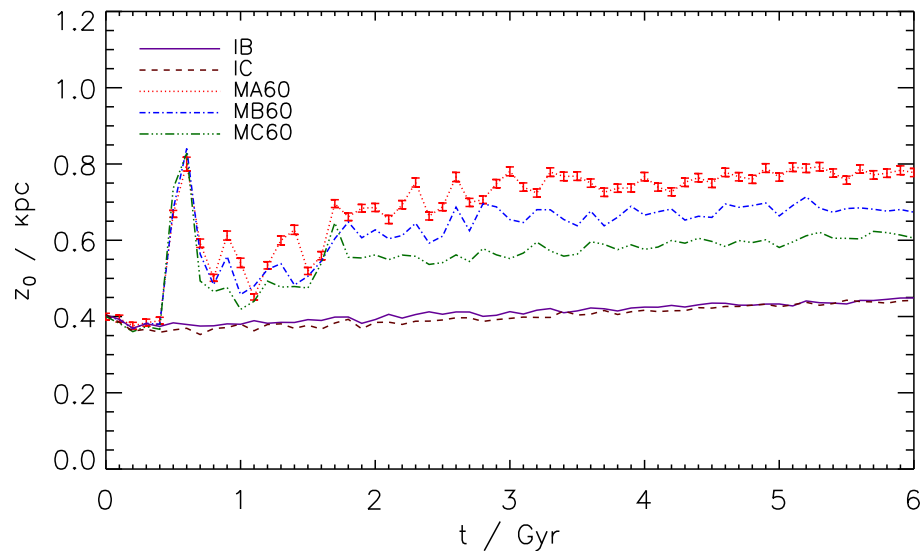
Figure 2.5 Evolution of the disc scaleheight for simulations with gas. The solid and the dashed lines show the isolated case while the other lines illustrate mergers with different gas fractions (0, 20 and 40 per cent for MA60, MB60 and MC60, respectively).
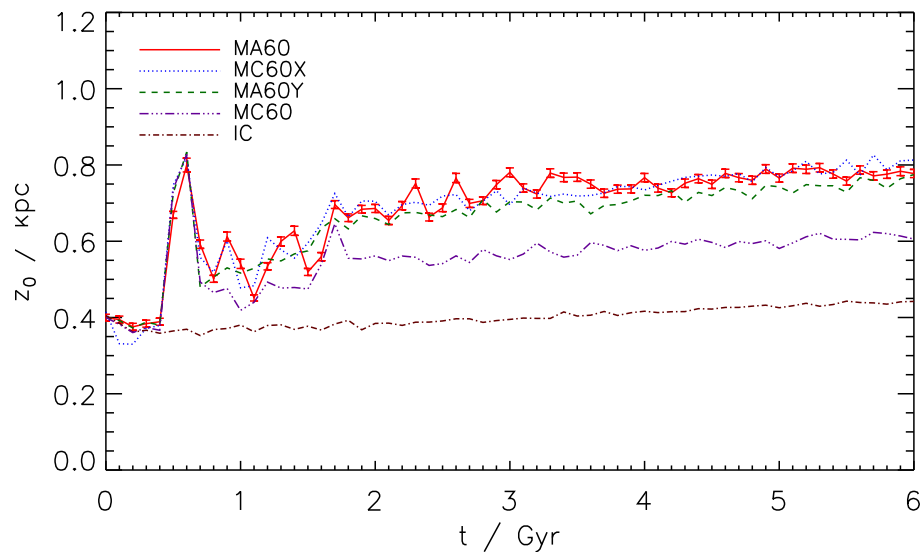
Figure 2.6 Evolution of the disc scaleheight for simulations without gas but with a more massive disc. The dotted lines shows the result for a simulation with an additional collisionless disc having the same mass and distribution as the gas disc in MC60. The dashed line shows the result of a simulation containing one stellar disc with increased mass (equal to the total baryonic mass in MC60). The solid and dot-dashed lines indicate the reference cases (MA60, MC60, IC). We see that the presence of dissipational gas, not the more massive disc, is responsible for the reduction in disc thickening.
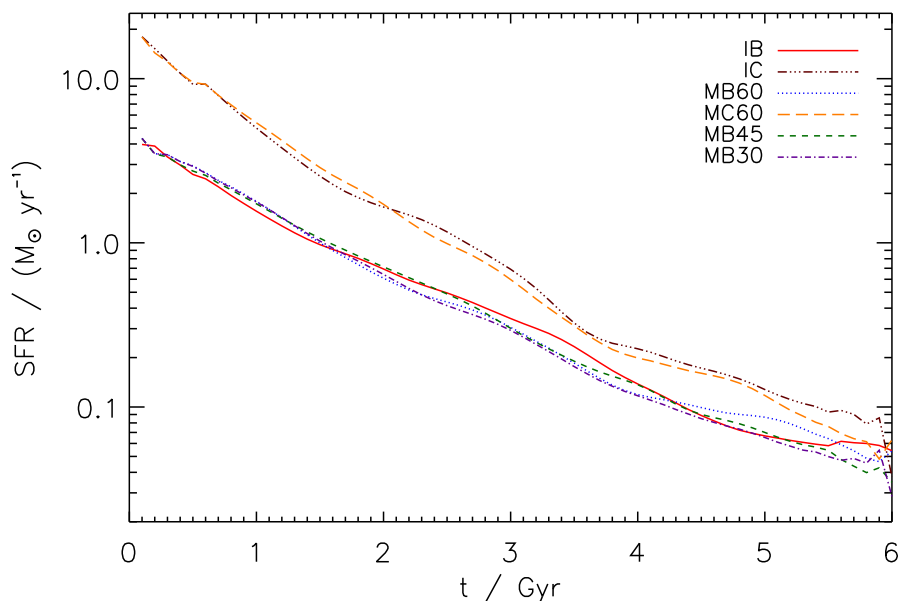
Figure 2.7 Star formation rates for isolated galaxies and mergers, with initial gas fractions of 20 (IB, MB60, MB45, MB30) and 40 per cent (IC, MC60) in the progenitor disc.

and MC60X. Figure 2.6 shows that in both collisionless simulations (MC60X and MA60Y) the disc scaleheight increases by a factor of ~ 2. The final scaleheights are equal or even larger than for the less massive galaxy without gas (MA60). This demonstrates that the suppression of the thickening in the runs including gas is not due to the additional potential of the gas disc but lies in the hydrodynamical nature of the particles.

In order to gain insights into the physical process that is causing this change in behaviour, we examine the SFR as a function of time. The results are shown in Figure 2.7. The galaxy with a gas fraction of 40 per cent (IC and MC60) naturally starts with a high SFR ($\sim 18 \ M_\odot \ \mathrm{yr}^{-1}$), while the galaxy with a gas fraction of 20 per cent (IB, MB60, MB45 and MB30) starts with a lower SFR of $\sim 4 \ M_\odot \ \mathrm{yr}^{-1}$. We see that 1:10 mergers do not have a noticeable impact on the SFR.

The SFR quickly drops to low values under $1 \ M_\odot \ \mathrm{yr}^{-1}$ (after 2.5 Gyr for a gas fraction of 40 per cent and 1.5 Gyr for the gas fraction of 20 per cent). This implies that most of the gas is consumed before the merger is complete. Thus, the galaxy is not able to reform a new thin stellar disc after the merger, which could pull heated stars towards the galactic plane again. This means that the dominant process preventing disc heating in the simulations above is the absorption of the kinetic impact energy of the satellite by the gas component. This can also be directly inferred from Figure 2.5: from about 2 Gyr, one can see that the growth of the scaleheight z_0 is slower in the simulations with gas, indicating that from the beginning the gas is absorbing the impact energy and preventing the disc from thickening considerably. If the main mechanism was the reforming of a new thin disc, one would see the disc thicken and then contract again. This would mean a different
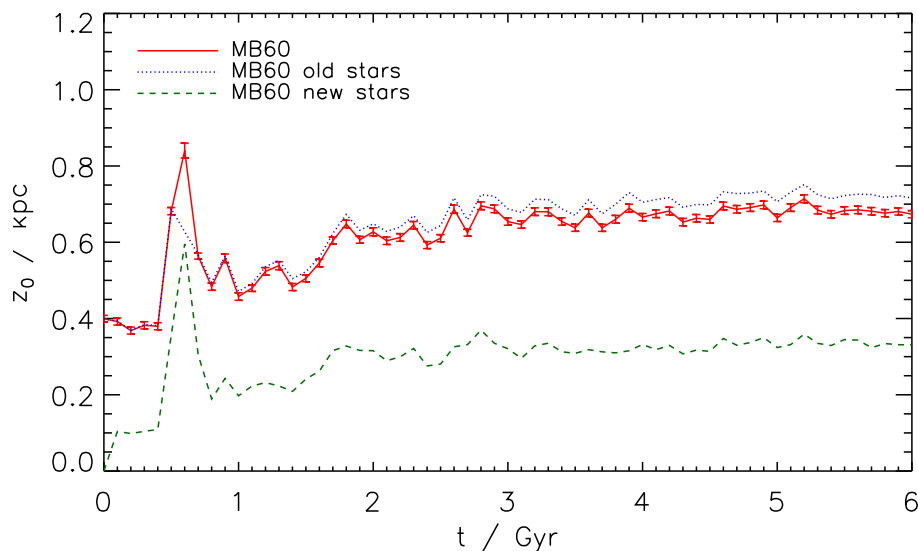
Figure 2.8 Evolution of the disc scaleheight for old stars (created in the initial conditions) and new stars (created during the simulation through star formation). The scaleheight for the combined sample is also shown for comparison.

slope for the z_0 time evolution in runs with different gas fractions, however, we find similar slopes for all gas fractions indicating that this process is not dominant.

Another way to demonstrate that the formation of a new disc does not reduce the disc thickening noticeably in our simulations is to compare the scaleheight of the stellar particles created in the initial conditions (old stars) to the scaleheight of the stellar particles that form during the simulation through star formation (new stars). In Figure 2.8 we compare the evolution of z_0 for old and new stars in our fiducial case MB60. The new stars clearly form a thinner disc than the old stars, however, the combined sample has a scaleheight which is only slightly thinner than the old stellar disc. This is due to the much larger mass contained in the old stellar disc component. Figure 2.9 shows the resulting edge-on projected surface brightness profile for the 40 per cent gas case at $8\,\mathrm{kpc}$ for old, new and all stars and a fit to the combined stellar disc using a sech^2 model. The combined profile does not show an obvious transition between the old and the new disc profile. However, one has to keep in mind that we are using a single sech^2 model to fit two distinct profiles, implying that the fitted scaleheight of the combined sample decreases due to the presence of the new thin disc. The new and old discs have a final scaleheight of 0.38 and $0.66\,\mathrm{kpc}$ while the total stellar disc has $z_0 = 0.61\,\mathrm{kpc}$. This shows that even for a gas fraction of 40 per cent (which is expected for disc galaxies at $z \sim 1$ but not for local galaxies at the present time), the new thin disc is not massive enough to reduce the total disc scaleheight significantly. In order to form a new thin disc with a mass comparable to the old stellar disc, the SFR after the merger would have to be much higher. This could occur in the case of an extremely gas-rich initial disc (≥ 90 per cent gas; Robertson *et al.* 2006b; Hopkins *et al.* 2008).
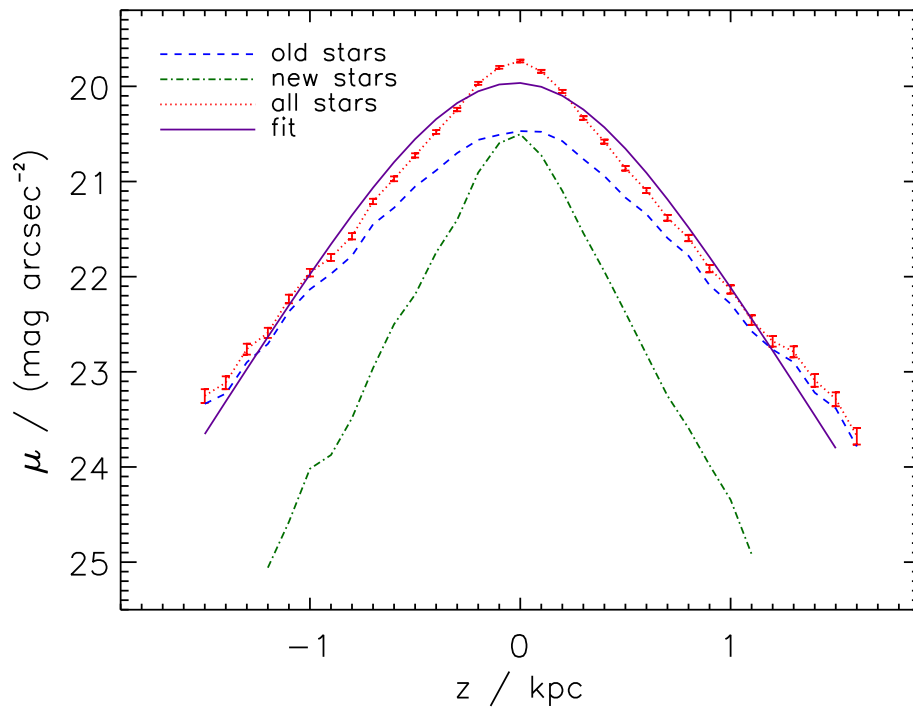
Figure 2.9 Final edge-on projected surface brightness profile for the 40 per cent gas case at a projected radius of $8\,\mathrm{kpc}$ for old, new and all stars. The solid line shows the fit to the combined stellar disc profile.
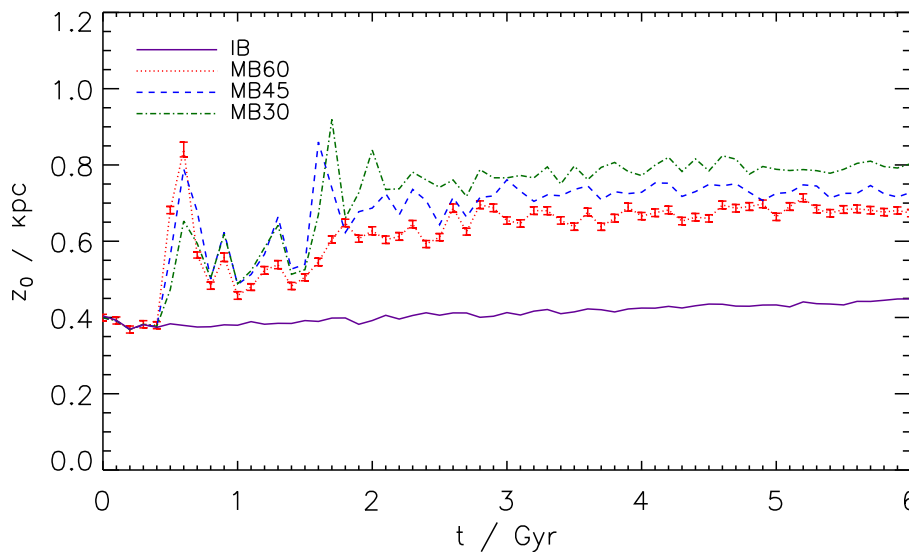
Figure 2.10 Evolution of the disc scaleheight for simulations with gas. The solid line shows the scaleheight of an isolated galaxy while the other lines illustrate mergers with different inclinations.
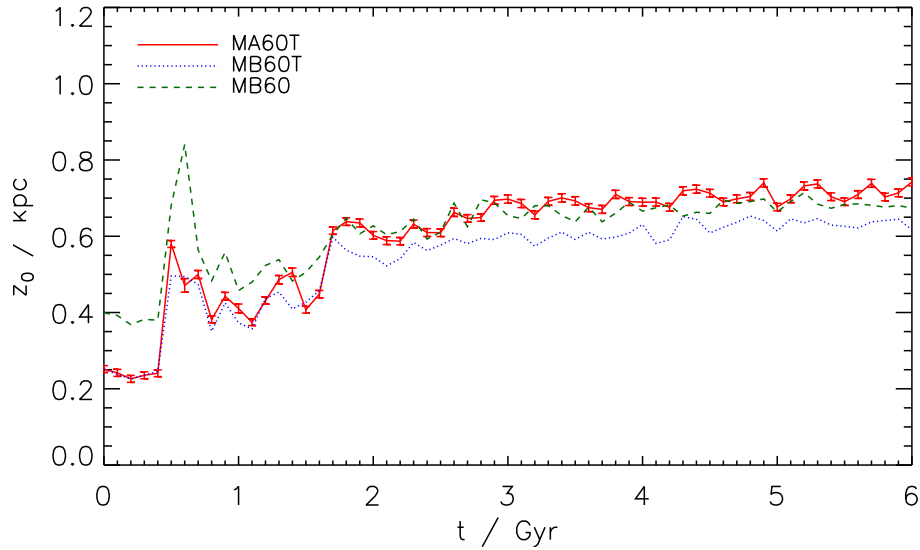
Figure 2.11 Evolution of the scaleheight for a disc with a smaller initial scaleheight. The solid line shows the 'thin disc' simulation without gas, the dotted line shows thin disc case with 20 per cent gas, and the dashed line shows the 20 per cent gas case with the original choice of initial scaleheight.

In order to investigate the influence of the orbital inclination on the disc thickening we compute the evolution of the scaleheight for mergers with gas fractions of 20 per cent for three different orbital inclinations $\theta = 60°, 45°, 30°$(MB60, MB45, MB30 respectively). We plot the results in Figure 2.10. The black solid line (IB) represents the isolated case with gas (20 per cent), which is seen to be very stable as in the no-gas case. The results for different orbital inclinations show that the value of θ has a small effect on the growth of the scaleheight. Regardless of the inclination, the overall increase of the scaleheight for simulations including gas is about 25 per cent smaller than in the respective dissipationless simulations.

2.5.5 A thinner initial disc

The choice of initial scaleheight for our primary disc was somewhat arbitrary. In order to investigate whether a thinner initial disc would result in a thinner disc today, we simulate a merger of a disc with an initial scaleheight of $z_0 = 0.25\,\mathrm{kpc}$ both without and with gas (20 per cent) and an inclination of $60°$. The resulting evolution of z_0 is shown in Figure 2.11. The final scaleheight of the disc without gas is as large as the scaleheight of the corresponding initially thicker discs. This may be due to the fact that an initially thicker disc is more robust to heating by accretion events (Kazantzidis *et al.* 2009). When gas is present, the final scaleheight is slightly smaller in the case with an initially thinner disc, but even a thinner initial disc is transformed into a system with a scaleheight of more than $0.6\,\mathrm{kpc}$. Thus, even when the effects of gas in the progenitor disc are
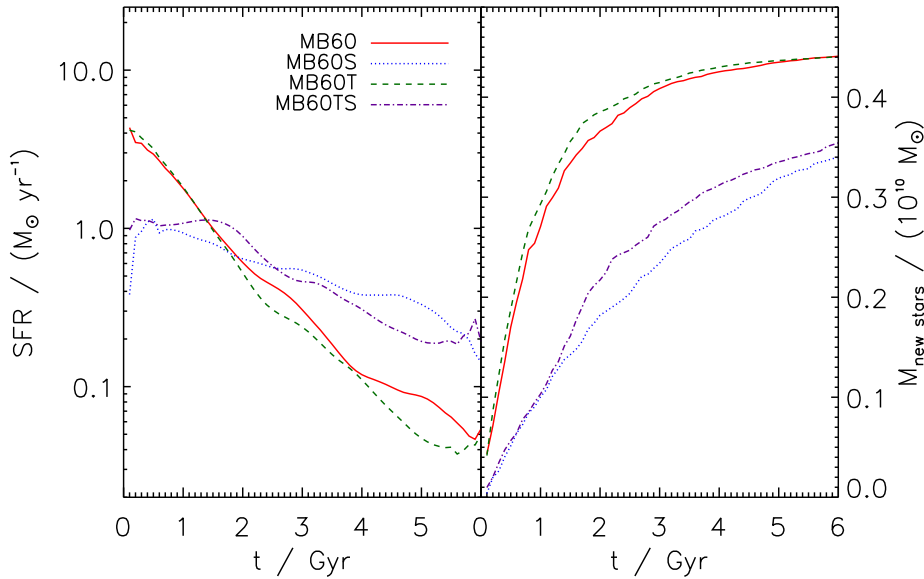
Figure 2.12 Left panel: SFR for simulations with the default (MB60, MB60T) and lowered star formation efficiencies (MB60S, MB60TS), for the disc with initial scaleheight $z_0 = 0.4$ kpc and $z_0 = 0.25$ kpc (T). Right panel: Mass of stellar particles formed during the simulations.

included, it seems to be difficult to obtain a disc with a scaleheight that is substantially smaller than this value following a minor (mass ratio greater than 1:10) merger.

2.5.6 Lower star formation efficiency

In order to investigate the sensitivity of our results to the parameters chosen for star formation and SN feedback, we have run some simulations with lower star formation efficiency. In particular, we were interested to see whether adopting a lower star formation efficiency would allow a more significant new thin disc to reform following the merger. For this test we employ a star formation time-scale $t_*^0 = 8.4$ Gyr, a cloud evaporation parameter $A_0 = 4000$ and a SN 'temperature' $T_{SN} = 4.0 \times 10^8$ K in order to have a SFR of $\sim 1\ M_\odot\ \mathrm{yr}^{-1}$ for a MW-like Galaxy (Springel *et al.* 2005a). We run this case for initial scaleheights of $z_0 = 0.4$ kpc and $z_0 = 0.25$ kpc, in both cases using our fiducial value of a 20 per cent gas fraction and an inclination of $60°$.

We first compare the SFRs of the simulations with lowered star formation efficiencies with our fiducial results. The left panel of Figure 2.12 shows the SFRs for the simulations MB60, MB60T, MB60S and MB60TS. As we see, the SFRs in MB60S and MB60TS are initially lower than those of MB60 and MB60T, respectively. After the merger ($t \sim 1.8$ Gyr) however, the simulations with the lower star formation efficiency have a higher SFR, since MB60 and MB60T have already consumed most of their gas supply. Due to the lower SFR during the early stages of the simulation, the amount of newly formed stellar mass is still lower in MB60S and MB60TS, as can be seen in the right panel of Figure 2.12. This means that the thin disc consisting of new stars affects
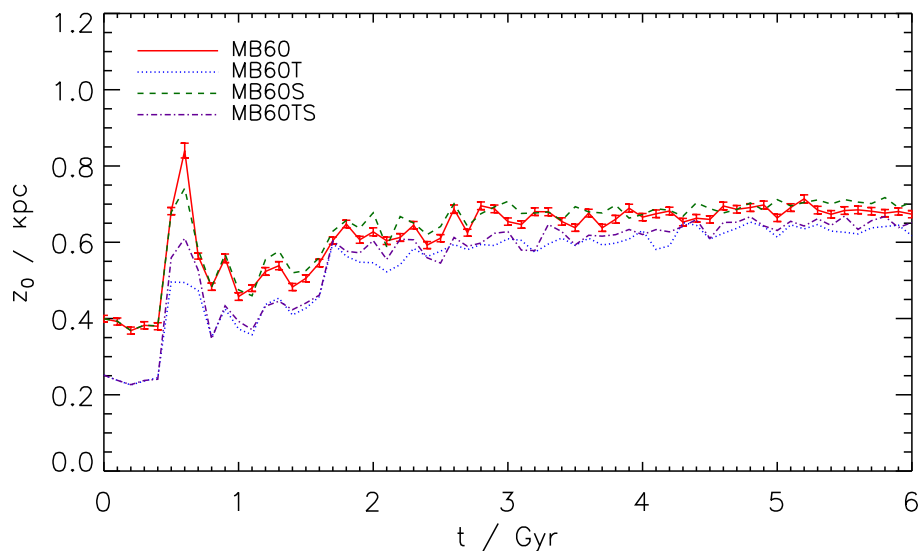
Figure 2.13 Evolution of the disc scaleheight for simulations with higher (MB60, MB60T) and lower star formation efficiencies (MB60S, MB60TS).

the overall disc scaleheight even less than in the simulations MB60 and MB60T. The resulting scaleheights are plotted in Figure 2.13. As expected from the SFRs, the scaleheights of MB60S and MB60TS are slightly larger than those of MB60 and MB60T, respectively.

Clearly, in order for the disc thickening problem to be solved by the growth of a new stellar disc following the merger, the mass of the new disc must be comparable in mass to that of the old stellar disc. This implies that a significant amount of gas must remain available at the end of the merger. Based on our results, when the star formation and SN feedback parameters are tuned be consistent with the empirical Kennicutt law, most of the gas tends to be consumed during the merger. Simulations with much higher initial gas fractions ($\sim$ 90 per cent) or which included a new source of cold gas (e.g. via cooling and accretion from a hot halo) might be able to regrow a more massive thin disc.

2.5.7 Conclusions and discussion

We investigated the role of dissipational gas physics in the vertical heating and thickening of disc galaxies by minor mergers (mass ratio $\sim$ 1:10). We used the parallel TreeSPH-code GADGET-2 to simulate a suite of minor merger simulations for a MW-like primary galaxy. The suite consists of collisionless simulations as well as runs containing gas in the disc. Using cosmologically motivated orbital parameters, we ran simulations with three different orbital inclinations ($60°$, $45°$ and $30°$) and two different initial disc scaleheights ($z_0 = 0.4$ kpc and $z_0 = 0.25$ kpc).

We fit for the value of the scaleheight z_0, assuming a sech^2 form for the vertical density profile. We showed that the scaleheight derived from a fit to the mass density is a strong function of the

radial distance to the disc axis: as is well known, minor mergers tend to cause flaring in the outer part of the disc. This results in projected edge-on surface density profiles which appear thicker than the actual three dimensional density profiles since stars that are at a large distance from the galactic centre and thus also more distant from the galactic plane are viewed along the line of sight.

We found that in dissipationless simulations, minor mergers (without gas) caused the scale-height of the disc to increase by about a factor of two, with the orbital inclination affecting the amount of thickening by only about five percent. Thus, in qualitative agreement with the results of P09, we find that in the absence of gas, cold thin discs are destroyed by minor mergers. However, it is interesting that in spite of the fact that the parameters of our simulations were chosen to be very similar to those of P09, they found that the scaleheight of the disc increased by a larger factor of ~ 3, leading to a final disc about twice as thick as ours (despite having the same initial scaleheight).

Although the discs in both simulation suites are stable against secular evolution effects, this does not necessarily ensure that both models are equally resistant to strong perturbative effects during an accretion event. Possible reasons for this discrepancy may be the use of a different IC generator and a different simulation code. The velocity dispersions for example are fixed differently; while in our ICs the radial and the vertical velocity dispersions are equal, the code used by P09 reproduces the velocity ellipsoid for the MW. This may result in an initially hotter disc for our typical galaxy (for a $M_{\mathrm{vir}} = 10^{12} M_\odot$ halo) which is more resilient to massive accretion events. Other intrinsic differences in the simulations of P09 are a more massive disc (which may potentially be less stable due the formation of a bar) and a larger stellar mass of the satellite (which results in a larger gravitational pull each time the subhalo passes the disc). We also note that P09 use a different concentration parameter (for both the primary halo and the subhalo) and chose a Sersic profile for the bulge and an NFW profile for the halo component while we use a Hernquist profile for both components. It is not obvious which of the mentioned differences has the largest impact on the resulting disc scaleheights.

We note that our results are consistent with those of Villalobos & Helmi (2008). These authors start with similar initial conditions but employ a thicker disc ($z_0 = 0.7\,\mathrm{kpc}$). The final scaleheights are between 1.0 and 1.3 kpc, depending on the orbital inclination and are not as extreme as found by P09. The relative thickening is even lower than in our simulations, confirming that initially thicker discs are more robust to accretion events.

We also investigated mergers in which the progenitor disc initially contained a gas fraction of 20 or 40 per cent. We found that the presence of gas reduces the final scaleheights by 25 per cent (50 per cent) for a gas fraction of 20 per cent (40 per cent). The final scaleheights were between 0.6 and 0.7 kpc (1.5 to 1.75 times larger than the initial value), depending on the initial gas fraction and the orbital inclination. We argued that the presence of gas can have an impact on disc thickening via two different mechanisms. One process is the absorption of kinetic impact

energy by the gas. This energy can then be dissipated via radiation. Another possible effect is the formation of a new thin disc, which can cause heated stars to re-contract towards the disc plane. We showed that in our simulations, in which the star formation and SN feedback parameters were set to be consistent with the empirical Kennicutt law for the initial disc, most of the gas is consumed during the merger, and therefore the regrowth of new thin discs has a negligible impact on the mass-weighted scaleheight of the post-merger galaxy. Therefore, it seems that the main process that suppresses disc thickening in the presence of gas in our simulations is the absorption of impact energy by the gas.

We computed scaleheights for old stars (i.e. stellar particles that were present in the initial conditions) and for new stars (stellar particles created during the simulation through star formation). The scaleheight for old stars was found to be slightly higher than the overall value (~ 0.73 kpc vs ~ 0.67 for our fiducial case of 20 per cent gas and a $60°$ inclination) while the scaleheight of the new stars was about half of that value (~ 0.35 kpc). We showed that the final mass of the new disc is small compared to that of the old disc. This indicates that although a new thin disc does form, it does not have a significant effect on the final thickness of the total disc. We argue that in order to have a noticeable effect, the new thin disc would need to be comparable in mass to the old disc, which would require that a significant mass of cold gas is still present at the end of the merger.

We ran simulations with two different initial scaleheights, $z_0 = 0.40$ kpc (fiducial case) and $z_0 = 0.25$ kpc (thin). As it turns out, thinner discs are more unstable to heating and are therefore thickened more by the merger than initially thicker discs. As a result, the two cases result in discs with nearly the same final scaleheight (~ 0.6 kpc for the 20 per cent gas fiducial case).

To study the sensitivity of our results to the parameters controlling star formation and SN feedback, we ran simulations with a lower star formation efficiency. In these simulations, less gas is consumed and so the SFR at the end of the merger is higher. However, we found that the final mass of the new disc was still lower than in the simulations with the higher star formation efficiency. This results in final scaleheights that are slightly larger than in the fiducial case. We conclude that in order to reform a new thin disc comparable in mass to the old disc, either the initial gas fraction would have to be much higher, or an external fuelling reservoir (such as cooling and accretion from a hot halo) would be needed (Sommer-Larsen *et al.* 2003; Kaufmann *et al.* 2006; Grcevich & Putman 2009; Peek 2009).

In the light of our results, we can now reassess whether disc thickening by minor mergers presents a serious problem for CDM. First, we need to compare the fraction of disc galaxies that are expected to have had a minor merger (mass ratio greater than 1:10 but less than about 1:4) since $z \sim 1$ with the fraction of observed galaxies with thin discs. Observations show that roughly 70 per cent of MW-sized haloes host late-type galaxies (Weinmann *et al.* 2006; van den Bosch *et al.* 2007). Based on an analysis of cosmological simulations, Stewart *et al.* (2008) find that 20 per cent of Galaxy-sized haloes did not experience any merger event of 1:10 or larger in the past 8 Gyr. This implies that 30 per cent of all MW-like galaxies did not have such a merger, and as a

result can be expected to have retained their thin disc. This means that if less than 30 per cent of all MW-like galaxies are found to have scaleheights that are substantially lower than those found in our simulations (~ 0.6 kpc) then there is no discrepancy.

Obtaining statistically unbiased observational measurements of scaleheights for a complete sample of galaxies is difficult, due to small sample sizes, dust extinction, and inclination effects. Still there have been many studies focusing on the vertical structure of galaxies (e.g. Shaw & Gilmore 1989, 1990; de Grijs & van der Kruit 1996; de Grijs *et al.* 1997; Pohlen *et al.* 2000; Kregel *et al.* 2002; Bizyaev & Kajsin 2004). All these studies suggest that the majority of observed galaxies with properties similar to those of the MW have sech^2 scaleheights in the range of $0.6 < z_0 < 1.0$ kpc with a ratio between scaleheight and scalelength between 0.2 and 0.3. These values have been determined from observed two-dimensional surface brightness profiles. Usually it is assumed that scalelength and scaleheight are independent parameters. A model 2d surface brightness profile consisting of an exponential radial factor and a vertical factor (sech^2, sech or exp) is then fitted to the observed 2d profile. All scaleheights cited here have been converted to a sech^2 profile.

A statistical study of the vertical structure of spiral galaxies is presented in Schwarzkopf & Dettmar (2000). They found that the majority (~ 60 per cent) of galaxies have vertical scaleheights less than 1.1 kpc, with a maximum between $0.4\,\mathrm{kpc} \leq z_0 \leq 0.8\,\mathrm{kpc}$, while galaxies with a very thin disc ($z_0 < 0.4\,\mathrm{kpc}$) are extremely rare. Similar results were obtained by Yoachim & Dalcanton (2006), who derived scaleheights for a sample of edge-on galaxies and presented a relation between scaleheight and circular velocity. They showed that Galaxy-sized systems are expected to have scaleheights in the range $0.6\,\mathrm{kpc} \leq z_0 \leq 1.2\,\mathrm{kpc}$. In order to compare our results to these studies, we compute 2d edge-on disc surface brightness profiles (as shown in Figure 2.1) and fit a model 2d profile consisting of an exponential radial and sech^2 vertical disc to the simulated profiles. For the collisionless fiducial run MA60 the final scaleheight is 0.74 kpc, while for the fiducial runs including a gas disc MB60 and MC60 the scaleheights are 0.66 and 0.62 kpc, respectively. These values fall precisely in the observed range.

Previous theoretical studies, such as P09, have focussed on whether the observed scaleheight of the MW is in conflict with the predictions of CDM models. We revisit this issue as well. There have been various studies of the vertical structure of the MW (e.g. Bahcall & Soneira 1980; Kent *et al.* 1991; Reid & Majewski 1993; Larsen & Humphreys 2003; Jurić *et al.* 2008). These studies find exponential scaleheights for the MW's old thin disc of $h_z \sim 0.3$ kpc and for the young star forming disc of $h_z \sim 0.1$ kpc. As is standard in the literature, we convert these exponential scaleheights to values corresponding to a sech^2 function using $z_0 = 2h_z$ (which yields very good agreement between the two profiles at $z \geq z_0$ and reasonable agreement at $z_0 > z$). This results in scaleheights of $z_0 = 0.6$ kpc (old disc) and $z_0 = 0.2$ kpc (young disc). The former is just what we find for the overall scaleheight in our fiducial merger with gas, while the latter is very close to what we find for the disc of new stars, as shown in Figure 2.8. Thus, in the light of our results,

even if the MW did experience a recent 1:10 merger, if the disc contained even 20 per cent gas (similar to the gas fraction today) at the time of the merger, there is no conflict with observations. Of course, it is also possible to explain the MW by assuming that it is one of the 30 per cent of systems that did not experience a 1:10 merger. It has been previously suggested by Hammer *et al.* (2007), based on the unusually low mass and angular momentum of the MW disc, that our Galaxy may have had a particularly quiescent formation history.

We also note that while we are fitting the scaleheight to mass profiles, observational studies use luminosity profiles to derive z_0 . Based on the models of Bruzual & Charlot (2003) for a single age stellar population, we expect the B-band mass-to-light ratio of very young stars ($t_a < 2$ Gyr) and old stars ($t_a > 8$ Gyr) to differ by a factor of ~ 4. This implies that the new stellar particles should carry a correspondingly larger weight in a luminosity-weighted fit, resulting in a smaller estimated scaleheight. However, as seen in Figure 2.12, the mass of such young stars formed in our simulations is very small (only about a tenth of the mass of the pre-existing stellar disc), so even if we accounted for the age-dependent mass-to-light ratio, the overall measured scaleheight would not differ significantly from the mass-weighted one. Moreover, young stars will also tend to be more enshrouded by dust, further reducing their impact on the measured scaleheight.

Finally, the simulations presented here still neglect the larger scale environment and cosmological growth of the galaxy. The progenitors of MW discs presumably had somewhat different properties (smaller masses, higher gas fractions, and possibly thicker discs) than their present-day counterparts. Perhaps most importantly, one expects these systems to have accreted a significant amount of new material over the course of the past 6 - 8 Gyr via accretion and cooling from a hot gas halo. This additional supply of cold gas to the disc could enhance the formation of a new, thin disc and further reduce the thickening by minor mergers. We plan to re-examine this problem in the context of simulations with a cosmologically motivated merger and accretion history, and including cooling from a hot halo, in chapter 4.

In final summary, in contrast with the conclusions reached by P09 using dissipationless simulations, we conclude that the existence of a thin disc in the MW is not in obvious conflict with the predictions of the CDM model. Although the MW may have had an unusually quiescent merger history, mooting the issue of disc thickening by minor mergers, our results indicate that one does not need to rely on such an argument. When we include a moderate amount of cold gas in the progenitor disc (similar to the gas fractions observed in typical spirals today), the scaleheights of simulated discs that have experienced a 1:10 merger are in good agreement with the observed values both for the MW thin disc and for external galaxies.

Chapter 3

Semi-Analytic Modelling

Semi-analytic models (SAMs) of galaxy formation are embedded within the framework of a ΛCDM initial power spectrum and the theory of the growth and collapse of fluctuations through gravitational instabilities. Following the formation of dark matter haloes, the models include a simplified yet physical treatment of gas cooling, star formation, SN and BH feedback, and merging of galaxies. They employ a Monte-Carlo approach which enables both the study of individual objects and global, statistical quantities. In contrast to numerical simulations, many realisations can be run in a very short amount of time. SAMs are thus an efficient way of exploring the large parameter space occupied by many uncertainties associated with the physics of e.g. cooling, star formation, feedback, and the IMF. As a result, studies using SAMs have been very successful in the prediction and explanation of observed statistical galaxy properties, such as invoking feedback mechanisms to model the galaxy luminosity function (Croton *et al.* 2006; Bower *et al.* 2006), explaining the tight correlation between radii, velocity dispersions and luminosities of elliptical galaxies ('fundamental plane', e.g. Hatton *et al.* 2003), reproducing the observed global star formation history (cf. Madau *et al.* 1996; Baugh *et al.* 1998) and solving the 'missing satellite problem' (cf. Moore *et al.* 1999; Macciò *et al.* 2010).

3.1   Merger trees

The starting point for every SAM is to specify the background cosmology. At the current date, this is usually a CDM universe with a cosmological constant (ΛCDM) and initial fluctuations that follow a Gaussian random distribution. Once the cosmological parameters have been determined, the pattern of primordial density fluctuations is defined and the time evolution of their collapse into gravitationally bound structures is set. The dark matter component forms haloes which can be termed the cradles of galaxy formation, as they provide the necessary potential well in which hot gas can cool and accrete into a cold disc, subsequently forming stars and thus creating a galaxy. The first step for every galaxy formation model thus has to be the sampling of the dark matter haloes which includes three main properties. One is the abundance of haloes at different masses and redshifts and specifies, how many haloes of a specific mass have formed at a certain redshift. This information is given by the halo mass function. The second property is the formation history
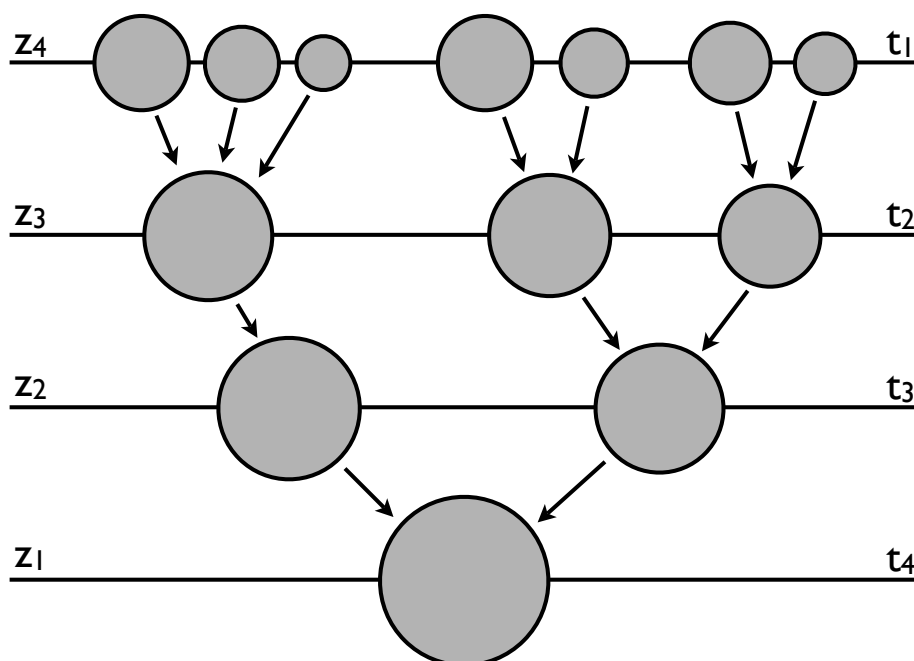
Figure 3.1 A schematic merger tree for a dark matter halo. The horizontal lines represent snapshots during the evolution of a halo and correspond to time-steps in a numerical simulation or Monte-Carlo realisation of the tree. The top line indicates the earliest time-step (high redshift) and the bottom line shows the latest time-step ($z = 0$). The size of the circles indicates the mass of each halo. The haloes grow through merger events and by accretion of objects below the resolution limit.

of the haloes which indicates how many smaller haloes were accreted onto a specific halo and at which time. This process will be especially important for the shaping of the galaxy structure and is commonly depicted by so-called merger trees. A schematic merger tree is shown in Figure 3.1: many small haloes at high redshift (top line) subsequently merge and form one large halo at $z = 0$ (bottom line). The last important property is the internal structure of each halo, i.e. the radial density profile and the angular momentum.

There have been two main approaches in the literature in order to model the halo population. The first is the EPS formalism which uses an analytic technique to built the individual merger trees with a Monte-Carlo method. Example of this method include Kauffmann & White (1993), Lacey & Cole (1993) and Somerville & Kolatt (1999). In the second approach, the haloes and the merger trees are directly extracted from an N-body simulation. This method has been applied by e.g. Kauffmann *et al.* (1999), Springel *et al.* (2001) and De Lucia *et al.* (2004). The advantages of the analytic method are the flexibility and the ability of creating many merger trees in a short

amount of time, while the advantages of the numerical method are the informations about positions and velocities of the haloes. In the following sections we will provide the basic ingredients of both methods.

3.1.1 Extended Press-Schechter formalism

The first attempts to calculate the abundance of gravitationally bound structures was made by Press & Schechter (1974). In order to describe the amplitude of the density fluctuations at the position $\boldsymbol{x}$ and time t, one defines the relative density contrast

$$\delta(\boldsymbol{x}, t) = \frac{\rho(\boldsymbol{x}, t) - \bar{\rho}(t)}{\bar{\rho}(t)}, \qquad (3.1)$$

where $\bar{\rho}$ denotes the mean cosmic matter density. When smoothed with a spherical top-hat window W_M of scale $R = (3M/4\pi\bar{\rho})^{1/3}$, the variance of this density field has the form

$$\sigma^2(M) = \frac{1}{2\pi^2} \int \mathrm{d}k \, k^2 \, P(k) \, W_M^2(k). \qquad (3.2)$$

Here k is the wavenumber and $P(k)$ is the power spectrum, which describes the level of structure as a function of the length scale $L = 2\pi/k$. It is defined as the average of the squared Fourier transform of the density contrast and assumed to be a power-law with slope n: $P(k) = \langle |\delta_k|^2 \rangle \propto k^n$. The normalisation of the power spectrum is fixed by requiring that σ_8, the variance of the linear density fluctuation field when it is smoothed with a top-hat filter of scale $R = 8h^{-1}\mathrm{Mpc}$ has a specified value. Press & Schechter assumed a Gaussian density field for which the fraction of the cosmic volume at which it exceeds some critical value δ_c is known. In order to derive an appropriate value for δ_c, they used the spherical collapse model (Gunn & Gott 1972). Thus the fraction of the total mass that is contained within haloes of mass M is obtained by integrating over the tail (i.e. $\delta > \delta_c$) of the probability function:

$$F(M) = \int_{\delta_c}^{\infty} \mathrm{d}\delta p(\delta) = \frac{1}{\sqrt{2\pi}\sigma(M)} \exp\left(-\frac{\delta^2}{2\sigma^2(M)}\right) = \frac{1}{2} \operatorname{erf}\left(\frac{\delta_c}{\sqrt{2}\sigma(M)}\right). \qquad (3.3)$$

The distribution of haloes over masses M is then simply $\partial F(M)/\partial M$ which results in the halo mass function

$$n(M)\mathrm{d}M = \sqrt{\frac{2}{\pi}} \frac{\bar{\rho}\delta_c}{\sigma(M)} \frac{\mathrm{d}\log\sigma(M)}{\mathrm{d}M} \exp\left(-\frac{\delta_c^2}{2\sigma^2(M)}\right) \frac{\mathrm{d}M}{M}. \qquad (3.4)$$

However, the derivation by Press & Schechter neglects underdense parts of the Universe and thus omits half the mass such that the expression of the halo mass function had to be multiplied by a factor of two. An alternative derivation of the halo mass function was discovered by Bond *et al.* (1991) who used a top-hat in Fourier space rather than in real space to smooth the density field.

This 'excursion' set formalism can explain the missing factor of two and led to the development of EPS theory (Bower 1991; Lacey & Cole 1993; Jedamzik 1995; Nagashima 2001). The extended version of the theory gives the distribution of masses of the progenitors of a halo at some earlier epoch which is called the conditional mass function.

With this formalism at hand it becomes possible to construct merger histories for individual haloes. A first method to do this was proposed by Kauffmann & White (1993), were a grid in mass and redshift is imposed. An ensemble of N_t possible sets of progenitors at redshift $z + \Delta z$ is constructed for a halo of mass M identified at redshift z. The number of progenitors with mass M' is given by $N(M') = N_t \, M \, \mathrm{d}N/\mathrm{d}M(M') \, \Delta M'$, where $\mathrm{d}N/\mathrm{d}M(M')$ is the mass function of the progenitors as computed from the EPS formalism. These progenitors are then partitioned into N_t sets, each corresponding to a possible history of the original halo. This is done one by one in order of decreasing mass. For each progenitor a set is randomly chosen with a probability that is proportional to the set's remaining free mass, with the constraint that the total mass of the progenitors cannot exceed the mass of the original halo. This process is then repeated for all steps in the redshift grid.

While being simple to implement and computationally efficient, this method has some disadvantages. First, as the progenitor mass function is sharply peaked around M for small M or small redshift intervals, the algorithm is sensitive to the binning used and is thus prone to numerical problems. Second, as one needs to introduce an effective mass cut-off, the total mass of the progenitors does not add up to M. On the other hand, it is also possible to encounter a situation were the next halo does not fit into any of the ensembles. Finally, although the mean of the distribution is reproduced by construction, the partitioning of the haloes into the ensembles is ad-hoc and might not reproduce higher order moments of the distribution. To overcome these problems, advanced algorithms have been proposed (Lacey & Cole 1993; Somerville & Kolatt 1999). However, even these methods generally give less precise representations of the merger trees than those extracted from N-body simulations (Somerville *et al.* 2000). In addition, the formation history of a halo is assumed to be independent of its environment, which is not found to be true in simulations.

3.1.2 N-body trees

Alternatively, it is possible to extract merger trees directly from cosmological N-body simulations. The first step is to create a random realisation of the dark matter distribution according to the initial Gaussian density fluctuation field. For this a uniform distribution of particles representing the unperturbed Universe is set up, usually in a cubic regular grid. The fluctuation spectrum for the desired cosmology can then be created using the Zeldovich approximation which is valid in the mildly non-linear regime and assumes a matter-dominated, flat universe. The perturbed position $\boldsymbol{r}$ of a particle as a function of its initial position is then given by $\boldsymbol{r} = a(t)\boldsymbol{q} + b(t)\boldsymbol{p}(\boldsymbol{q})$, where $a(t)$ is the scale factor and $\boldsymbol{p}$ is the perturbation function with time dependence $b(t)$. This displacement

field depends on the gradient of the gravitational potential which can be computed from the power spectrum with Fourier techniques. These initial conditions can then be evolved using an N-body method such as those described in section 2.1. In order to be able to follow the evolution of the particles in these simulations, snapshots have to be stored for a set of redshifts.

Once a cosmological N-body simulation has been run, one has to identify the dark matter haloes. This is done by a so-called 'halo-finding-algorithm' which yields a catalogue of haloes that includes all the properties of the haloes at every stored redshift. The most widely used halo-finding algorithms are the friends-of-friends (FOF; Davis *et al.* 1985; van Kampen 1995) and the spherical overdensity algorithm (Lacey & Cole 1994).

The FOF method links pairs of particles together if their distance is smaller than a certain linking length. It starts with a random particle and links every particle within a sphere of radius $bd/2$ to it. Here, d is the mean distance between particles and b is the linking parameter. When no more particles can be linked to the group a new particle is selected and the process is repeated. Usually $b = 0.2$ is adopted which leads to particle groups with a mean overdensity of about 200. The hierarchical FOF method (Klypin *et al.* 1999) solves the problem that apparently distinct haloes are merged if the linking radius is too large or that some haloes are missed if the radius is small.

The FOF algorithm is not able to identify bound structures within the parent haloes, i.e. the subhaloes. These can be found with a post-processing method such as SUBFIND (Springel *et al.* 2001), which assigns a density to every particle in the parent halo and then identifies locally over-dense regions. Each substructure candidate is then subject to a gravitational unbinding procedure which checks for every particle, if its total energy is positive, and if so, removes the particle from the subhalo. After all substructures are identified they are extracted from the FOF halo so that it can also be subject to the unbinding procedure. To compute a virial mass estimate for each FOF halo, a sphere is placed on the centre of the gravitational potential within the group with a radius that encloses a mean density of Δ_v times the critical density. Commonly, either $\Delta_v = 200$ is assumed or it is computed from a cosmology dependent fitting function (Bryan & Norman 1998).

The spherical overdensity algorithm finds haloes as maxima of mass inside a sphere of a given overdensity by iteratively moving randomly placed small spheres until the centre of mass in the sphere coincides with the centre of the sphere. However, as a fixed overdensity and thus a fixed radius is assumed, it is not possible to find haloes in both low and high density environments. Therefore this method is only used to identify the centres of haloes and the radius of the sphere corresponds to the scale of the smallest objects one tries to identify. Then the virial radius of each halo is computed such that it contains a mean overdensity Δ_v. The code DENMAX (Gelb & Bertschinger 1994) and its offsprings SKID (Governato *et al.* 1997) and BDM (Klypin & Holtzman 1997) introduce a procedure that removes unbound particles. If the density profile is flattening inside the virial radius, the halo is expected to be a subhalo and its radius is truncated at that point. One thus gets a first estimate for the mass and the radius of the halo. Assuming an

NFW profile all unbound particles are then removed from the subhalo and a new mass and radius are determined. This procedure is repeated several times. In contrast to SUBFIND, the particle lists of different haloes are in general not disjoint. This means that a particle of a subhalo that is bound to the host appears both in the parent halo list and the subhalo list.

Finally, when all haloes have been identified at all output redshifts, one can construct the merger trees. This can either be done by identifying descendants in a later snapshot (Springel *et al.* 2005b), or by identifying progenitors in an earlier snapshot (Maulbetsch *et al.* 2007; Hirschmann *et al.* 2010). Because haloes merge hierarchically in a CDM universe, a given halo can have several progenitors, but generally only one descendant. It is therefore simple to start at the earliest snapshot and use the unique IDs of the particles to track them between outputs. For every given halo, all haloes, that contain some of its particles in the following snapshot, are identified. The particles can be weighted by giving a higher weight to those particles that are more tightly bound in the original halo. The descendant halo is then selected as the halo with the highest summed weight. Once each descendant of the haloes at a given redshift is determined, the procedure is repeated at the next redshift until the last output has been reached. Alternatively, one can start at the lowest redshift, and track the progenitors of each halo. In this approach a halo at redshift z_1 is identified as the most massive progenitor (MMP) of a halo at redshift $z_0 < z_1$ if at least a fraction $f_{\min} = 0.2$ of its particles are found in the progenitor, and the overlap of particles divided by the number of particles in the larger halo is maximal. For all progenitors that are merging in a time-step at least half of their particles are required to be found in their descendant.

Compared to the analytic EPS theory, running and analysing an N-body simulation is much more time consuming. Furthermore, there are some numerical difficulties: objects that a group finder identified as a structure in a given output may later fly part, and when objects merge, the mass of the remnant may not always equal the mass of the progenitors. This means that the mass of a halo in a tree may not always increase monotonically with time. However, there are also many advantages: N-body simulations contain spatial information for the haloes and their subhaloes which can be used to study clustering. On the whole, N-body trees are more accurate and incorporate environmental effects. Since the cosmological parameters are now determined to a very high accuracy, it is reasonable to stick to one cosmological model and abandon the advantage of quickly varying the cosmology in the EPS theory.

3.2   Baryonic physics

With the merger trees at hand, one can populate the dark matter haloes with luminous galaxies. However, the baryonic processes are far more complex and difficult to model than the gravitational instability, as they are dissipative and non-linear. The physics behind these phenomena are generally not well understood, such that they are modelled with simple recipes containing free parameters. These parameters are then tuned by demanding that the model reproduces a subset of
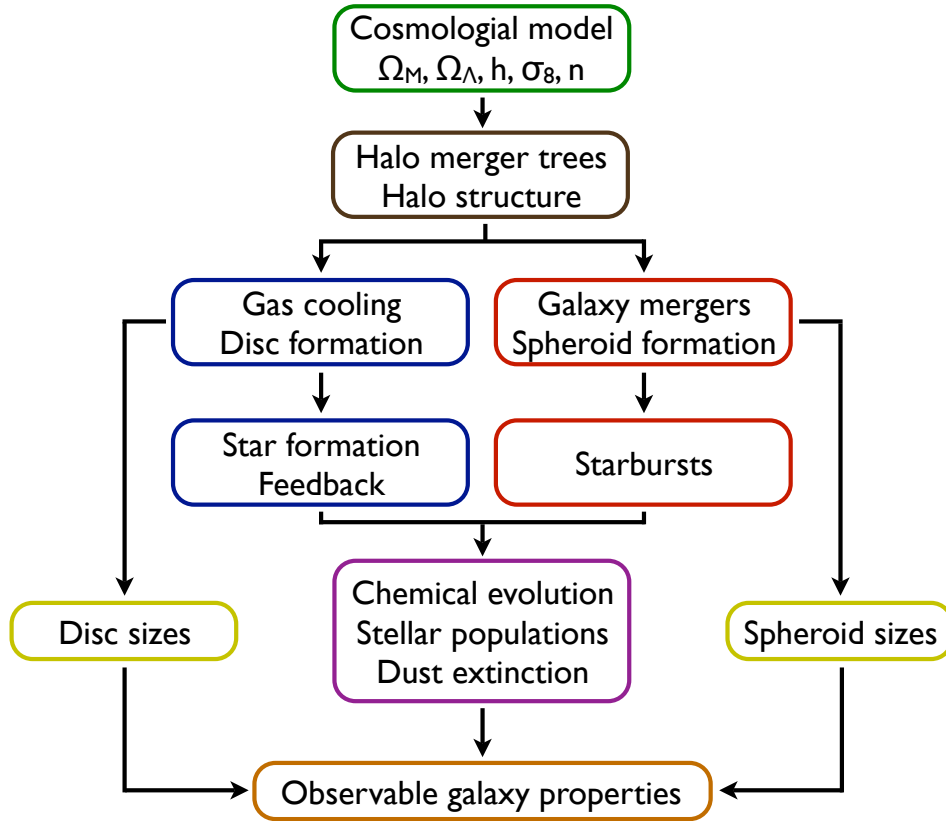
Figure 3.2 Schematic overview of the processes incorporated in semi-analytic models.

the available observations, typically at low redshift. The form of the adopted recipe that describes a process is either motivated by results from a more detailed numerical simulation, or from observations. A schematic overview of the processes typically included in SAMs is shown in Figure 3.2, adopted from Cole *et al.* (2000).

3.2.1 Gas cooling

The cooling of gas is essential to the formation of galaxies, as it sets the rate at which the material for star formation is acquired. The standard model of gas cooling in a dark matter halo was developed by White & Frenk (1991), based on work by Rees & Ostriker (1977) and Silk (1977). This model assumes that the gas initially has the same spatial distribution as the dark matter. In massive systems and at low redshift, the gas is heated by shocks as it falls into the gravitational well of a dark matter halo, producing a hot gaseous halo that is supported against further collapse by the pressure of the gas (*static hot halo regime*). The gas attains the virial temperature of the halo $T_{\mathrm{vir}} = \mu m_{\mathrm{p}} V_{\mathrm{vir}}^2 / 2k = 35.9 \, [V_{\mathrm{vir}}/(\,\mathrm{km}\,\mathrm{s}^{-1})]^2$ K, where μm_{p} is the mean particle mass, k is the Boltzmann constant, and $V_{\mathrm{vir}} = \sqrt{GM_{\mathrm{vir}}/r_{\mathrm{vir}}}$ is the virial velocity of the halo. From this hot halo

reservoir, gas can subsequently cool at a rate that depends on its temperature. As the gas cools, its pressure decreases and the removal of pressure support causes the gas to sink to the centre of the halo on a specific time-scale. Assuming conservation of angular momentum, the cold gas forms a cold, rotationally supported disc. Thus the cooling rate depends upon how fast the gas can cool (i.e. the cooling time) and how fast the cooled gas can move from the halo to the disc. This time has originally been proposed to be equal to the Hubble time, but newer models adopt either the time since the last major merger or the dynamical time of the halo $t_{\mathrm{dyn}} = r_{\mathrm{vir}}/V_{\mathrm{vir}} = 0.1/H(z)$ which has been shown to agree better with numerical simulations.

The cooling time is conventionally taken as the ratio of the specific thermal energy of the gas to the cooling rate per unit volume:

$$t_{\mathrm{cool}} = \frac{(3/2)n_{\mathrm{g}}kT}{n_{\mathrm{g}}^2\Lambda(T_{\mathrm{vir}}, Z_{\mathrm{g}})} = \frac{3}{2}\frac{\mu m_{\mathrm{p}}kT}{\rho_{\mathrm{g}}(r)\Lambda(T_{\mathrm{vir}}, Z_{\mathrm{g}})} \, , \qquad (3.5)$$

where $\rho_{\mathrm{g}}(r)$ is the gas density profile. The cooling function Λ depends on the temperature and metallicity of the gas Z_{g}. The main processes that determine the cooling function are photon emission after collisions between partially ionised atoms and electrons ($10^4\mathrm{K} < T < 10^6\mathrm{K}$), and Bremsstrahlung as electrons are accelerated in an ionised plasma ($T \gtrsim 10^6\mathrm{K}$). After the gas density profile has been defined, one can compute a cooling radius r_{cool}. The gas enclosed within r_{cool} has had sufficient time to cool since the halo was formed. The cooling radius propagates outwards until either all of the hot gas has cooled, or a new hot halo forms as the result of a merger with another halo.

In low mass haloes or at high redshifts, the formal cooling radius may lie outside the virial radius $r_{\mathrm{cool}} > r_{\mathrm{vir}}$. The post-shock gas then cools in less then one sound crossing time and cannot maintain the pressure needed to maintain an accretion shock at large radius. All infalling gas is then accreted immediately on to the central disc. In this *rapid cooling regime* the cooling rate is therefore set equal to the rate at which new diffuse gas is added to the halo. This regime is also used to capture the effects of 'cold streams' found in numerical simulations at high redshifts, where gas is funnelled down filaments onto the galaxy and thereby never heated above $\sim 10^4$ K.

Cooling can be suppressed in low mass haloes due to the presence of a background of photo-ionising radiation. This background of high energy photons may be created by quasars or massive stars and heats the intergalactic medium, thus increasing its pressure. Thus baryons are restricted from falling into haloes with low virial temperatures which decreases the baryonic fraction in these haloes. In addition, this radiation increases the ionisation of the hot gas which removes cooling channels following the excitation of atoms and ions in collisions.

3.2.2 Star formation and feedback

The lack of a theory of star formation has forced SAMs to take a pragmatic approach and incorporate an effective model. Based on a dimensional argument, a simple estimate of the SFR is $\dot{m}_* \propto m_{\mathrm{cold}}/\tau$, where m_{cold} is the amount of cold gas in the disc and τ is a characteristic time-scale. Typically, τ is assumed to be the dynamical time of the galaxy $r_{\mathrm{disc}}/v_{\mathrm{disc}}$ and star formation is only present above a critical surface density, as found in observations. The Schmidt-Kennicutt law $\dot{\Sigma}_* \propto \Sigma_g^N$ can be rewritten in this simple form. All stars are supposed to be formed in an exponential disc. Its scalelength can be computed by assuming that the disc has the same specific angular momentum as the dark matter halo: $R_{\mathrm{disc}} = r_{\mathrm{vir}}\lambda/\sqrt{2}$ (Fall & Efstathiou 1980). An improved calculation by Mo *et al.* (1998) includes realistic density profiles for the dark matter and the gas, the gravity of the disc and bulge, and the reaction of the halo to the gravity of the collapsed baryons, which causes a contraction of the dark matter halo.

From the first calculations of the galaxy luminosity function, the need for physical processes that modify the efficiency of galaxy formation as a function of halo mass was recognised. Specifically at the faint and bright ends, the luminosity of galaxies in models without such feedback processes is over-predicted, even if the variations of the cooling time of the hot gas with halo mass are considered. The most common form of feedback is the ejection of cold gas from the central disc by SN-driven winds. The reheated gas is either trapped within the potential well of the halo and deposited in the hot halo from where it can subsequently cool (*retention* feedback), or, provided the wind velocity is large enough, it may even be ejected from the halo into the intergalactic medium (*ejection* feedback). As SN feedback is intended to reduce the efficiency of star formation in low mass haloes, the rate of reheating of cold gas is typically modelled as a strong function of circular velocity of the halo.

In order to reproduce the break at the bright end of the luminosity function, several processes have been invoked, including a higher cooling time due to a constant density core of the gas, thermal conduction in the hot halo and 'superwinds'. State-of-the-art SAMs employ feedback from AGN. For this, it becomes necessary to track the evolution of BHs. As observationally, one finds a correlation between BH mass and bulge mass (Magorrian *et al.* 1998; Ferrarese & Merritt 2000; Häring & Rix 2004) the models tie the evolution of BHs to the process that is responsible for shaping bulges, i.e. galaxy mergers. During the 'quasar mode', the mass of the BH is built up due to mergers of existing BHs and accretion of cold gas in starbursts. During the 'radio mode', the BH accretes gas directly from the hot halo which releases energy back into the hot halo and is hence responsible for suppressing the cooling flow in massive haloes. This heating is modelled with a parametric form which depends on the virial temperature of the halo and the mass of the BH.

3.2.3   Mergers and morphology

In the hierarchical galaxy formation scenario, systems are assumed to grow through mergers and accretion. While the galaxies survive the mergers of their parent haloes as they are highly concentrated, the dark matter halo of the smaller system gets stripped when orbiting in the larger halo. This leads to a picture in which a dark matter halo contains a massive central galaxy surrounded by smaller satellite galaxies that were formerly central galaxies in the progenitors of the current halo. As these satellites orbit the central galaxy they gradually lose energy due to dynamical friction. When the orbital energy of a satellite has been removed completely it merges with the central galaxy. This merger triggers a burst of star formation as the cold gas loses angular momentum and falls to the centre owing to gravitational torques during merger events. In the dense centre the gas quickly forms stars and the 'bursted' mass depends on the initial gas fractions of the galaxies and on their mass ratio. In addition, a merger of sufficient mass ratio changes the morphology of the system. In early models, a threshold was defined above which the disc of the central galaxy was destroyed and all of the stars involved in the merger form a spheroidal remnant. In newer models, a continuum is assumed, where larger mass ratios result in a transfer of more material to the spheroidal component.

3.2.4   Chemical evolution and luminosities

The formation of stars changes the metal content of the gas of a galaxy. Through SN explosions or stellar wind, stars return material to the gas with an enhanced metallicity. SNe of type Ia happen on long time-scales ($\sim 1\,\mathrm{Gyr}$) and dominate the production of iron, while SNe Ib and SNe II happen on short time-scales ($\sim 10\,\mathrm{Myr}$) and are responsible for the production of nuclei formed by α particles. In most SAMs, only SNe II are modelled. In a given time-step a quantity of metals, determined by the yield for the chosen IMF, is generated instantaneously.

In order to compare the predictions of the model to observations one has to compute the galaxy luminosity in different energy bands (i.e. as a function of wavelength). This is done by storing the star formation history of every galaxy which specifies how many stars of a given metallicity have formed at which time. This information is then combined with a stellar population synthesis model which predicts the luminosity for a single-age population of stars in a given band as function of their age and metallicity. For this a distribution of masses (IMF) is assumed.

Absorption of galactic light by dust in the interstellar medium causes galaxies to appear fainter and redder. In SAMs, this effect is modelled by invoking a uniformly mixed slab of dust and stars. The optical depth of the slab is determined empirically from observed correlations between the face-on optical depth of dust in galactic discs and the total luminosity of the galaxy.

3.3 The *Santa Cruz* semi-analytic model

In this work we employ the SAM by Somerville & Primack (1999) in its current form (Somerville *et al.* 2008a). This model can be used both with merger trees from EPS and N-body simulations. Each dark matter halo is assigned two properties: the spin parameter λ which defines its angular momentum and the concentration parameter c which describes the matter density profile. Each top-level halo is assigned a value of λ by selecting values randomly from a lognormal distribution with mean $\bar{\lambda} = 0.05$ and width $\sigma_\lambda = 0.5$, independent of halo mass and redshift. The halo at the next stage of the merger inherits the spin parameter of its largest progenitor. The initial density profile of each halo is described by the NFW form. Unless N-body merger trees are used, where the concentration parameter is extracted from the simulation, the fitting formula by Macciò *et al.* (2008) is employed to compute c as a function of halo mass. The model assumes a universal Chabrier (2003) IMF.

3.3.1 Gas cooling

The cooling time is calculated with the cooling function by Sutherland & Dopita (1993) and is set equal to the dynamical time of the halo. The gas density profile is assumed to be that of a singular isothermal sphere: $\rho_\mathrm{g}(r) = m_\mathrm{hot}/(4\pi r_\mathrm{vir} r^2)$. The cooling radius is then defined as:

$$r_\mathrm{cool} = \sqrt{\frac{t_\mathrm{dyn} m_\mathrm{hot} \Lambda(T_\mathrm{vir}, Z_\mathrm{g})}{6\pi \mu m_\mathrm{p} k T r_\mathrm{vir}}} \, . \tag{3.6}$$

Writing the expression for the mass within r_cool and differentiating, the rate at which the gas can cool is given by

$$\frac{\mathrm{d}m_\mathrm{cool}}{\mathrm{d}t} = \frac{m_\mathrm{hot}}{2t_\mathrm{dyn}} \frac{r_\mathrm{cool}}{r_\mathrm{vir}} \, . \tag{3.7}$$

In order to model the effects of a photo-ionising background, the model follows Gnedin (2000) and defines a 'filtering mass' M_F. Haloes less massive than M_F contain fewer baryons than the universal average. The fraction of collapsed baryons for a redshift z and halo mass M_vir is

$$f_\mathrm{cb}(z, M_\mathrm{vir}) = \frac{f_\mathrm{b}}{[1 + 0.26 M_\mathrm{F}(z)/M_\mathrm{vir}]^3} \, , \tag{3.8}$$

where the filtering mass is a function of redshift and depends on the re-ionisation history of the Universe. A fitting function, parametrized according to the redshift when most of the medium is re-ionised, is presented in Kravtsov *et al.* (2004).

3.3.2 Star formation and feedback

Star formation in the 'quiescent' phase is based on the empirical Schmidt-Kennicutt law, and the SFR density is given by $\dot{\Sigma}_* = A_K \Sigma_{gas}^N / \tau_0^*$, where $A_K = 1.67 \times 10^{-4} M_\odot \, \mathrm{yr}^{-1} \, \mathrm{kpc}^{-2}$ is the normalisation appropriate for a Kroupa IMF, $N = 1.4$, and τ_0^* is a free parameter of order unity. The cold gas profile is assumed to be an exponential disc with a scalelength proportional to the scalelength of the stellar disc $R_{gas} = \chi R_{disc}$, where χ is assumed to be 1.5. Only gas lying above a critical surface density threshold Σ_{crit} is available for star formation. A value of $\Sigma_{crit} = 6 M_\odot \, \mathrm{pc}^{-2}$ is adopted. The radius within which the gas surface density exceeds this value is $R_{crit} = -\log(\Sigma_{crit}/\Sigma_0)$, where $\Sigma_0 = m_{cold}/(2\pi R_{gas}^2)$ is the central surface density. This results in a SFR of

$$\frac{dm_*}{dt} = \int_0^{R_{crit}} \dot{\Sigma}_* 2\pi R dR = \frac{2\pi A_K \Sigma_0^N R_{gas}^2}{N^2 \tau_0^*} \left[1 - \left(1 + \frac{N R_{crit}}{R_{gas}} \right) \exp\left(-\frac{N R_{crit}}{R_{gas}} \right) \right]. \quad (3.9)$$

The mass-loss from stars is accounted for by forming a mass $dm_* = (1 - \beta)\dot{m}_* dt$ of long-lived stars in a time-step dt for an instantaneous SFR $\dot{m}_*$.

The rate of reheating of cold gas by SN-driven winds is given by

$$\frac{dm_{rh}}{dt} = \epsilon_0^{SN} \left(\frac{200 \, \mathrm{km \, s}^{-1}}{V_{max}} \right)^{\alpha_{rh}} \frac{dm_*}{dt}, \quad (3.10)$$

where $\epsilon_0^{SN} \sim 1.3$ and $\alpha_{rh} \sim 2$ are free parameters and V_{max} is the maximum rotation velocity of the halo. The fraction of gas that is ejected from the halo is $f_{ej}(V_{vir}) = [1 + (V_{vir}/V_{ej})^6]^{-1}$, where V_{ej} is a free parameter in the range $100 - 150 \, \mathrm{km \, s}^{-1}$. The ejected gas is collected in a 'diffuse gas reservoir', which re-collapses into the halo later at a rate $\dot{m}_{re-in} = \chi_{re-in}(m_{ej}/t_{dyn})$, where m_{ej} is the mass in the diffuse reservoir, t_{dyn} is the dynamical time of the halo and $\chi_{re-in} \sim 0.1$ is a free parameter.

Every top-level halo in the merger tree is assumed to contain a BH with mass $M_{seed} \sim 100 M_\odot$, which is growing during a galaxy merger, according to $\log(M_{BH}/M_{sph}) = -3.27 + 0.36 \, \mathrm{erf}[(f_{gas} - 0.4)/0.28]$ as found by Hopkins *et al.* (2007). Here M_{BH} and M_{sph} are the masses of the BH and the spheroid component after the merger, respectively, and f_{gas} is the effective cold gas fraction before the merger. Feedback is provided from the BH by two modes: In the 'bright mode', the energy released during the rapid growth of the BH triggered by a merger event drives a galactic wind. The resulting outflow rate is computed by equating the momentum associated with the radiative energy from the accreting BH with the momentum of the wind. In the 'radio mode' accreting gas is converted into energy, reheating the gaseous halo. The gas is accreted onto the BH at the Bondi-Hoyle accretion rate $\dot{m}_{Bondi} = \pi(GM_{BH})^2 \rho_0 c_s^{-3}$, where ρ_0 is the density at the Bondi accretion radius $r_A = 2GM_{BH}c_s^{-2}$, and c_s is the sound speed of the gas.

The accretion rate can be rewritten as

$$\frac{\mathrm{d}m_{\mathrm{radio}}}{\mathrm{d}t} = \kappa_{\mathrm{radio}} \left(\frac{kT}{\Lambda(T, Z)} \right) \left(\frac{M_{\mathrm{BH}}}{10^8 M_\odot} \right) , \qquad (3.11)$$

where κ_{radio} is a free parameter. Whenever gas cools in the static hot halo regime, the central BH accretes at this rate and the energy that effectively suppresses the cooling is given by $L_{\mathrm{BH}} = \kappa_{\mathrm{radio}} \eta_{\mathrm{rad}} \dot{m}_{\mathrm{radio}} c^2$, where $\eta_{\mathrm{rad}} \sim 0.1$ is the efficiency with which mass is converted to energy near the event horizon, and c is the speed of light. This injection of energy compensates in part for the cooling, yielding a modified infall rate of $\dot{m}'_{\mathrm{cool}} = \dot{m}_{\mathrm{cool}} - 4L_{\mathrm{BH}}/3V_{\mathrm{vir}}^2$. This cooling rate is never allowed to fall below zero.

3.3.3 Starbursts and remnant morphology

The time it takes for a satellite galaxy to lose all of its angular momentum due to dynamical friction and merge with the central galaxy is computed with the formula given by Boylan-Kolchin *et al.* (2008). The efficiency of star formation in a merger-triggered burst is parametrized as a function of the mass ratio of the merging pair μ. For this, the total mass of baryons and dark matter in the central part of the system is used by defining $\mu = (m_{\mathrm{c},1} + m_{\mathrm{b},1})/(m_{\mathrm{c},2} + m_{\mathrm{b},2})$, where the 'core mass' m_{c} is the dark matter mass within twice the NFW scaleradius r_{s}, and m_{b} is the mass total baryonic mass (cold gas and stars). The burst efficiency e_{burst}, which is the fraction of cold gas that is consumed by the burst, is calculated with the model proposed by Hopkins *et al.* (2009a). This analytic recipe is tuned to match numerical simulations and depends on the merger orbit, the disc mass fraction and the cold gas fraction. At the beginning of the merger, a reservoir of $m_{\mathrm{burst}} = e_{\mathrm{burst}} m_{\mathrm{cold}}$ is allocated, where m_{cold} is the combined cold gas mass of both galaxies. The burst SFR declines exponentially until the reservoir is exhausted on a time-scale τ_{burst}, which is taken from a fit to numerical results. In Somerville *et al.* (2008a) it is assumed that during every merger with a mass ratio above $\mu = 0.1$, a fraction

$$f_{\mathrm{sph}} = 1 - \left[1 + \left(\frac{\mu}{f_{\mathrm{el}}} \right)^8 \right]^{-1} \qquad (3.12)$$

of the disc stars is transferred to the spheroidal or bulge component. Here, $f_{\mathrm{el}} \sim 0.25$ is a free parameter that determines the transition between violent and non-violent mergers. However, we note that in the current version of the SAM, the more complex model presented in Hopkins *et al.* (2009a) is employed.

An orbiting satellite may eventually lose so much of its mass that it becomes tidally disrupted. Per orbital period, it is assumed to lose ~ 30 per cent of its mass and when the mass has been stripped down to the mass within the NFW scalelength r_{s} it is considered to be tidally destroyed, and its stars are transferred to a diffuse stellar component that can be associated with a stellar halo.

3.3.4   Chemical evolution

In a given time-step, in which a stellar mass of mass $\mathrm{d}m_*$ is formed, a mass of metals $\mathrm{d}M_{\mathrm{Z}} = y\mathrm{d}m_*$ is created, which is assumed to instantaneously mix with the cold gas in the disc. The yield y is a constant free parameter. The metallicity of the cold gas Z_{cold} is tracked and when new stars are created they are assumed to have the mean metallicity of the cold gas at that time-step. Metals are ejected from the disc along with gas and are either mixed with the hot gas in the halo or ejected from the halo into the diffuse gas reservoir, in the same proportion as the reheated gas.

The photometric properties of the galaxies are calculated using the stellar population synthesis models of Bruzual & Charlot (2003). Dust extinction is based on the empirical results of Wang & Heckman (1996) who find that the extinction optical depth of a galaxy is a function of its blue luminosity. The extinction is then related to the inclination of the galaxy using a standard slab geometry. A random inclination is assigned to each galaxy and the extinction correction is only applied to the disc component.

3.4   Application: the merger trees of Milky Way-like galaxies

Having the galaxy formation model at hand, we can now study the properties of the galaxy merger trees. This allows us to determine which types of mergers are common and need to be studied in high-resolution merger simulations, and which mergers are uncommon and can be neglected in merger simulations. Typically the parameters used for merger simulations are drawn from a multidimensional grid which results in a very large parameter space. By finding out, which regions of this parameter space have a high probability we can reduce its effective size. Semi-analytic merger trees are the ideal tool for this study, as the predictions for the merger properties and rates are cosmologically motivated.

For this study we use dark matter merger trees drawn from an N-body simulation. The parent halo masses at $z = 0$ range between $10^{10} M_\odot$ and $10^{15} M_\odot$, and we especially focus on systems with masses that are comparable to the MW ($\log M_{\mathrm{halo}}/M_\odot \approx 12.0$ and $\log M_*/M_\odot \approx 10.5$). After populating the halo merger trees with galaxies according to the SAM, we study the probabilities for mergers as a function of halo mass, mass ratio, gas fraction and morphology. Additionally, we investigate, if galaxy mergers are binary (i.e. two galaxies merge in isolation), or whether multiple mergers are more important.

3.4.1   Simulation and merger trees

The dark matter merger trees used in this work are drawn from an N-body simulation run with the GADGET-2 code on a SGI AltixII at the University Observatory Munich. The cosmological parameters of the simulation are chosen to match results from WMAP-3 (Spergel *et al.* 2007) for a flat ΛCDM cosmological model: $\Omega_m = 0.26$, $\Omega_\Lambda = 0.74$, $h = H_0/(100\,\mathrm{km\,s^{-1}\,Mpc^{-1}}) = 0.72$,

$\sigma_8 = 0.77$ and $n = 0.95$. The initial conditions were generated using the GRAFIC software package (Bertschinger 2001). The simulation was done in a periodic box with a side length of 100 Mpc, and contains 512^3 particles with a particle mass of $2.8 \times 10^8 M_\odot$ and a comoving force softening of 3.5 kpc. Starting at a redshift of $z = 43$, there have been 94 snapshots stored until $z = 0$, equally spaced in expansion factor ($\Delta a = 0.01$).

Dark matter haloes are identified in the simulation snapshots using a FOF halo finder with a linking parameter of $b = 0.2$. Substructures inside the FOF groups are then identified using the SUBFIND code. For the most massive subgroup in a FOF group the virial radius and mass are determined with a spherical overdensity criterion using the fitting function by Bryan & Norman (1998). The minimum particle number of a halo is set to 20, resulting in a minimum halo mass of $5.6 \times 10^9 M_\odot$. The number of parent haloes found at $z = 0$ with this method is $\sim 135\,000$. The merger trees are constructed for all parent haloes at $z- = 0$ by connecting haloes between the 94 catalogues. The branches of the trees were determined by linking every halo to its most massive progenitor at previous snapshots with the method outlined in section 3.1.2. In total, 41 000 merger trees have been created. These merger trees are then used as the input for the SAM which populates them with galaxies. In this way galaxy merger trees are created.

3.4.2 Number of mergers depending on halo mass

The first and most basic quantity we want to study, is the number of mergers a system has since a given redshift. This is necessary to understand how common and thus important merger events are for a specific galaxy. If the number is very low, mergers are probably an unimportant process for shaping the properties of the galaxy, while for a large number of mergers, the galaxy's properties – especially its morphology – are mainly dependent on the type of mergers it has. In order to study this, we divide the merger trees according to the mass of their parent halo M_{halo} at $z = 0$ with a bin size of $\Delta \log(M/M_\odot) = 0.5$. For each mass bin we then count the number of halo mergers (i.e. a subhalo enters the parent halo) above a given mass ratio since a given redshift and divide that number by the number of systems in each mass bin. This is done for the three mass ratios $\mu = 0.25, 0.10$ and 0.03 (denoted as 1:4, 1:10 and 1:30 mergers) and the three redshifts $z = 1, 2$ and 5. We use the virial mass of the merging haloes to compute μ and the redshift at which the haloes merge to determine z.

The results of this analysis are shown in Figure 3.3. As we can see, 1:4 (major) mergers are very uncommon for systems below a mass of $\log(M/M_\odot) \lesssim 13$ since $z = 1$, with only every tenth system having such a merger. If we consider a larger look back time, the fraction of systems with a major merger increases to roughly 20 per cent since $z = 2$ and 50 per cent since $z = 5$. In massive systems on the other hand, major mergers are very common. Haloes of mass $\log(M/M_\odot) \approx 14$ have roughly one 1:4 merger per system since $z = 1$, two 1:4 mergers since $z = 2$, and three 1:4 mergers since $z = 5$. For these massive systems, the number of mergers per system is a strong

function of halo mass. This implies that major mergers are mainly important for massive galaxies.

Minor mergers are much more common, even for low-mass systems. Since $z = 1$ roughly every fifth systems with a mass of $\log(M/M_\odot) \approx 11$ experiences a 1:10 merger and every other system has a 1:30 merger. The fraction of systems with 1:10 and 1:30 mergers since $z = 2$ is ~ 0.6 and ~ 0.8, respectively, while since $z = 5$ it is ~ 1.0 and ~ 1.5, respectively. Massive systems with $\log(M/M_\odot) \approx 14$ have on average three 1:10 and seven 1:30 mergers since $z = 1$, five 1:10 and ten 1:30 mergers since $z = 2$, and eight 1:10 and eighteen 1:30 mergers since $z = 5$. Overall, except for haloes with very low mass, every system experiences one or more minor mergers on average. This means that minor mergers are very important for shaping galaxy properties in almost every system.

Finally, we study the number of mergers for a MW-sized galaxy with $\log(M/M_\odot) \approx 12$. If we consider all mergers since $z = 1$, we find that there are very few major mergers (~ 10 per cent). Although this number increases to 50 per cent if all mergers since $z = 5$ are considered, major mergers seem to be rather unimportant for shaping the properties of MW-sized galaxies. This may explain, why the majority of these systems are spiral galaxies, and only few galaxies are ellipticals. Minor mergers on the other hand are very common for MW-sized systems. About 70 per cent of them experience a 1:10 merger and the number of 1:30 mergers is on average 1.5. If all mergers since $z = 5$ are considered, the number increases to 2 and 4.5 for 1:10 and 1:30 mergers, respectively. This means that minor mergers are a very important process for MW-sized galaxies and are responsible for many properties of these galaxies. The thickness of the stellar disc and the mass in the stellar halo are two examples, where minor mergers are the dominant process that determine the galaxy property.
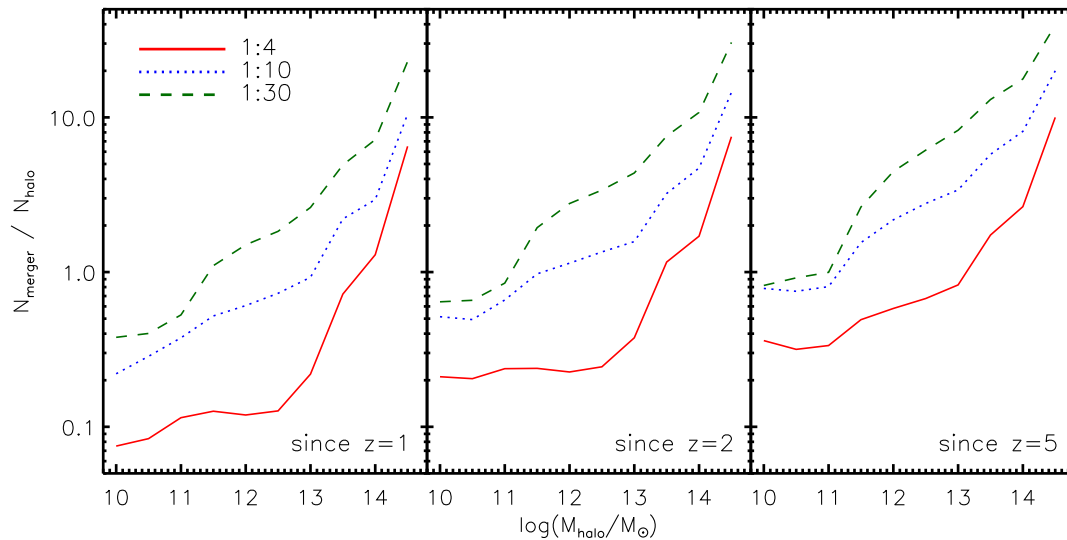
Figure 3.3 Number of mergers per halo above a given halo mass ratio since a given redshift.

3.4.3 Probability of multiple mergers

The next question we want to address is whether mergers happen isolated, or if they are usually multiple. In an 'isolated' merger (also called 'binary' merger), two galaxies have enough time to merge after their haloes have merged, before the remnant merges with another galaxy. In 'multiple' mergers, two galaxies have not had enough time to merge when another galaxy already enters their common halo. If isolated mergers are the standard event, then it is possible to study single merger events with specified parameters (e.g. in simulations) and then 'stack' these merger events for a given merger history, in order to determine the effects of the mergers on the galaxy. This can be seen as a linear process. However, if multiple mergers are more common, then it is no longer possible to string the results from binary merger simulations together. One then has to study the events with three or more galaxies involved which will have a different impact on the galaxy properties as two or more binary mergers. The merger process then becomes non-linear and the (already large) parameter space for the merger parameters multiplies.

In order to study this problem we divide the merger trees according to the mass of their parent halo at $z = 0$ with a bin size of $\Delta \log(M/M_\odot) = 0.5$. We then identify all merger trees of these systems with two or more halo mergers and for every pair of mergers we record the time difference between the halo mergers. If e.g. the halo of the satellite galaxy A merges with the halo of the central galaxy C at a cosmic time $t_1 = 8.0$ Gyr and later the halo of the satellite galaxy B merges with the halo of the central galaxy at $t_2 = 10.0$ Gyr, we store the time difference $\Delta t = 2.0$ Gyr. We divide this time by the dynamical time of the halo $t_{\mathrm{dyn}} = r_{\mathrm{vir}}/V_{\mathrm{vir}}$ at the time of the first halo merger t_1 and distribute the resulting number in bins of width $\Delta t/t_{\mathrm{dyn}} = 1$. Finally, we count the number of mergers pairs with a given mass ratio sequence and since a given redshift for each time bin. The sequence 1:4 $\rightarrow$ 1:10 for example means that the first merger has a mass ratio above 1:4 and the second merger has a mass ratio above 1:10. In order to get the probability for a merger sequence we normalise this number by dividing it by the number of mergers with the mass ratio of the first merger.

We show the results of this analysis in Figure 3.4. The probability for two mergers happening within a few dynamical times of the halo is always higher than the probability for a larger time difference. This indicated that usually the second satellite galaxy enters the parent halo before the first satellite had time to merge with the central galaxy, which happens only after several dynamical times, depending on the mass ratio of the merger. For the mergers that happen since $z = 1$ this trend is most obvious. Here, the second satellite enters the halo within three dynamical times after the first satellite entered for more than 50 per cent of all merger pairs independent of mass ratio. If we start at a higher redshift, the merger pairs are on average a little more separated. Still for more the 50 per cent of all merger pairs, the second satellite enters the halo within five dynamical times after the first one since $z = 5$.

As a result we find that multiple mergers are more common than sequences of isolated binary
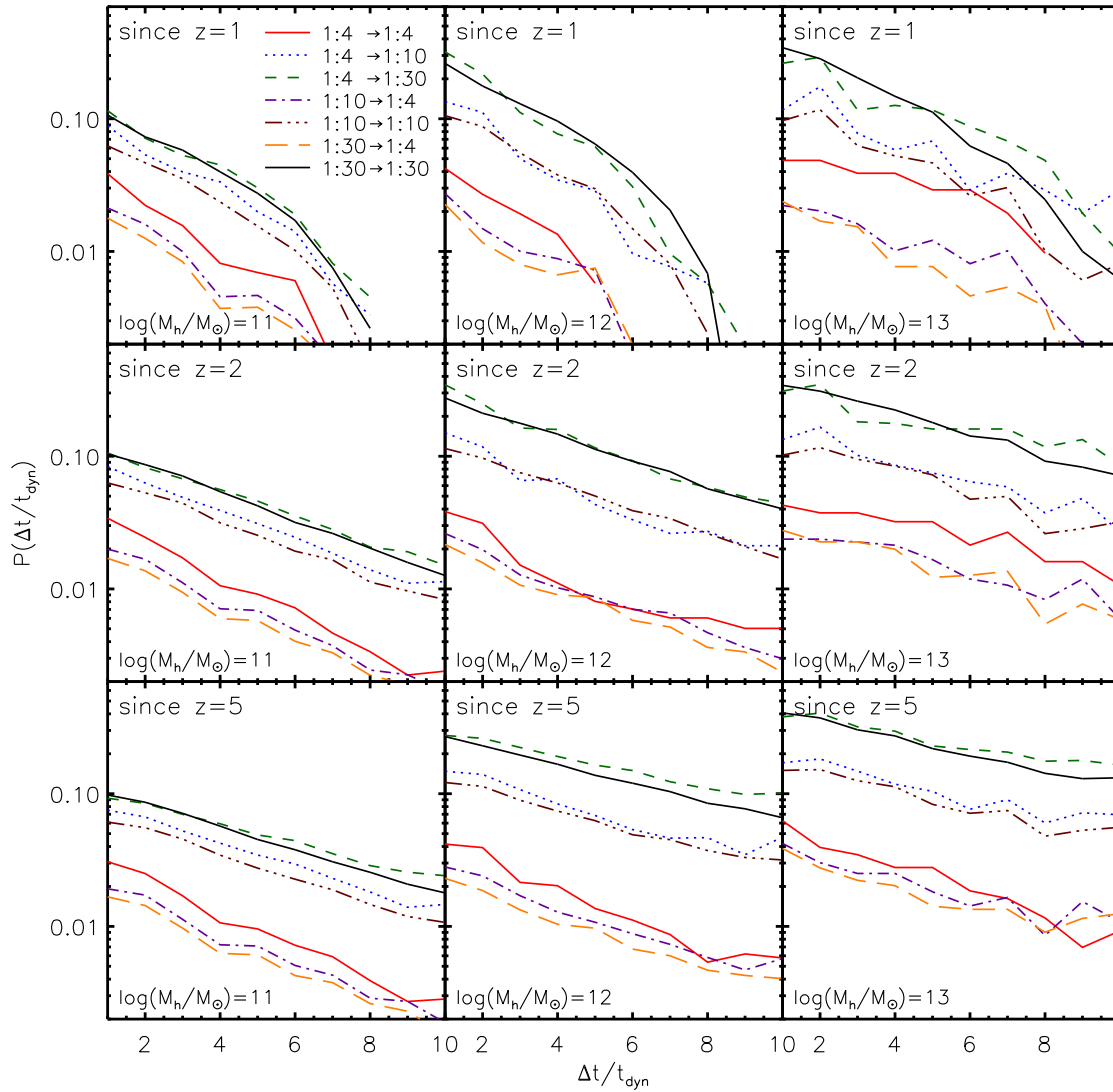
Figure 3.4 Probability for multiple mergers. The lines give the probability for a sequence of mergers with the indicated mass ratios as a function of the time difference between the mergers in units of the dynamical time of the parent halo.

mergers. Therefore it is not sensible to focus on binary mergers and afterwards try to string their effects together. The first satellite that enters the halo usually has not enough time to merge with the central galaxy, before the next satellite enters the halo and affects the evolution of the two galaxies that are still in the progress of merging. Thus merger simulations which consider several satellites that enter the parent halo after each other before the previous galaxy has merged with the central one, have to be performed and analysed. If parameters for the galaxies and the orbits are chosen from a multidimensional grid, the parameter space is then too large to cover. This means that one has to reduce this huge parameter space by selecting only those parameters that are

common for the chosen cosmology. Semi-analytic merger trees offer this option and are therefore very practical to use as initial conditions for the merger simulations.

3.4.4 Dependence on mass ratio

As we have seen before, the probability for a merger to happen depends on its mass ratio. In order to study, which mass ratio has the highest probability, we bin the (inverse) mass ratio $m_1/m_2 = \mu^{-1}$, i.e. the mass of the larger galaxy divided by the mass of the smaller one, in steps of $\Delta\mu^{-1} = 1$. We then count all galaxy mergers (i.e. the satellite galaxy merges with the central one) in the simulation box with a given mass ratio either for a given redshift z or a given stellar mass of the more massive galaxy $m_g = m_1$. In each redshift or stellar mass bin, the number of mergers for a given mass ratio is then normalised by dividing by the total number of mergers in order to get the merger probability. This analysis is done for both the baryonic mass ratio $m_{\mathrm{bar}} = m_* + m_{\mathrm{cold}}$, and the central mass $(m_{\mathrm{core}} + m_{\mathrm{bar}})$ as defined and used in the SAM.

The results of this study are presented in Figure 3.5. Equal baryonic mass mergers are rare in the early Universe but become more frequent in the late Universe. On the other hand, mergers with a larger ratio in baryonic mass, are more common in the early Universe and happen less often at $z = 0$. This can be explained with the evolution of the stellar-to-halo mass ratio. At early times, stellar mass is a steep function of halo mass. This leads to a rough correspondence between halo mass ratio and baryonic mass ratio in a merger. As equal halo mass mergers are less common than merger with a large halo mass ratio this correspondence results in the same trend for the baryonic mass. In the late Universe however, the shape of the stellar-to-halo mass ratio has been altered drastically by feedback mechanisms. As a result stellar mass is a weaker function of halo mass than at high redshift. This means that even if the halo mass ratio is large, which is also common at low redshift, the baryonic mass of the merging galaxies is likely to be similar. Thus equal baryonic mass mergers are more frequent.

The dependence on stellar mass is more obvious. Massive galaxies tend to have more equal baryonic mass mergers and less mergers with a larger ratio, while low-mass galaxies have few equal-mass mergers and many minor mergers. The reason is similar as before: stellar mass is a steep function of halo mass on the low mass end, and a shallow function on the massive end. Therefore, massive galaxies live in haloes with a large spread in mass and thus, independent of the halo mass ratio, the baryonic mass ratio will be close to unity. In low-mass galaxies on the other hand, there is a correspondence between halo and baryonic mass ratio and thus the dependence of the merger probability on baryonic mass ratio is similar to that of the dependence on halo mass ratio: few major mergers and many minor mergers. In terms of the central mass ratio (including dark matter), the merger probability is much more similar to the probability for a given halo mass ratio. At high redshift there are much more major mergers than minor mergers (but almost no equal mass mergers), while at $z = 0$, the dependence on the mass ratio is weaker. The probability
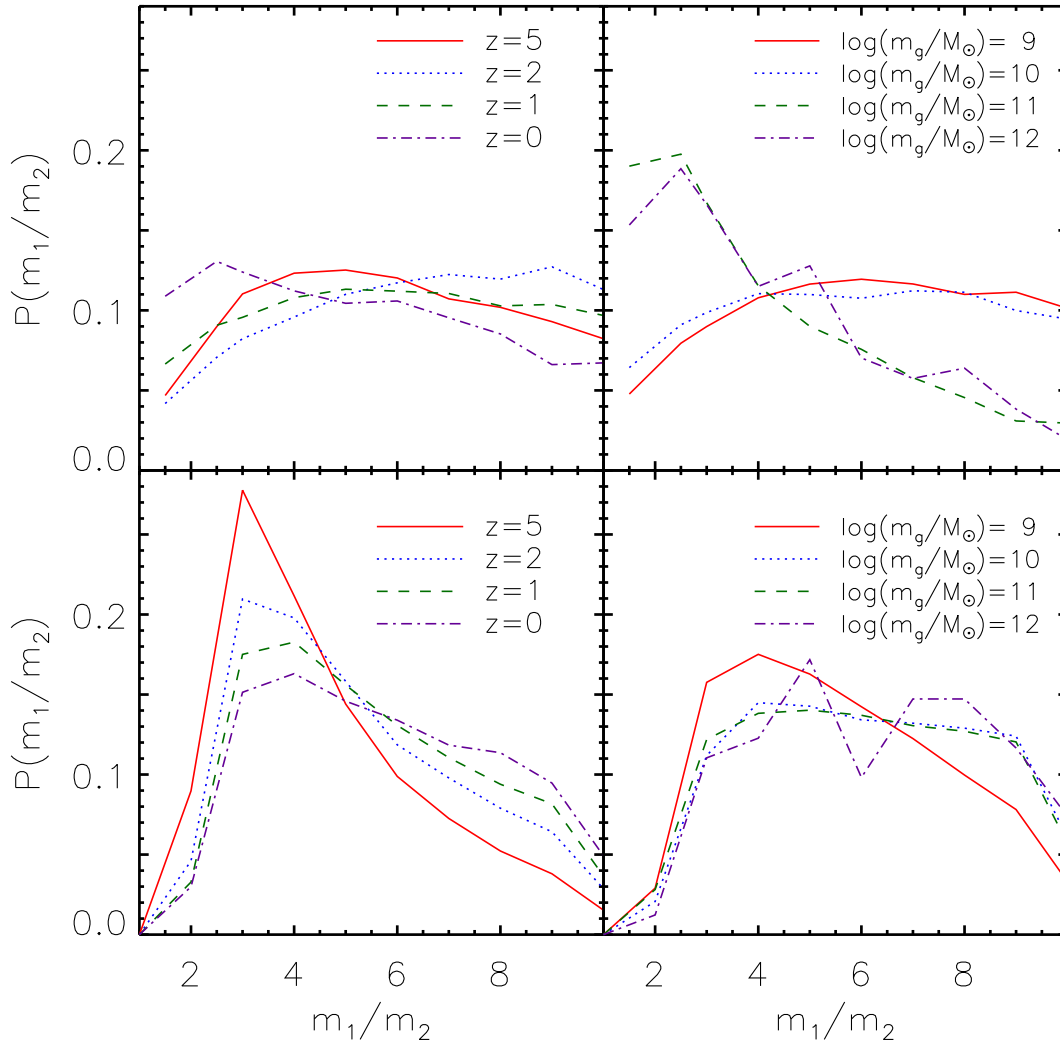
Figure 3.5 Probability for a merger with a given mass ratio. The top panels show the merger probability for the baryonic mass ratio while the bottom panels show the merger probability for the central mass ratio (dark matter, stars and cold gas). In the left panels the results are presented for given redshift bins and in the right panels for given stellar mass bins where the mass of the more massive galaxy was used.

for a certain central mass ratio is almost equal for all galaxy masses.

3.4.5   Dependence on gas fraction

The fraction of cold gas in the disc f_{gas} is a very important parameter for galaxy mergers. After major mergers the gas can form a new cold gas disc, from which a stellar disc subsequently forms that affects the morphology of the merger remnant. In minor mergers the cold gas disc is important for stabilising the stellar disc as it can radiate some of the impact energy away and thus reduce
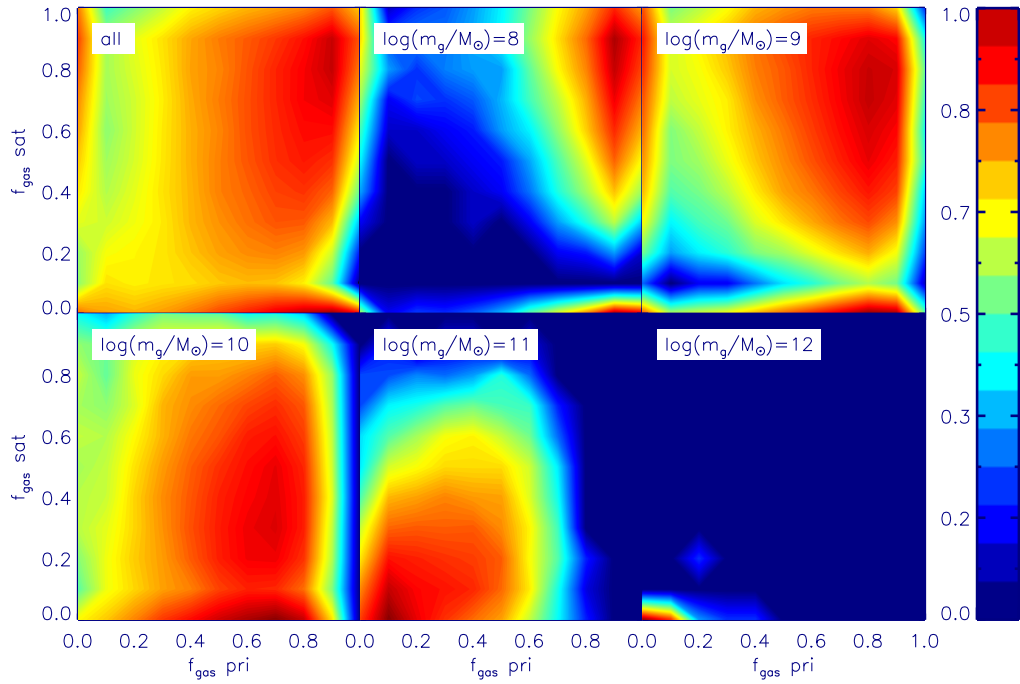
Figure 3.6 Probability for combinations of gas fractions of the primary and the satellite galaxies in mergers. Red colour indicates a high probability for a combination of gas fractions, while blue colour indicates a low probability. The panels represent samples of different stellar masses.

the thickening of the disc. It is therefore important to understand which gas fractions are common in mergers. Specifically, we want to study the joint probability for a merger with a gas fraction $f_{\mathrm{gas,pri}}$ in the primary galaxy and a gas fraction $f_{\mathrm{gas,sat}}$ in the satellite galaxy. For this we divide all mergers in the simulation box into samples with equal stellar mass of the primary galaxy and samples with equal redshifts of the mergers. We then count the number of galaxy mergers for a given pair of gas fractions in the primary and satellite galaxies. Finally we divide the this number by the maximum number in each stellar mass and redshift bin to get the probability for the given pair of gas fractions.

The results are shown in Figure 3.6 for the stellar mass bins and Figure 3.7 for the redshift bins. A red colour indicates a high probability and a blue colour indicates a low probability. Primary galaxies of low mass tend to have very high gas fractions ($\sim 60-90$ per cent), while their satellites can have a wide range of gas fractions from $0-100$ per cent (although there seems to be a gap at $f_{\mathrm{gas,sat}} \approx 0.2$). For more massive primary galaxies, the gas fraction decreases. In addition, also the gas fraction of their satellites decreases while still maintaining a wider range than the primary galaxy. For very massive galaxies, both the primary and the satellite galaxies have very low gas fractions of $f_{\mathrm{gas}} \lesssim 0.1$.

High redshift primary galaxies tend to have large gas fractions, as do their satellites for which the range of gas fractions is a larger, however. This indicates, that most of the galaxies have just
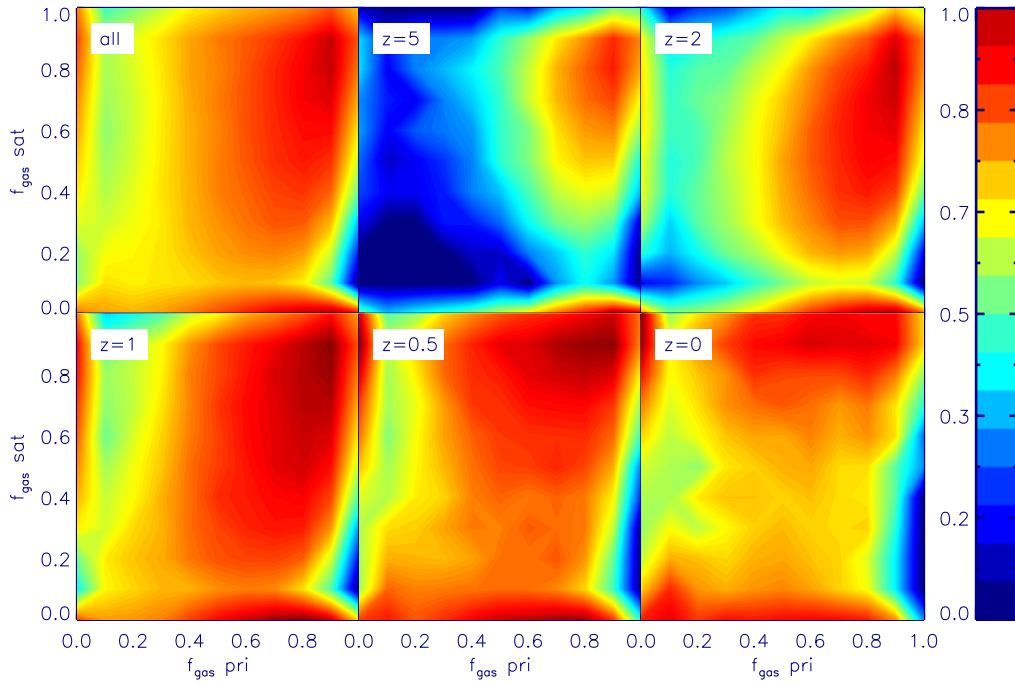
Figure 3.7 Probability for combinations of gas fractions for different redshifts.

formed a cold gas disc and did not have enough time yet, to convert the gas into stars. There are also some mergers at high redshift with a large gas fraction in the primary galaxy and a very low gas fraction in the satellite. With decreasing redshift the range of gas fractions in the primary galaxy increases, which shows that many galaxies convert their gas discs partly into stellar discs. At low redshift there seem to be two types of mergers: one with very high gas fractions in the satellite ($f_{\mathrm{gas,sat}} \approx 0.9$) which are probably galaxies that are unable to convert gas into stars as they are below the critical star formation threshold, and a second type with very low gas fractions in the satellite ($f_{\mathrm{gas,sat}} \lesssim 0.1$). These are galaxies that were very efficient in transforming gas to stars, and have probably been expelled all of their gas by massive winds. Moreover they are unable to acquire new gas through cooling as there exists a dominant source of heating. The gas fractions in the primary galaxies on the other hand are widely spread.

3.4.6   Dependence on morphology

Typically, when studying galaxy mergers, only mergers of disc galaxies are considered. Sometimes the bulges are neglected, sometimes they are included. However, it has been shown that the morphology of a galaxy has a large impact on the outcome of its merger. Therefore we study, how the probability for a given merger to happen depends on its morphology. For this we divide the mergers in the simulation box between major mergers ($\mu \geq 0.25$) and minor mergers ($\mu < 0.25$). For major mergers we count the number of galaxy mergers between spiral galaxies S-S (where
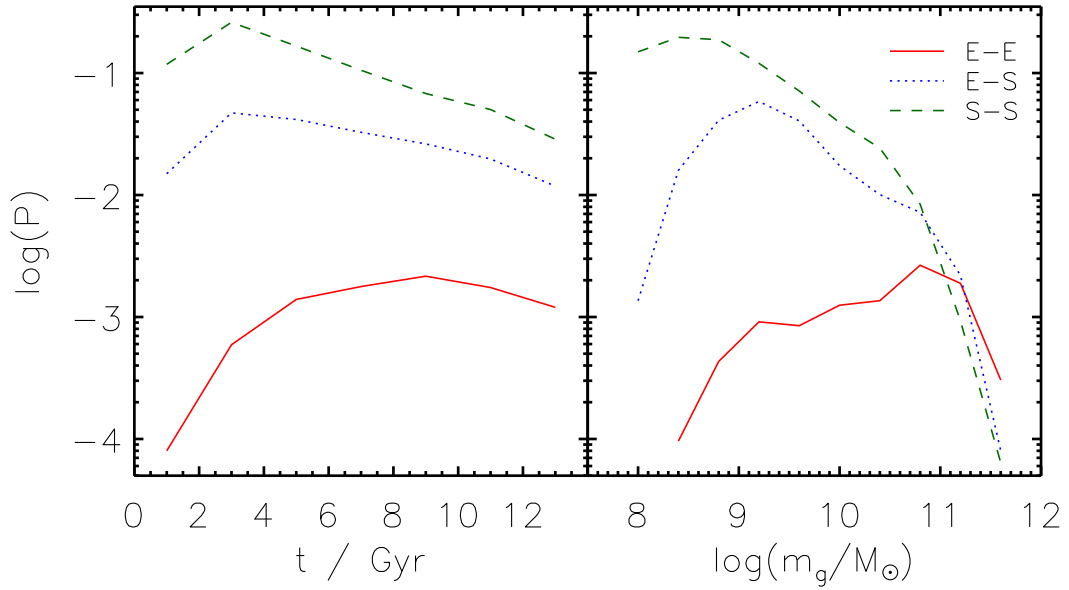
Figure 3.8 Probability for a given morphology for major mergers. The lines give the probability for mergers between ellipticals (E-E), spirals (S-S) and ellipticals with spirals (E-S). The left panel shows the probability as a function of cosmic time and the right panel gives the probability as a function of the stellar mass of the primary galaxy.

the bulge-to-total ratio is $B/T < 0.5$), between elliptical galaxies E-E (where $B/T \geq 0.5$) and between elliptical and spiral galaxies E-S as a function of cosmic time and the stellar mass of the primary galaxy. This number is then normalised by dividing by the total number of major mergers to get the probability.

We show the results in Figure 3.8. In the early Universe, the probability for mergers between spirals is highest and then decreases with time. On the other hand, mergers between ellipticals are very rare early but then become much more frequent at late times. However, they are still one order of magnitude rarer than mergers between spirals. This trend can be easily explained with the 'merger hypothesis', which states that major mergers lead to elliptical galaxies. This means that because of the many mergers between spirals at early times, more elliptical galaxies are created while spiral galaxies are destroyed. As a result the number of mergers between spirals decreases, while the number of mergers between ellipticals increases. The probability for mergers between ellipticals and spirals are is almost constant with time, although there is a slight decrease in the late Universe. It is almost as high as the probability for mergers between spirals. This shows that it is important to also consider these events in merger simulations.

If we consider the merger probability as a function of stellar mass, we see two obvious trends. The frequency of spiral mergers is very high for low-mass galaxies and very low for massive galaxies. On the other hand, mergers between ellipticals are very rare for low-mass galaxies and much more common for massive systems. The reason is that low mass galaxies are typically
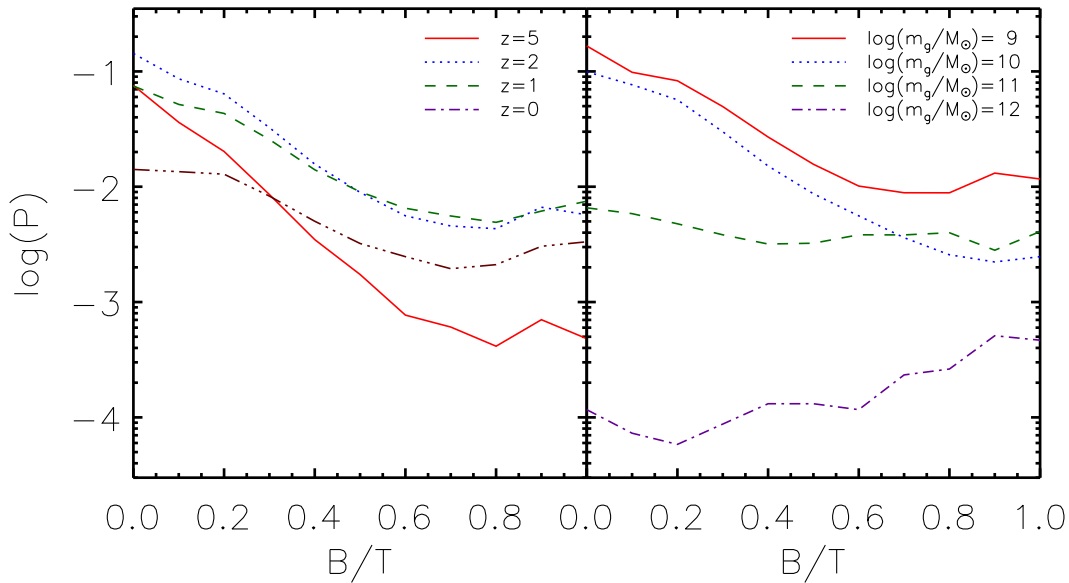
Figure 3.9 Probability for morphology for minor mergers. The lines give the probability for mergers as a function of their bulge-to-total ratio. The left panel shows the probability for a set of redshift bins and the right panel gives the probability for a set of stellar mass bins.

spiral galaxies as they undergo rather few merger events. Massive galaxies however, are typically elliptical galaxies, as the probability for them to have a major merger is very high. Thus as most low-mass systems are spirals and most massive systems are ellipticals, major mergers between systems in these mass regimes are S-S and E-E mergers, respectively. At the massive end, mergers between ellipticals are thus much more common than spiral mergers.

Finally we study the dependence on the morphology of the primary galaxy in minor mergers. For this we count the galaxy mergers as a function of the bulge-to-total ratio in the primary for a set of redshift and stellar mass bins. Again we normalise this number by dividing by the total number of mergers. The results are presented in Figure 3.9. As we can see, the dependence on B/T is almost the same at every redshift. Mergers with a low $B/T \lesssim 0.3$ are preferred. At high redshift ($z = 5$), this trend is even stronger, as there has not been enough time to built up large bulges in the merging galaxies. Therefore, mergers with a high B/T are rare. This trend is the same for galaxies of low stellar mass. These systems usually have rather few mergers, which results in low bulge fractions. Massive galaxies, however, typically have large bulge fractions before mergers. The reason is the same as in the major merger sample: high mass systems experience a lot of mergers during their evolution. As a result they tend to form large spherical components leading to a large B/T. Hence, these galaxies are typically ellipticals when they accrete a satellite.

Altogether we have seen that the probability for a certain merger depends on many parameters: the mass of the system, the mass ratio between the merging galaxies, the gas fractions in the galaxies and their morphology. Our analysis shows that some mergers are more common than

others and hence that the parameter space that has to be covered can be reduced. However, it is still impossible to cover the whole parameter space. A simple and elegant path around this can be taken, if we do not take the parameters from a multidimensional grid, but use the semi-analytic merger trees for the initial condition of galaxy merger simulations. In this way, we automatically select mergers that are highly common in the Universe. Thus, the necessary parameter space is naturally covered.

.

Chapter 4
Accretion from the Halo

In the last chapter we have seen that semi-analytic merger trees provide natural initial conditions for merger simulations with high resolution. However, if we compare the galaxy models predicted by the SAM to the model galaxies used in merger simulations, we immediately recognise a main difference: the standard initial conditions in merger simulations neglect the accretion of material both from a hot gaseous halo and from material that is accreted from outside the initial virial radius. Considering the dark matter part, the code used to create the model galaxies presented in section 2.4 only employs a dark matter halo of fixed mass. This means that all material that falls into the halo which is not included in the merger tree (since it is too small to be resolved) is not taken care of. For the baryonic part, the problem is even more serious. The hot gaseous halo component, which is responsible for fuelling the cold gaseous disc from which stars can form, is not considered at all. The galaxy creator simply assumes that before the simulation is started, a cold gaseous has already been formed. If the accretion of gas from the halo is neglected, however, the stellar mass of the galaxy at the end of the simulation will be too low, as the only material from which stars can form is the preexisting cold gas, which will be depleted quickly.

Therefore, in order to be able to use all components that can be predicted with the SAM, we have to extend the code that creates the initial conditions for the merger simulations. We model the accretion of dark matter material that is too small to be resolved as a halo in the merger trees, by placing additional dark matter particles around the halo. The distance to the halo centre is chosen such that they fall into the virial radius of the halo at a specified time. This time can be extracted from the merger tree. The hot gaseous component is modelled as a slowly rotating halo with a spherical density profile. We compute the temperature profile such that the halo is in hydrostatic equilibrium which means that it is supported by pressure. The halo is then able to cool and as the accreting material conserves its angular momentum, a cold gas disc can form. In this chapter we outline, how these two additional components are modelled, and we present several results from merger simulations were the hot halo component has been included.

4.1   Modelling the growth of the dark halo

A basic property of dark matter is that it is 'self-similar'. This means that there is no preferred scale associated with it since dark matter particles only interact through gravitation which is a long-ranged force. Dark matter haloes can have an extend of several Mpc in clusters, but in high resolution simulations they have also been found at scales of several parsecs. Of course, only sufficiently large haloes have a potential well in which gas can cool and form a galaxy, so that there are no galaxies below a certain mass limit. As both merger trees extracted from N-body simulations and trees created with a Monte-Carlo method cannot resolve arbitrarily small haloes, the halo trees are typically cut at a lower mass limit. This means that all haloes that are smaller than this mass limit and falling into a larger halo are not considered as merging haloes, but as so-called 'smooth accretion'. Thus, even if there are no mergers in a given time-step, the parent halo gains mass. In (non-cosmological) simulations of galaxies or mergers this smooth accretion is usually neglected.

The most direct way to model this accretion is to distribute the additional dark matter particles uniformly on shells that surround the parent halo. The radius of the shells can then be chosen such that each shell crosses the virial radius at a given time such that the accretion history of the merger tree is reproduced. In practice however, this method has several disadvantages: First, it is known that dark matter clusters on all scales, which means that shells of uniform density are a poor representation of the dark matter distribution. Second, when a shell contracts, the density in the shell increases until it reaches the centre of the halo, where it has a very high density. This additional potential perturbs the central components of the system and affects the stability of the disc. Third, when particles in uniform shells fall to the centre, they can keep all of their energy. This means that when the shell has contracted the particles have the maximum velocity, which is again transformed into potential energy afterwards. Thus, unless the mass that fell into the halo after the shell is very large, the particles can possibly escape the halo again.

Therefore we choose a different implementation of the smooth accretion. Instead of distributing additional particles in shells, we place these particles into small spherical systems which will be denoted as 'blobs' in the following. In this way, the accreted mass represents the many sub-resolution systems that are expected. Furthermore this representation has the advantage that every dark matter blob that enters the parent halo feels a dynamical friction force. Due to this force, the blobs lose kinetic energy and are drawn to the centre such that the accreted particles stay within the virial radius. Similarly to the shell model, we place all blobs at specific distance to the halo centre such that the accretion rate of the blob matches the smooth accretion rate of the merger tree. The blobs are uniformly distributed around the halo. In order to prevent the blobs from falling to the very centre of the halo and thereby disturbing the disc, we give the blobs an initial velocity in a random direction orthogonal to the radius vector. This of course, reduces the initial distance to the centre compared to freely falling particles. As we require a density profile that leads to a quick

dissolving of the blob once it enters the halo we employ a three dimensional Gaussian density profile. Note, that we do not add gas particles to the blobs.

4.1.1 Creating a spherical particle distribution

In order to model a blob, we have to first choose a density profile and then distribute the particles of each blob according to this profile. After that each particle is assigned a velocity such that the density profile is stable in isolation. In order to describe the complex system one introduces the distribution function f which yields the probability $f(\boldsymbol{x}, \boldsymbol{v})\mathrm{d}^3\boldsymbol{x}\mathrm{d}^3\boldsymbol{v}$ that one finds a mass m within this phase space element. Thus f is normalised such that its integral over all phase space yields the total mass of the system. From the conservation of mass it follows that the distribution function obeys the collisionless Boltzmann equation.

We model each blob with a three dimensional Gaussian density profile

$$\rho(r) = \frac{M_{\mathrm{blob}}}{\left(\sqrt{2\pi}r_{\mathrm{blob}}\right)^3} \exp\left(-\frac{r^2}{2r_{\mathrm{blob}}^2}\right), \tag{4.1}$$

where M_{blob} is the total mass of the blob and r_{blob} is a scalelength. The mass enclosed within a radius r is then given by:

$$M(r) = \sqrt{\frac{2}{\pi}} \frac{M_{\mathrm{blob}}}{r_{\mathrm{blob}}^3} \left[\sqrt{\frac{\pi}{2}} r_{\mathrm{blob}}^3 \mathrm{erf}\left(\frac{r}{\sqrt{2}r_{\mathrm{blob}}}\right) - r r_{\mathrm{blob}}^2 \exp\left(-\frac{r^2}{2r_{\mathrm{blob}}^2}\right) \right]. \tag{4.2}$$

The gravitational potential is found by integration Poisson's equation which yields:

$$\Phi(r) = -\int_r^\infty \frac{GM(r')}{r'^2}\mathrm{d}r' = -\frac{GM_{\mathrm{blob}}}{r} \mathrm{erf}\left(\frac{r}{\sqrt{2}r_{\mathrm{blob}}}\right). \tag{4.3}$$

For $r \to 0$ this potential approaches $\Phi_0 = -\sqrt{(2/\pi)}GM_{\mathrm{blob}}/r_{\mathrm{blob}}$. Using N particles of mass m_i for each blob this density profile can be simply achieved by drawing a random number from a Gaussian distribution with width $r_{\mathrm{blob}}/\sqrt{3}$ for each cartesian coordinate. Deriving the velocity for each particle is more complicated and has to be done using the distribution function.

The Jeans theorem states that any solution to the collisionless Boltzmann equation can be written as a function of integrals of motion. It can be shown, that for a spherical, isotropic model f can be expressed solely as a function of the total specific energy. One can define a relative potential $\Psi = -\Phi$ and a relative energy $\mathcal{E} = -E = \Psi - v^2/2$. Then the distribution function can be written as a function of the relative energy $f(\mathcal{E})$. In order to derive it, we relate the density to the distribution function by integrating over all velocity space

$$\rho(r) = 4\pi \int \mathrm{d}v v^2 f(\Psi - v^2/2) = 4\pi \int_0^\Psi \mathrm{d}\mathcal{E} f(\mathcal{E})\sqrt{2(\Psi - \mathcal{E})}, \tag{4.4}$$

and as Ψ is a monotonic function of r, we can regard ρ as a function of Ψ. After differentiating $\rho(\Psi)$ with respect to Ψ, the relation can be inverted with an Abel transform to get

$$f(\mathcal{E}) = \frac{1}{\sqrt{8}\pi} \left[\int_0^{\mathcal{E}} \frac{\mathrm{d}\Psi}{\sqrt{\mathcal{E} - \Psi}} \frac{\mathrm{d}^2\rho}{\mathrm{d}\Psi^2} + \frac{1}{\sqrt{\mathcal{E}}} \left(\frac{\mathrm{d}\rho}{\mathrm{d}\Psi} \right)_{\Psi=0} \right] , \tag{4.5}$$

which is called the Eddington equation. Thus we have to relate the density to the potential and can then solve this equation.

As this cannot be done analytically, we create a logarithmically spaced array in r with 10^5 bins. We fix the minimum and maximum of the bins at 10^{-3} and 10^2 times the scalelength. On this finely space grid, we define the values for $\rho(r)$, $M(r)$ and $\Psi(r)$ and obtain the derivatives by finite differencing. The distribution function is then obtained by numerically integrating the Eddington equation. We find that it is well approximated by the fitting function

$$f(\mathcal{E}) = \frac{2.2 \times 10^{-3} M_{\odot}}{(\,\mathrm{kpc\,km\,s^{-1}})^3} \sqrt{\frac{M_{\odot}\,\mathrm{kpc}^3}{M_{\mathrm{blob}} r_{\mathrm{blob}}^3}} \, Q \left[\left(\frac{Q}{0.3} \right)^{-3.871} + \left(\frac{Q}{0.3} \right)^{0.166} \right]^{-5.4} , \tag{4.6}$$

where $Q = \mathcal{E}/\Psi_0$ and $\Psi_0 = \sqrt{2/\pi}GM_{\mathrm{blob}}/r_{\mathrm{blob}}$ is the maximum relative potential. We plot this distribution function in Figure 4.1 and compare it to that of the Hernquist profile.

With the distribution function, we can now find the velocity for each particles with a rejection sampling technique introduced by von Neumann. For a particle with a distance to the centre of mass r, we compute the escape velocity as $v_{\mathrm{esc}} = \sqrt{-2\Phi(r)}$. We then select a random number x from a uniform random distribution between 0 and 1 and choose a velocity $v_{\mathrm{guess}} = x v_{\mathrm{esc}}$. The relative energy is then $\mathcal{E} = \Psi(r) - v_{\mathrm{guess}}^2/2$, and we define $f_{\mathrm{guess}} = v_{\mathrm{guess}}^2 f(\mathcal{E})$ and $f_{\mathrm{max}} = v_{\mathrm{esc}}^2 f[\Psi(r)]$. We then draw a random number y from a uniform random distribution between 0 and 1 and check whether $f_{\mathrm{guess}} \leq y f_{\mathrm{max}}$. If this is true, the guessed velocity is accepted, if not, a new velocity is guessed and the process is repeated until a valid velocity is found. The direction of the velocity is randomly chosen from the unit sphere.

We test this model by creating N-body realisations of a blob of mass $M_{\mathrm{blob}} = 10^9 M_{\odot}$. This mass is below the resolution limit of the cosmological simulation used in section 3.4 and is thus accounted for as smooth accretion. We model the blob with $N = 100, 200$ and 1000 particles and a scalelength of $r_{\mathrm{blob}} = 2, 5$ and $10\,\mathrm{kpc}$. We let each realisation evolve in isolation for 5 Gyr and measure the scalelength at every time-step. The results of this analysis are shown in Figure 4.2. All models are stable over the 5 Gyr of evolution, independent of the initial scalelength. For $N = 100$ the scalelength increases by about 50 per cent until the end of the simulation, while for larger particle numbers the scalelength deviates only slightly from the initial value. For all particle numbers, models with a larger initial scalelength are more stable. This shows that we can use the model with several hundreds of particles and scalelengths of several kpc.
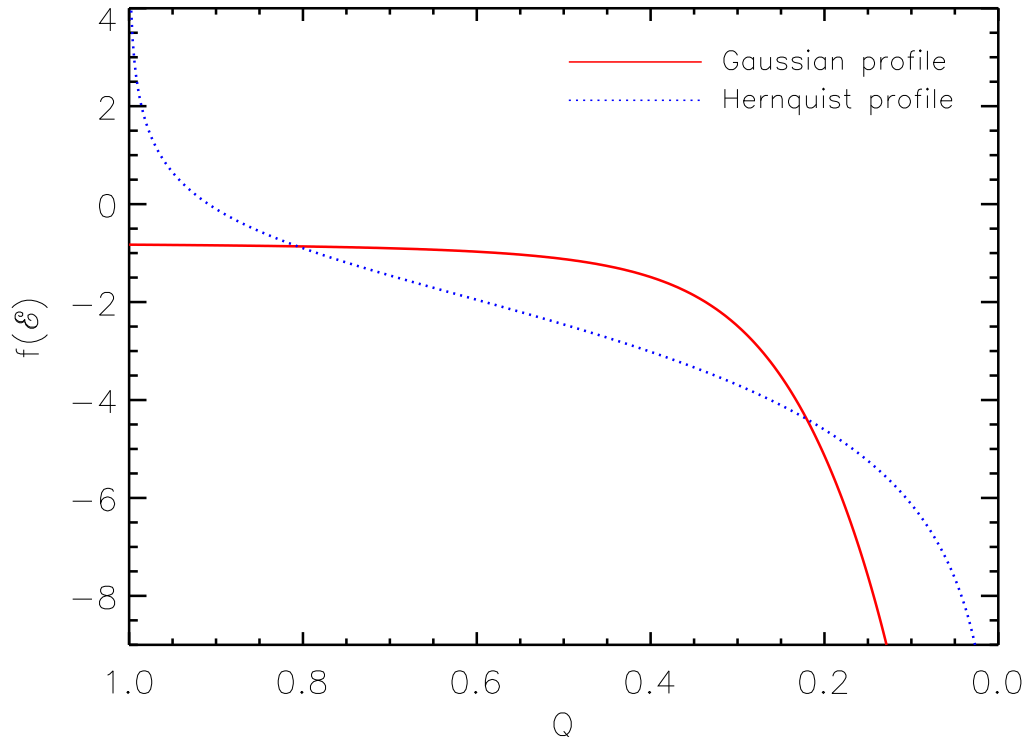
Figure 4.1 Distribution function for a Gaussian and a Hernquist density profile where $Q = \mathcal{E}/\Psi_0$. Units are such that $G = M = r_{\mathrm{blob}} = a = 1$.

4.1.2 Placing the dark matter systems around the halo

With the model presented in the last section we can create blobs of dark matter that are stable in isolation, but due to their shallow potential they dissolve quickly when orbiting a dark matter halo. The next step to model the smooth accretion of a dark matter halo is to place dark matter at the right position, such that the accretion history of the halo is reproduced. Thus, the main difficulty here is, where to position the blobs and with which mass.

As we want to simulate merger trees, we first extract the mass accretion history of the 'main branch' from the merger tree, i.e. the mass of the main halo and its most massive progenitors as a function of cosmic time. Of course, this mass consists of all material that has been accreted by the halo: smooth accretion and mergers. The next step is to choose a starting redshift z_{start} which corresponds to a starting time t_{start}, at which we start the simulation. If we assume that the profile of the parent halo does not change, which is true for our initial conditions, the virial mass of the parent halo increases as the background density decreases towards lower redshift (for a lower ρ_{crit} the radius that contains a certain overdensity becomes larger). We thus subtract the increasing virial radius at every time-step such that we are left with the accreted mass. Furthermore, we subtract the mass that has been accreted through mergers of resolved smaller haloes, as those will
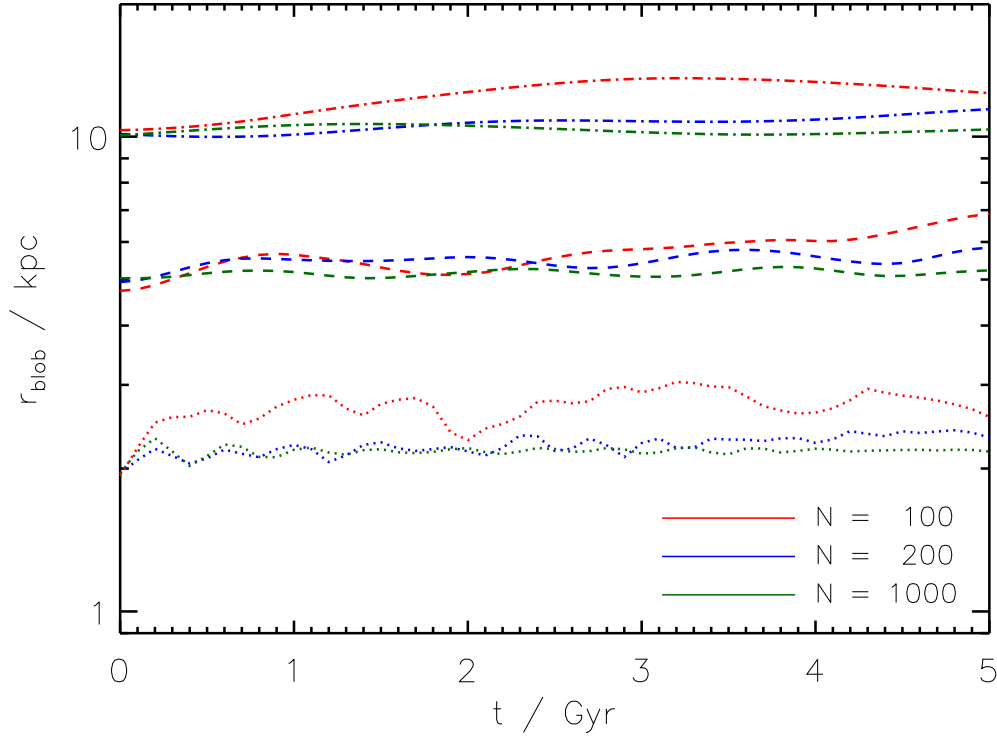
Figure 4.2 Evolution of the scalelength of a Gaussian blob in simulations with 100, 200 and 1000 particles. Initial scalelength are 2, 5 and 10 kpc represented by the dotted, dashed and dash-dotted lines, respectively.

be explicitly simulated as merging haloes. We are thus left with the mass $M_{\mathrm{smooth}}(t)$ that has been added to the parent halo due to smooth accretion.

In the next step we choose the number of blobs N_{b} which is equal to the number of time-steps we will use for the model. We then interpolate $M_{\mathrm{smooth}}(t)$ for every time-step t_i using a Bezier curve which traces the mass accretion history and is equal to the mass found in the merger tree at t_{start} and $t_{N_{\mathrm{b}}}$. We then compute the mass that is accreted within every time-step $M_{\mathrm{blob}}(t_i)$, and use this mass for the blob the corresponds to this time-step. If this mass is smaller than zero (i.e. the parent halo loses mass), we set the mass of the corresponding blob to zero (i.e. the blob is omitted). However, we store this lost mass and set the mass of the blobs that correspond to the following time-steps to zero, until the lost mass is balanced by accreted mass. Thus the total mass that is added through smooth accretion is kept constant. If the mass of a blob is larger than a given threshold (e.g. the minimum halo mass used to create the merger trees or a hundredth of the parent halo's mass) we redefine the number of blobs and restart the procedure. Finally, we set the particle mass for each blob particle equal to the mass of the dark matter halo particles m_{dm} and compute the number of particles of each blob: $N_i = M_{\mathrm{blob}}(t_i)/m_{\mathrm{dm}}$.

Having determined the mass of each blob, we now need to specify, where to place them. For

this we make use of the free-fall time for a point mass at a radius r

$$t_{\text{ff}} = \pi \sqrt{\frac{r^3}{8GM(r)}}, \tag{4.7}$$

where $M(r)$ is the total mass enclosed within r. The time it takes a blob to enter the virial radius of the halo $t_{\text{enter}} = t_i - t_{\text{start}}$ is shorter than the free-fall time and only slightly larger than the free-fall time at radius r minus the free-fall time at the virial radius r_{vir}, as the blob already has a velocity towards the centre when crossing the virial radius. We can thus assume that t_{enter} has a value of $t_{\text{enter}} \gtrsim t_{\text{ff}}(r_i) - t_{\text{ff}}(r_{\text{vir}})$, where r_i is the initial distance of the blob from the halo centre and r_{vir} is the virial radius of the halo at t_i. The initial distance of each blob is then given by

$$r_i \approx \left(\frac{\sqrt{8GM(r)}}{\pi} t_{\text{enter}} + r_{\text{vir}}^{3/2} \right)^{2/3}, \tag{4.8}$$

and we place the centre of each blob randomly on a sphere with radius r_i. In order to prevent the blobs from passing through the centre of the halo, we assign an initial velocity to every blob in a random direction orthogonal to the radius vector. This leads to a larger time it takes a blob to enter the virial radius which partly compensates for smaller estimate of t_{enter}.

We are thus left with three free parameters: the number of blobs N_{b}, the scalelength of the blobs r_{blob}, and the initial velocities of the blobs v_{init}. In order to fix these values we select a merger tree from the simulation box, presented in section 3.4, that has no mergers above a mass ratio $\mu = 0.02$. We can thus assume that all mass accreted by the parent halo is from smooth accretion. The index number of this merger tree is *1811* and the virial mass at $z = 0$ is $10^{12} M_{\odot}$. We start the simulation at $z_{\text{start}} = 1$, where the parent halo has a virial mass of $6.5 \times 10^{11} M_{\odot}$, a virial velocity of $V_{\text{vir}} = 150 \, \text{km s}^{-1}$, a concentration parameter of $c = 4.4$, and a spin parameter of $\lambda = 0.038$. We construct an N-body realisation of this halo with the initial conditions generator as described in section 2.4 with $N_{\text{halo}} = 200\,000$ particles, and add dark matter particles in blobs to this model with the method outlined above. For this we choose the fiducial parameters as $N_{\text{b}} = 400$, $r_{\text{blob}} = 5 \, \text{kpc}$ and $v_{\text{init}} = 30 \, \text{km s}^{-1}$, and vary each parameter around these values, while keeping the other two parameters fixed. For about 400 blobs the number of particles per blob is ≈ 200 which we have shown to be sufficient for stable blobs in isolation. We evolve each system until $z = 0$ with a softening length of $\epsilon = 0.7 \, \text{kpc}$.

For each simulation we measure the virial mass as a function of cosmic time using a spherical overdensity criterion and the fitting function by Bryan & Norman (1998). The results are presented in Figure 4.3, where the virial mass measured in the simulations is compared to that found in the merger tree. For our fiducial parameters, we are able to reproduce the accretion history of the halo very well. In the left panel the number of blobs is varied. We see that neither a lower nor a higher value than the fiducial one results in a difference for the mass that can be accreted. In
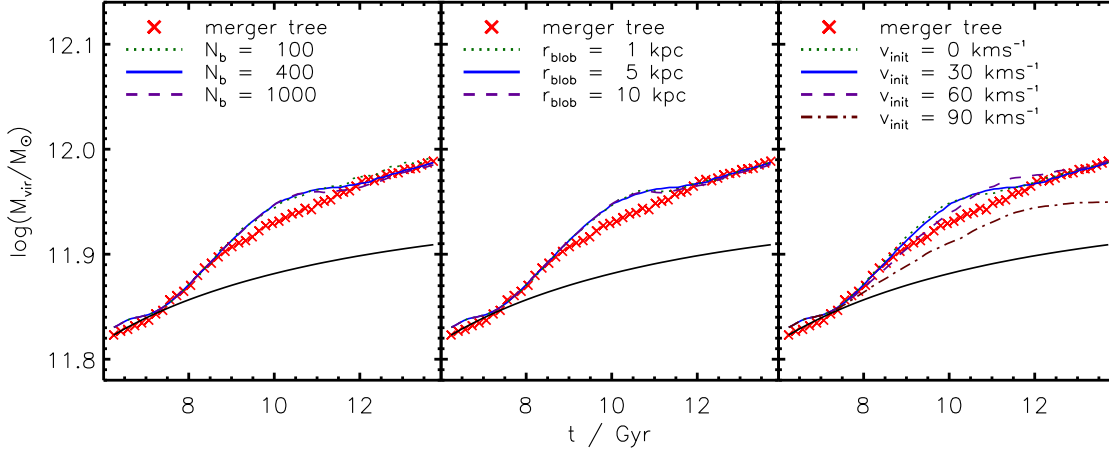
Figure 4.3 Growth of the halo mass due to smooth accretion from dark matter blobs. The virial mass measured in the isolated simulations (lines) is compared to that found in the merger tree (symbols). In the left, middle and right panels different numbers of blobs, blob scalelengths and initial velocities have been used, respectively. Unless otherwise noted, the fiducial values $N_{\mathrm{b}} = 400$, $r_{\mathrm{blob}} = 5\,\mathrm{kpc}$ and $v_{\mathrm{init}} = 30\,\mathrm{km\,s^{-1}}$ have been used. The black line shows the mass evolution, if no smooth accretion is modelled.

the middle panel we vary the scalelength of the Gaussian profile. Also for this parameter we see that the result is independent of its value. In the right panel the initial velocity is varied. Values of $v_{\mathrm{init}} = 0$ and $30\,\mathrm{km\,s^{-1}}$ lead to a very similar mass accretion history. For $v_{\mathrm{init}} = 60\,\mathrm{km\,s^{-1}}$ the blobs enter the virial radius slightly later, as the orbital energy is higher and the blobs need to lose some angular momentum first. For higher values ($v_{\mathrm{init}} \gtrsim 90\,\mathrm{km\,s^{-1}}$) the virial mass of the halo is too low, compared to the merger tree. The reason is that for some blobs the initial velocity is high enough, such that they orbit within the virial radius of the parent halo just for a short time, or even not at all. Instead their pericentric distance has the same dimension as the virial radius. Thus they do not fall towards the centre, but orbit the halo on a large distance where the density is not high enough such that they can lose their angular momentum due to dynamical friction. This means that they initial velocities of the blobs should not be larger than half of the virial velocity of the halo. Altogether we find that our model is able to reproduce the smooth accretion history of a dark matter halo very well and does not depend on the exact values of the model parameters.

We finally need to check whether the Gaussian blobs remain bound when the enter the parent halo, or if they are quickly dissolved such that they can be seen as smooth accretion as intended. For this we compute surface density maps of the system at six redshifts. In Figure 4.4 the maps are plotted on the scale of 1 Mpc for the model with the fiducial parameters. As the virial radius is of the order of 200 kpc (depending on redshift), the total halo is shown. Blue colour indicates regions of low density and red colour represents high density regions. The virial radius is approximately given by the envelope of the green region. In the first panel at $z = 1$, all 400 blobs are clearly visible, as their density is larger than the surrounding background density. As time elapses, the
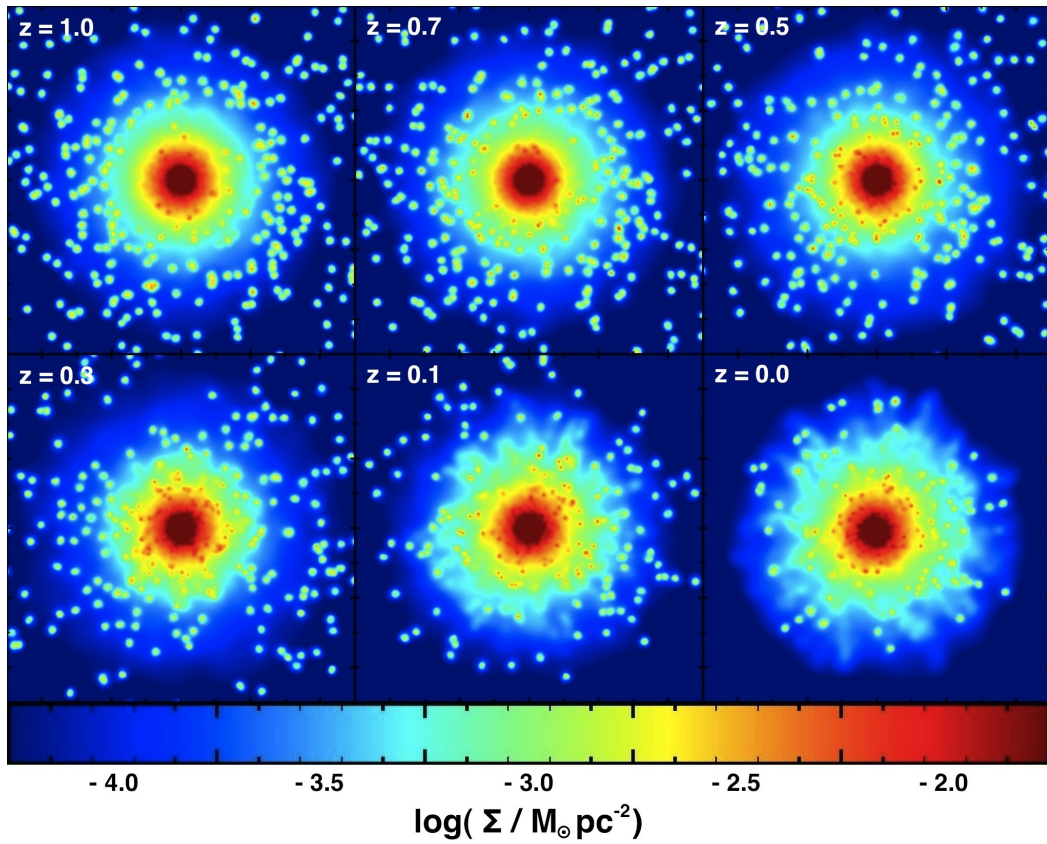
Figure 4.4 Projected dark matter surface density for the smooth accretion model using the fiducial parameters. Blue colour represents regions of low density and red colour depicts high densities. Each panel measures 1 Mpc on a side and the redshift is displayed in the upper left corner of each panel. The virial radius of the halo is given by the envelope of the green region.

blobs fall towards the centre of the halo. When the blobs enter the halo, they are able to stay bound for a short amount of time, corresponding to less than half an orbital period, and are then dissolved. In the last panel at $z = 0$, most of the blobs have been destroyed. Only those blobs that have just entered the halo are still bound as they have not been within the halo long enough to be stripped.

As most of the blobs can remain bound for almost half an orbital period, they are able to reach the pericentre of their orbit before they are dissolved. If the blobs are freely falling, this would be problematic for a central disc of stars, since the constant bombardment of small objects can disturb the disc and possibly thicken it. Therefore we modelled the bobs with an initial velocity, such that the pericentre is large enough and the blobs do not perturb the disc. In Figure 4.5 the surface density maps are plotted on a scale of 50 kpc such that the region within half of the Hernquist scalelength of the halo is shown. This is the typical scale up to which exponential discs with scalelengths of a few kpc can be resolved. As we can see, the density profile remains the same
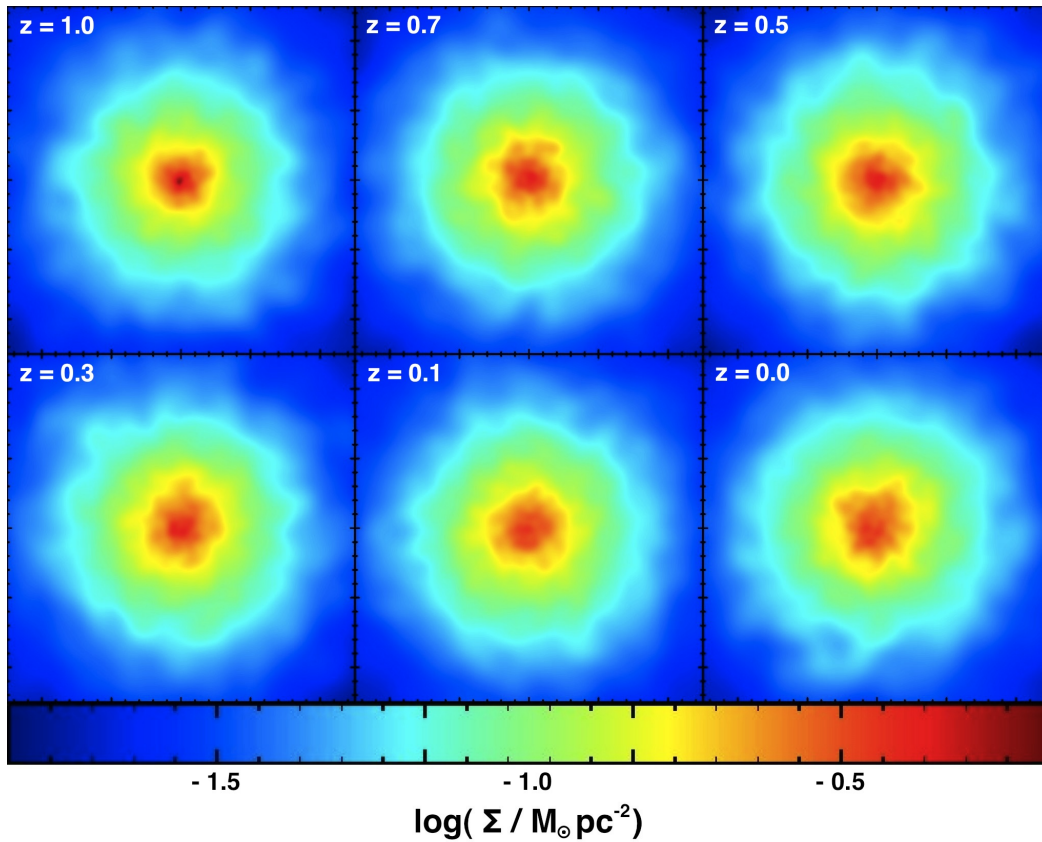
Figure 4.5 Same as Figure 4.4, but for the core of the halo with a panel side length of 50 kpc. The envelope of the green region corresponds to approximately half the Hernquist scaleradius.

throughout the simulation, and no blobs can be identified in this region. The reasons for this are the sufficient pericentric distance due to the initial velocity, such that the blobs rarely reach the central region, and the low density of the blobs, which is lower than the density of the halo in this region, such that their contribution to the total density is negligible. This shows that our method, that models the smooth accretion with small bound objects instead of a uniform distribution of dark matter particles, does not lead to a perturbation of central objects.

4.2   Modelling a hot gaseous halo

The other form of accretion we have to consider in our model is the accretion of gas from the hot gaseous halo. As the hot gas cools it loses its pressure support and falls to the centre. Because it thereby conserves its angular momentum it accretes onto a cold gaseous disc. In the galaxy creator code we presented in section 2.4, this hot gaseous component is not included. Instead, it is assumed that a cold gaseous disc is present at the start of the simulation, and that all stars form from this component. However, this leads to the problem that as soon as the cold gas disc

is depleted or destroyed, there is no more raw material for star formation available and the SFR approaches zero. In merger simulations this problem has been neglected so far, as the time scale of these simulations is usually small (a few Gyr), and the amount of cold gas is sufficient to ensure a considerable SFR throughout the simulation time. Still, merger simulations with a cold disc but without hot component tend to incorporate relatively high gas fractions, in order to be able to reproduce galaxy properties, since the gas disc is not refuelled and all of the material has to be present at the initial time. Especially for simulations with longer time scales, like the simulation of semi-analytic merger trees, the accretion from the hot halo becomes very important.

In the following we extend the galaxy creator with a hot gaseous component. This is done with a spherical density profile where the temperature profile is determined by requiring hydrostatic equilibrium. In order to be able to accrete the material on a disc, we initialise the hot halo with some angular momentum, which depends on the angular momentum of the dark matter halo. We test our model in isolated simulations and constrain it by demanding that the stellar mass and scalelength of a MW-like galaxy as a function of time be reproduced. In section 4.3 the model is then applied in major merger simulations, and we study how the SFR, the starburst efficiency and the morphology of the merger remnant chances with respect to the model that only employs a cold gaseous disc. Furthermore we extend the study of disc thickening during minor mergers that was presented in section 2.5, by including a hot gaseous halo in the initial conditions. As we found that a cold gas disc affects the galaxy properties after the merger, we investigate how cooling from a gaseous halo onto the central disc affects the galaxy mergers.

4.2.1 Extending the galaxy models

To construct the galaxy models used in our simulations we apply and extend the method described in 2.4. Each system is composed of a cold gaseous disc, a stellar disc and a stellar bulge with masses M_{cg}, M_{disc} and M_b embedded in a halo that consists of hot gas and dark matter with masses M_{hg} and M_{dm}. The gaseous and stellar discs are rotationally supported and have radial profiles described by an exponential law. The scalelength of the gaseous disc r_g is related to that of the stellar disc r_d by $r_g = \chi r_d$. The vertical structure of the stellar disc is described by a radially independent sech^2 profile with a scaleheight z_0. The spherical stellar bulge is non-rotating and is constructed by using the Hernquist profile with a scalelength r_b. The dark matter halo also has a Hernquist profile with a scalelength r_s, a concentration parameter $c = r_{vir}/r_s$ and a halo spin λ.

For MW-like galaxies there have been no observations yet, that constrain the profile of the gaseous hot halo. Therefore, we choose the observationally motivated β-profile (Cavaliere & Fusco-Femiano 1976; Jones & Forman 1984; Eke *et al.* 1998) which has been found in galaxy clusters:

$$\rho_{hg}(r) = \rho_0 \left[1 + \left(\frac{r}{r_c} \right)^2 \right]^{-\frac{3}{2}\beta} . \tag{4.9}$$

It has three free parameters: the central density ρ_0, the core radius $r_{\rm c}$ and the outer slope parameter β. The temperature profile can be fixed by assuming an isotropic model and hydrostatic equilibrium inside the galactic potential. The halo temperature at a given radius r is then determined by the cumulative mass distribution $M(r)$ of the dark, stellar and gaseous components beyond r and by the density profile $\rho_{\rm hg}(r)$ of the hot gas:

$$T(r) = \frac{\mu m_p}{k_B} \frac{1}{\rho_{\rm hg}(r)} \int_r^\infty \rho_{\rm hg}(r) \frac{GM(r)}{r^2} dr \;, \tag{4.10}$$

where m_p is the proton mass, G and k_B are the gravitational and Boltzmann constants and μ is the mean molecular weight.

In addition, the hot gaseous halo is rotating around the spin axis of the discs. The angular momentum of the hot gaseous halo is set by requiring that the specific angular momentum of the gaseous halo $j_{\rm hg} = J_{\rm hg}/M_{\rm hg}$ is a multiple of the specific angular momentum of the dark matter halo $j_{\rm dm} = J_{\rm dm}/M_{\rm dm}$ such that $j_{\rm hg} = \alpha j_{\rm dm}$. A value of $\alpha = 1$ matches the commonly used assumption that there is no angular momentum transport between the spherical dark matter halo and the gaseous halo. The angular momentum distribution is assumed to scale with the product of the cylindrical distance from the spin axis R and the circular velocity at this distance: $j(R) \propto R\, v_{\rm circ}(R)$. The vertical velocity of the gas halo particles is set equal to zero.

4.2.2   Parameters of the gaseous halo

Our extension of the initial condition model, the hot gaseous halo, is parameterised with four parameters: the central density ρ_0, the core radius $r_{\rm c}$, the slope parameter β and the spin factor α. For the density profile, we adopt $\beta = 2/3$ (Jones & Forman 1984) and $r_{\rm c} = 0.22 r_{\rm s}$ (Makino *et al.* 1998) and fix ρ_0 such that the baryonic fraction within $r_{\rm vir}$ (stellar and gaseous discs, bulge and gaseous halo) is the universal one. Thus there is a central core with a constant density and the slope at the outer halo is -2. This leaves one free key parameter, the spin factor α which needs to be constrained. In high resolution cosmological simulations one finds that at low redshift ($z \lesssim 2$) α is generally larger than 1, as feedback processes preferentially remove low angular momentum material from the halo (Governato *et al.* 2010).

In order to fix the spin factor for MW-like galaxies we model a typical MW-like galaxy at $z = 1$ and let it evolve to $z = 0$ using different values for α. We then employ two observational evidences (stellar mass and disc size) to determine the correct α. A typical MW-like galaxy with $M_{\rm dm}(z = 0) \sim 10^{12} M_\odot$ has a halo concentration of c=8.43 at z=0 (Macciò *et al.* 2008) which fixes both parameters of the Hernquist profile. Assuming that the halo profile does not change from $z = 1$, we can compute the virial mass and the halo concentration given the higher background density at $z = 1$, resulting in $M_{\rm dm,z=1} = 8.0 \times 10^{11} M_\odot$ and $c_{z=1} = 3.64$. Using the redshift-dependent stellar-to-halo mass relation derived by Moster *et al.* (2010), we assign a stellar mass

Table 4.1 Parameters kept constant for all simulations. Masses are in units of $10^{10} M_\odot$, scale and softening lengths are in units of kpc and pc, respectively

System	$M_{\rm dm}$	$M_{\rm b}$	$r_{\rm d}$	$r_{\rm g}$	$r_{\rm b}$	z_0	c	λ	$N_{\rm dm}$	$N_{\rm bulge}$
Z1	80	0.500	2.50	3.75	0.50	0.6	3.64	0.030	500 000	20 000
G3	110	0.890	2.85	8.55	0.62	0.4	6.00	0.050	240 000	20 000
$MB_{\rm pri}$	100	0.600	3.00	3.0	0.50	0.4	9.65	0.034	4 000 000	500 000
$MB_{\rm sat}$	10	0.063	0.00	0.0	0.30	0.0	11.98	0.034	900 000	100 000

of $M_{*,z=1} = 2.5 \times 10^{10} M_\odot$ (converted to Salpeter IMF) to the system. Distributing 80 per cent of this stellar mass into the exponential disc yields a stellar disc mass of $M_{\rm disc} = 2.0 \times 10^{10} M_\odot$ and a bulge mass of $M_{\rm b} = 5 \times 10^9 M_\odot$. A bulge scalelength of $r_{\rm b} = 0.5$ kpc is assumed. In order to determine the mass of the gaseous disc we use the recipe by Stewart *et al.* (2009) which is based on data by McGaugh (2005) and Erb *et al.* (2006). This recipe predicts that central galaxies with $M_* = 2.5 \times 10^{10} M_\odot$ at $z = 1$ have a gas fraction of $f_{\rm gas} = M_{\rm cg}/(M_{\rm cg} + M_{\rm disc}) = 0.4$ which yields a mass for the gaseous disc of $M_{\rm cg} = 1.33 \times 10^{10} M_\odot$. The scalelength for the stellar disc at $z = 1$ is set to $r_{\rm d} = 2.4$ kpc consistent with observations from GEMS (Barden *et al.* 2005; Somerville *et al.* 2008b) and corresponds to a spin parameter of $\lambda = 0.03$. We assume that the scalelength of the gaseous disc $r_{\rm g}$ is a factor of $\chi = 1.5$ larger. The scaleheight of the stellar disc is set to $z_0 = 0.6$ kpc, typical for MW-like galaxies (Schwarzkopf & Dettmar 2000; Yoachim & Dalcanton 2006). The mass of the hot gaseous halo within $r_{\rm vir}$ is $M_{\rm hg} = 1.2 \times 10^{11} M_\odot$, such that the baryonic fraction within $r_{\rm vir}$ is the universal one. The system is modelled with $N_{\rm dm} = 500,000$ dark matter, $N_{\rm disc} = 100,000$ stellar disc, $N_{\rm cg} = 33,333$ gaseous disc, $N_{\rm bulge} = 20,000$ bulge and $N_{\rm hg} = 375,000$ gaseous halo particles. We set the gravitational softening length to $\epsilon = 100$ pc, 140 pc and 400 pc for stellar, gas and dark matter particles, respectively. We summarise the parameters that are kept constant for all simulations in Table 4.1, and parameters that differ for the various simulation runs are summarised in Table 4.2.

In order to fix the angular momentum of the gaseous halo, we run five simulations with different settings for the spin factor α. These are one simulation with no gaseous halo at all (Z1), and simulations with $\alpha = 1, 2, 4$ and 8 (Z1A1, Z1A2, Z1A4, Z1A8). We evolve these simulations in isolation from $z = 1$ to $z = 0$ which corresponds to 7.6 Gyr. We adopt the standard parameters for the multiphase model in order to match the Kennicutt law as specified in 2.3.1. The star formation time-scale is set to $t_*^0 = 2.1$ Gyr, the cloud evaporation parameter to $A_0 = 1000$ and the SN 'temperature' to $T_{\rm SN} = 10^8$ K. We employ a Salpeter IMF which sets the mass fraction of massive stars $\beta = 0.1$. The simulations include stellar winds for which we adopt a mass-loading factor of $\eta = 2$ motivated by observations (Martin 1999; Rupke *et al.* 2005; Martin 2005), and a wind speed of $v_w \sim 480\,{\rm km\,s}^{-1}$ typical for a MW-sized galaxy at low redshift. We do not include feedback from accreting black holes (AGN feedback) in our simulations.

Table 4.2 Parameters for the different simulation runs. Masses are in units of $10^{10} M_\odot$, and softening lengths are in units of pc.

Run	f_{gas}	M_{disc}	M_{cg}	M_{hg}	α	N_{disc}	N_{cg}	N_{hg}	ϵ_{gas}	θ
Z1	0.40	2.00	1.33	0.0	-	100 000	33 333	0	140	-
Z1A1	0.40	2.00	1.33	12.0	1	100 000	33 333	375 000	140	-
Z1A2	0.40	2.00	1.33	12.0	2	100 000	33 333	375 000	140	-
Z1A4	0.40	2.00	1.33	12.0	4	100 000	33 333	375 000	140	-
Z1A8	0.40	2.00	1.33	12.0	8	100 000	33 333	375 000	140	-
G3	0.23	4.11	1.20	0.0	-	100 000	15 000	0	140	30°
G3f0	0.00	5.31	0.00	0.0	-	130 000	0	0	-	30°
G3f4	0.40	3.20	2.11	0.0	-	80 000	25 000	0	140	30°
G3f8	0.80	1.07	4.24	0.0	-	30 000	50 000	0	140	30°
G3h	0.23	4.11	1.20	11.0	4	100 000	15 000	175 000	140	30°
G3hf0	0.00	5.31	0.00	11.0	4	130 000	0	175 000	140	30°
G3hf4	0.40	3.20	2.11	11.0	4	80 000	25 000	175 000	140	30°
G3hf8	0.80	1.07	4.24	11.0	4	30 000	50 000	175 000	140	30°
MB	0.20	2.40	0.60	0.0	-	1 000 000	125 000	0	70	60°
MBh	0.20	2.40	0.60	16.0	4	1 000 000	125 000	3 700 000	70	60°

We compare the results from these simulations to two observational evidences: stellar mass and disc scalelength. For every time-step of the simulation we measure the virial mass of the dark matter halo and use the stellar-to-halo mass recipe by Moster *et al.* (2010) at that redshift, to compute the mean stellar mass expected for this halo mass and compare it to the stellar mass measured in the simulation. We also compute the radial density profile of the stellar disc and fit an exponential to it in order to measure the scalelength. These values are compared to the mean observed scalelength for disc galaxies of the mean stellar mass at the given redshift (Barden *et al.* 2005; Somerville *et al.* 2008b). For example, the considered halo has a virial mass of $M_{\text{dm}} = 0.9 \times 10^{12} M_\odot$ at $z = 0.4$. The mean stellar mass of galaxies in this halo at this redshift is $M_* = 4 \times 10^{10} M_\odot$ and the mean observed scalelength for galaxies of this mass is $r_{\text{d}} = 2.82$ kpc. The values for stellar mass and scalelength measured in the simulations have to obey these constraints.

We show the results of the simulations in Figure 4.6. For the simulation without a gaseous halo the evolution of the scalelength agrees well with the observed values at $z \gtrsim 0.4$ while after that it deviates and stays too small. The stellar mass evolution, however, completely disagrees with that of a typical galaxy of this halo mass. The reason for this is the lack of cold gas from which the stars form. As the initial cold gaseous disc is depleted quickly, but does not get refuelled from an external reservoir, there is not enough gas available to increase the disc mass by a factor of 2 until $z = 0$. This shows that the hot gaseous halo is very important in order to reproduce the
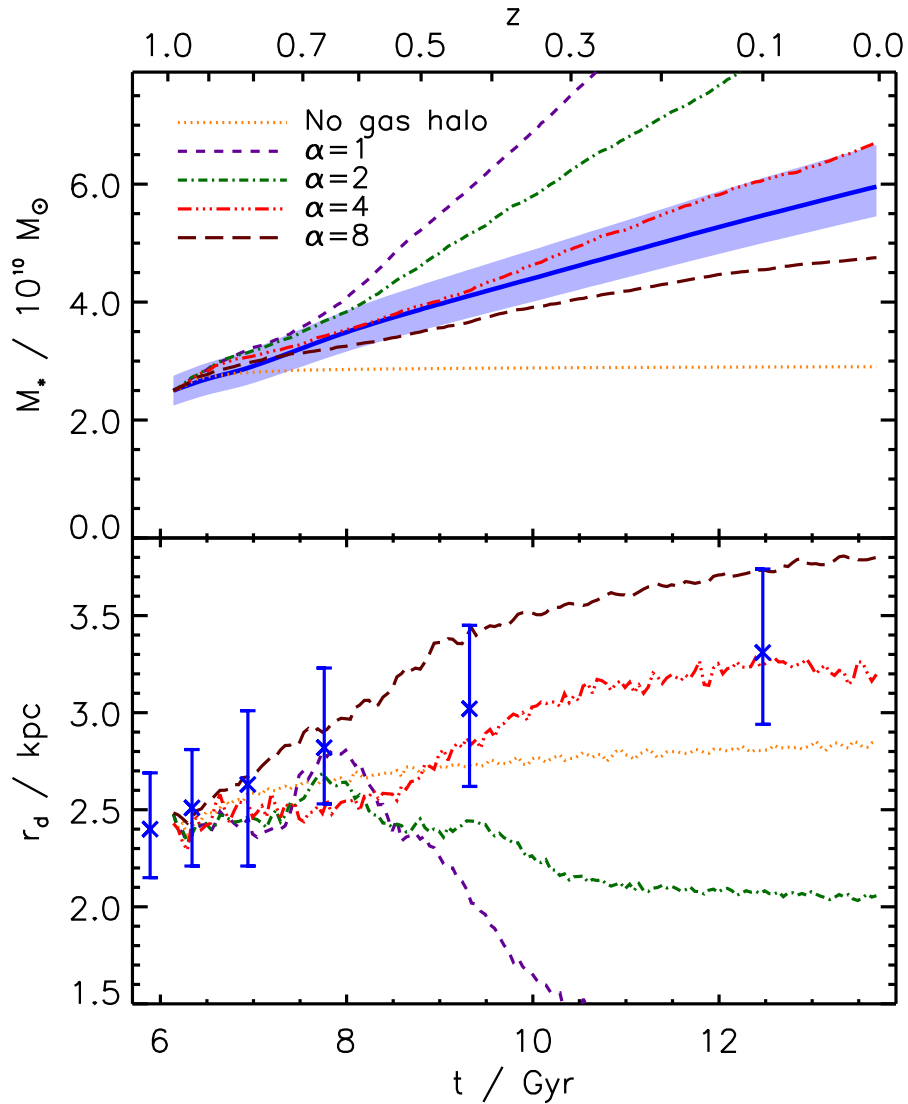
Figure 4.6 *Upper panel:* Stellar mass as function of time for different spin settings. The values measured in the simulations (lines) are compared to the observationally motivated predictions (bold line and shaded area). *Lower panel:* Disc scalelength as function of time for different α. Symbols show the observed values by Barden *et al.* (2005). Only the simulation with $\alpha = 4$ agrees well with both constraints.

star formation history of galaxies, as the gas from the halo cools and accretes onto the disc. This process prevents the depletion of the cold gaseous disc and results in realistic SFRs.

The simulations with a gaseous halo show a much larger SFR which depends on the selected spin factor α. For low values of α (1 and 2), the stellar mass of the galaxy increases too fast and becomes too large at $z = 0$, while the scalelength quickly decreases and reaches values that are much smaller than the observed ones. These effects are due to the low angular momentum of the

halo gas at the start of the simulation. When the gas cools, it is no longer supported by pressure, but only by angular momentum. This means that a lower initial angular momentum results in a lower orbital distance and thus in a lower scalelength. Additionally, since the centrifugal barrier is lower, much more material can reach densities where star formation is active, which yields a much higher SFR and thus a larger stellar mass. For values of $\alpha \lesssim 3$, too much material concentrates at small distances from the galactic centre which results in too massive and too compact discs compared to observations. On the other hand, large values of α (8) yield a stellar disc which is not massive enough and which has a scalelength that is too large. Due to the larger initial angular momentum the cooling gas can retain large orbital distances resulting. This also leads to much fewer dense star forming material and thus to lower stellar masses. For values of $\alpha \gtrsim 6$, we find that gas settles in too large discs and does not form enough stars compared to observations.

The model that agrees best with the observational constraints is that with a spin factor of $\alpha = 4$. For this value we find a stellar mass and a scalelength which are within the observational constrains for MW-like galaxies. As a result we use this value throughout the rest of this work for all systems, which are all in the halo mass range of the MW. We note that different values of α (representing different merger histories, feedback efficiencies, etc.) can span up a range of stellar masses and scalelength which is in agreement with the wide spread of these quantities for MW-like systems.

4.3   Application: merger simulations with a hot gaseous halo

Since the 'merger hypothesis' has been proposed by Toomre & Toomre (1972) there have been many numerical simulations studying the dynamics of galaxy mergers and the properties of merger remnants (Gerhard 1981; Barnes 1988; Hernquist 1989, 1993; Barnes & Hernquist 1996; Mihos & Hernquist 1994; Di Matteo *et al.* 2005; Naab *et al.* 2006; Cox *et al.* 2006b; Jesseit *et al.* 2007). In the last years several groups have produced very large libraries of major merger simulations, considering different orbital parameters of the merger, the effect of the implemented gas physics, star formation algorithms and feedback schemes (Robertson *et al.* 2006b; Cox *et al.* 2006a; Burkert *et al.* 2008; Bois *et al.* 2010). One clear outcome of those simulations has been the need of including gas physics in order to reproduce basic properties of observed galaxies. Gas plays an important role in shaping the properties of galaxy mergers and their remnants, because unlike stars and dark matter, gas can cool radiatively and therefore lose kinetic energy efficiently. Furthermore, gas can lose angular momentum owing to gravitational torques during merger events. After the merger an extended cold gas disc can form in the remnant from high angular momentum gas in the outer regions of the progenitors. By the accumulation of cold gas in the centre of a merger remnant the central potential changes and increases the velocity dispersion of the stars. Additionally, the gas is eventually transformed into stars, leading to a new stellar component which is rotating and kinematically cold. It has been shown that in numerical simulations even major mergers of disc

galaxies can produce remnants with large discs if the cold gas fractions in the progenitors are sufficiently high (Springel & Hernquist 2005; Robertson *et al.* 2006a; Governato *et al.* 2007, 2009). This has also been seen in observations of high-redshift discs that are probably reforming after mergers (van Dokkum *et al.* 2004; Kassin *et al.* 2007; Genzel *et al.* 2008; Puech *et al.* 2008).

Detailed studies of elliptical galaxies have shown that they can be classified into two groups with respect to their structural properties (Davies *et al.* 1983; Bender 1988; Bender & Nieto 1990; Kormendy & Bender 1996). Faint spheroids exhibit isotropic rotation that is along the photometric major axis (with little minor-axis rotation) and have discy deviations of their isophotal contours from perfect ellipses. They have power-law surface brightness profiles (Lauer *et al.* 1995; Faber *et al.* 1997) and show little or no radio and X-ray emission (Bender *et al.* 1989). Large, luminous spheroids, on the other hand, have box-shaped isophotes, show flat cores and strong radio emissions and X-ray luminosities. They rotate slowly, are supposed to be supported by velocity anisotropy and have a large amount of minor-axis rotation.

The distinct physical properties of elliptical galaxies lead to the viewpoint that the two classes have different formation histories and form through different mechanisms. Many studies find that collisionless merger simulations lead to slowly rotating, pressure supported, anisotropic remnants (Negroponte & White 1983; Barnes 1988; Hernquist 1992). Along this line of reasoning, Bendo & Barnes (2000) and Naab & Burkert (2003) argue that fast rotating low luminosity ellipticals are produced by dissipationless minor mergers. However, remnants of dissipationless disc galaxies are in conflict with observations, as they are not able to reproduce the de Vaucouleurs profiles in the inner parts. The reason for this is that low phase-space density spirals cannot produce the high central phase-space densities of ellipticals because according to Liouville's theorem, phase-space density is conserved during a collisionless process (Carlberg 1986). In dissipationless simulations, this problem could only be overcome by include large bulge components in the progenitor systems.

Another way to circumvent this problem is to take into account the gas component in the progenitors, which is able to increase the phase-space density through radiation (Lake 1989). It has been argued by Kormendy & Bender (1996) and Faber *et al.* (1997) that the observed stellar discs embedded in rotating ellipticals (Rix & White 1990; Ferrarese *et al.* 1994; Scorza *et al.* 1998; Rix *et al.* 1999; Lauer *et al.* 2005) are signatures of dissipation during their formation while non-rotating systems would form from pure dissipationless mergers. This idea has been explored by several studies (Bekki & Shioya 1997; Bekki 1998; Naab *et al.* 2006). Focusing on equal mass mergers, Cox *et al.* (2006b) confirm that slowly rotating anisotropic spheroids can be formed in dissipationless simulations. Furthermore they show that if a massive gaseous disc is included in the simulation, a consistent fraction of merger orbits leads to systems with significant rotation. Those remnants are able to reproduce the observed distribution of projected ellipticities, rotation parameter and isophotal shapes. One open issue is that these results relay on very high (possibly too high) gas content in the discs of the merger progenitors and that only a fraction of

the considered orbits lead to fast rotators. Possibly the abundance of disc galaxies with such gas fractions is not high enough in order to explain the large number of fast rotating elliptical galaxies observed in the local Universe.

Similarly, the importance of the dissipational component has been shown in minor mergers and is known to play an important role in stabilising galactic discs. The effect of dissipational gas physics on the vertical heating and thickening of disc galaxies during minor mergers was addressed in section 2.5. We found that when the presence of gas in the disc is taken into account the thickening is reduced with respect to collisionless simulations and we argued that the presence of gas can reduce disc heating via two mechanisms: absorption of kinetic impact energy by the gas and/or formation of a new thin stellar disc that can cause heated stars to re-contract towards the disc plane.

On the other hand most hydrodynamical simulations performed so far, have limited their attention only to cold gas inside the stellar disc. Current models of galaxy formation (Kauffmann *et al.* 1993; Bower *et al.* 2006; De Lucia & Blaizot 2007; Monaco *et al.* 2007; Somerville *et al.* 2008a) as well as full cosmological hydrodynamical simulations (e.g. Stinson *et al.* 2010) both predict a large amount of hot gas in hydrostatical equilibrium within the gravitational potential of the dark matter halo (e.g. Hansen *et al.* 2010). From the smooth accretion of gas from these haloes the discs of spiral galaxies are then able to form (Abadi *et al.* 2003; Sommer-Larsen *et al.* 2003). As the gas mainly cools via thermal bremsstrahlung it radiates mostly in the soft X-ray band.

Since this halo X-ray luminosity depends highly on the mass of the system, observational studies are naturally biased towards very massive haloes. Hence, hot gas in massive ellipticals has been observed in galaxy clusters and in isolated systems (see Mathews & Brighenti 2003, and references therein). In galactic haloes, however, the gas temperature can be lower than 10^6K and thus difficult to observe by current X-ray telescopes, as the radiation is only detectable in very soft bands. Still, studies performed in the last years have identified X-ray emissions from diffuse hot gas in various energy bands (Benson *et al.* 2000; Wang *et al.* 2003; Strickland *et al.* 2004; Tüllmann *et al.* 2006; Rasmussen *et al.* 2009). In the MW, X-ray absorption lines produced by local hot gas have been detected in the spectra of several AGN. Sembach *et al.* (2003) and Tripp *et al.* (2003) have argued that these emissions come from the interface between warm clouds and the ambient hot medium. Given the existence of hot gaseous haloes, it is important to include these in simulations of isolated galaxies and mergers.

In the last years there have been several studies that have taken the gaseous halo into account. Mastropietro *et al.* (2005) and Mastropietro *et al.* (2009) employ a hot halo component to study the hydrodynamical and gravitational interaction between the Large Magellanic Cloud and the MW. Sinha & Holley-Bockelmann (2009) run mergers simulations of galaxies consisting of dark matter and hot halo gas in order to study the change of temperature and X-ray luminosity induced by shocks during the mergers. Those studies, however, use adiabatic simulations, neglecting cooling and star formation. Focusing on isolated systems, Kaufmann *et al.* (2006) and Kaufmann *et al.*

(2009) simulate systems consisting of a dark and a hot halo component to study the evolution and cooling behaviour of the hot halo and the formation of discs via cooling flows. Similarly, Viola *et al.* (2008) run simulations of a gas halo embedded in a dark matter halo to study the cooling process and assess how well simple models can represent it. So far, no study has employed a rotating, cooling gaseous halo in merger simulations.

The goal of our study is to test the impact of such a large gas reservoir on the properties of merger remnants, both in case of major and minor mergers. For the first time we include a gradual gas cooling from the halo (as expected in a cosmological context) in our galaxy models. We then present a detailed analysis of the effects of this new gas component. For major merger we focus our attention on three main quantities: the SFR during mergers, triggering of stellar bursts and the morphology and kinematics of merger remnants. The hot gaseous component is expected to refuel the cold gas disc after a merger which can subsequently form stars thus impacting the morphology of the remnant. For minor mergers we revisit the issue of disc stability, formation of a thick disc and the regrowth of a thin disc after mergers. Here, the continuous accretion of gas is expected to have a stabilising effect on the stability of the disc.

Merger Simulation Parameters

To study equal mass mergers of disc galaxy we adopt the model galaxy G3 proposed by Cox *et al.* (2008) which is tuned to match SDSS observations of local galaxies. The stellar mass of this galaxy was chosen to be $M_* = 5 \times 10^{10} M_\odot$. The bulge-to-disc ratio of $B/D = 0.22$ is taken from de Jong (1996) resulting in a stellar disc mass of $M_{\mathrm{disc}} = 4.11 \times 10^{10} M_\odot$ and a bulge mass of $M_{\mathrm{b}} = 8.9 \times 10^9 M_\odot$. The gas fraction in the disc of 0.23 has been determined from the gas-to-stellar mass scaling relation from Bell *et al.* (2003) and yields a mass for the cold gaseous disc of $M_{\mathrm{cg}} = 1.2 \times 10^{10} M_\odot$. The sizes of the stellar disc and bulge were chosen to agree with the stellar mass-size relation of Shen *et al.* (2003) resulting in $r_{\mathrm{d}} = 2.85$ kpc and $r_{\mathrm{b}} = 0.62$ kpc. The scalelength of the gaseous disc was assumed to be a factor of $\chi = 3$ larger than that of the stellar disc, such that $r_{\mathrm{g}} = 8.55$. The scaleheight of the stellar disc was set to $z_0 = 0.4$ kpc. The mass and concentration of the dark matter halo were selected such that the rotation curves lie on the baryonic Tully-Fisher relation (Bell & de Jong 2001; Bell *et al.* 2003) which yields a virial mass of $M_{\mathrm{dm}} = 1.1 \times 10^{12} M_\odot$ and a concentration parameter of $c = 6$. In order to explore the effects of different gas fractions in the disc on starbursts and remnant morphologies we construct additional galaxy models with a modified disc gas fractions of 0, 40 and 80 per cent (G3f0, G3f4 and G3f8). In some simulations we extend this model to also include a hot gaseous halo (G3hf0, G3h, G3hf4, G3hf8) with a mass of $M_{\mathrm{hg}} = 1.1 \times 10^{11} M_\odot$ within r_{vir} and a gas halo spin factor of $\alpha = 4$. We set the gravitational softening length to $\epsilon = 100$ pc, 140 pc and 400 pc for stellar, gas and dark matter particles, respectively.

We follow Cox *et al.* (2008) and choose a nearly unbound elliptical orbit with an eccentricity

of $\epsilon = 0.95$, a pericentric distance of $r_{\mathrm{min}} = 13.6\,\mathrm{kpc}$ and an initial separation of $d_{\mathrm{start}} = 250\,\mathrm{kpc}$. The resulting interactions are fast and nearly radial, consistent with orbits found in N-body simulations (Benson 2005; Khochfar & Burkert 2006). We employ a prograde orbit; the spin axes of the first galaxy and the orbit are aligned while the second galaxy is tilted by $\theta = 30°$ with respect to the orbit such that the interaction is not entirely coplanar. We evolve all simulations for 5 Gyr.

In a second set of simulations we extend the study on disc stability in section 2.5 and include a hot gaseous component. We use the primary disc galaxy system MB which has a virial mass of $M_{\mathrm{dm}} = 10^{12} M_\odot$, a concentration parameter of $c = 9.65$ and a spin parameter of $\lambda = 0.034$. The stellar disc mass is $M_{\mathrm{disc}} = 2.4 \times 10^{10} M_\odot$ and the bulge mass is $M_{\mathrm{b}} = 6 \times 10^9 M_\odot$. The gas fraction in the disc is 20 per cent, resulting in a mass for the cold gaseous disc of $M_{\mathrm{cg}} = 6 \times 10^9 M_\odot$. The scalelengths of the stellar and the gaseous disc were set to $r_{\mathrm{d}} = 3\,\mathrm{kpc}$, the bulge radius to $r_{\mathrm{b}} = 0.5\,\mathrm{kpc}$ and the scaleheight of the stellar disc to $z_0 = 0.4\,\mathrm{kpc}$. We extend this model and also include a gaseous halo with $M_{\mathrm{hg}} = 1.6 \times 10^{11} M_\odot$ within r_{vir} and a gas halo spin factor of $\alpha = 4$. The primary system is modelled with $N_{\mathrm{dm}} = 4{,}000{,}000$ dark matter, $N_{\mathrm{disc}} = 1{,}000{,}000$ stellar disc, $N_{\mathrm{cg}} = 125{,}000$ gaseous disc, $N_{\mathrm{bulge}} = 500{,}000$ bulge and $N_{\mathrm{hg}} = 3{,}700{,}000$ gaseous halo particles. The satellite system consists of only dark matter with $M_{\mathrm{dm}} = 10^{11} M_\odot$ and $c = 11.98$, and a stellar bulge with $M_{\mathrm{b}} = 6.3 \times 10^8 M_\odot$ and $r_{\mathrm{b}} = 0.3\,\mathrm{kpc}$. It is modelled with $N_{\mathrm{dm}} = 900{,}000$ dark matter and $N_{\mathrm{bulge}} = 500{,}000$ bulge particles. We set the gravitational softening length to $\epsilon = 50\,\mathrm{pc}$, $70\,\mathrm{pc}$ and $100\,\mathrm{pc}$ for stellar, gas and dark matter particles, respectively. The merger orbit has been chosen to be consistent with cosmological simulations and has a eccentricity of $\epsilon = 0.89$, a pericentric distance of $r_{\mathrm{min}} = 18\,\mathrm{kpc}$ and an initial separation of $d_{\mathrm{start}} = 120\,\mathrm{kpc}$. We use a prograde orbit with an angle of $\theta = 60°$ between the spin axes of the disc and the orbit and evolve the simulations for 6 Gyr. The parameters that are kept constant for all simulations are summarised in Table 4.1, while parameters that differ for the various simulation runs are given in Table 4.2.

4.3.1 Star formation in major mergers

We have simulated the fiducial major merger using four different modes: one without stellar winds and without hot gaseous halo (G3G3), one with stellar winds and no gaseous halo (G3G3w), one without winds but with a gaseous halo (G3G3h) and finally one with winds and a gaseous halo (G3G3wh). These simulations are used to study the effects of winds and the hot gaseous halo on starburst and the morphology of the merger remnant. The surface density in the orbital plane is shown in Figures 4.7 (G3G3) and 4.8 (G3G3wh) for the stellar component (upper panels) and the gaseous component (lower panels).

The discs become tidally distorted when reaching pericentre ($t \sim 0.8\,\mathrm{Gyr}$) leading to long tidal tails that drive out loosely bound material while the central regions form bar-like structures.
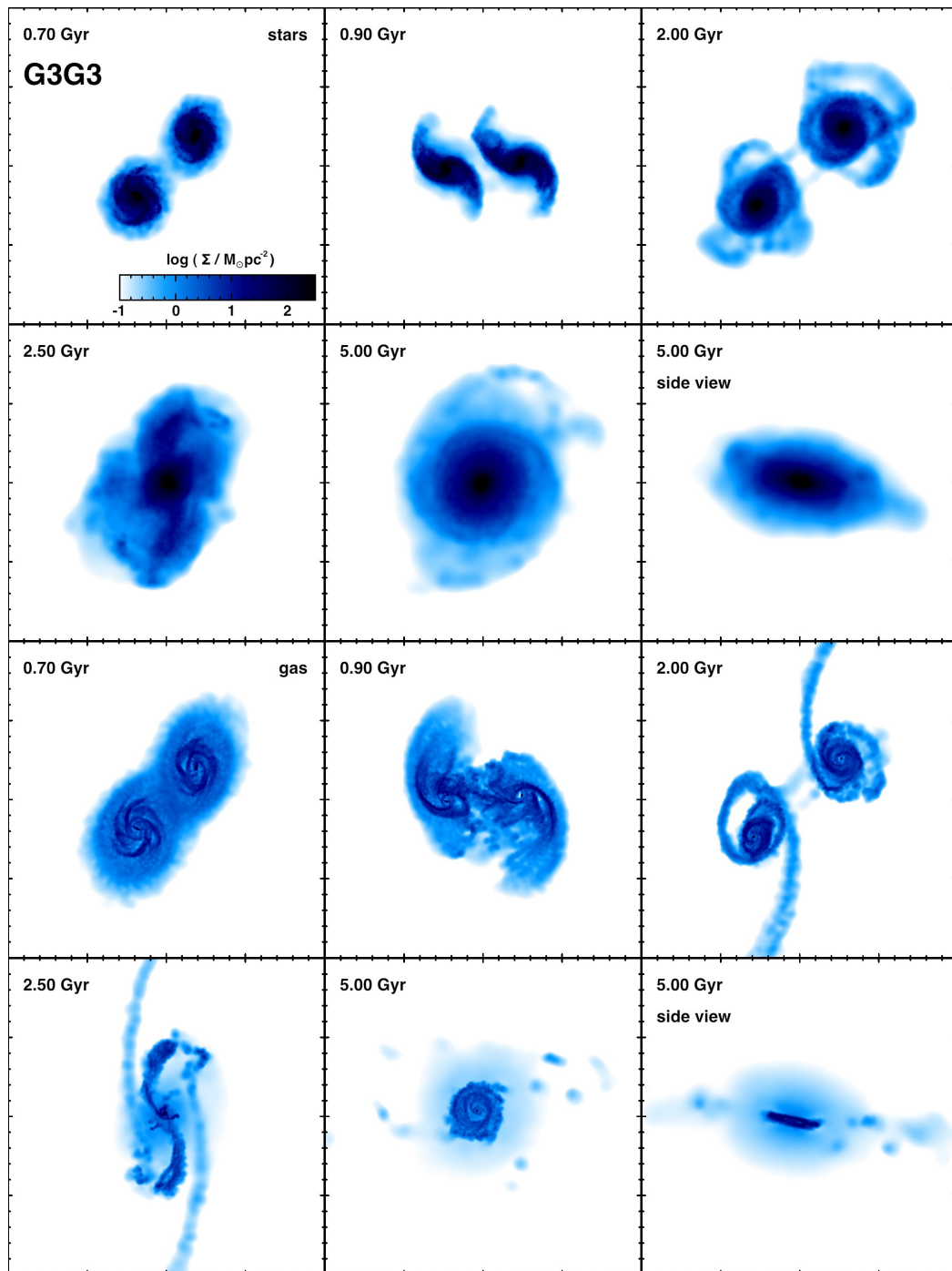
Figure 4.7 Projected surface density for the stellar component (upper two rows) and the gaseous component (lower two rows) during the merger without hot gaseous halo and without stellar winds as viewed in the orbital plane. Each panel measures 200 kpc on a side and the time in Gyr is displayed in the upper left corner of each panel. The right-hand panels in the second and bottom rows show a side view of the final merger remnant.
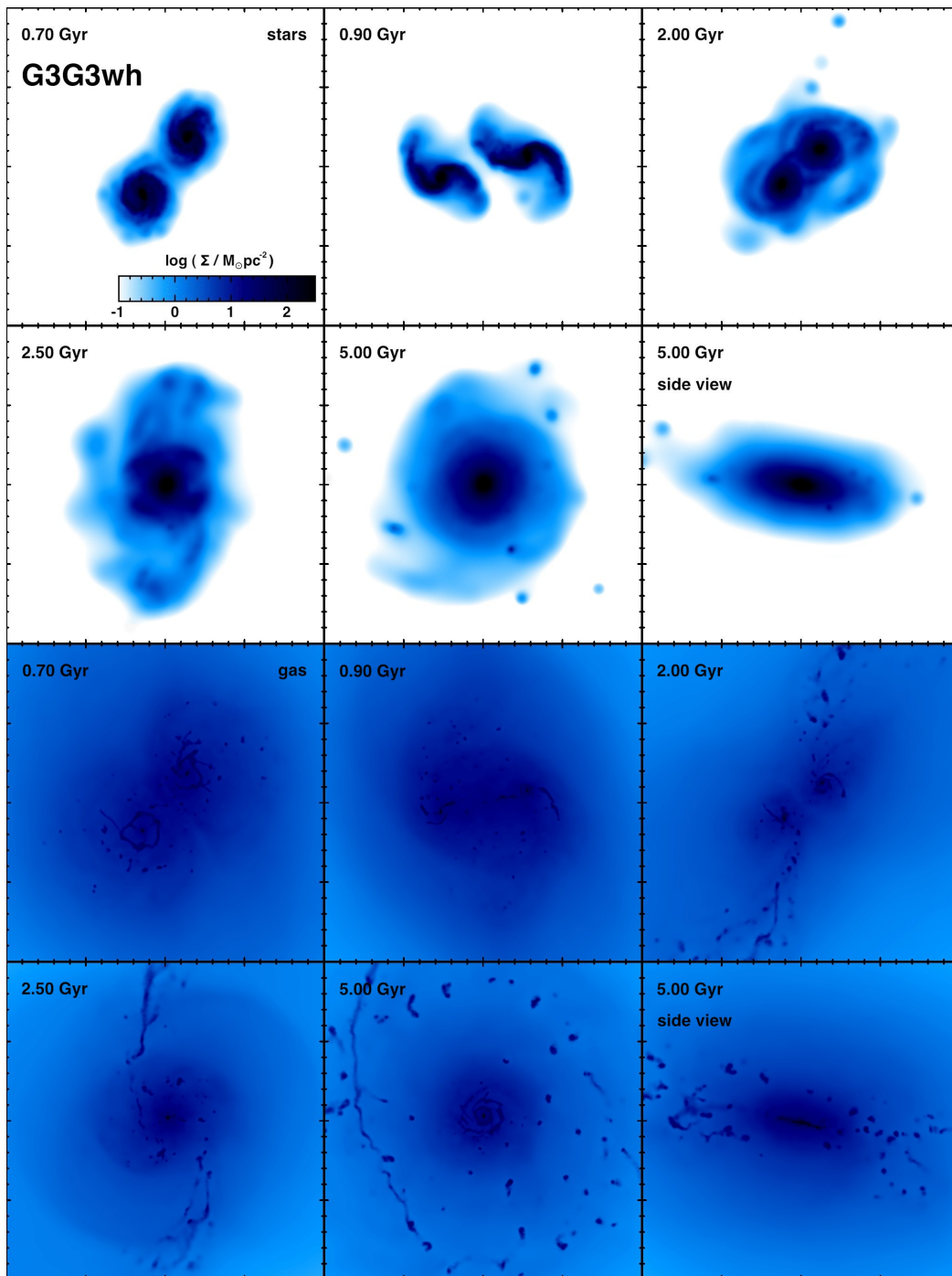
Figure 4.8 Similar to Figure 4.7, but for the simulation with stellar winds and a hot gaseous halo.

Due to dynamical friction, orbital energy decreases while the spin of the haloes increases which re-
sults in an almost radial orbit after the first encounter. During the second encounter ($t \sim 2.3$ Gyr)
both discs are destroyed and the remnant is a spheroidal-looking object. Due to shocks, kinetic

energy of the gas is transformed to thermal energy and then radiated away resulting in an offset between the stellar and the gaseous components. This drags the gas into the dense central regions where the cooling time is very short leading to a starburst. In the G3G3 run, heated low-density gas expands from the central region and forms a (low mass) hot gaseous halo after the merger. Gas from this halo cools again and accretes onto the orbital plane where it forms a cold gaseous disc, subsequently forming a nuclear stellar disc. The G3G3wh run is similar, however, due to the additional potential, the galaxies merge earlier ($\sim$ 150 Myr). Furthermore, after the merger there is still a large reservoir of hot gas left in the halo which has received most of the orbital angular momentum. This massive hot halo can reform a much more prominent cold gaseous disc after the merger which is thinner than in the G3G3 run. In both simulations we find several tidal condensations which formed from loosely bound tidal material and consist of gas and new stars.

In the following, we study the effects of the stellar winds and the presence of the hot gaseous halo on the SFRs and the efficiency of the starburst. For this we compare the SFRs and the new stellar mass that forms during the simulations between the four fiducial mergers and for isolated constituent galaxies. This shows how the quantities associated with the merger, are affected by winds, the gaseous halo and the combination of both.

The star formation history for all of our four fiducial mergers is shown in the first row of Figure 4.9. The simulation without stellar winds and no gaseous halo (G3G3) agrees very well with the results of Cox *et al.* (2008): The SFR of the merger (solid line) is clearly enhanced compared to the isolated runs (dotted line). The maximum SFR during the merger ($\sim 30 M_\odot$ yr^{-1}) is 30 times larger than the summed SFR of the isolated discs ($\sim 1 M_\odot$ yr^{-1}), as shown in the second row of Figure 4.9. The starburst starts shortly before the final coalescence, and after the merger the SFR quickly drops ($\sim$ 500 Myr) to the value of two isolated discs. We find that in both cases the SFR after 3 Gyr ($< 1 M_\odot$ yr^{-1}) is very low compared to the SFR at the beginning of the simulation ($\sim 6 M_\odot$ yr^{-1}). This is due to the limited amount of cold gas which is not refuelled during the simulation. We show the amount of cold star forming gas (i.e. cold gas which also fulfils the density criterion $\rho > \rho_{th}$) in the third row of Figure 4.9. The amount of dense star forming gas strongly increases just before the burst, due to the torques. This star forming gas reservoir is used up in the burst after which there are no more torques which would lead to high concentrations of gas.

The SFR in the simulation with stellar winds included (G3G3w) drops much quicker for the isolated galaxies, as cold gas is expelled from the disc through winds. After $\sim$ 3 Gyr the SFR has dropped by a factor of 100. During the merger we also find a starburst, with an enhanced SFR ($\sim 6 M_\odot$ yr^{-1}) that is $\sim$ 30 times larger than the summed SFR of the isolated discs ($\sim 0.2 M_\odot$ yr^{-1}). With respect to the simulation with no winds, the absolute value of the SFR during the starburst is five times lower. Another effect is that the duration of the starburst is significantly increased with respect to the windless case. The SFR in the merger is always larger than in the isolated case and only equals that of the isolated discs only at the end of the simulation. The amount of dense star
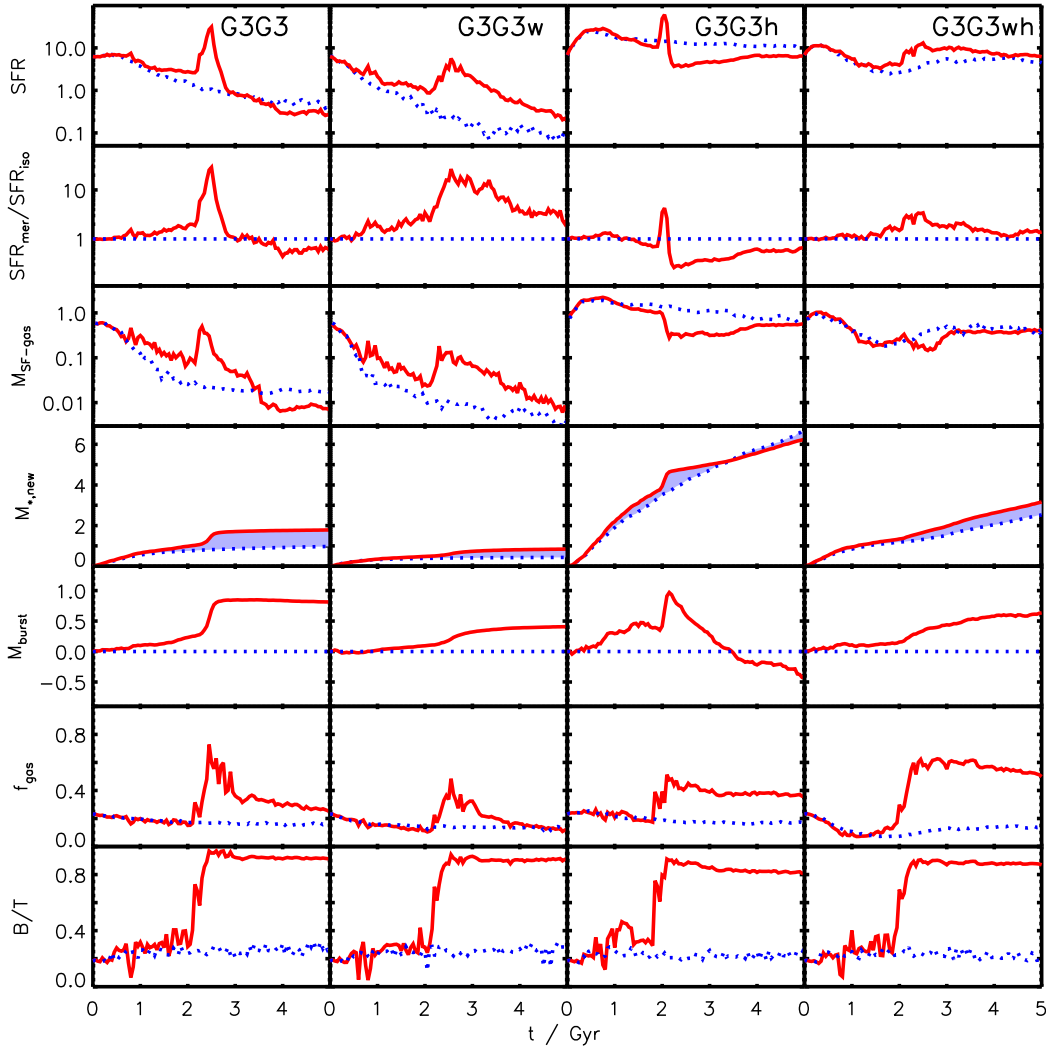
Figure 4.9 The rows from top to bottom show the SFR, SFR normalised by the SFR of both isolated galaxies, the mass of dense star-forming gas available, the new stellar mass formed in the simulation, the burst mass, the gas fraction in the disc and the bulge-to-total ratio for the fiducial simulations G3G3, G3G3w, G3G3h and G3G3wh, from left- to right-hand side. The results for the mergers are given by the solid lines and for the combined isolated galaxies by the dotted lines. All SFRs are given in $M_\odot$ yr^{-1} and all masses in $10^{10} M_\odot$.

forming gas is lower than in the no wind case during the burst. After the burst, however, there is as much star forming gas available as in the G3G3 run, leading to a similar SFR. The reason for this longer duration of the starburst is the stellar wind. During the starburst it prevents parts of the cold gas to reach the dense star forming centre. This material is then located in a halo around the galaxy and can subsequently cool and accrete onto the disc, leading to a higher SFR.

In the run without winds, but with a hot gaseous halo (G3G3h) the SFR for the isolated galaxies

stays relatively constant during the simulation ($\sim 6M_\odot$ yr^{-1} per galaxy), as the cold gas in the disc is constantly refuelled through cooling form the halo. The starburst has an enhanced SFR of ($\sim 60M_\odot$ yr^{-1}) which is a factor of 5 times larger than the summed SFR of the isolated discs. However, after the burst the SFR drops to a value that is lower with respect to the isolated case ($\sim 5M_\odot$ yr^{-1}). The reason for this is the lower amount of star forming gas available after the burst. This means that the cold gas at the centre of the galaxy which is compressed and quickly used up during the burst, is not replenished, indicating that there is a process that hinders the accreting gas from becoming dense and forming stars.

Finally, the SFR for the isolated galaxies in the simulation including winds and a gaseous halo (G3G3wh) is also relatively constant ($\sim 2M_\odot$ yr^{-1} per galaxy), but lower than in the G3G3h case due to the stellar winds which remove dense gas from the centre. Although in the merger case there is clearly an enhanced SFR, the peak is not as prominent and the burst is spread over a much larger time interval than in the other cases. With respect to the isolated case, the maximum SFR ($\sim 13M_\odot$ yr^{-1}) is enhanced by only a factor of 3. After the burst, the SFR decreases again and reaches a value that is similar to that of the two isolated systems. The reason for this is that the amount of dense star forming gas is the same in both runs.

In summary we can point out two major effects: (1) In simulations with stellar winds included, the starburst is spread over a much larger time interval than in the windless case. The reason for that is the removal of cold gas from the dense star forming region in the centre. This material is moved to a halo around the galaxy and can then cool and accrete back to the centre which results in an enhanced SFR. (2) In simulations that include a hot gaseous halo the enhancement of the SFR in a merger with respect to isolated galaxies is much smaller than in systems that do not include a gaseous halo. The reason for that is the continuous accretion of cold gas from the halo. In simulations without this accretion, most of the gas is already used up by the time of the merger, and the rest is then quickly converted into stars during the burst resulting in a high SFR. Isolated galaxies, however, have a very low SFR at the same time which results in a large difference between merging and isolated galaxies. If the gaseous halo is taken into account, also isolated galaxies have a considerable SFR, such that the difference between the enhanced SFR during mergers and isolated systems is not large any more.

4.3.2 Starburst efficiency

In order to quantify the merger-driven star formation it is common to focus on quantities that use the gas consumption rather than details of the time-dependent star formation history, since the latter depends on the adopted feedback model. To this end, various authors make use of the 'burst efficiency' e which is defined as the fraction of cold gas consumed during the merger minus the fraction of cold gas consumed by constituent galaxies evolved in isolation (Cox *et al.* 2008; Somerville *et al.* 2008a). The definition is then useful to predict the additional mass due to the
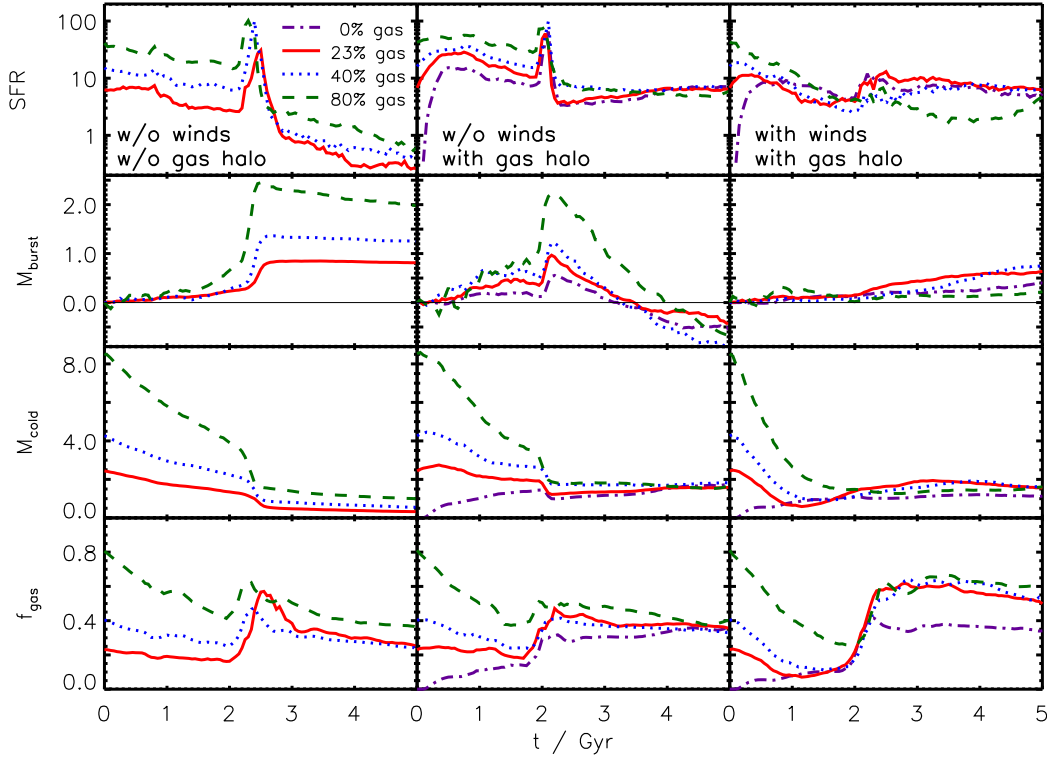
Figure 4.10 The rows from top to bottom show the SFR, the burst mass, the cold gas mass and the gas fraction in the disc for the simulations G3G3, G3G3h and G3G3wh from left- to right-hand side. The different lines represent initial cold gas fractions in the disc. All SFRs are given in $M_\odot \, \mathrm{yr}^{-1}$ and all masses in $10^{10} M_\odot$.

starburst as a function of initial cold gas mass. An equivalent definition is $e = M_{\mathrm{burst}}/M_{\mathrm{cold}}$, where the 'burst mass' $M_{burst} = M_{*,\mathrm{new}}(\mathrm{merger}) - M_{*,\mathrm{new}}(\mathrm{isolation})$ is the stellar mass that formed due to the merger and M_{cold} is the mass of cold gas in the galaxy before the merger. The two main quantities to determine the burst efficiency are thus burst mass and the cold gas mass. It is important at which time these quantities are defined: the cold gas mass has to be defined just before the final coalescence where the gas will lose angular momentum. The burst mass has to be defined just after the merger, i.e. when the SFR of the merging system is at the same level of the isolated galaxies again, otherwise it depends on the SFR after the merger.

Dependence on winds and gaseous halo

In the fourth row of Figure 4.9 we show the new stellar mass formed during the simulation for the isolated (dotted line) and the merger case (solid line). The difference between the isolated and the merger lines is shaded. In the fifth row, the burst mass is plotted while in the sixth row, we show the cold gas fraction in the disc $f_{\mathrm{gas}} = M_{\mathrm{cold}}/(M_{\mathrm{cold}} + M_{*,\mathrm{disc}})$.

The new stellar mass formed in the simulation G3G3 is enhanced during the starburst, such that the burst mass is $M_{\mathrm{burst}} = 0.84 \times 10^{10} M_\odot$. With an cold gas mass just before the burst of $M_{\mathrm{cold}} = 1.25 \times 10^{10} M_\odot$ (for both galaxies) this results in a starburst efficiency of $e = 0.68$. Due to the stellar winds, the starburst in the G3G3w case is less efficient: it has a burst mass of $M_{\mathrm{burst}} = 0.4 \times 10^{10} M_\odot$ and a cold gas mass before the burst of $M_{\mathrm{cold}} = 0.9 \times 10^{10} M_\odot$ which results in an efficiency of $e = 0.45$. This shows that any parameterisation of the starburst efficiency depends on the stellar wind model and its parameters.

In the simulation with a gaseous halo and no winds the mass of the merging system also increases during the burst with respect to the isolated systems. It has a burst mass of $M_{\mathrm{burst}} = 0.97 \times 10^{10} M_\odot$ and a cold gas mass before the burst of $M_{\mathrm{cold}} = 1.92 \times 10^{10} M_\odot$ resulting in an efficiency of $e = 0.51$. The presence of the hot gaseous halo thus reduces the efficiency. In addition to that, as the SFR of the merger remnant is lower than that of the isolated systems after the burst, the summed stellar mass of the isolated galaxies increases faster, such that both simulations have the same stellar mass at $t \sim 3.5$ Gyr. At the end of the simulations, the summed stellar mass in the isolated galaxies is larger than that of the merger remnant. The SFR after the starburst is lower than that of the isolated systems, since the amount of dense star-forming gas available is a factor of ~ 4 lower. The initial cold gaseous disc is consumed during the starburst, so that the the SFR after the burst depends only on the amount of gas that can be accreted to the dense centre from the hot halo. This means that the accretion is more effective in the isolated case than after the merger.

In order to explain what prevents the gas from cooling and becoming dense enough to form stars we compare the specific angular momentum and the temperature of the hot gaseous halo between the merger remnant and the isolated system at $t \sim 2.5$ Gyr. The specific angular momentum of the gaseous halo in the merger remnant is 25 per cent higher than that of the isolated system, leading to larger centrifugal barrier. As we have shown in section 4.2.2, a larger angular momentum decreases the accretion rate and the amount of gas that can reach high enough densities to form stars. While in the isolated case the specific angular momentum stays constant throughout the simulation, in the merger run the angular momentum of the remnant is dominated by the angular momentum of the merger orbit. For our prograde, almost coplanar orbit this results in a larger specific angular momentum after the merger is complete, leading to fewer cold gas available at the centre and thus to a lower SFR.

There is also a second effect that leads to a lower SFR after the merger. When the two gaseous haloes collide, shocks occur and heat the gas, transferring orbital energy to thermal energy. At $t \sim 2.5$ Gyr, just after the starburst, the temperature of the halo gas is ~ 70 per cent higher than in the isolated run. This leads to a cooling time which is ~ 35 per cent higher, so that the hot gas in the halo needs more time to cool and subsequently fall to the disc. This further reduces the accretion rate and thus the amount of cold gas that is able to form stars.

This shows that if the hot gaseous halo is considered in merger simulations, it is possible

(depending on orbit, gaseous halo mass, etc.) that isolated systems have a higher SFR than merging systems, leading to higher masses of non-merging systems. This is a serious challenge for the simple picture that is widely used in SAMs, in which a merger leads to an additional formation of stellar mass. In specific cases, a merger can lead to a lower SFR after the starburst, such that if the constituent galaxies had not merged, their stellar mass would be higher.

In the simulation with a gaseous halo and stellar winds the mass of the merging system is increased during the burst with respect to the isolated systems. The burst mass is $M_{\text{burst}} = 0.64 \times 10^{10} M_\odot$ and with a cold gas mass before the burst of $M_{\text{cold}} = 1.45 \times 10^{10} M_\odot$ the efficiency is $e = 0.44$. This value is slightly smaller than that for the case with winds but no gaseous halo, so that the presence of the halo reduces the efficiency also in the case with winds. After the burst the SFR of the merger remnant is still higher than that of the isolated systems and reaches a similar value at the end of the simulation, such that the stellar mass of the merger remnant is larger than the summed mass of the isolated galaxies. In the isolated runs the winds subsequently remove small parts of the gas from the dense centre, so that the overall SFR is lower than in the case without winds. This material is redistributed into the hot gaseous halo and accretes back to the disc at the same rate as the other hot gas. In the merger run, a lot of material is removed from the centre during the burst (since the wind rate is proportional to the SFR) in a short time interval, such that suddenly there is a lot of extra material in the hot gaseous halo. This more massive halo is then able to accrete cold gas at a higher rate, leading to more cold dense gas and thus to a higher SFR than in the isolated case. This shows, that if stellar winds are included, merger remnants can form more stellar mass than isolated galaxies.

Another effect is that the stellar mass formed during the simulations with a gaseous halo is much larger than in the runs without it. The final mass of the new stars in the G3G3h (G3G3wh) run is a factor of 3.5 (3.7) times larger than the mass in the G3G3 (G3G3w) run, which shows that the gaseous halo is very important to model galaxies with realistic masses. In both of the runs with the gaseous halo, all of the initial cold gas in the disc has been consumed by the end of the simulation, while in the other two runs parts of the initial cold gas are still left. This left-over gas does not reach densities that are high enough to form stars. If the gaseous halo is taken into account, however, the constant accretion refuels the gas disc and ensures that the gas reaches densities high enough to form stars.

Dependence on gas fraction

Up to now we have just studied mergers with one fixed initial gas fraction in the disc (23 per cent). In the following, we study how the starburst efficiency depends on the gas fraction. In very gas rich systems, the amount of stellar mass to form a bar which can remove angular momentum from the gas is low. The angular momentum loss due to a gaseous bar is not efficient, as a stellar bar is needed to drag the gas. Therefore a decrease of the starburst efficiency with increasing gas fraction

Table 4.3 Burst efficiency for different gas fractions.

Run	$f_{g,init}$ [a]	$f_{g,burst}$ [b]	M_{gas} [c]	M_{burst} [d]	e [e]
G3G3	0.23	0.16	1.253	0.849	0.678
G3G3f4	0.40	0.25	2.119	1.365	0.644
G3G3f8	0.80	0.41	3.809	2.448	0.643
G3G3hf0	0.00	0.14	1.371	0.553	0.403
G3G3h	0.23	0.18	1.920	0.968	0.504
G3G3hf4	0.40	0.24	2.640	1.218	0.461
G3G3hf8	0.80	0.38	3.580	2.220	0.620
G3G3whf0	0.00	0.11	1.048	0.400	0.382
G3G3wh	0.23	0.11	1.446	0.636	0.440
G3G3whf4	0.40	0.11	1.287	0.672	0.522
G3G3whf8	0.80	0.26	1.405	0.224	0.159

[a] gas fraction in the initial disc
[b] gas fraction in the disc just before the starburst
[c] cold gas mass just before the starburst in $10^{10} M_\odot$
[d] burst mass just after the starburst in $10^{10} M_\odot$
[e] starburst efficiency

is expected and was also previously found for the case with no stellar winds and no gaseous halo (Cox *et al.* 2008; Hopkins *et al.* 2009a). For this study we use our fiducial models, keep the total mass of the disc fixed but modify the gas content in the disc to 0, 23, 40 and 80 per cent. All other parameters remain unchanged form the fiducial values.

The results are plotted in Figure 4.10 for the simulations G3G3, G3G3h and G3G3wh from left- to right-hand side. From top to bottom the SFR, the burst mass, the cold gas mass and the gas fraction in the disc are shown as a function of time. In order to compute the burst efficiency, we use the cold gas mass and gas fraction just before the starburst, and the burst mass just after it. The resulting quantities are given in Table 4.3.

For the case without winds and gaseous halo (G3G3) we find that the starburst efficiency is slightly decreasing with increasing gas fraction. This means that if more gas is available in the disc, it is harder to convert all of the gas into stars during the burst. If a hot gaseous halo is included, however, the starburst becomes more efficient with increasing gas fraction. In order to explain this it is important to state that the efficiency mainly depends on the amount of cold gas available for the starburst. This material is of course not the total mass of cold gas in the simulation, but only the cold gas that is close enough to the centre where the burst happens. Thus the efficiency is a strong function of the spatial (and density) distribution of the cold gas.

In the G3G3 series, the fraction of the cold gas at the centre ($< 5\,kpc$) is very similar in all runs which means that the amount of gas available for the starburst scales with the total gas mass.

In the G3G3h series, however, we find that the fraction of the cold gas at the centre is higher for the runs with a large gas fraction. For these runs, most of the dense initial gas disc is still present when the burst occurs and can participate in it, while for runs with a lower gas fraction, large parts of the initial gas disc have already been consumed such that a large fraction of the cold gas is material that has been accreted from the halo. This accreted material is distributed in a much more extended area and cannot contribute in the starburst, as it is far from the centre. The result is that systems with a high initial gas fraction have a higher fraction of material that can participate in the burst than systems with a low initial gas fraction, such that they are more efficient. The efficiency of runs with gaseous haloes, where parts of the cold gas were accreted from the halo and are not centrally concentrated, are always lower than for the corresponding runs without gaseous haloes, where all the cold gas resides in the centrally concentrated initial disc.

In the simulations with stellar winds there are three runs with the same gas fraction just before the merger (11 per cent), but with a different burst efficiency which increases with increasing initial cold gas mass. The explanation is the similar than in the case with no winds: runs with a larger initial cold gas mass, retain a larger amount of the initial dense disc, while in runs with a lower initial gas mass, there is a larger fraction of gas that has accreted from the halo and is not as centrally concentrated. Thus the mass of the gas that can participate in the burst is larger in runs with a higher initial gas fraction, resulting in a larger burst efficiency.

The run with 80 per cent initial gas fraction, has a lower efficiency than the other G3G3wh runs, as the burst mass is very low. The main question is why the run with the high initial gas fraction has a decreased efficiency with respect to lower initial gas fractions, while for the simulations without winds the runs with a higher initial gas fraction have a larger efficiency. To answer this, we measure the mass of the stellar disc just before the burst: In the G3G3h series the disc mass is very similar for all runs, as most of the initial gas disc has been transformed into the stellar disc. In the G3G3wh series, however, the stellar mass of the disc is very low for high initial gas fractions, since the stellar winds remove a lot of gas from the disc and thus lower the SFR. The stellar disc mass of G3G3whf8 is just the half of the stellar disc mass of G3G3wh just before the burst. As a consequence the amount of stellar mass to form a bar which can remove angular momentum from the gas is lower in the G3G3whf8 run, resulting in less material that can be dragged into the centre during the burst. Therefore the burst efficiency is reduced.

Overall, we find that the starburst efficiency, depends heavily on the presence of the hot gaseous halo and the stellar winds (and on their parameterisation). When both are neglected, the burst efficiency is a week function of gas fraction and decreases with increasing f_{gas}. Both the gaseous halo and the winds reduce the burst efficiency. When the gaseous halo is considered, the efficiency decreases with decreasing gas fraction, as the initial dense disc is replaced by accreted gas from the halo which is spatially much more extended. When furthermore winds are considered, the efficiency for systems with a high initial gas fraction is decreased, since the winds prevent the formation of a massive stellar disc before the merger, which is needed to form a bar
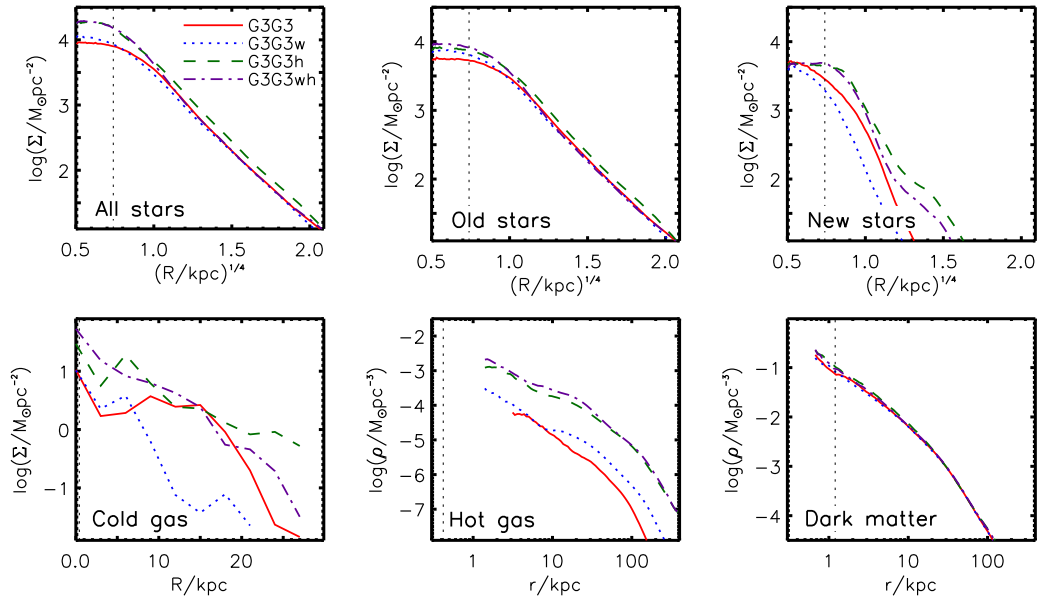
Figure 4.11 *Upper panels*: Surface density profiles averaged over 100 projections for all, old and new stars from left- to right-hand side. *Lower left panel*: Surface density profiles of the cold gas as seen face-on. *Lower middle panel*: 3d density profiles of the hot gaseous haloes. *Lower right panel*: 3d density profiles of the dark matter halo. The different lines denote the different simulations: G3G3 (no winds, no gaseous halo), G3G3w (with winds, no gaseous halo), G3G3h (no winds, with gaseous halo) and G3G3wh (with winds, with gaseous halo). The dotted vertical lines denote three times the softening length and hence indicates the scale resolution limit.

that can drag the gas to the centre of the burst.

4.3.3 Morphology of the major merger remnant

Having investigated how the SFR changes during the merger, we now focus on the properties of the merger remnant at the end of the simulation. To this end, we decompose the stellar particles into a spherical and a disc component. For every particle, we compute the angular momentum along the spin axis and divide this by the angular momentum the particle would have on a circular orbit at the same radius. The spherical component is then distributed around a value of 0, while the disc component is centred at 1, such that the two components can be separated easily (Abadi *et al.* 2003). In the lower panels of Figure 4.9, we plot the resulting bulge-to-total ratio $B/T = M_{\text{bulge}}/M_*$ for the four fiducial runs. In all simulations the disc component just after the starburst is almost destroyed. In the runs without the gaseous halo, the B/T after the burst is ~ 0.9 and stays at this value until the end of the simulation. If a gaseous halo is included, the B/T after the burst is also ~ 0.9, but then decreases to ~ 0.8 for G3G3h and ~ 0.85 for G3G3wh. The reason for this is that due to the accretion of gas from the halo, a much larger cold gaseous disc can form after the burst which leads to a much larger stellar disc. Because of the stellar winds in

G3G3wh, cold gas is subsequently removed from the disc, leading to a lower mass of the stellar disc at the end of the simulations and thus to a larger B/T compared to G3G3h. Still, all four remnant systems are very much bulge dominated.

In order to study how the stellar mass is distributed within the merger remnants, we compute the azimuthally averaged surface density profiles for old, new and all stars, where old stars are the stellar particles which have been present before the burst (i.e. particles created for the initial conditions and particles formed through star formation) and new stars are those stellar particles that have formed through star formation during and after the burst. The upper panels of Figure 4.11 show the results for the four fiducial runs. The profiles for all stars at scales beyond $\sim 1\,\mathrm{kpc}$ are very similar for all remnants following the observed $r^{1/4}$ profile. The slope is identical for all runs and only the normalisation of G3G3h is higher than that of the other runs, as the stellar mass before the burst was already much larger. This can also been concluded from the profiles of the old stars: as the mass of the old stars component is very similar for all runs, except for G3G3h, their final profiles have the same normalisation. The contribution from new stars at these scales is very small for all runs.

At small scales ($R \lesssim 1\,\mathrm{kpc}$) the stellar surface density of the systems with a gaseous halo is higher compared to the other two simulations. Not only is the surface density of the new stars higher which can be simply explained by the more massive stellar discs in the centre, but also the surface density of the old stars higher. The reason for this is the central concentration of new stars that steepens the potential well and draws the old stars into the centre. We note that, up to the resolution limit of ~ 3 times the softening length (e.g. Klypin *et al.* 2001), the surface density profiles of the runs with a gaseous halo follow the observed $r^{1/4}$ profile and show neither a cusp nor a core.

In the lower left panel of Figure 4.11 we show the face-on density profiles of the cold gas component. In the G3G3 run, the profile of the gas disc is very flat up to $15\,\mathrm{kpc}$ but has a very dense central concentration ($R < 2\,\mathrm{kpc}$). When stellar winds are enabled much of the cold gas is ejected from the disc, leading to a very low surface density, except for a dense centre. For the runs with a gaseous halo, a lot of gas is accreted from the halo which settles in an exponential disc. The scalelength of this disc is lowered if winds are included.

The lower middle and right panels show the 3d density profiles for the hot gas and dark matter, respectively. The density of the hot gas for runs with an initial gaseous halo are almost identical. Only at scales of $5 - 50\,\mathrm{kpc}$, the density in the G3G3wh run is a little higher, as gas that is heated and ejected from the disc through the winds is added to the hot gas reservoir and accumulated at these scales. For the runs without an initial gaseous halo, we see that a hot halo forms due to the merger. In the G3G3 run this hot halo form from gas that is shock-heated during the merger and has expanded into the halo. In the G3G3w run, the density of this halo is enhanced by the wind material. The dark matter profile is the same for all runs: an NFW-like profile modified by the baryonic contraction, with a slightly higher central density for systems with a gaseous halo.

Kinematic properties

Having determined the mass distribution of the merger remnants, we now study their kinematic properties, i.e. how much the remnants are supported by rotation. The elliptical shape of a rotating galaxy, can be understood solely as a result of flattening induced by their rotation. The elliptical structure of a non-rotating galaxy, however, must be supported by something other than rotation, most likely by velocity anisotropy. This trend can be visualised by plotting the rotation velocity v_{maj} divided by the central velocity dispersion σ against the ellipticity ϵ. In this anisotropy diagram v_{maj}/σ is a measure for the rotational support and ϵ indicates the deviation from a circle. It has been shown by Binney (1978) that oblate isotropic rotators obey the relation

$$(v/\sigma) = \sqrt{\epsilon/(1-\epsilon)} \ .$$

If viewed face on ($\epsilon = 0$) no rotation can be observed, while edge-on ($\epsilon \gg 0$) the observed rotation velocity is highest.

In order to compute these three quantities, we follow Cox *et al.* (2006b) and refer to this for details. Here, we just give a brief outline the procedure. First, the stellar particles are projected to a plane as if observed from a random viewing angle. Then we determine the isodensity contour that encloses half of the stellar mass and fit an ellipse to it. The ellipticity is computed as $\epsilon = 1 - b/a$, where a is semi-major and b the semi-minor axis of the ellipse. A slit is then placed along the major axis with a length of $3a$ and a width of $a/4$. This slit is divided into 26 bins, lengthwise and the line-of-sight velocity distribution is computed for each bin. Then the mean velocity and the velocity dispersion are extracted from each bin. Finally, v_{maj} is defined as the average absolute value of the maximum and minimum mean velocity along the slit and σ is the average dispersion of the bins within $a/2$.

Figure 4.12 shows the resulting anisotropy diagram for our fiducial merger remnants. The left panel compares the four runs and shows v_{maj}/σ vs. ϵ for 1000 random projections for each remnant. The merger simulation with no winds and no gaseous halo leads to a remnant which is only slowly rotating, with a maximum rotation velocity of $\sim 50\,\mathrm{km\,s^{-1}}$ and a maximum v_{maj}/σ of ~ 0.25. This means that the G3G3 remnant is mostly supported by velocity dispersion and not by rotation. The main contribution to the rotation comes from the stellar disc at the centre of the remnant. This explains why the rotational support increases with increasing ellipticity, as when viewed edge-on both ϵ and the observed rotation velocity of the disc are maximal. When viewed face-on, one cannot observe any rotation of the disc. For the simulation with winds, the stellar disc is much smaller, leading to an even smaller disc contribution to the rotation. Lower values for v_{maj}/σ and a anisotropy diagram which is similar to that of a remnant in a dissipationless simulation are the results.

When a gaseous halo is included, v_{maj}/σ increases strongly with increasing ϵ, which can be explained by the more massive stellar disc that forms after the merger. When viewed edge-on,
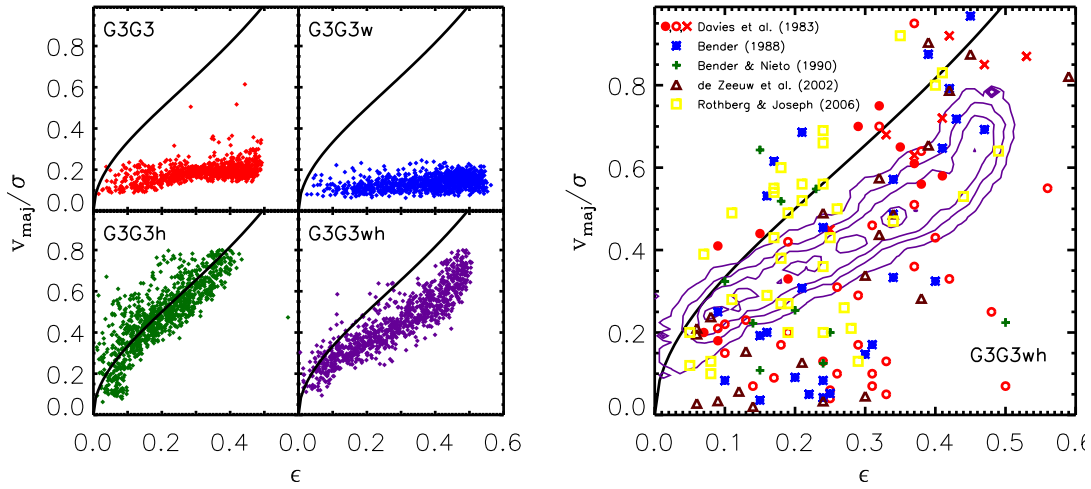
Figure 4.12 Anisotropy diagram: v_{max}/σ vs. ellipticity, where v_{max} is the maximum rotation velocity measured in a slit along the major axis and σ is the velocity dispersion averaged within half of the half-mass radius. The ellipticity is measured at the half mass isophote. The solid line is that expected for an oblate isotropic rotator (Binney 1978). *Left panel:* Comparison between the four fiducial simulations, where every point corresponds to one projection. *Right panel:* Comparison between the simulation with winds and a gaseous halo and data from observed elliptical galaxies. The contours indicate the 10, 50, 70 and 90 per cent probability of finding a merger remnant in the enclosed area.

the stellar disc dominates in the slit in which the velocity is measured and thus leads to a higher mean rotation velocity. The different projections trace the line of the oblate isotropic rotator. This means that the elliptical shape of the remnant at the half-mass isophote ($R \sim 5$ kpc) is mostly due to rotation. If stellar winds are included in the simulation, the mass of the stellar disc is lower, leading to a smaller contribution to the velocity profiles compared to the run with no winds. This also results in lower values of v_{maj}/σ, however, the remnant is still mostly supported by rotation. This shows that by taking the hot gaseous component into account, rotationally supported systems can be created even for moderate initial cold gas fractions, and for orbits which lead to systems that are supported by velocity dispersion when the gaseous halo is not included.

The right panel of Figure 4.12 compares the remnant of the G3G3wh run to data from several observational samples (Davies *et al.* 1983; Bender 1988; Bender & Nieto 1990; de Zeeuw *et al.* 2002; Rothberg & Joseph 2006). The contours give the 10, 50, 70 and 90 per cent probability of finding a G3G3wh merger remnant in the enclosed area. As we can see, the simulated remnant agrees well with the observations. There are two main possibilities to change the area of $v_{maj}/\sigma - \epsilon$ combinations that the simulated remnant can cover. First, by decreasing (increasing) the wind efficiency, we can achieve larger (smaller) values of v_{maj}/σ for a given ϵ, up to the limit of no winds (G3G3h) and thus covering the observed remnants with a large rotational support. Second, by lowering the initial mass of the gaseous halo, we can achieve smaller values of v_{maj}/σ for a
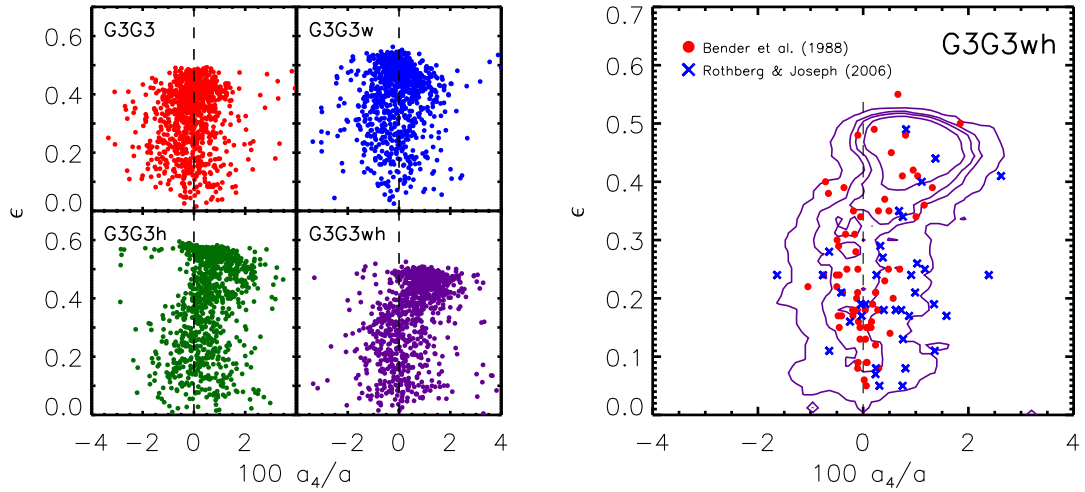
Figure 4.13 Ellipticity ϵ vs. characteristic shape parameter a_4, both measured at the half mass isophote. *Left panels:* Comparison between the four fiducial simulations, where every point corresponds to one projection. *Right panel:* Comparison between the simulation with winds and a gaseous halo and data from observed elliptical galaxies.The contours indicate the 10, 50, 70 and 90 per cent probability of finding a merger remnant in the enclosed area.

given ϵ and are thus able to cover the observed remnants with a small rotational support. Note that by employing the universal baryonic fraction in the initial conditions we have used an upper limit for the mass of the gaseous halo. Through feedback, it is possible to decrease the mass of the halo before the merger.

Isophotal shape

Finally, we study how the shape of the isophotes change, when a gaseous halo is included in the merger simulations. To this end, we measure the deviations of the isodensity contour of a projection to the fitted ellipse. The residuals are expanded in a Fourier series and the Fourier coefficient a_4 is computed. Positive values of a_4 indicate discy isopotes, while negative values indicate boxy isophotes. The results of this analysis are shown in Figure 4.13 which plots the ellipticity against the shape parameter a_4 (normalised by the semi-major axis and multiplied by a factor of 100) for our fiducial simulations with 1000 projections each. The left panel compares the four runs: the simulations with no winds and no gaseous halo, can appear discy and boxy, depending on the viewing angle, with a tendency to boxy isophotes. If wind are included, the isophotes can still be discy, however, they are more boxy on average. When a gaseous halo is included, the shape of the isophotes is more discy, especially at high ellipticities. If both winds and a gaseous halo are present the isophotal projections are mostly discy. However, at low ellipticities ($\epsilon < 0.3$) the probability for boxy and discy isophotes is equal.

As a result, we find that including a gaseous halo and thus more cold gas at the centre leads

to more discy isophotes. This is in agreement with results by Cox *et al.* (2006b) and Naab *et al.* (2006), who find that mergers with gas increase the fraction of discy isophotes. Naab *et al.* (2006) argue that the reason for the lack of boxy projections in simulations with gas is the different behaviour of minor-axis tube orbits (which are the dominant family around the half-mass radius) in axisymmetric and triaxial potentials. Dissipational mergers lead to more axisymmetric potentials, and in those, minor-axis tubes look less boxy and more discy in all projections. Additionally, the fraction of box orbits and boxlets, which can support a boxy shape is reduced.

The right panel of Figure 4.13 compares the remnant of the G3G3wh run to data from observational samples (Bender *et al.* 1988; Rothberg & Joseph 2006). The contours give the 10, 50, 70 and 90 per cent probability of finding a G3G3wh merger remnant in the enclosed area. The simulated merger remnant agrees very well with the isophotal shapes of observed ellipiticals. At low ellipticities, there are both discy and boxy projections, with an equal probability. At higher ellipticites ($\epsilon > 0.4$) the chances to find boxy isophotes are very small. These trends are seen both in the simulation and in the data.

4.3.4   Disc thickening in minor mergers

With our last set of simulations we want to study the effects of the hot gaseous halo on disc stability during a minor (1:10) merger. There have been numerous studies based on collisionless simulations that have tried to quantify the effects of these minor mergers on the thickness and stability of stellar discs (e.g. Villalobos & Helmi 2008; Purcell *et al.* 2009). For MW-like systems, it was found that these events transform the discs into structures that are roughly two to three times thicker than the initial disc, regardless of the orbital configuration of the merger. However, the inclusion of gas physics is known to play an important role in stabilising galactic discs. Cold gas in the disc may be able to absorb some of the kinetic impact energy of the merging satellite, subsequently radiating this energy away by cooling; or, gas may be able to cool and reform a new thin disc after the merger, forcing heated stars to contract again onto the disc plane.

It has been shown in section 2.5, that when the presence of cold gas in the disc is taken into account, the thickening of the stellar disc is reduced. For an initial disc gas fraction of 20 per cent (40 per cent), the thickening was reduced by 25 per cent (50 per cent) with respect to collisionless simulations. As in the initial conditions only the cold gas in the disc was accounted for (neglecting the gaseous halo), most of the gas was consumed during the merger, and therefore the regrowth of a new thin disc had a negligible impact on the scaleheight of the post-merger galaxy. This lead to the conclusion that the main process that suppresses disc thickening when only cold gas in the disc is present, is the absorption of impact energy by the gas. Furthermore, we concluded that in order to reform a new thin disc comparable in mass to the old disc, an external fuelling reservoir, such as cooling and accretion from a gaseous halo, would be needed.

We extend this study and re-simulate the 1:10 merger in section 2.5 with 20 per cent of cold
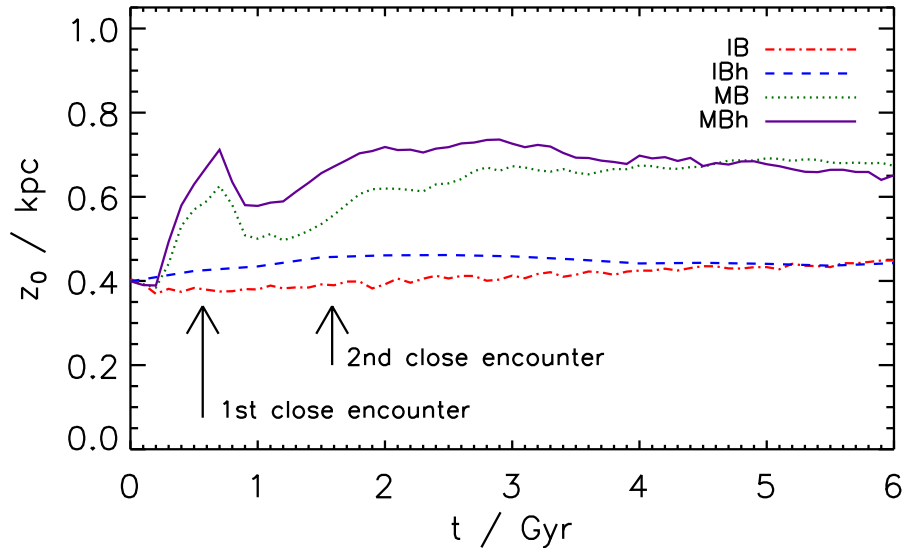
Figure 4.14 Evolution of the disc scaleheight for simulations with and without a gaseous halo. The dashed and dot-dashed lines show the isolated case while the solid and dotted lines give the scaleheight for the mergers.

gas in the disc, an orbital inclination of $60°$ and an initial disc scaleheight of $z_0 = 0.4 \, \mathrm{kpc}$ (MB60) and include a gaseous halo. We employ the universal baryonic fraction in order to maximise the accretion effects. We also run the system in isolation, in order to study how the accretion of gas from the halo acts on the scaleheight. For all time-steps, we compute the edge-on projected stellar surface density as a function of the distance to the galactic plane at a radius of $R_\odot \sim 8 \, \mathrm{kpc}$ by applying a vertical slice at $R_\odot$. We then fit for the value of z_0 assuming a sech^2 profile.

In Figure 4.14 we show the resulting time evolution of z_0 for the isolated and merger runs. While the scaleheight of the isolated galaxy without gaseous halo (IB), increases only slightly with time, the scaleheight of the isolated galaxy including a gaseous halo (IBh) quickly increases to reach a value of $z_0 = 0.45 \, \mathrm{kpc}$ at $t = 1.5 \, \mathrm{Gyr}$ where it remains constant until the end of the simulation. After 6 Gyr both isolated runs have the same scaleheight again. This means while the scaleheight of IB increases only due to numerical reasons, the scaleheight of IBh is mostly determined by how the gas accretes from the halo. The profile of the cold gas disc quickly adjusts to this resulting in a slightly higher scaleheight. This also leads to the larger scaleheight of the stellar disc. This z_0 is then constant throughout the simulation and is not further increased by numerical heating.

The scaleheight of the merger simulation without a gaseous halo (MB) increases during the first and the second encounters, reaches a value of $z_0 = 0.7 \, \mathrm{kpc}$ at $t \sim 3 \, \mathrm{Gyr}$ and afterwards stays constant until the end of the simulation. This means that the thin disc of new stars that has formed during the simulation is not massive enough to lower the scaleheight of the total stellar profile after the thickening. In the simulation with a gaseous halo, however, after reaching a

maximum scalelength of 0.75 kpc, z_0 decreases and reaches a final value of 0.65 kpc at the end of the simulation. This means that although the disc has been thickened during the first and second close encounters as much as in the run without a gaseous halo (even slightly more), the galaxy has been able to form a new thin disc which leads to a lower overall scaleheight. There are two possible effects that can cause this: one option is that the potential of the new stellar disc forces heated stars to contract again onto the disc plane; the other possibility is that the new disc is both thin and massive, such that the contribution to the density profile of the total disc is large.

In order to investigate this further, we compute the scaleheight at the end of the simulations for old stars (i.e. stars which have been set up as initial conditions) and new stars (i.e. stars that formed during the simulation). We find a scaleheight of the new thin disc in MBh of $z_{0,new} = 0.43$ kpc while the old stellar disc has $z_{0,old} = 0.86$ kpc. In the MB run, the scaleheight of the new disc is $z_{0,new} = 0.33$ kpc and that of the old disc is $z_{0,old} = 0.73$ kpc. Thus, although for MBh both the new and the old discs are thicker than the respective ones of MB, the total scaleheight is thinner. This can only be explained by the differences in mass of the new disc between MB and MBh.

To demonstrate this, we plot the SFR, the total mass of new stars formed during the simulation and the cold gas mass in Figure 4.15. While the SFR after the second close encounter is already very low for the MB simulation ($< 1 M_\odot$ yr^{-1}), the MBh run maintains a high SFR throughout the simulation ($\sim 5 M_\odot$ yr^{-1}). As a result of this the mass of the new thin disc is much higher in the MBh run and even exceeds that of the old stellar disc component at the end of the simulation. As the new thin disc is comparable in mass to the old disc, the contribution to the total density profile and thus to the total scaleheight is of the same order as that of the old disc. As a result the scaleheight of the total disc in MBh is smaller than that of MB, although both the new and the old discs are thicker than those found in MB.

Thus we found that the scaleheight of a MW-like galaxy can decrease again after having been increased by a 1:10 merger, if cooling and accretion from a gaseous halo are considered. With respect to collisionless simulations ($z_0 = 0.8$ kpc), the presence of 20 per cent cold gas in the initial disc reduces the thickening by ~ 25 per cent ($z_0 = 0.7$ kpc). Through the accretion of gas from the hot halo the thickening is further reduced by ~ 20 per cent ($z_0 = 0.65$ kpc). This final scaleheight is similar to that of a simulation without a gaseous halo but with 40 per cent initial cold gas fraction. We thus conclude that in order to retain thin discs as those observed in the Universe, it is not necessary to have very high initial gas fractions. We also note that even with a hot gaseous halo it is not possible to obtain discs with a scaleheight of $z_0 < 0.6$ after a 1:10 merger.

4.3.5   Conclusions and discussion

We investigated the role of a cooling gaseous halo in merger simulations. For this we have extended the initial conditions to include a hot gaseous halo (in addition to a dark matter halo, a stellar bulge and a disc consisting of stars and cold gas). We adopted the observationally moti-
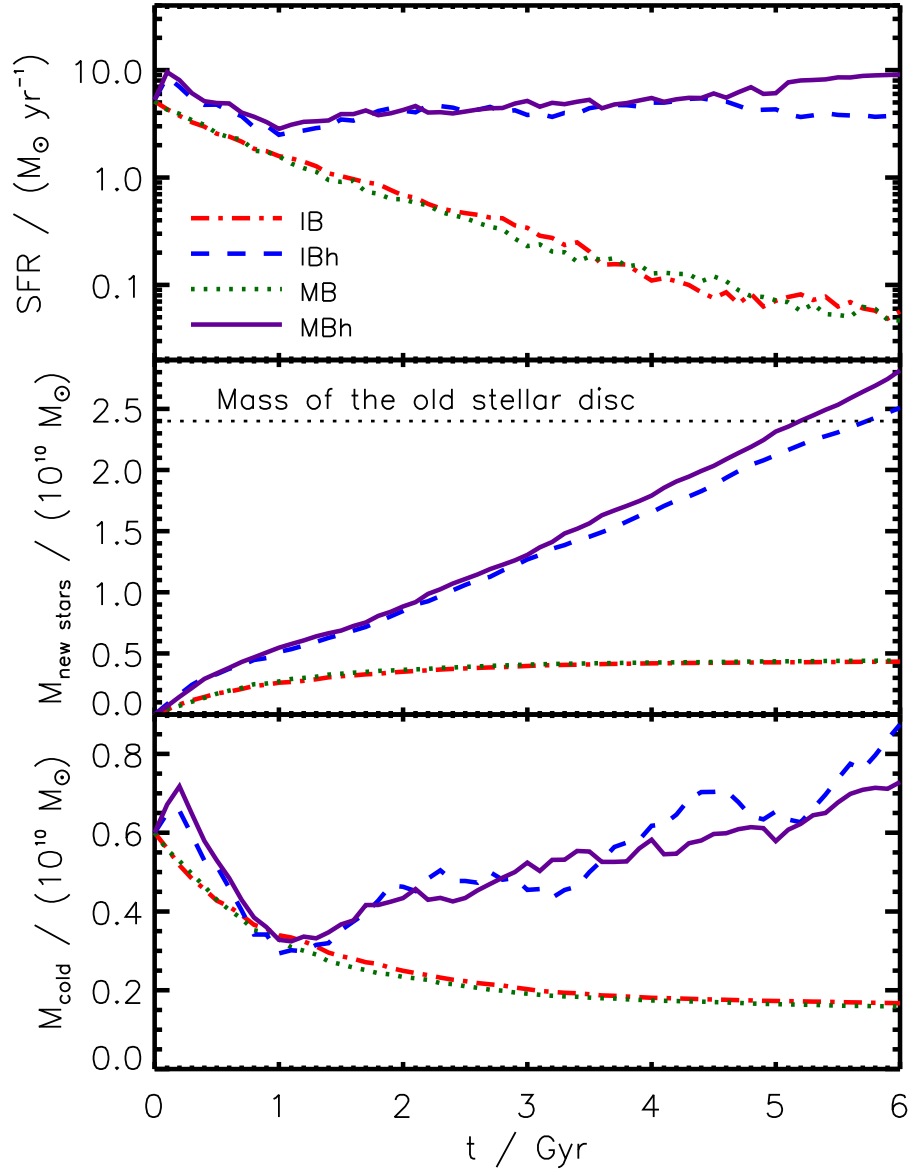
Figure 4.15 The rows from top to bottom show the SFR, the total mass of new stars formed during the simulation and the cold gas mass for the simulations with and without a gaseous halo.

vated β-profile and demanded that the halo is in hydrostatic equilibrium. Furthermore the gaseous halo is rotating around the spin axis of the disc. We have fixed its angular momentum by requiring that the specific angular momentum of the gas halo is a multiple α of the specific angular momentum of the dark matter halo and treated α as a free parameter.

In a hierarchical scenario for galaxy formation there are three key assumptions: (1) the angular momentum originates from tidal torques (Hoyle 1953), (2) the angular momentum distributions of gas and dark matter in virialised systems are identical (Fall & Efstathiou 1980), and (3) the specific

angular momentum of the gas is conserved during cooling (Mestel 1963). Under these assumptions
the specific angular momentum of the gas and the dark matter should be equal and the spin factor
is $\alpha = 1$. However, it has also been shown that under these assumptions realistic disc galaxies
cannot be created in numerical simulations (e.g. Steinmetz & Navarro 1999). This implies that
either one of the assumptions is incorrect, or that an additional assumption has to be made. The
first assumption has been tested and verified in many studies (Peebles 1969; Barnes & Efstathiou
1987; Bullock *et al.* 2001). The second assumption was tested for the time of halo formation (van
den Bosch *et al.* 2002). The third assumption lead to problems in numerical simulations, as a
large transfer of angular momentum from the gas to the dark matter was measured. However, this
was identified as a numerical problem and high resolution simulations show that the gas can retain
its angular momentum during cooling (e.g. Governato *et al.* 2004).

Since all three assumptions have been supported by previous studies, the conclusion is that
there has to be an additional effect that includes previously missing physics and must be able
to modify the angular momentum of star forming gas. Feedback processes have been found to
be important in preventing galaxies from becoming too massive and can explain the dependence
of star formation efficiency on halo mass. Since disc dominated systems are more common in
low mass systems (where SN feedback is more effective), feedback can also be the main driver
in altering the angular momentum distribution of the gas after halo collapse. When low angular
momentum material at the centre of the galaxy forms stars the following feedback removes the
surrounding low angular momentum gas from the galaxy leading to a difference in the angular
momentum distributions of gas and dark matter. This process has been found in recent simulations
(Governato *et al.* 2010) which show an outflowing gas with much lower angular momentum than
the gas that remains in the system. Thus the spin factor measured in these simulations deviates
from $\alpha = 1$. Therefore α is a free parameter and needed to be constrained.

This was done by modelling a typical MW-like galaxy at $z = 1$ and letting it evolve in isolation
up to $z = 0$ using different values of α. We employed two observational evidences, stellar mass
and disc scalelength, in order to determine the correct α. The results for the control simulation
without a hot halo completely disagreed with the observations, stressing the importance of the
gaseous halo. Simulations with a low value of α showed both an increase of stellar mass which
was too large and scalelength that were too small compared to observations. Large values of α
leaded to too large discs and stellar masses that are too low. Only for a value of $\alpha \sim 4$, stellar
masses and scalelengths were within the observational constraints for MW-like galaxies. This
value is therefore used throughout the rest of this work.

In order to fix the mass of the gaseous halo we required that the baryonic fraction within the
virial radius is the universal one. This was done, as we wanted to demonstrate the maximum
effects that the hot halo can have in galaxy mergers. Of course, due to feedback processes and
stellar winds, the baryonic fraction in galaxies can be lower, leading to a lower mass for the
gaseous halo. In the past, several studies have raised the question whether the massive gaseous

haloes, predicted by galaxy formation models and employed in our simulations, could be seen in X-ray observations. In a first study addressing this, Benson *et al.* (2000) compared X-ray observations of three massive spirals to predictions of simple cooling flow models and found that the model overpredicted the X-ray luminosity by more than an order of magnitude. However, the models were deliberately simplified versions of general semi-analytic ones.

Current observational limits on the 0.3-2 keV X-ray luminosity of MW-like systems indicate limits of several 10^{39}erg s^{-1} (Wang *et al.* 2003; Strickland *et al.* 2004; Tüllmann *et al.* 2006; Li *et al.* 2007). In a recent paper Rasmussen *et al.* (2009) have compared these observational limits to the X-ray luminosities found in cosmological simulations. They found no tension between simulations and observations (for a simulated MW-like galaxy they found 0.3-2 keV X-ray luminosities of $\sim 10^{38}$erg s^{-1}). Similarly, we can compute X-ray luminosities from our initial conditions. For this we integrate the emissivity over the volume of the halo in the 0.3-2 keV band (see Navarro *et al.* 1995 for a prescription to do this for SPH simulations). For our galaxies Z1A4, G3h and MBh we find $L_X = 2, 1$ and 10×10^{38}erg s^{-1}, respectively. We thus conclude that our modelled gaseous haloes are not in conflict with X-ray observations.

We have used MW-like galaxy models including a gaseous halo in a series of binary merger simulations. We have run all mergers both with and without galactic winds using the 'constant wind' model by Springel & Hernquist (2003) where the mass-loss rate carried by the winds is proportional to the SFR and the wind speed is constant. However, this model has some deficiencies as the wind speed for low mass galaxies is the same as for high mass galaxies resulting in too much heating for low mass systems. In the last years models have been developed that overcome these problems and present a more realistic match to observed quantities, e.g. momentum-driven winds (Oppenheimer & Davé 2006). These models, however, show that both the wind speed and the mass loading factor for MW-like galaxies do not vary much after $z = 1$. Since we are merging systems of equal mass which are expected at low redshift, we are confident that a more sophisticated wind model would leave our results unchanged.

We have studied the impact of a gaseous halo and stellar winds on the SFR using four 'fiducial' runs: without gaseous halo and without winds (G3G3), without gaseous halo but with winds (G3G3w), without winds but with a gaseous halo (G3G3h) and with both winds and gaseous halo (G3G3wh). We found that in simulations without a gaseous halo, the maximum SFR during a starburst is ~ 30 times larger than that of the constituent galaxies evolved in isolation. When a gaseous halo is included, this enhancement is much smaller (factor of ~ 5). The reason for this is the higher SFR of the isolated systems when a cooling halo is included. Isolated systems without a hot halo, however, consume most of their gas at the beginning of the simulation, such that the SFR is very low at the respective time of the starburst in the merger simulation. We also found that when stellar winds are included, the starburst is spread over a much larger time interval than in simulations without winds. This happens, because the winds removes material from the cold gas in the centre which is relocated in the halo around the remnant. From there it can cool and accrete

back to the centre resulting in a higher SFR than in the case without winds.

Furthermore, we studied the effects of the gaseous halo on the starburst efficiency which we defined as the stellar mass which formed due to the burst divided by the mass of cold gas in the galaxies just before the merger. For the G3G3 run we found an efficiency of $e = 0.68$ while for G3G3w it is only $e = 0.45$ showing that the efficiency depends on the wind model and its parameters. The presence of a gaseous halo reduces the efficiency in G3G3h to $e = 0.51$. Additionally, the SFR after the burst is lower than the SFR of the constituent galaxy evolved in isolation, resulting in a stellar mass of the remnant which is lower than that of the two isolated galaxies. This has two reasons: first, the specific angular momentum of the merger orbit is higher than that of the isolated systems, due to orbital angular momentum. This leads to a higher centrifugal barrier and thus to a lower accretion rate and SFR. Second, due to shocks that occur during the merger, the temperature of the gaseous halo is higher than in the isolated case, leading to a higher cooling time and a lower SFR. The fact that two non-merging galaxies can have a larger stellar mass than if they had merged poses a challenge for SAMs, which assume that a merger always leads to an additional formation of stellar mass.

We have also studied, how the starburst efficiency depends on initial disc gas fraction and found that without gaseous halo, it decreases with increasing gas fraction. Higher gas fractions imply a lower stellar mass which is less efficient in dragging the gas to the centre as in systems with massive stellar components. If a gaseous halo is taken into account, however, the efficiency increases with increasing gas fraction, as the initial dense gas disc is replaced by accreting gas from the halo which is spatially much more extended. Systems with higher initial gas fractions retain more of their initial dense gas at the time of the merger which then leads to a more efficient burst. If additionally winds are considered, the formation of massive stellar discs in very gas rich galaxies is prevented such that the efficiency is decreased again.

Our simulations are closely related to prior studies on the efficiency of starbursts. At this point, we would like to compare our results obtained neglecting the gaseous halo and winds to those obtained by Cox *et al.* (2008) and Hopkins *et al.* (2009a). Using the same progenitor galaxies (G3) but a different star formation model, Cox *et al.* (2008) find a starburst efficiency for G3G3 of $e = 0.5$. However, in the definition of e, they have used the gas fraction at the start of the simulation rather than just before the burst. As the gas fraction decreases until the time of the burst, the efficiency increases to $e = 0.67$ (for the definition used by us). This is in excellent agreement with our value of $e = 0.68$. Hopkins *et al.* (2009a) used a large suite of simulations to develop an analytic model for the burst efficiency. For our orbit, mass ratio and gas fraction this model predicts an efficiency of $e = 0.74$ However, this small difference ($\lesssim 10$ per cent) is expected, as the simulations used by Hopkins *et al.* (2009a) to tune their model use a 'softer' EOS ($q = 0.25$; see Springel *et al.* 2005a for details). As a result more gas can lose angular momentum and fall to the centre during the starburst, such that more stellar mass is formed. However, in contrast to their conclusions, we find that due to the presence of a gaseous halo, the initial cold gas

fraction is not of major importance for the stellar mass growth during the merger. Instead, due to cooling the cold gaseous disc is subsequently refuelled.

We have also addressed the question, how the gaseous halo affects the morphology of merger remnants. Analysing the systems $\sim 3\,\mathrm{Gyr}$ after the final coalescence, we found that when a gaseous halo is included in the simulations, the bulge-to-total ratio is decreased. This is a consequence of cooling and accretion of gas from the halo into a cold gas disc at the centre which subsequently forms stars, leading to a new stellar disc. However, all remnants were still bulge-dominated ($B/T \sim 0.8$-0.9). Furthermore, we found that the presence of a gaseous halo affects the surface brightness profiles of the remnants. While systems with no gaseous halo deviate from the observed $r^{1/4}$ profile at small scales, systems with a hot halo match the observed profile. The reason is the new stellar disc which leads to a higher surface density at the centre.

A kinematic analysis of the merger remnants showed that if the progenitor galaxies contain only ~ 20 per cent cold gas and no gaseous halo, the chosen orbit leads to a remnant which is slowly rotating and only supported by velocity dispersion. When a gaseous halo is included, however, the rotational support of the remnant strongly increases. This can be also explained by the presence of a massive stellar disc in the centre that forms after the merger. The rotation of this disc contributes to the total rotational support in a mass-weighted average and leads to a larger potential at the centre, which causes 'old' stars to fall towards the centre and to increase their rotational velocity due to conservation of angular momentum. We have further studied the impact of the gaseous halo on the isophotal shape of the remnants and found that including a gaseous halo leads to remnants that are more discy on average. We found that both the kinematic structure and the isophotal shape of the remnants with a gaseous halo agrees very well with observed ellipticals.

Studying the effects of cold gas fraction in progenitor galaxies on the kinematic structure of major merger remnants, Cox *et al.* (2006b) conclude that in order to form realistic low-luminosity elliptical galaxies in merger simulations, the progenitor galaxies must have high gas fractions of ~ 40 per cent. In the light of our results, we would like to address the question, whether such massive cold gas discs are needed in the progenitors or if just 'gas' is needed. We agree with the statement that in order to form realistic ellipticals, a large amount of cold gas has to be present at the centre after the merger which then can reform a massive stellar disc. But contrary to the conclusions reached by Cox *et al.* (2006b) we conclude that the progenitor galaxies need not have high gas fractions. It is only important, that a reservoir is present, from which gas can accrete and settle in a cold gas disc which can subsequently form a rotating stellar disc. As we have shown, this can be achieved by considering the gaseous halo in galaxy mergers.

However, this leads to a different problem for massive ellipticals: if a gaseous halo (which is expected in all progenitor galaxies) always leads to a rotationally supported system, how can slow rotators form? This is related to the problem, how elliptical galaxies can have low SFRs and red colour, if a gaseous halo would lead to the accretion of cold gas discs and thus to a high SFR. Possible solutions to these problems are: first, subsequent minor mergers can destroy the

newly formed stellar disc and the cause for the rotational support. Second, by lowering the mass of the gaseous halo before the merger, which can be achieved e.g. by massive stellar winds, the accretion rates after the merger are lowered, leading to a less massive disc. This would also solve the problem of too much star formation in elliptical galaxies. Last, by introducing a source of feedback, which is most effective in massive systems and after major mergers such as AGN feedback, the SFRs in remnants could be lowered.

In a last set of simulations we have revisited the question, if thin discs like the one observed in the MW, can survive minor merger events. In collisionless simulations of a 1:10 merger such a disc is destroyed, while we have have shown that if also the cold gas component in the disc is considered, the thickening due to the merger can be reduced. The reason for that is the absorption of impact energy by the gas. We extended this study in order to also consider the hot gas component in the halo and found that the thickening, with respect to collisional simulations that only consider gas in the disc, is further reduced by 20 per cent (in addition to the effect of the cold gas). This is due to the cooling and accretion of cold gas which leads to the formation of a new thin disc and forces heated stars to contract again onto the disc plane. Similar to the conclusions reached in major merger simulations, we find that high gas fractions of ~ 40 per cent are not needed in order to form realistic galaxies with properties as found in observations. The subsequent cooling of the gaseous halo compensates for lower initial cold gas fractions.

Chapter 5

Simulations of Semi-Analytic Merger Trees

In chapter 2 we have shown that simulations of galaxy mergers are a very useful method to model and predict galaxy properties. As the particles are only in the regions of interest, they can achieve a very high resolution, which is needed to correctly model the galactic structure on the relevant scales of $\lesssim 100$ pc. In addition to this, it is possible to incorporate gas with high resolution. We have shown that the gas physics is very important for the evolution of galaxy properties such as the scaleheight of thin disc galaxies (cf. Figure 2.5 in section 2.5). However, typical merger simulations do not have initial conditions that are motivated by the cosmological background model, but the parameters for the merger are taken from grids. As a consequence the possible parameter space is very large, but only a small fraction of this space is cosmologically realistic.

Semi-analytical models, which were introduced in chapter 3, are a powerful tool to create a large sample of galaxies that is able to reproduce statistically observable galaxy properties. Although, there is little or no information about the internal structure of the model galaxies and their spatial location, SAMs can model galaxy properties in a cosmologically motivated fashion. As a key prediction, SAMs can produce a set of galaxy merger trees, which fully describe the merger history of a given galaxy. Using a statistical sample of merger trees, a SAM can determine which galaxy mergers are common in the Universe and which mergers are not. Each single semi-analytic merger tree thus represents a cosmologically motivated model history for a sample galaxy. Analysing a set of N-body merger trees we found that multiple mergers (i.e. a second merger starts before the first merger is completed) are very common and thus cannot be neglected in merger simulations (cf. Figure 3.4 in section 3.4).

In order to be able to use all relevant components of a galaxy system in a merger simulation, we extended the initial conditions generator in chapter 4, such that both smooth accretion of dark matter and accretion of gas from a hot gaseous halo is taken into account. The smooth accretion of the dark matter halo has to be modelled in order to correctly reproduce the halo mass of a given system as a function of cosmic time. The accretion of gas from a hot halo is important as it refuels the cold gas in the disc and ensures a roughly constant SFR. The galaxy thus continues to form stars even after the cold gas in the initial disc has been depleted. In major merger simulations, for

example, this leads to the reformation of a gaseous and a stellar disc after the final coalescence which is important for both structural properties of the merger remnant (cf. Figure 4.11 in section 4.3.3), as well as kinematic properties (cf. Figure 4.12 in section 4.3.3).

In this chapter we combine the advantages of merger simulations (high resolution and detailed treatment of gas physics) with the advantages of SAMs (cosmological background), by using the predictions of the SAM which mergers are common for a given galaxy, as the source for merger simulations. Specifically, we use the galaxies in the semi-analytic merger trees as the initial conditions for multiple merger simulations. In this way the important requirements needed to model galaxy properties on small scales – high resolution, gas physics and cosmological background – are taken into account. Simultaneously the computational cost is comparably low, such that a large sample of galaxy systems can be modelled in a short amount of time.

In order to describe our new method, we present a schematic view in Figure 5.1. In a first step we select a dark matter merger tree and use the SAM to predict the properties of the baryonic components of each halo at every time-step. A resulting merger tree is shown in the left side of Figure 5.1 where the time runs from top to bottom. We then choose a starting time t_i after which we want to simulate this tree. In our simple example, the main system experiences four mergers after t_i. We then use the predictions by the SAM for the central galaxy of the main halo at t_i and create a particle realisation with the galaxy generator, as indicated by the brown arrow. This model galaxy is shown in the top right of Figure 5.1 and in our example consists of a dark matter halo (grey), a hot gaseous halo (red), a cold gaseous disc (blue), a stellar disc (yellow) and a small stellar bulge (green). We evolve this galaxy with our hydrodynamical code until the time t_1 when the first satellite galaxy S_1 enters the main halo. A particle realisation is then created from the semi-analytic prediction and included in the simulation at the virial radius of the main halo. We evolve this merger with the hydrodynamical code, until the next satellite galaxy enters the main halo. In our example, two galaxy enter the halo at the same time, thus we create particle realisations using the predictions by the SAM for both galaxies S_2 and S_3 and include them in the simulation by positioning them at the virial radius. This procedure is repeated for all merging satellites until the final time t_f. In this way, we naturally include multiple mergers, when an already merging galaxy has not been fully accreted as the next galaxy is entering the halo. This is indicated at t_3 when the galaxy S_3 is still orbiting while the satellite S_4 enters the halo. In the example shown in Figure 5.1, the central galaxy grows through accretion of dark matter and gas (e.g. from t_i to t_1 or from t_3 to t_f) and through mergers of satellite galaxies (e.g. from t_1 to t_2). As indicated in the sketch, mergers increase the mass and size of the bulge and thicken the stellar disc, as found in isolated simulations.

Our model thus requires two main steps: creating particle realisations of galaxies as predicted by the SAM and combining the these initial conditions in a simulations as determined by the merger tree (i.e. every galaxy has to enter the simulation at the specified time and position). This means we first have to specify how the information about the galaxy properties that is computed
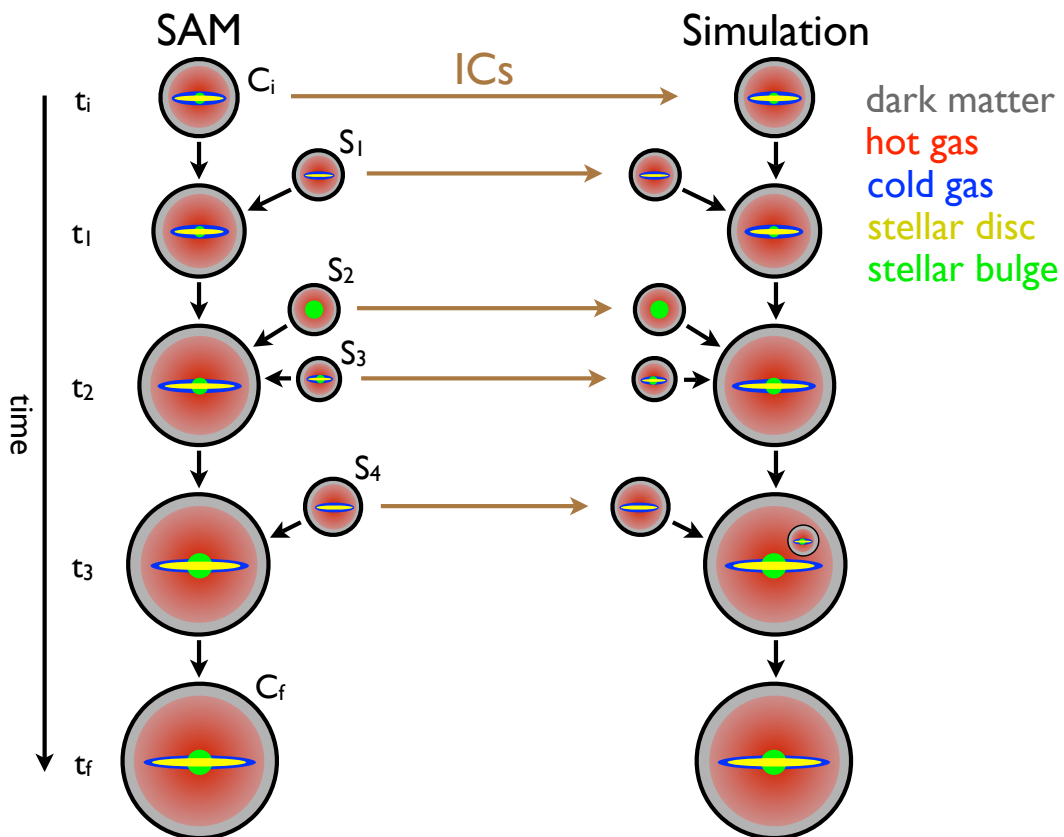
Figure 5.1 Schematic view of the combination between semi-analytic models and merger simulations. On the left side the semi-analytic merger tree is shown and the time runs from top to bottom. At the starting time t_i, initial conditions for the central galaxy are created using the properties of the central galaxy in the SAM at this time. This system is then simulated with the hydrodynamical code until the time of the first merger t_1, where the first satellite S_1 galaxy is put into the simulation using the properties predicted by the SAM. The resulting merger is simulated until the next galaxies (S_2 and S_3) enter the main halo at t_2, at which point they are also included in the simulation. This procedure is repeated for all mergers until the final time of the run t_f.

with the SAM, is transformed into three dimensional galaxy models that can be simulated with a hydrodynamic code. Then we have to determine how the satellite galaxies are included in the simulation, so their position and velocity have to be calculated.

We note that the starting time t_i, or the starting redshift z_i, respectively, can also be chosen such that the simulation starts at a very early epoch. In this case the central galaxy consists only of a dark matter halo and hot gas in this halo. The dark matter will then grow by mergers and smooth accretion, and the stellar disc and bulge will form as a result of cooling and accretion of gas, and merger events.

5.1   Creating particle realisations of semi-analytic galaxies

In order to create particle realisations of the semi-analytic galaxies, we need to specify those galaxies that are included in our simulation. For this we first have to choose a starting redshift z_i and a minimum merger ratio μ_{min}. We define this ratio as the mass of the dark matter in the entering subhalo divided by the dark matter mass of the main halo at the time the satellite passes the virial radius. As satellite galaxies that have much less mass then the central galaxy only have a negligible effect on the evolution of the central galaxy (Kazantzidis *et al.* 2008, 2009), a minimum mass ratio of $\mu_{\mathrm{min}} = 0.03 - 0.1$ can be assumed in order to correctly model the central galaxy. If one is instead interested in the satellite population, this ratio can be chosen much lower.

We read in the complete semi-analytic merger tree and identify the central galaxy at the starting redshift, all satellite galaxies within the virial radius at this time (which have not merged with the central galaxy yet) and all satellite galaxies that enter the main halo at a later time. From these galaxies we only select those that fulfil our merger mass ratio criterion. For every selected galaxy we record the value for the time the galaxy enters the main halo t_{enter}, the virial mass of the dark matter halo M_{vir}, its concentration c, its spin parameter λ, and the semi-analytic predictions for the masses of the hot gaseous halo M_{hg}, the cold gaseous disc M_{cg}, the stellar disc $M_{\mathrm{disc},*}$ and the stellar bulge M_{bulge}, and the scalelength of the stellar disc r_{disc}. All these quantities are taken at t_i for the central galaxy and satellites that are already with the main halo at t_i, and at t_{enter} for all satellite galaxies that are entering the main halo after t_i. Additionally, for all satellite galaxies we record the dynamical friction time, i.e. the time the galaxy orbits in the halo before it is merging with the central galaxy. This quantity is also predicted by the SAM.

The structural parameters of every galaxy that are not predicted by the SAM are determined with free parameters. The scaleheight of the stellar disc is assumed to be a fraction of its scalelength $z_0 = \zeta r_{\mathrm{disc}}$, where typically $\zeta = 0.15$. Similarly the scalelength of the gaseous disc is related to that of the stellar disc by $r_{\mathrm{gas}} = \chi r_{\mathrm{disc}}$, with a standard value of $\chi = 1.5$. The core radius r_c of the hot gaseous halo is related to the scalelength of the dark matter halo r_s by $r_c = \xi r_s$ with a fiducial value of $\xi = 0.22$ and the slope parameter of the β-profile is set to $\beta_{\mathrm{hg}} = 2/3$. We choose a specific angular momentum of the gaseous halo that is a factor of α times larger than that of the dark matter halo (see section 4.2.2 for details), and typically adopt $\alpha = 4$.

In order to select the number of particles in every component of the galaxies, we determine the semi-analytic prediction for the final stellar mass of the central galaxy $M_{*,f}$ and choose a number of stellar particles in the central galaxy N_* that we would like to obtain at the end of our simulation. If the final stellar mass of the simulated galaxy is equal or close to the final stellar mass in the SAM, i.e. if the SFR and accretion rate in the simulation and SAM are similar, we can assume that every stellar particle has a mass of $m_* = M_{*,f}/N_*$ and the final number of stellar particles in the simulation will be close to N_*. This ensures the maximum resolution for all merger trees, while keeping the total number of particles (and thus the computational cost) at

a manageable level. As our simulation code can produces N_g generation of stellar particles from every gas particle due to star formation (where N_g is typically 2), we set the mass of every gas particle to $m_{\mathrm{gas}} = N_g m_*$. In this way, all stellar particles have the same mass. The mass of the dark matter particles is finally selected as $m_{\mathrm{dm}} = \kappa m_*$ where κ is a free parameter. If κ is chosen too low, the dark matter particles have a very low mass which results in a very large number of dark matter particles and thus in a high computational cost. For high values of κ the mass of the dark matter particles can become too large, such that these massive particles perturb the disc component which results in numerical disc heating. Typically values of $\kappa \sim 15$ are both computationally efficient and lead to no measurable heating (cf. values in section 2.5).

Additionally, for simulations were we are interested in the satellite population and not in the central galaxy, we allow for a higher resolution in the satellite galaxies. This is done by dividing the mass of the particles of every satellite by a number $N_{\mathrm{res,sat}}$. This number, however, should not be chosen too high, since the particle masses of the satellite would be much lower than the particle masses of the main system. This can lead to mass segregation, which means that the particles of higher mass (i.e. the central galaxy particles) will preferentially settle at the bottom of the potential. Since this is a numerical effect, it has to be avoided which implies that $N_{\mathrm{res,sat}} \lesssim 10$.

With these particle masses we can easily compute the initial number of particles for every galaxy. The number of dark matter particles is thus given by $N_{\mathrm{dm}} = M_{\mathrm{dm,tot}}/m_{\mathrm{dm}}$, where $M_{\mathrm{dm,tot}}$ is the total mass of the halo and the number of particles in the gaseous halo is $N_{\mathrm{hg}} = M_{\mathrm{hg,tot}}/m_{\mathrm{gas}}$, where $M_{\mathrm{hg,tot}}$ is the total mass of the gaseous halo up to its truncation radius. The particle numbers for the gaseous disc, stellar disc and stellar bulge components are $N_{\mathrm{cg}} = M_{\mathrm{cg}}/m_{\mathrm{gas}}$, $N_{\mathrm{disc},*} = M_{\mathrm{disc},*}/m_*$ and $N_{\mathrm{bulge}} = M_{\mathrm{bulge}}/m_*$, respectively. In order to prevent that a component is unstable due to a low number of particles, we remove a component if its number of particles is lower than a minimum particle threshold N_{min}.

Using this recipe, we create particle realisations of all selected galaxies. These can now be used as initial conditions for the hydrodynamical simulation. The next task is thus to specify when a galaxy enters the main halo, and at which positions and with which velocity.

5.2 Performing the multiple merger simulation

We start with the particle realisation of the central galaxy and move into its rest frame (i.e. the centre of mass is in the origin and there is no bulk motion). For all satellite galaxies we have to compute the relative position and velocity with respect to the central galaxy at the time when they are included in the simulation. If analytic EPS merger trees are used, the positions and velocities are not specified. In this case we set the initial position of each satellite randomly on a sphere of the virial radius of the main halo at t_{enter}. The velocity is then computed by drawing the radial and tangential velocity from a Gaussian distribution with the peaks at 90 and 60 per cent of the virial velocity, respectively, and a scatter of 30 per cent of the virial velocity (Benson 2005). The

angles between the angular momentum axis of the orbit, the axis of the central galaxy and the axis of the satellite, are assumed to be random. If mergers trees drawn from simulations are used, we can directly extract the relative initial positions and velocities from the tree. As t_{enter} is defined as the time when a satellite galaxy passes the virial radius of the main halo, the initial distance is always equal to the virial radius at t_{enter}.

However, we have to divide between those galaxies that are already within the main halo at z_i and those galaxies that enter the halo at a later time. For those galaxies that have entered the halo before z_i, we expect that they have already lost some of their angular momentum due to dynamical friction and are therefor closer to the central galaxy than the virial radius. Therefore we scale their initial distance and velocity by

$$ r' = r\sqrt{1 - \frac{t_i - t_{\text{enter}}}{t_{\text{df}}}} \quad \text{and} \quad v' = v\sqrt{1 - \frac{t_i - t_{\text{enter}}}{t_{\text{df}}}}, \tag{5.1} $$

where t_i is the starting time of the simulation, t_{enter} is the time the satellite entered the main halo and t_{df} is the dynamical friction time (i.e. the time it takes the satellite to merge with the central galaxy). The direction of the position and velocity vectors are unaltered.

The last parameter that needs to be fixed is the gravitational softening length ϵ. In order to ensure that the maximum gravitational force exerted from a particle is independent of its mass, we scale the softening lengths of all particle species (dark matter, gas and stars) with the square root of the particle mass (Dehnen 2001). The normalisation of this relation is obtained with a free parameter ϵ_1 that specifies the softening length for a particle of one internal mass unit of the code (i.e. $10^{10} M_{\odot}$). The softening length is thus given as $\epsilon = \epsilon_1 \sqrt{m_{\text{part}}/10^{10} M_{\odot}}$, were m_{part} is the mass of the particle. For our fiducial choice of $\epsilon_1 = 32 \, \text{kpc}$ and a typical particle mass of $10^4 M_{\odot}$ this results in a softening length of 32 pc.

Before the simulation is started we include all satellite galaxies that have entered the main halo before t_i and all satellites that are entering the halo at t_i in the initial conditions. We evolve this system with the hydrodynamical code until the time when the first satellite enters the main halo $t_{\text{enter},1}$ as specified by the merger tree. At this time we interrupt the evolution of the simulation and include the particle realisation of this satellite galaxy in the simulation using the relative position and velocity as determined above. Thus the satellite galaxies are only included when they enter the virial radius of the main halo. We then resume the evolution of the simulation and run the hydrodynamical code until the time when the first satellite enters the main halo $t_{\text{enter},2}$. At this point the evolution of the simulation is interrupted again and the particle realisation of the satellite is included in the simulation at the virial radius. The simulation is then resumed again and this process is repeated until the final time of the simulation t_f.

The main advantage of including the satellite galaxies only when they enter the main halo, is that the computational cost is reduced. The satellites are only simulated when they affect (or are affected by) the main system. Up to this point we use the SAM to compute the evolution of the

Table 5.1 Summary of the parameters used for the simulations of merger trees and their fiducial value.

Parameter	Description	Fiducial value
z_i	Redshift at the start of the simulation	1.0
μ_{min}	Minimum dark matter mass ratio	0.03
ζ	Ratio of scaleheight and scalelength of the stellar disc	0.15
χ	Ratio of scalelengths between gaseous and stellar disc	1.5
ξ	Ratio of gaseous halo core radius and dark matter halo scaleradius	0.22
β_{hg}	Slope parameter of gaseous halo	0.67
α	Ratio of specific angular momentum between gaseous and dark halo	4.0
N_*	Expected final number of stellar particles in the central galaxy	200 000
κ	Ratio of dark matter and stellar particle mass	15.0
$N_{res,sat}$	Ratio of satellite and central galaxy particle mass	1.0
N_{min}	Minimum number of particles in one component	100
ϵ_1	Softening length in kpc for particle of mass $m = 10^{10}M_\odot$	32.0
t_0^*	Gas consumption time-scale in Gyr for star formation model	3.5[†]
A_0	Cloud evaporation parameter for star formation model	1250.0[†]
β_{SF}	Mass fraction of massive stars for star formation model	0.16[†]
T_{SN}	Effective supernova temperature in K for feedback model	1.25×10^8[†]
η	Mass loading factor for wind model	1.0
v_{wind}	Initial wind velocity in $\mathrm{km\,s^{-1}}$ for wind model	500.0

[†] The star formation parameters assume a Kroupa IMF.

satellite galaxy's properties. However, a possible future extension of our method is to simulate the satellite galaxies before they have entered the main halo. If these galaxies evolve in isolation up to this point, the improvement with respect to the SAM is small, but if the galaxies experience merger events, their properties can be modelled in a more realistic way, when they are simulated.

In Table 5.1, we summarise the free parameters of our model and present our fiducial values. We have tested these values mainly on merger trees of MW-like galaxies. For systems of higher or lower halo mass they have to be adjusted, accordingly. We also list the free parameters that are used in the hydrodynamical code and its cooling, star formation and wind models.

5.3 Application: simulations of Milky Way-like galaxies

We employ our model in simulations of MW-like galaxies, i.e. disc galaxy systems with a dark matter halo mass of $M_h \approx 10^{12} M_\odot$. The aim of this study is to investigate how a central disc galaxy evolves from redshift $z = 1$ to $z = 0$ while subsequently experiencing minor mergers. In addition, we study the evolution of the satellites while orbiting the central galaxy. Finally we analyse the systems at $z = 0$ and study how much mass of the final central galaxy has been

Table 5.2 Properties of the galaxies in the merger trees. For the main system the properties are given at the starting time of the simulation t_i, while for the satellites the properties are given at the time when they enter the main halo t_{enter}. All masses are in solar units and all scales are given in kpc.

ID	t_{enter}	t_{merge} [a]	μ^{-1}	$\log(M_h)$	c	λ	$\log(M_*)$	B/T	f_{gas} [b]	r_{disc}
					Tree 1775					
Main	6.25	-	-	11.55	4.71	0.041	10.16	0.15	0.41	2.53
Sat 1	7.72	14.47	14.42	10.43	7.01	0.041	7.47	0.00	0.90	1.13
Sat 2	7.88	13.33	9.48	10.68	6.77	0.041	9.25	0.37	0.37	1.36
Sat 3	11.76	15.47	8.04	10.96	9.01	0.041	9.22	0.00	0.43	1.87
					Tree 1808					
Main	6.25	-	-	11.70	4.56	0.028	10.11	0.00	0.51	1.65
Sat 1	6.90	13.48	9.87	10.76	6.02	0.028	8.92	0.00	0.37	1.04
Sat 2	7.07	12.52	15.58	10.62	6.30	0.028	8.73	0.00	0.58	1.66
Sat 3	10.42	22.29	22.80	10.57	8.71	0.028	8.66	0.18	0.53	1.43
					Tree 1877					
Main	6.25	-	-	11.53	4.73	0.035	9.88	0.00	0.41	2.08
Sat 1	6.25	10.03	7.80	10.64	5.73	0.035	8.81	0.00	0.56	1.06
Sat 2	6.74	14.16	13.12	10.53	6.17	0.035	8.78	0.00	0.41	0.91
Sat 3	9.49	24.84	16.86	10.51	8.14	0.035	8.17	0.00	0.71	1.46
Sat 4	9.64	23.02	10.57	10.75	7.91	0.035	8.76	0.00	0.70	2.69
Sat 5	9.96	15.56	8.77	10.93	7.83	0.035	9.26	0.05	0.56	2.53
Sat 6	13.31	27.59	23.16	10.58	10.95	0.035	6.41	0.00	1.00	4.19
					Tree 1968					
Main	6.25	-	-	11.60	4.66	0.047	10.02	0.00	0.41	3.09
Sat 1	6.08	13.76	10.52	10.52	5.72	0.047	8.22	0.00	0.70	1.38
Sat 2	6.41	11.04	6.08	10.86	5.61	0.047	8.80	0.00	0.74	1.96
Sat 3	6.57	20.96	21.52	10.41	6.21	0.047	7.96	0.00	0.81	1.65
Sat 4	12.05	39.86	21.00	10.57	9.96	0.047	8.57	0.06	0.70	2.13
					Tree 1975					
Main	6.25	-	-	11.57	4.69	0.053	9.84	0.05	0.68	3.57
Sat 1	5.27	8.31	6.08	10.61	5.07	0.053	8.62	0.16	0.61	0.95
Sat 2	7.39	14.30	24.23	10.24	7.05	0.053	7.70	0.00	0.82	0.92
Sat 3	7.56	12.81	5.42	10.97	6.18	0.053	9.33	0.09	0.52	2.50
Sat 4	7.56	18.16	10.87	10.66	6.56	0.053	8.11	0.24	0.92	2.30
Sat 5	8.37	22.92	26.00	10.46	7.41	0.053	8.11	0.08	0.79	1.52
Sat 6	8.85	27.09	21.83	10.58	7.57	0.053	8.31	0.00	0.82	2.23

[a] Time when satellite merges onto central galaxy, computed with dynamical friction recipe
[b] Gas fraction in the disc

Table 5.2 cont.

ID	t_{enter}	t_{merge} ^{a}	μ^{-1}	$\log(M_h)$	c	λ	$\log(M_*)$	B/T	f_{gas} ^{b}	r_{disc}
				Tree 1990						
Main	6.25	-	-	11.37	4.90	0.039	9.66	0.00	0.53	2.15
Sat 1	6.41	11.35	6.81	10.55	5.94	0.039	8.28	0.00	0.74	1.55
Sat 2	6.74	13.44	10.13	10.50	6.22	0.039	8.17	0.04	0.70	0.84
Sat 3	9.80	18.33	14.04	10.63	8.18	0.039	8.72	0.17	0.78	2.87
Sat 4	10.11	15.01	10.39	10.83	8.10	0.039	9.07	0.00	0.30	1.45
				Tree 2048						
Main	6.25	-	-	11.50	4.76	0.024	9.97	0.01	0.36	1.15
Sat 1	6.57	11.26	9.81	10.58	6.03	0.024	8.48	0.00	0.86	3.37
Sat 2	6.90	11.80	8.49	10.78	6.01	0.024	8.82	0.00	0.67	2.39
Sat 3	7.23	15.89	20.99	10.51	6.59	0.024	9.35	0.03	0.00	1.07
				Tree 2092						
Main	6.25	-	-	11.39	4.88	0.039	9.79	0.24	0.56	2.15
Sat 1	6.08	10.61	14.27	10.20	6.07	0.039	8.64	0.00	0.83	1.66
Sat 2	6.25	13.08	11.11	10.34	6.04	0.039	8.98	0.00	0.78	1.54
Sat 3	8.37	20.41	11.29	10.68	7.12	0.039	9.01	0.00	0.56	2.76
				Tree 2126						
Main	6.25	-	-	11.52	4.75	0.023	9.87	0.05	0.38	1.12
Sat 1	7.23	11.65	8.07	10.69	6.32	0.023	8.84	0.00	0.42	1.14
Sat 2	7.56	14.06	11.33	10.67	6.57	0.023	8.94	0.00	0.40	1.55
Sat 3	11.91	17.82	8.30	10.90	9.22	0.023	9.34	0.30	0.55	2.60
Sat 4	12.20	22.71	14.57	10.72	9.79	0.023	8.74	0.00	0.67	2.36
Sat 5	13.45	23.69	21.42	10.63	10.97	0.023	7.97	0.00	0.94	3.38
				Tree 2181						
Main	6.25	-	-	11.46	4.80	0.061	9.66	0.00	0.70	3.90
Sat 1	7.56	10.64	6.62	10.70	6.53	0.061	8.79	0.00	0.44	1.25
Sat 2	8.37	11.02	13.31	10.54	7.32	0.061	7.07	0.00	0.98	1.79
Sat 3	8.37	19.33	20.04	10.36	7.56	0.061	8.23	0.00	0.72	1.54
Sat 4	8.53	12.18	9.71	10.74	7.15	0.061	8.87	0.00	0.49	1.44
Sat 5	8.85	17.34	10.50	10.81	7.24	0.061	9.50	0.03	0.21	1.38

accreted from satellites and at which radii this mass is deposited. In a kinematic analysis, we investigate whether stars that have been formed in the satellites can be distinguished from stars that originated from the central galaxy by an observer, located in the central disc at the solar radius $R_\odot \approx 8$ kpc.

For this we use dark matter merger trees drawn from the N-body simulation, that has been presented in chapter 3. This simulation employed cosmological parameters that match results from WMAP-3 and was run in a periodic box with a side length of 100 Mpc. Haloes have been identified with a FOF algorithm and the merger trees were created by linking every halo to its most massive progenitor. The dark matter merger trees are then used as the input for the SAM which

yields galaxy merger trees. As we are interested in systems that experience only minor mergers after $z = 1$, we select 10 trees with a final halo mass of $M_h \approx 10^{12} M_\odot$, that have only mergers with a mass ratio of $\mu < 0.2$. The properties of these trees are presented in Table 5.2. As a starting redshift we use $z_i = 1$ which corresponds to a cosmic time of $t = 6.25\,\mathrm{Gyr}$. We employ the fiducial model parameters presented in Table 5.1 and simulate all trees up to a redshift $z = 0$ with the SPH code GADGET-2.

All simulations were performed on the PIA cluster of the Max-Planck-Institute for Astronomy. Using 32 processors in parallel, one merger tree can be simulated within 100 hours (i.e. four days) at a resolution that corresponds to $\sim 200\,000$ stellar particles in the central galaxy. A full cosmological simulation of a MW-like system with a comparable resolution (e.g. Governato *et al.* 2010), which is typically run on ~ 128 processors, needs to be run for ~ 100 days. Per processor, this implies a run time that is 100 times larger than what is needed in our approach. As a result we are able to simulate far more systems than with the traditional method and are thus able to make statistical predictions. In this way, uncertainties due to the resolution, recipes used in the SAM and implementations of physical processes in the simulation code can be reduced.

The surface density for a typical merger tree (*2126*) is shown in Figures 5.2 (face-on projection) and 5.3 (edge-on projection) for the stellar component (upper panels) and the gaseous component (lower panels). The central galaxy evolves in isolation for $\sim 1\,\mathrm{Gyr}$ until the first two satellites enter the halo. These satellites pass the central galaxy at a pericentric distance of 55 and 90 kpc, respectively. While the first satellite continues orbiting around the central galaxy and subsequently loses angular momentum and energy, which leads to a decrease of the pericentric distance, the second satellite has enough orbital energy to leave the main halo again. Near the end of the simulation the last three satellites enter the halo and pass the central galaxy.

During the evolution of the simulation, the stellar disc of the central galaxy is heated which results in an increase of its thickness. At the same time, a stellar halo forms as a result of two processes. First, due to the close passage of the satellites, some stars in the disc are scattered out of the disc, as energy and angular momentum is transferred. Second, some satellite stars are accreted onto the central galaxy. These stars still retain some of the angular momentum of the satellite such that they do not settle in the disc, but in the halo. Additionally, we are able to identify several stellar streams which originate from the destruction of the satellites. However, due to the limited resolution in this pilot study, the number of particles in these streams is not very high, so that a detailed study is not possible. This limitation can be overcome in future studies by increasing the parameter $N_\mathrm{res,sat}$, so that there are more particles in the satellites and thus more particles in the streams.

In the gaseous component we can identify a lot of structures. The hot gaseous halo of the main system is very smooth while the system evolves in isolation. However, at the centre, close to the disc, gravitational instabilities lead to the formation of small clouds that accrete onto the disc, preferentially in its plane. Most of the accretion of cold gas is due to these clouds. When
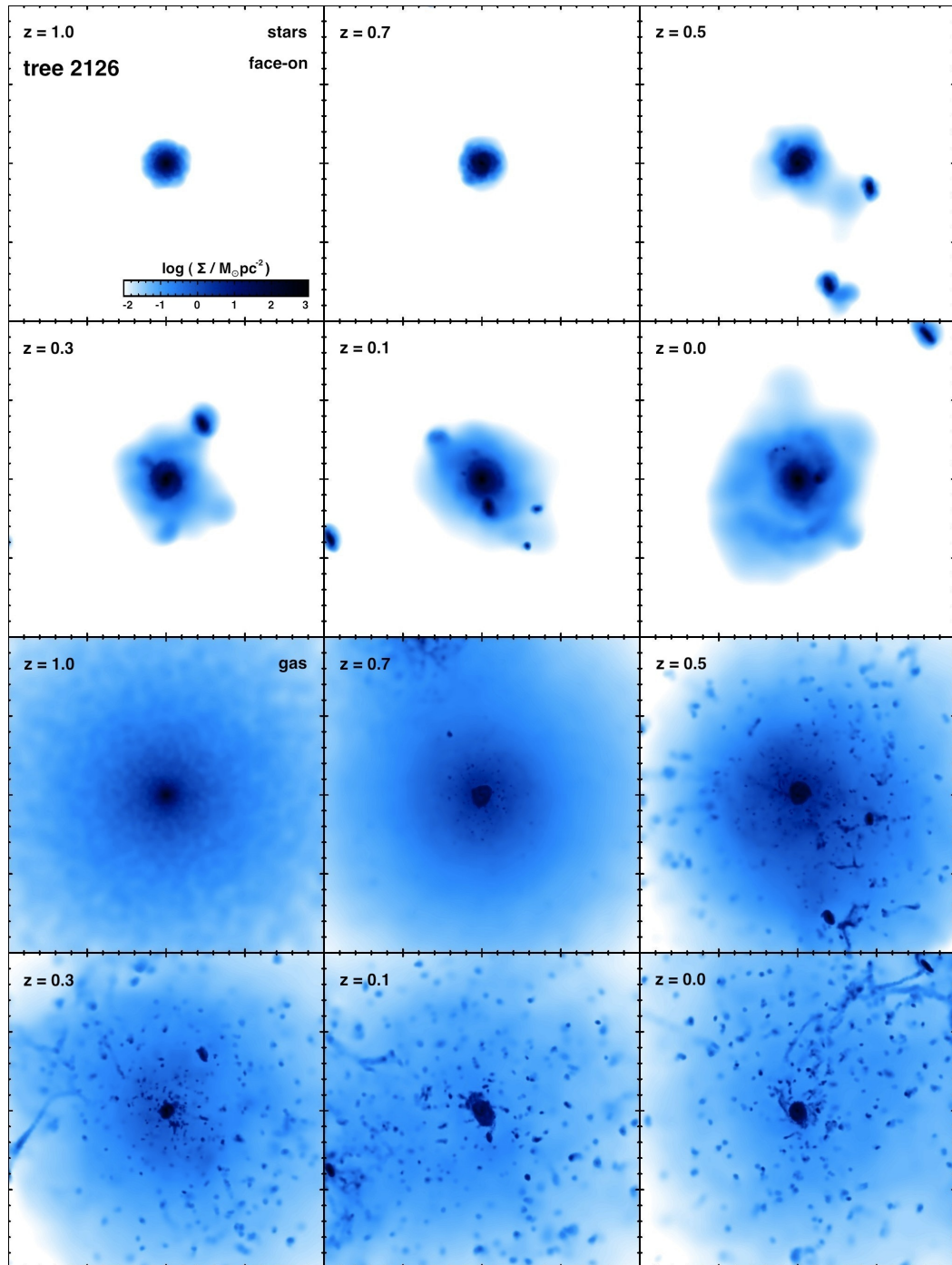
Figure 5.2 Projected surface density for the stellar component (upper two rows) and the gaseous component (lower two rows) for the typical merger tree *2126* as viewed from face-on. Each panel measures 200 kpc on a side and the redshift is displayed in the upper left corner of each panel.

the satellite galaxies enter the halo, much of their cold gas is stripped and is drawn to the centre of the system. Thus some of the stars in the central galaxy form from gas that has been removed
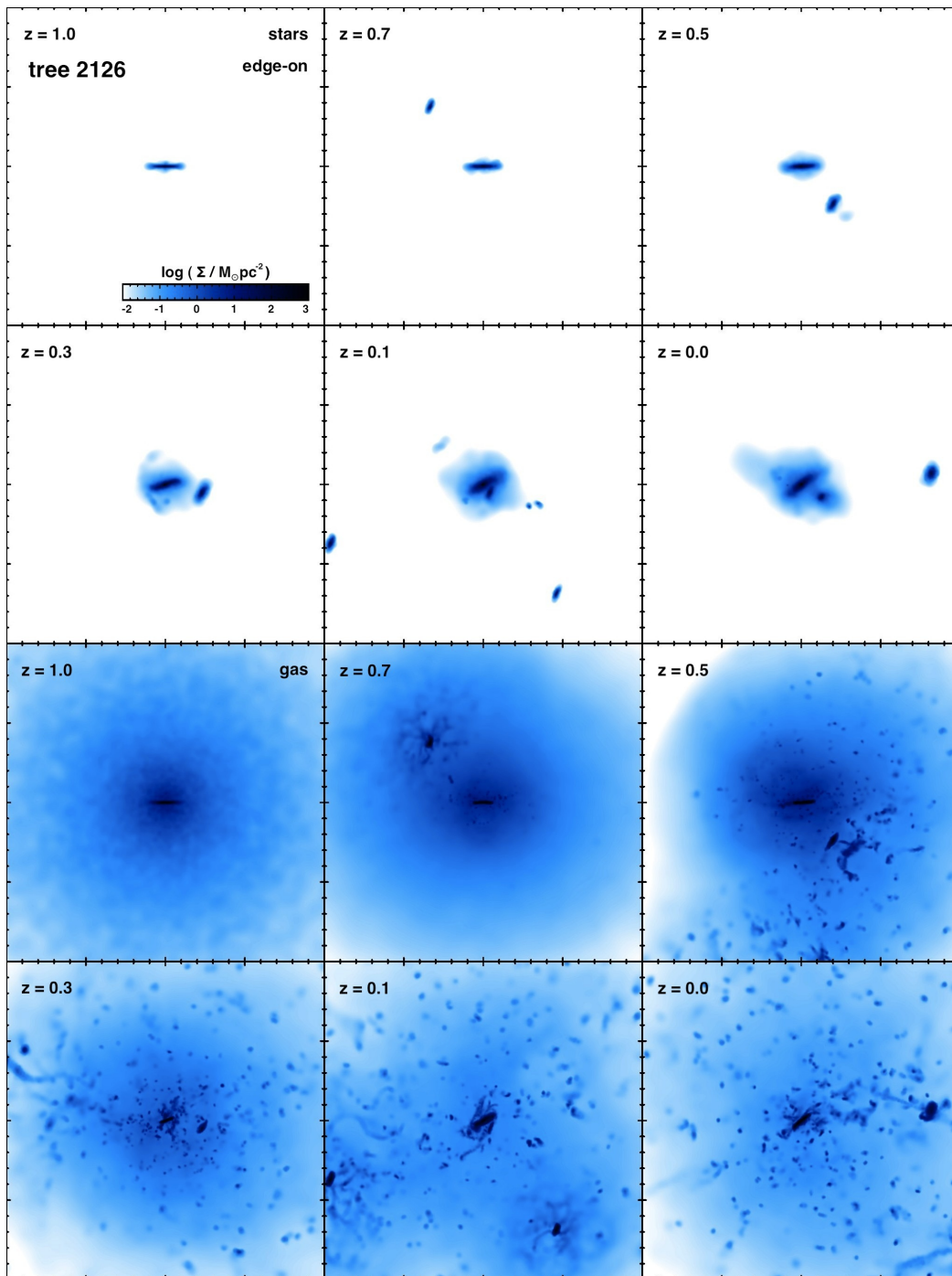
Figure 5.3 Similar to Figure 5.2, but for an edge-on projection.

from satellites and was accreted onto the central gaseous disc. Interestingly, the most massive clouds that are stripped from the satellites are able to form stars, although there is no dark matter overdensity associated with them. At the end of the simulation there are many clouds of cold gas
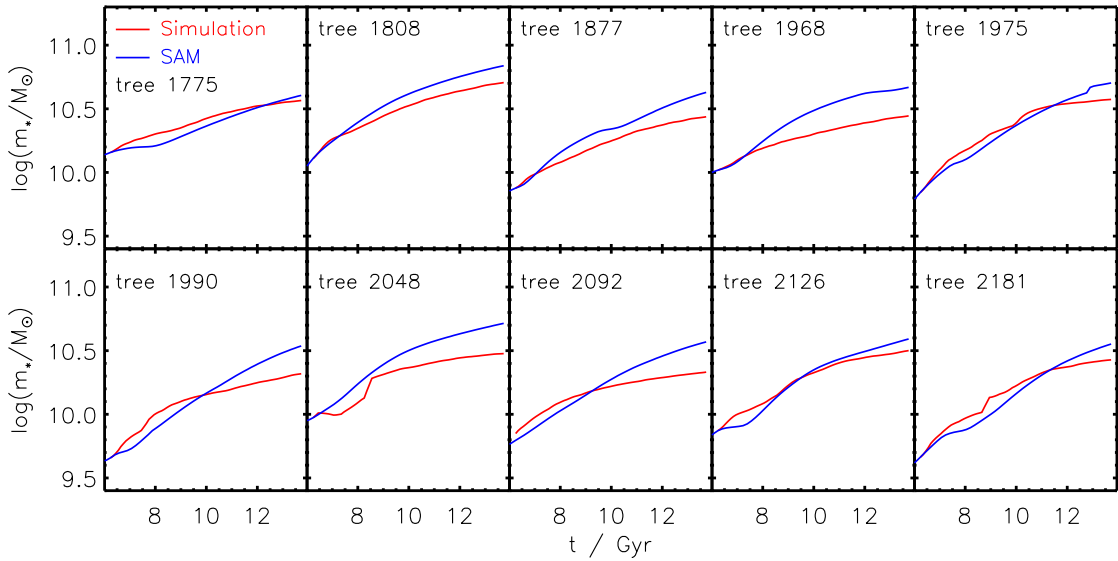
Figure 5.4 Evolution of the stellar mass in the central galaxy in each merger tree. The measured stellar mass in the simulation (red line) is compared to the prediction by the SAM (blue line).

orbiting around the centre of system at velocities of the order $v \sim 150 - 200 \, \mathrm{km \, s^{-1}}$.

5.3.1 Properties of the central galaxies

As a first step, we analyse the properties of the central galaxy in each merger tree and their evolution during the course of the simulation. Arguably, the most important quantity is the stellar mass of the central galaxy, which is also simple to measure in the simulation. For this we identify all stellar particles within the virial radius of the main halo, that are gravitationally bound with respect to the centre of the halo (i.e. their total energy is negative). From this set of particles we remove those particles that are more tightly bound to any satellite within the virial radius (i.e. the total energy with respect to the halo centre is larger than the total energy with respect to the centre of the satellite). The total stellar mass is then the summed mass of the remaining particles. This analysis is done for every output time.

We plot the resulting evolution of the stellar mass for all merger trees in Figure 5.4. The results of the simulations are given by the red line, while the semi-analytic prediction is given by the blue line. We find that all systems increase their stellar mass and have a final stellar mass that is a more than twice of the value at $z = 1$. The stellar masses found in the simulation at $z = 0$ range from $\log(m_*/M_\odot) = 10.3$ to 10.7, while the majority of systems has a stellar mass close to $\log(m_*/M_\odot) = 10.5$. These results are in excellent agreement with those obtained by Moster *et al.* (2010) using a statistical halo occupation model. For some merger trees the prediction by the SAM agrees very well with the result of the simulation (e.g. the trees *1775*, *1975* and *2126*), while for other trees the semi-analytic prediction for the final stellar mass is much higher than what we
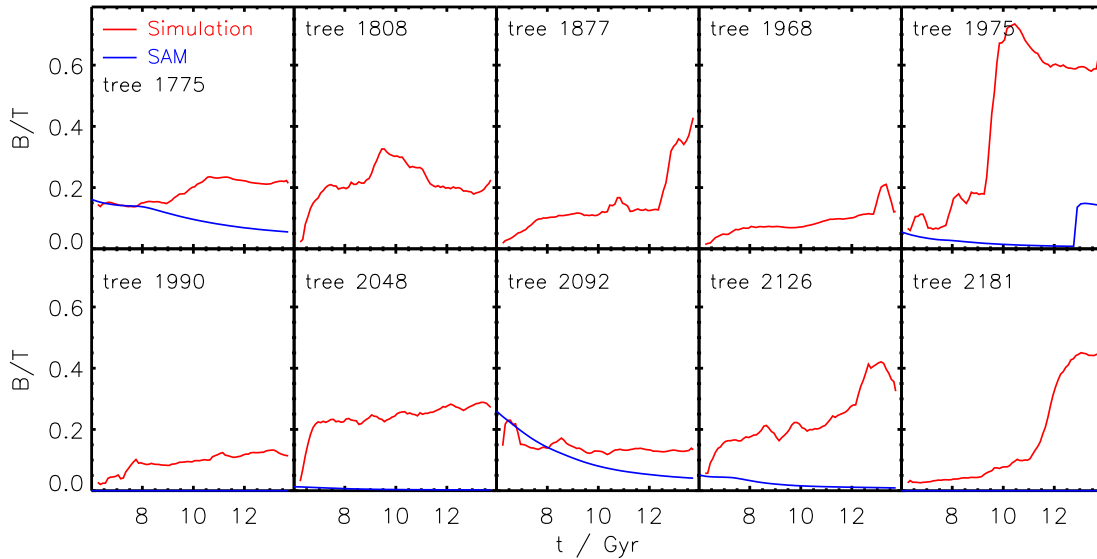
Figure 5.5 Bulge-to-total ratio of the central galaxy in each merger tree. The measured B/T in the simulation (red line) is compared to the prediction by the SAM (blue line).

find in the merger simulation (e.g. the trees *1968*, *1990* and *2048*). We note that the semi-analytic values for the stellar mass tend to exceed the average stellar mass for a halo of mass $10^{12} M_\odot$.

In the evolution of the stellar mass, we see that at some times the mass increases quickly in a short time interval. This is not due to an increased SFR when a satellite passes the central galaxy, but is a result of the accretion of a satellite. Examples can be seen for tree *1975* ($t = 10$ Gyr), tree *2048* ($t = 8$ Gyr) and tree *2181* ($t = 9$ Gyr). Overall however, we find that most stars in the central galaxy have formed from the cold gaseous disc that is accreted from the gaseous halo (in-situ formation), and only few stars in the central galaxy originate from accreted satellites (ex-situ formation).

The next property we study is the central galaxy's morphology. For this we compute the bulge-to-total ratio B/T of the central galaxy as a function of time with the method outlined in section 4.3.3. The stellar particles are decomposed into a spheroidal and a disc component by computing $L_z/L_{\rm circ}$, where L_z is the angular momentum along the spin axis and $L_{\rm circ}$ is the angular momentum the particle would have on a circular orbit at the same radius. The spheroidal component is then distributed around a value of 0, while the disc component is centred at 1, and we are thus able to distinguish between both components. The resulting B/T is plotted in Figure 5.5 for all merger trees. The red lines show the results of the simulations while the blue lines give the result of the SAM. As we can see, almost all of the central galaxies are disc dominated systems ($B/T < 0.5$) at the end of the simulation. Only the merger tree *1975* leads to a bulge dominated system at $z = 0$. This shows, that minor mergers are in general not able to transform disc galaxies into elliptical galaxies, but a major merger is needed.

Another interesting effect is that all systems built up a bulge component. For most galaxies this process involves the quick formation of a spheroidal component due to the close passage of a satellite, followed by a rather slow growth phase. In the quick growth phase, the passing satellite transfers energy and angular momentum to some of the disc stars which are then transferred into the bulge component, while at the same time some of the satellite's stars are stripped and captured by the potential well of the central galaxy, such that they end up in the bulge. The same effects happen when a satellite is finally merging onto the central galaxy, with the difference that much more material is transferred into the bulge. The slow growth phase on the other hand is a result of gravitational instabilities in the disc and the long range forces of the satellite population. In this phase the bulge component grows slowly at a rate that is comparable to the growth rate of the disc, such that B/T is roughly constant.

If we compare the results of our simulations to the predictions of the SAM, we see that bulge component is always much smaller in the SAM. This has two reasons: the first is the neglect of the slow growth phase, i.e. the bulge mass in the SAM only grows as a result of a merger between satellite and central galaxy. While the central galaxy evolves passively, the bulge component does not grow, even if a satellite passes closely to or through the centre. The second reason is that the recipe, used to compute the mass fraction of the disc which is transferred to the spheroid in a galaxy merger (see section 3.3.3), only considers mergers with a minimum mass ratio of $\mu = 0.1$. As a consequence the bulge mass computed by the SAM only increases, for a small number of mergers. This small growth is not sufficient compared to our high resolution simulations. On the other hand, we note that the specific set of merger trees we have employed in the simulations, is not a statistical, cosmological sample. Instead, we have focused on systems that have many minor mergers after $z = 1$. These are the systems that are especially challenging for the semi-analytic recipe, as they include many satellites that perturb the central galaxy while orbiting. As this effect is not considered in the SAM, but is prevalent in our simulated merger trees, the semi-analytic predictions for B/T deviate from the simulations. While this is problematic for the sample used here, the effect is rather negligible for a large statistical sample, such that the SAM is able to predict the average B/T in agreement with observations. However, as a result we find that the recipe in the SAM can be improved by a detailed analysis of the bulge formation in our simulations, in order to model these specific cases correctly. This is only one example where our new method can be helpful in order to improve existing models for complex physical processes.

The last property of the central galaxy we study, is the evolution of the scale parameters of the stellar components, i.e. the scalelength and height of the stellar disc and the scaleradius of the bulge. In order to measure these quantities in our simulations, we first use the decomposition of the particles into disc and spheroidal components. For the disc component we then compute the face-on surface density profile by projecting all stellar central galaxy particles onto the disc plane and averaging azimuthally. Finally we fit an exponentially declining function to the profile from which we obtain the disc scalelength. Similarly, we compute the projected edge-on surface
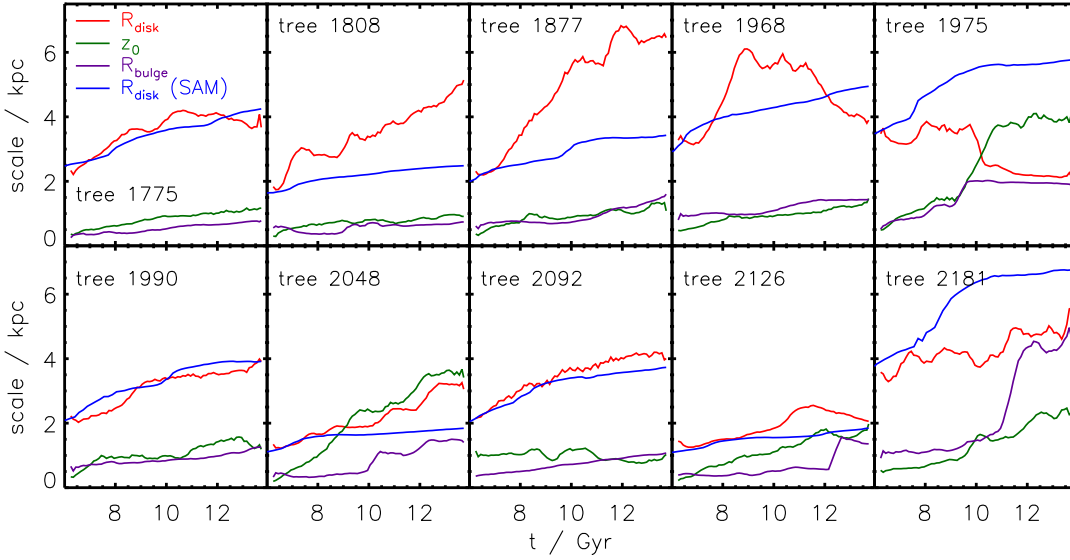
Figure 5.6 Scale parameters of the central galaxy in each merger tree. The red line shows the measured disc scalelength in the simulation, the green line shows the measured disc scaleheight and the purple line shows the measured bulge scalelength. The prediction for the disc scalelength by the SAM is added for comparison (blue line).

density at a radius of $R = 8\,\mathrm{kpc}$, and fit a sech^2 function to it from which we obtain the disc scaleheight. For the bulge component we derive the projected surface density profile (averaging over 10 random projections) and determine the half mass radius, which is defined as the radius at which the enclosed mass is equal to half of the total bulge mass. We employ this radius as the scalelength of the bulge.

We plot the resulting scaleparameters in Figure 5.6 for all merger trees. The disc scalelength R_{disc} is given by the red line, the disc scaleheight z_0 is given by the green line, and the bulge scalelength R_{bulge} is given by the purple line. For comparison we included the prediction for the disc scalelength by the SAM which is shown by the blue line. For some systems, the scalelength in the simulation and the SAM agree very well (trees *1775*, *1990* and *2092*), while for other systems the scalelength predicted by the SAM differs from the one found in the simulation (trees *1808*, *1877* and *1975*). Interestingly, while the scalelength in the SAM always increases with time, the scalelength measured in the simulation can both increase and decrease. Overall, we find a broad range of scalelengths for MW-like systems, which is also found observationally (Barden *et al.* 2005).

The disc scaleheight evolves slowly with time, as long as no satellite merges with the central galaxy. For most systems the ratio between the scaleheight and scalelength is roughly constant throughout the simulation. Final scaleheights range from $z_0 = 0.6$ to $1.2\,\mathrm{kpc}$, consistent with results form observations of MW-like systems (Schwarzkopf & Dettmar 2000; Yoachim & Dalcanton 2006). In some merger trees (trees *1975* and *2048*), the thin disc is completely destroyed

due to mergers and only a thick disc with a final scaleheight of $\approx 4\,\mathrm{kpc}$ is remaining. The gradual built-up of the bulge components results in scalelength of $R_{\mathrm{bulge}} = 0.5 - 1.5\,\mathrm{kpc}$ at $z = 0$. If a galaxy merger occurs, however, the scalelength quickly increases and reaches higher values (e.g. trees *1975*, *2048* and *2181*). In this way final bulge sizes of up to $4\,\mathrm{kpc}$ can be reached.

5.3.2 Properties of the satellite galaxies

After having studied the properties of the central galaxies and their evolution, we now focus on the properties of the satellite population. In order to do this we first determine the centre of every satellite in every time-step by iteratively moving spheres of radius $1\,\mathrm{kpc}$ until the centre of mass is equal to the centre of the sphere. We then find all particles belonging to a satellite, by identifying those particles that are gravitationally bound with respect to the centre of the satellite, and remove those particles that are more tightly bound to the central galaxy or any other satellite. For every satellite we sum the stellar mass, the cold gas mass and the SFR of its constituent particles and compute the distance to the central galaxy.

We plot the results of this analysis in Figure 5.7 for every merger tree. The top panels show the distance of the satellites to the central galaxy. In the second, third and fourth row, the evolution of the stellar mass, the specific SFR (i.e. the SFR divided by the stellar mass of the satellite), and the cold gas mass are shown. Different colours represent the different satellites. We first study the orbits of the satellites and find that while most satellites orbit within the main halo during the simulation, some satellites only pass the central galaxy once and leave the main halo afterwards. In tree *1968* for example, satellite 2 passes the central galaxy at a distance of 60 kpc, moves away from the central galaxy almost reaching the virial radius of the halo and then returns to pass the central galaxy again at the end of the simulation. Satellites 1 and 3 on the other hand pass the central galaxy once at the start of the simulation, and then leave the halo and never return. This is in disagreement with the common assumption used in SAMs, that satellite galaxies always remain in the main halo once they have entered it. We can also identify some galaxies that lose all of their angular momentum and merger with the central galaxy before the end of the simulation. Examples are satellites 1 and 3 in tree *1975* and satellite 5 in tree *2181*. There is even one satellite that has a nearly circular orbit and spirals onto the central galaxy with a constantly decreasing distance (satellite 2 in tree *2048*). Overall we find that most satellites with a mass ratio of $\mu \lesssim 0.1$ entering the main halo after $z = 1$, have not merged with the central galaxy until $z = 0$, but continue orbiting.

For the evolution of the stellar mass the satellites can be divided into three categories. In the first type, the satellite has few cold gas when it enters the main halo. In addition to this, its hot gaseous halo is stripped at this time due to ram pressure, and it is not able to accrete new gas onto the disc and form stars. When such a satellite passes the central galaxy, tidal forces act on it and remove parts of its stellar mass (i.e. stellar mass is stripped). As the satellite continues orbiting
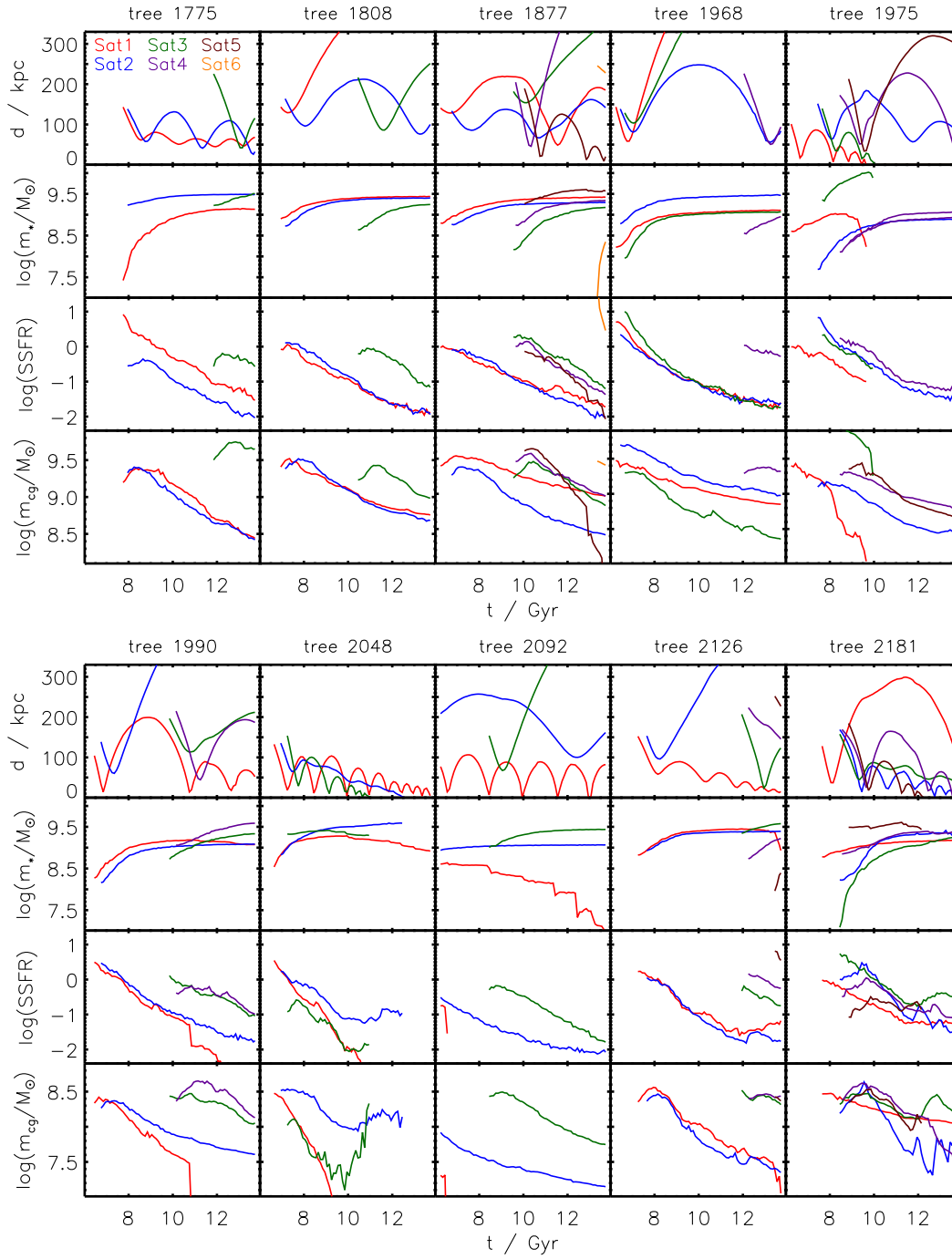
Figure 5.7 Satellite orbits, stellar masses, specific SFRs and cold gas masses in each merger tree. The top panels plot the distance between satellites and central galaxy as a function of time. The second row panels show the evolution of the stellar mass of each satellite. The third row panels give the specific SFR while in the fourth row panels, the evolution of the cold gas mass is shown. Different colours represent different satellites as indicated in the upper left panel.

the central galaxy it loses a fraction of its stars in every close encounter. Thus its stellar mass decreases in steps until it finally merges with the central galaxy. An example of such a galaxy is satellite 1 in the merger tree *2092*. It has no cold gas left when it enters the main halo and loses parts of its initial stellar mass of $\log(m_*/M_\odot) = 8.6$, during every close passage. Due to the low initial mass it loses angular momentum on a low rate such that it is still orbiting at the end of the simulation. At this point however, almost all of its stellar mass has been stripped.

In the second category, the satellite has a considerable cold gaseous disc when it enters the main halo, but has few or no close encounters, and might even leave the main halo again. These satellites are even able to accrete some gas of their hot halo before it is stripped. As a result they are able to form stars at a high rate while orbiting the central galaxy. When their hot gas is stripped and only cold gas is left, this SFR exponentially declines so that the satellites reach a maximum stellar mass. Since these satellites have few close encounters (usually at a pericentric distance that is much larger than their size) the stellar mass that is stripped is negligible. Even if they lose some of their stellar mass, the mass loss is compensated by star formation such that the stellar mass always increases. Examples of such satellites are satellite 1 in tree *1775*, satellites 1 and 2 in tree *1808* and satellite 2 in tree *2048*.

The third type of satellite galaxies is a combination of type one and two: the galaxy is able to form stars from its cold gaseous disc and thus increases its stellar mass until it gets close to the central galaxy. At this point the mass loss rate from tidal stripping is larger than their SFR which results is a net loss of stellar mass. As a result the stellar mass increases when such a satellite enters the main halo, reaches a maximum value while orbiting, and then subsequently loses mass until it merges with the central galaxy. Typical galaxies of this type are satellite 1 in tree *1975* and satellite 1 in tree *2048*. Independent of type, most satellites lose their hot gaseous halo as soon as they enter the main halo due to ram pressure. As a consequence, the amount of cold gas constantly decreases due to star formation. Only few satellites are able to accrete gas from the main halo, which results in a monotonically decreasing cold gas mass for most satellites.

5.3.3 Contamination by satellite stars

In this last study we address the question, how many stars in the central galaxy originate from satellites, at which radii they are accreted, and whether it is possible to distinguish these stars from those that have been formed in the central galaxy. As a first step, we identify all stars that have formed in a given satellite. This sample consists of those stars that were created in the initial conditions of the satellites at the start of the simulations, and the stars that form within a satellite during the simulation. For this we track the centre of each satellite, and for every new-born stellar particle within the tidal radius of the subhalo, we check whether this particle is more tightly bound to the satellite centre or to the centre of the main halo. If it is bound more tightly to the satellite, we include it in the list of particles that formed in this satellite. In this way we are able to locate
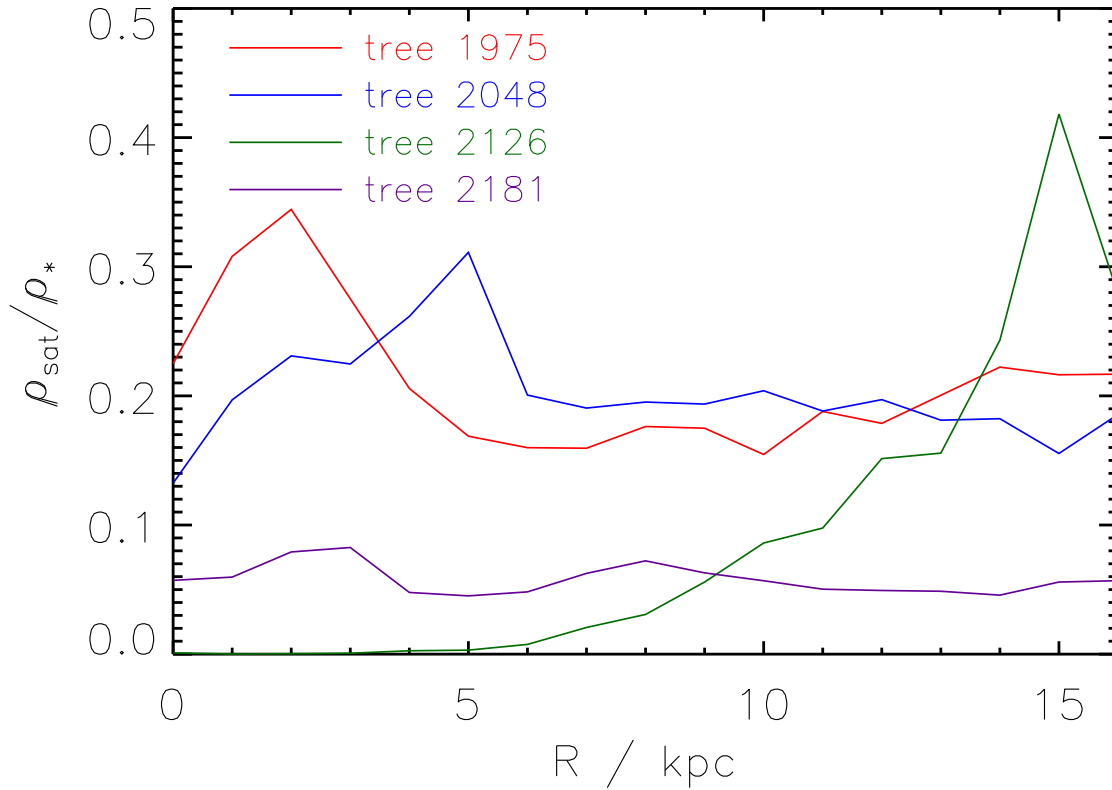
Figure 5.8 Contamination of the central galaxy by satellite stars. The stellar mass of all satellite particles is divided by the total stellar mass in rings around the disc axis centred at the disc centre. The four lines show the results at $z = 0$ for the four merger trees with the highest satellite contamination.

all stellar particles at $z = 0$, that originate from satellite galaxies.

We now measure the total mass of the stellar satellite particles and the total stellar mass in rings in the plane of the central galaxy centred around the disc axis. Each ring has a height of $\Delta z = 4 \, \text{kpc}$ and a width of $\Delta R = 1 \, \text{kpc}$. In each ring, we compute the contamination by satellite stars by dividing the total mass of stellar satellite particles by the total stellar mass. This analysis is done at $z = 0$. The results for the four merger trees with the highest satellite contamination are shown in Figure 5.8. Our results show that some systems can have a contamination by satellite stars of about 20 per cent. Locally, the relative abundance of satellite stars can be even higher with up to 50 per cent or more. In all other merger trees the relative density of satellite stars was lower than in the systems shown here. As we can see, in some systems the satellite stars are mostly located at the galactic centre (tree *1975*), in some systems the amount of satellite stars is highest at large radii (tree *2126*), while in other systems the satellite stars are equally distributed within the galaxy (trees *2048* and *2181*). Overall, there does not seem to be a preferred radius, at which satellite stars are located, since this strongly depends on the initial orbits of the satellites.

Finally we investigate whether it is possible to distinguish stars that originate from satellite

galaxies (ex-situ formation) and stars that are born in the central galaxy (in-situ formation) employing a purely kinematic analysis. This question has been addressed by previous studies: Helmi & White (1999) employed numerical simulations of the disruption of satellite galaxies in a constant analytic potential and found that the accretion of satellite galaxies can leave kinematic fossil signatures in the present-day components, which are clearly observationally detectable. Especially the *GAIA* mission (Lindegren & Perryman 1996) will provide very precise astrometry, so that the full six-dimensional phase-space information will be available. In a related study, Helmi & de Zeeuw (2000) analysed the space of integrals of motion after a numerical simulation with a fixed, analytic potential. The total energy E, angular momentum L and angular momentum along the spin axis L_z are conserved quantities for collisionless components. In the initial distribution the particles of each satellite form a clump not only in configuration space, but also in the integrals of motion space, as all particles in a satellite have a similar energy and a similar angular momentum. If E, L and L_z are also conserved for every particle (or evolve only slightly) during the course of the simulation, their initial clumping has to be present even after the satellites have been disrupted. Thus in the integrals of motion space the satellite particles remain well distinguishable. Therefore Helmi & de Zeeuw (2000) were able to identify disrupted satellite particles by using a FOF algorithm to connect particles in the integrals of motion space.

However, as the central galaxy and main halo were only represented by a static, analytic potential in their simulations, this result is a necessary consequence. The problem with a static potential is that the satellite particles are not able to interact with it, i.e. they are not able to transfer energy and angular momentum to it. In reality, the potential is created by gas, stars and dark matter particles, such that satellite stars are well able to get rid of their energy and angular momentum which will alter their position in the integrals of motion space. Therefore an analytic potential is not ideal to study the evolution of satellite stars. Instead the global potential should be modelled with particles, thus our simulations of merger trees are ideal for this kind of study. At $z = 0$ we compute E, L, L_z and $E_z = mv_z^2/2 + m\Phi(z, R) - m\Phi(0, R)$ for every particle. The approximate integral of motion E_z can be thought of as the contribution to the total energy due to a position above the disc plane or a velocity parallel to the disc axis and is roughly conserved for axisymmetric systems.

In Figure 5.9 we present the location of all satellite particles in the integrals of motion space for the tree *2048*. In this tree, two satellites have been accreted onto the central galaxy and one satellite is close to being accreted at $z = 0$. The four panels on the left-hand side show the four projections of the integrals of motion. The symbols of different colours represent stellar particles of different satellites while the contours indicate the probability of finding a central galaxy particle. In the panels on the right-hand side the spatial distribution of satellite particles is shown. The particles of satellite 2 have transferred much of their energy and angular momentum to the central galaxy and the main halo during orbiting. As it had enough time to reach an equilibrium with particles of the central galaxy, its particles trace the central galaxy distribution in the integrals of motion space. Therefore it is impossible to distinguish this satellite from the stars that formed in the
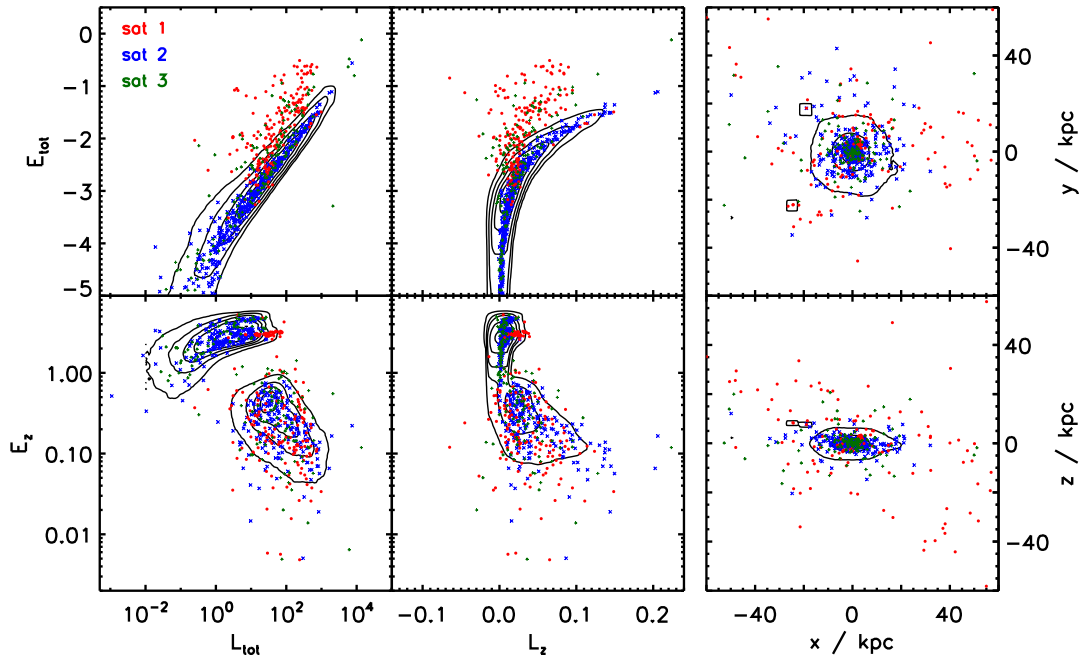
Figure 5.9 Location of all satellite particles in the integrals of motion space for tree *2048*. The symbols of different colours represent stellar particles of different satellites (note that only 1 per cent of all satellite particles are shown). The contours indicate the 10, 30, 50, 70 and 90 per cent probability of finding a central galaxy particle in the enclosed area. In the right-hand side panels the spatial distribution of satellite particles is shown. Energy units are $10^{10} M_\odot \, \text{km}^2 \, \text{s}^{-2}$ and angular momentum units are $10^{10} M_\odot \, \text{kpc} \, \text{km} \, \text{s}^{-1}$.

central galaxy. Satellite 3, however, is still distinguishable from the central galaxy, especially in the (E,L) and (E,L_z) projections, although it has been accreted already 3 Gyr before the end of the simulation. Here we see that for a fixed amount of angular momentum the satellite particles have been able to retain more energy. Similarly, satellite 1 can be distinguished from the central galaxy particles. As this satellite has not fully merged yet, its particles still have more total energy than the particles of the central galaxy. However, it is not possible to distinguish satellite 1 from satellite 3 in any integrals of motion projection. Interestingly, the time at which a satellite merges onto the central galaxy, has less impact on whether its stars can be distinguished from the stars of the central galaxy, than the orbit of the satellite. While satellite 1 merges much earlier than satellite 2, it has a more radial orbit which allows its stars to retain a different position in the integrals of motion space than the central galaxy stars.

We are thus able to identify some of the satellite stars in a kinematic analysis, if phase-space coordinates for all stars in the galactic system are available. Observationally, however, it is very difficult to obtain these quantities for some locations, especially for the stars near the galactic centre, as these are obscured by dust. Moreover the stars at the other side of the galactic plane can hardly be observed. Therefore it is more useful to study the integrals of motion space in
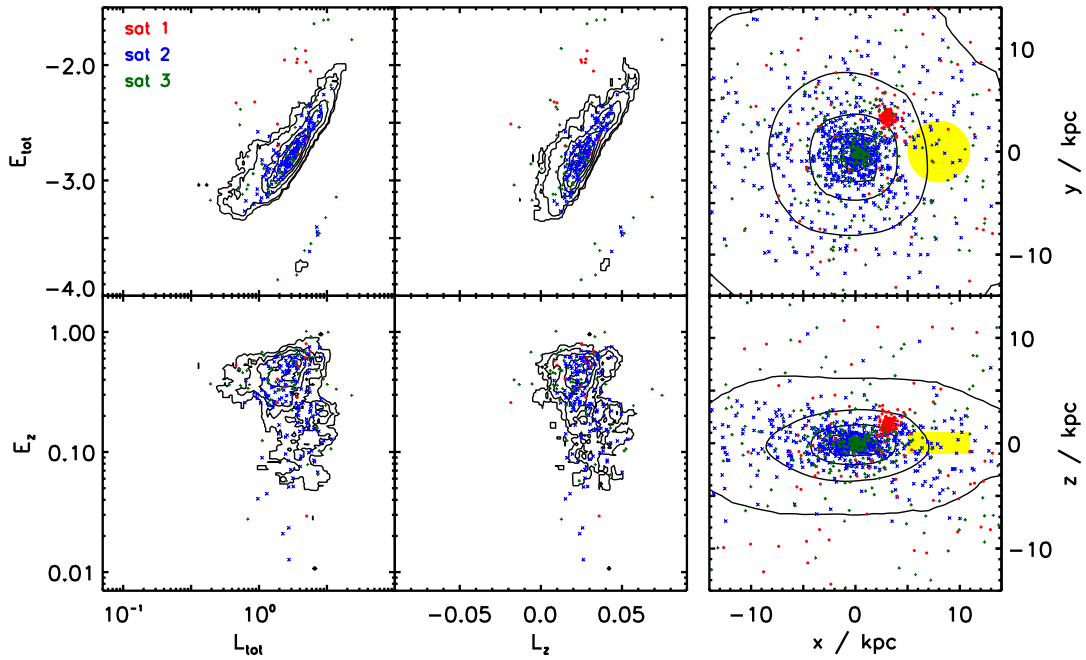
Figure 5.10 Location of the satellite particles in the solar neighbourhood in the integrals of motion space (tree *2048*). The symbols of different colours represent stellar particles of different satellites and the contours indicate the 10, 30, 50, 70 and 90 per cent probability of finding a central galaxy particle in the enclosed area. For the integrals of motion projections only particles in a cylinder with radius $R = 3\,\mathrm{kpc}$ and height $\Delta z = 2\,\mathrm{kpc}$, centred at $(x, y, z) = (8\,\mathrm{kpc}, 0, 0)$ have been used. This cylinder is indicated by the yellow area in the right-hand side panels.

the solar neighbourhood, as this is the region, where the observed phase-space coordinates can be measured most accurately. For this reason, we plot the integrals of motion projections for all stars in the solar neighbourhood in Figure 5.10, i.e. all stars in a cylinder with radius $R = 3\,\mathrm{kpc}$ and height $z = 2\,\mathrm{kpc}$ centred at the solar position $(x, y, z) = (8\,\mathrm{kpc}, 0, 0)$. Again, the symbols of different colours represent stellar particles of different satellites and the contours indicate the probability of finding a central galaxy particle located in the cylinder around the sun. In the right-hand side the spatial location of all satellite particles is shown, and the yellow region indicates the cylinder.

The particles of satellite 2 are clearly indistinguishable from the central galaxy in all projections of the integrals of motion space. This shows that it is impossible for some accreted satellite galaxies to separate their stars from the stars born in the central galaxy through a pure kinematic study. For these satellite stars it is necessary to invoke additional information, such as their chemical fingerprint. If their metal content differs from the central galaxy stars, it indicates that the star formed from gas with a different metallicity. This means that it is likely to be born in a satellite which had a different amount of star formation and SN feedback. For the other two satellites the situation is less problematic, especially in projections involving the total energy. Independent of
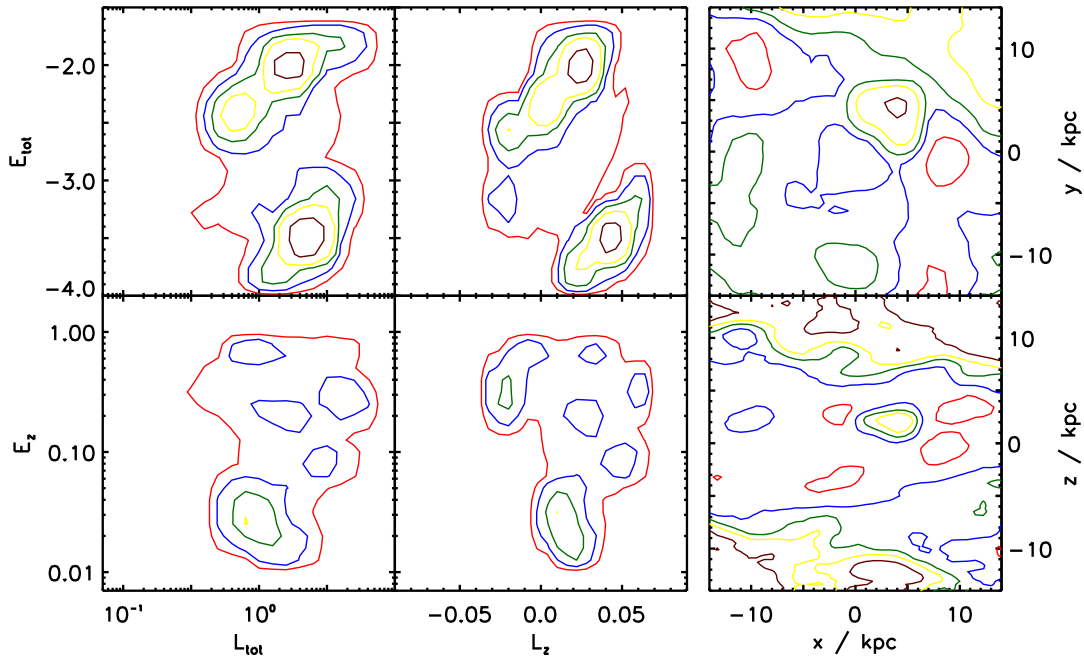
Figure 5.11 Probability that a given star in the integrals of motion space stems from a satellite (tree *2048*). The contours indicate the 10 (red), 30 (blue), 50 (green), 70 (yellow) and 90 (brown) per cent probability.

their angular momentum, the stellar particles of these satellites have retained a higher total energy than the central galaxy stars. However, it is virtually impossible to distinguish between particles of satellite 1 and 2, as both occupy the same regions in the plots. Therefore we conclude that even if a star can be identified as a satellite star due to its integrals of motion, we are not able to infer from which satellite a star originated or how many satellites have been accreted onto the central galaxy.

In order to be able to better identify satellite particles we plot the probability of finding a satellite star at a given location in a integrals of motion projection in Figure 5.11. The probability has been computed by dividing the number of satellite particles in a region by the total number of stellar particles in this region. For the projections involving the total energy, we can identify two regions of high probability. For a given angular momentum satellite stars can be either found at higher or lower energy then the typical energy of a central galaxy particle. For the projections involving E_z this distinction is more difficult, but our analysis indicates that satellite stars preferentially have a lower E_z than the central galaxy stars. In configuration space we see that the probability of finding an accreted satellite star is highest in the outer parts of the disc and in the halo, or if a satellite has not been disrupted yet satellite stars locally dominate.

In summary we can say that we have tested our new method in studies of MW-like systems and that our method showed clear advantages over other methods. As only the particles in the

regions of interest are used in the simulations, the time that is need for a run is much lower than in traditional cosmological simulations, such that more systems can be simulated in the same time. On the other hand, our method is able to incorporate a high resolution and predict galaxy structures on small scales, which is not possible with a SAM. In this first application we have used our new method to study the evolution of MW-like galaxies since $z = 1$, and find good agreement with observations for the total stellar masses and disc scalelengths. Studying the satellite population we were able to determine three types of satellite galaxies: one where the satellite subsequently loses stellar mass due to tidal stripping, one where the satellite constantly gains mass due to star formation, and a combination of both. Analysing the kinematic properties of the stars in the galaxy we found that only some satellite stars can be identified and distinguished from the stars born in the central galaxy. Even if a star can be attributed to an accreted satellite, it is not possible to determine in which satellite the star was born.

Chapter 6
Conclusions and Outlook

The necessary requirements for every galaxy formation and evolution model, that aims to capture the physical processes at small scales driving the transformation of the baryonic component, are a high resolution, a correct treatment of the gas physics and a cosmological background. The aim of this thesis was to develop a novel method to study the evolution of galaxies by combining semi-analytic models with merger simulations. Using the predictions of the semi-analytic model as the initial conditions for a multiple merger simulation we were able to include the cosmological background in the high resolution hydrodynamical method.

Hydrodynamical simulations of binary galaxy mergers are a very useful tool to study the evolution and morphological transformation of single galaxies due to the merger effects, although they are not representative for a certain cosmology. Instead, they can be regarded as a method to study the effects of a single encounter in a detailed manner, rather than the complete evolution of a galaxy. For these merger simulations one creates pre-formed galaxies, that are stable in isolation, with parameters drawn from a grid or motivated by observations. These model galaxies are then set on an orbit and evolved with a hydrodynamical code. We studied the effect of dissipational gas physics on the vertical heating and thickening of disc galaxies during minor mergers, i.e. mergers with a halo mass ratio of 1:10. We produced a suite of minor merger simulations for MW-like galaxies. This suite consists of collisionless simulations as well as hydrodynamical runs including a gaseous component in the galactic disc. We found that in dissipationless simulations minor mergers cause the scale height of the disc to increase by up to a factor of approximately two. When the presence of gas in the disc is taken into account this thickening is reduced by 25 per cent (50 per cent) for an initial disc gas fraction of 20 per cent (40 per cent), leading to a final scale height z_0 between 0.6 and 0.7 kpc (for a sech^2 profile), regardless of the initial scale height. We argued that the presence of gas reduces disc heating via two mechanisms: absorption of kinetic impact energy by the gas and/or formation of a new thin stellar disc that can cause heated stars to re-contract towards the disc plane. We showed that in our simulations most of the gas is consumed during the merger and thus the regrowth of a new thin disc has a negligible impact on the z_0 of the post merger galaxy. Final disc scale heights found in our simulations are in good agreement with studies of the vertical structure of spiral galaxies where the majority of the systems are found

143

to have scale heights of $0.4 \, \mathrm{kpc} \lesssim z_0 \lesssim 0.8 \, \mathrm{kpc}$. We also found no tension between recent measurements of the scale height of the MW thin disc and results coming from our hydrodynamical simulations. Even if the MW did experience a recent 1:10 merger it is possible to reproduce the observed thin disc scale height, assuming that the disc contained at least 20 per cent gas (similar to the gas fraction today) at the time of the merger. We concluded that the existence of a thin disc in the MW and in external galaxies is not in obvious conflict with the predictions of the CDM model.

Although binary mergers are a useful tool to study the evolution of a galaxy during a single encounter, they are not able to predict the typical galaxy properties at a given redshift, as the cosmological background, i.e. the merger history of each galaxy is not taken into account. For this reason, we studied the merger histories of galaxies using merger trees drawn from a large N-body simulation. We found that major mergers (1:4) are very uncommon for MW-sized haloes since $z = 1$ with only every tenth system experiencing such a merger. Although this fraction rises to 50 per cent if all mergers since $z = 5$ are considered, major mergers seem to be rather unimportant for shaping the properties of a MW-sized system. On the other hand, minor mergers are very common for these systems, as 70 per cent of them experience a 1:10 merger since $z = 1$ and the average number of 1:30 mergers is 1.5. Since $z = 5$ the number of mergers is 2 and 4.5 for 1:10 and 1:30 mergers, respectively, indicating that minor mergers are important processes for MW-sized galaxies. We further studied, whether mergers happen isolated or if they are usually multiple, i.e. if two galaxies generally have enough time to merge after their haloes have merged, before the remnant merges with another galaxy. We found that the probability for two mergers happening within a few dynamical times of the halo is always higher than the probability for a large time difference between mergers. In our merger trees, the second satellite enters the halo within three dynamical times after the first satellite entered for more than 50 per cent of all merger pairs independent of mass ratio. This indicates that multiple mergers are more common than sequences of isolated binary mergers. As a consequence, it is not sensible to focus on binary mergers, but rather on merger simulations which consider several satellites that enter the parent halo one after each other.

We further employed a SAM to study the dependence of the merger probability on baryonic properties. For the early Universe, we found that equal baryonic mass mergers are rare while they become more frequent in the late Universe. Similarly, massive galaxies tend to have more equal baryonic mass mergers and less mergers with a larger ratio, while low-mass galaxies have few equal-mass mergers and many minor mergers. We also found that primary galaxies of low mass systems tend to have very high gas fractions, while their satellites can have a wide range of gas fractions. For more massive primary galaxies, the gas fractions of the central and satellite galaxies decrease while that of the satellite still maintains a wider range. Finally we studied the merger probability as a function of morphology: the frequency of spiral mergers is very high for low-mass galaxies and very low for massive galaxies. On the other hand, mergers between ellipticals are very rare for low-mass galaxies and much more common for massive systems.

The analysis of merger probabilities showed that it is impossible to cover the whole parameter space in merger simulations, if the parameters are drawn from a grid. Instead, a simple and elegant path can be taken, if we use semi-analytic merger trees for the initial condition of galaxy merger simulations. In this way, we automatically select mergers that are highly common in the Universe. However, in order to do this, we had to extend the code that creates the particle representations of galaxies used in simulations, as smooth accretion of dark matter and the hot gaseous halo component were not taken into account before. We modelled the smooth accretion of dark matter material that is too small to be resolved as a halo in the merger trees, by placing additional dark matter particles around the halo. These particles were placed into small spherical systems with a Gaussian density profile to represent the many sub-resolution systems that are expected to be accreted. The distance to the halo centre was chosen such that they fall into the virial radius of the halo at a specified time extracted from the merger tree. In order to model a system that is stable in isolation, we computed the distribution function for a Gaussian profile and the velocity of each particle with a rejection sampling technique. We tested this smooth accretion model for an isolated MW-sized halo and found an excellent agreement with the results from a full cosmological simulation. Furthermore we verified, that the small spherical systems are quickly dissolved once they enter the halo.

In order to mode the cooling and accretion of gas onto the disc we included a slowly rotating hot gaseous halo in the initial conditions generator. So far, this component has been neglected in simulations of binary galaxy mergers, although it can contain up to 80 per cent of the total gas within the galaxy virial radius. We modelled the density distribution of the hot gaseous halo with a β-profile, that is found in galaxy clusters. The temperature profile was fixed by requiring hydrostatic equilibrium inside the galactic potential. We determined the angular momentum of the gaseous halo by relating it to the angular momentum of the dark matter halo, and demanding that the evolution of the stellar mass and the disc scale length in an isolated simulation reproduces the average values of these quantities found by observations. In our simulations we find a roughly constant SFR that is comparable to the one found in the MW. Furthermore, for the first time we presented a series of hydrodynamical simulations of galaxy mergers, both major and minor, that include the diffuse, rotating, hot gaseous halo component. We showed that adding this new component into galaxy major mergers is a key ingredient to reproduce the properties of observed elliptical galaxies, like the abundance of fast rotators and an $r^{1/4}$ surface brightness profile also at small scales. We made a detailed study of the star formation efficiency during mergers and found that the presence of a hot gaseous halo reduces the starburst efficiency compared to a quiescent evolution. Moreover we found cases where the stellar mass of the merger remnant is lower that the sum of the stellar mass of two merging galaxies when evolved in isolation. This poses a challenge to galaxy formation models which assume that a merger always leads to additional star formation. Finally we studied the effect of this new gaseous component on the vertical structure of a stellar disc during minor mergers. Because of this new gas reservoir stellar discs are more

resistant against vertical heating. This is due to the accretion of cold gas from the hot medium, that leads to the formation of new thin stellar disc.

With the extended model for the initial galaxies, we were able to develop our novel method that uses semi-analytic predictions as initial conditions for a multiple merger simulation. Choosing a starting redshift, we first created particle representations of the central galaxy at this time, and the satellite galaxies at the time when they enter the main halo. We set the mass resolution by requiring that the final number of stellar particles equals a fixed parameter, provided the final stellar mass in the SAM and the simulation are equal. The multiple merger simulation was then performed by evolving the central galaxy until the first satellite enters the main halo, at which point the particle realisation of the satellite was included in the simulation at the virial radius. After this the simulation was resumed and the procedure repeated until the end of the run. We applied our method for ten merger trees drawn from a large numerical simulation, for which the main systems are MW-sized at $z = 0$ and have no major merger after the starting redshift $z = 1$. Each of these merger tree could be simulated on 32 processors within 100 hours with a resolution that corresponds to $200\,000$ stellar particles in the central galaxy. For all ten trees we analysed the evolution of the properties for both the central galaxy and the satellite population. We found a very good agreement between the stellar mass in our simulations at $z = 0$ and values obtained by observations. Similarly, the disc scale lengths in our simulations agree well with the observed range of scale lengths. Overall we also found good agreement with the predictions by the SAM, although the bulge-to-total ratios computed by the SAM were usually much lower than the values found in the simulations.

For the satellite population we were able to identify three types: the first type has few cold gas when it enters the main halo and therefore ceases to form stars. When it passes the central galaxy, parts of its stellar mass are stripped due to tidal forces. The second type has a prominent gaseous disc and no close encounters with the central galaxy. As a result, they have a high SFR and no mass is stripped such that their stellar mass increases. The third type is a combination of the other types, such that the satellite first is able to gain mass before it gets close to the centre where it loses mass due to stripping. In a final study we addressed the question, how many stars in the central galaxy originate from satellites, and whether it is possible to distinguish these stars from those that have been formed in the central galaxy employing a pure kinematic analysis. For this we studied the space of integrals of motion at the end of the simulation of one tree and tried to identify groups of particles as fossil signatures of satellites. We found that one satellite had transferred much of its total angular momentum and total energy to the central galaxy such that it traces the distribution of central galaxy stars in the integrals of motion space. Two other satellites could be distinguished from the central galaxy, but not between each other. We thus concluded that for some stars it is not possible to identify their origin through a pure kinematic study, and even if this can be achieved, it is very hard to distinguish different satellites. For these satellite stars it is necessary to invoke additional information, such as their chemical fingerprint.

In final summary we can state that we have tested our novel method in studies of MW-like systems and that our method agrees well with predictions from SAMs and observations. Due to the combination of two techniques, hydrodynamical simulations and SAMs, our method showed clear advantages over others. As only the particles in the regions of interest are used in the simulations, the time that is need in order to model a galaxy is much lower than in traditional cosmological simulations, such that more systems can be simulated within the same time and statistical studies can be conducted. On the other hand, our method is able to incorporate a high resolution and predict galaxy structures on small scales, which is not possible with a semi-analytic galaxy formation model.

Outlook

In this thesis we developed a novel method combining semi-analytic predictions with hydrodynamical merger simulations, that allows the study of galaxy formation and evolution to small scales. However, there is still a number of model implementations that can be improved and physical processes that can be included. Full cosmological simulations have shown, that in addition to the hot cooling mode there is a process through which massive galaxies can obtain cold gas (Kereš *et al.* 2005; Dekel & Birnboim 2006). In this 'cold flow' mode, the gas is able to cool along the filaments of the large scale structure and can fuel the central gaseous disc very efficiently. This process is dominant in massive haloes at a redshift of $z > 2$. Thus one possible improvement of our method is to model these cold streams. To do this, one can use the zoom-in technique and re-simulate a chosen system at a higher resolution using only the dark matter component. This can be done in a short amount of time, as it only involves the computation of gravitational interactions. It is then possible to analyse this simulation at the desired starting redshift and identify the filaments that extend out of the dark matter halo. Finally, one can use this information and include the filaments in the hydrodynamic merger simulation such that they consist of dark matter and cold gas in a specified fraction (e.g. the universal fraction). In this way the gas can cool along the potential of the filaments and provide fuel for the central disc.

Another improvement is the inclusion of additional or more realistic feedback processes. In our simulations we have used a constant wind model, which is a fair representation of galactic winds if only systems of a comparable mass are studied. However, as the wind speed for low mass galaxies is the same as for high mass galaxies this model results in too much heating for low mass systems. A more realistic match to observed quantities is provided by more sophisticated wind models that have been developed in the last years, e.g. momentum-driven winds (Oppenheimer & Davé 2006). Another form of feedback that is not considered in our simulations yet is AGN feedback. The processes that result from gas accretion onto a central BH can provide much energy that is perhaps able to reduce the cooling of the halo after a major merger. In this way the high SFR that we found in the major merger remnant could be reduced, leading to an elliptical galaxy

that is not able to form stars. This would result in a red elliptical and could explain the bimodality in the colour-magnitude relation.

The novel method, that has been developed in this thesis opens a path to possible future applications. Not only can it be used to study galaxies in great detail, but it is also a tool to improve existing semi-analytic descriptions and even develop new ones. Possible improvements include a better model for the cooling and accretion of gas, a more detailed starburst model that captures the effects of the gaseous halo and a model that predicts the mass and size of the bulge component in better agreement to high resolution simulations. A new semi-analytic recipe can be developed that is able to predict the disc scale height and its evolution in minor mergers. In addition to the development of new semi-analytic prescriptions, our method can be employed to study the morphology of galaxies in great detail. This includes two main current research topics in galaxy formation and evolution: the origin and evolution of the fundamental plane, and stellar stripping and morphological modification of satellite galaxies. While the first topic focuses on the primary galaxy and its transformation during a merger event, the second topic focuses on the satellite population and its destruction. These two topics are thus complementary and cover both massive and low mass objects.

The origin and evolution of the fundamental plane of merger remnants

Normal elliptical galaxies populate a so-called 'fundamental plane' (FP). This FP is an observed relationship between the average surface brightness, the effective radius and the central velocity dispersion. Any one of these parameters can be derived from the other two, as together they describe a plane in their three-dimensional space. In order to explain this relation, hydrodynamical simulations have been performed and find that the FP for merger remnants is very sensitive to the gas fraction of the progenitors. The presence of gas causes more dissipation and the formation of a more compact remnant which 'tilts' the FP. Dry mergers (i.e. mergers with a low gas fraction) move galaxies along the FP. It has also been suggested that BHs have a FP which results from the FP of the host spheroids, as more compact spheroids of a given stellar mass have BH of larger mass. This implies that studying the BHFP is a key for understanding BH formation and AGN feedback.

Previous hydrodynamical simulations addressing this issue, however, have only focused on major mergers of pure disc galaxies. For this, 'grids' of parameters (gas fractions, orbits, mass, etc.) have been used which were not motivated by a cosmological context. Also, the hot halo component has been completely neglected in these studies, although the gas inflow and the associated star formation from the hot halo has consequences on the morphology and stellar mass of the merger remnant. These problems can be attended with our method as it ensures that the initial conditions for the mergers are cosmologically motivated, including orbital parameters, B/T ratios and stellar masses, as well as smooth accretion of dark matter and gas from the halo. The main

questions that can be addressed are: Do the models predict the correct galaxy FP and BHFP and what is the predicted time evolution? How do multiple mergers change the results from the binary merger case? How is the primary galaxy morphologically transformed and how does the B/T ratio change?

Stellar Stripping and morphological modification of satellite galaxies

The currently favoured CDM model of structure formation makes the specific prediction that a galaxy like the MW forms hierarchically, from a series of accretion events involving lower mass systems. This leads naturally to the expectation that the stellar halo should be formed at least in part, from disrupted accreted systems. Remnants of these disrupted satellites can be seen today as stellar streams in the MW and the Andromeda galaxy. The most spectacular example is the disrupting Sagittarius dwarf spheroidal galaxy. Thanks to the forthcoming *PanSTARRs* and *PAndAS* surveys many more will be detected in the near future. Stellar streams provide an additional test to constrain theoretical modelling of galaxy formation. On surviving satellite galaxies strong tidal fields are acting which can cause stellar stripping and a morphological modification. This 'galaxy harassment' leads to the transformation from disc galaxies into spheroidal systems.

Several numerical studies have been undertaken in recent years, attempting to understand and reproduce the observational data, and to make useful prediction for the next generation of surveys. However, very high spatial and mass resolution is needed to perform these studies: the number of particles resolving a satellite is a key ingredient to have a robust prediction for both its orbit and its mass loss. Most of the simulations so far, have only considered a static potential, neglecting the response to the satellite merging process and have not considered the gas component (neither in the host system nor in the satellite). Cosmological simulations including gas and stars, however, are not useful for these studies as they do not reach the required resolution.

Our new method can be used to study the effects of tidal stripping on the satellite population and the disruption of satellites with particular attention to extended sources that resemble observational features, like the giant stream seen in the Andromeda galaxy. Here, the flexibility of our method can be used to achieve a high resolution only in the components we are interested in (i.e. satellites) while using a rather low resolution in the other components. In this way we not only have the high resolution needed to study the stripping of galactic satellites but also the full cosmological orbital evolution of both satellites and the central galaxy. This is not possible in cosmological simulations. Moreover our method allows for satellite-satellite interactions and includes a 'live' response of the central halo. It is also possible to simulate a subsample of satellites (i.e. only 'interesting' cases) and neglecting others without affecting the results on the simulated satellites making this method very flexible. By including also the gaseous components we are able to study effects like the induced star formation due to gas compression and ram pressure stripping in great detail. The main questions that can be addressed are: stellar stripping as a function of

satellite morphology – do discs and spheroids lose stars at the same rate? How do stellar streams form and get transformed due to secular evolution? How does the morphology of satellite galaxies change (satellite harassment)? Since a hydrodynamical approach is used we can also study how much gas gets stripped from satellites and how it accretes onto the main halo. Although the focus is on the satellite population we can also address the question how star formation is triggered in the main halo due to the satellites.

Appendix A
Conventions and Acronyms

Cosmological parameters		
Total density	Ω	1.00
Matter density	Ω_m	0.26
Vacuum density	Ω_Λ	0.74
Universal baryonic fraction	f_b	0.17
Hubble parameter	h	0.72
Power spectrum normalisation	σ_8	0.77
Power spectrum slope	n	0.95
GADGET-2 units		
Distance	r	kpc
Velocity	v	$\mathrm{km\,s^{-1}}$
Mass	M	$10^{10}\,M_\odot$

2dFGRS	Two Degree Field Galaxy Redshift Survey
AGN	active galactic nuclei
AMR	adaptive mesh refinement
BH	black hole
B/T	bulge-to-total
CDM	cold dark matter
CPU	central processing unit
EPS	extended Press-Schechter
FOF	friends-of-friends
FP	fundamental plane
IMF	initial mass function
MMP	most massive progenitor
MW	Milky Way
PM	particle-mesh
PP	particle-particle
SAM	semi-analytic model
SDSS	Sloan Digital Sky Survey
SFR	star formation rate
SN	supernova
SPH	smoothed particle hydrodynamics

Appendix B
Additional Visualisation Material

Additional visualisation material in the form of animations of the density distributions for the stellar and gaseous components are provided on a DVD, together with an electronic version of this thesis. An overview is given in the start.html file in the root directory of the DVD.

Bibliography

Abadi, M. G., Navarro, J. F., Steinmetz, M., & Eke, V. R. 2003. Simulations of Galaxy Formation in a Λ Cold Dark Matter Universe. II. The Fine Structure of Simulated Galactic Disks. *ApJ*, **597**, 21–34.

Appel, A. W. 1981. *An Investigation of Galaxy Clustering Using an Asymptotically Fast N-Body Algorithm*. Senior Thesis, Princeton University.

Appel, A. W. 1985. An Efficient Program for Many-Body Simulations. *SIAM Journal on Scientific and Statistical Computing*, **6**, 85–103.

Bahcall, J. N., & Soneira, R. M. 1980. The universe at faint magnitudes. I - Models for the galaxy and the predicted star counts. *ApJS*, **44**, 73–110.

Barden, M., *et al.* . 2005. GEMS: The Surface Brightness and Surface Mass Density Evolution of Disk Galaxies. *ApJ*, **635**, 959–981.

Barnes, J., & Efstathiou, G. 1987. Angular momentum from tidal torques. *ApJ*, **319**, 575–600.

Barnes, J. E. 1988. Encounters of disk/halo galaxies. *ApJ*, **331**, 699–717.

Barnes, J. E. 2002. Formation of gas discs in merging galaxies. *MNRAS*, **333**, 481–494.

Barnes, J. E., & Hernquist, L. 1996. Transformations of Galaxies. II. Gasdynamics in Merging Disk Galaxies. *ApJ*, **471**, 115.

Bate, M. R., & Burkert, A. 1997. Resolution requirements for smoothed particle hydrodynamics calculations with self-gravity. *MNRAS*, **288**, 1060–1072.

Baugh, C. M., Cole, S., & Frenk, C. S. 1996. Faint galaxy counts as a function of morphological type in a hierarchical merger model. *MNRAS*, **282**, L27–L32.

Baugh, C. M., Cole, S., Frenk, C. S., & Lacey, C. G. 1998. The Epoch of Galaxy Formation. *ApJ*, **498**, 504.

Bekki, K. 1998. Unequal-Mass Galaxy Mergers and the Creation of Cluster S0 Galaxies. *ApJ*, **502**, L133.

Bekki, K., & Shioya, Y. 1997. Formation of Boxy and Disky Elliptical Galaxies in Early Dissipative Mergers. *ApJ*, **478**, L17.

Bell, E. F., & de Jong, R. S. 2001. Stellar Mass-to-Light Ratios and the Tully-Fisher Relation. *ApJ*, **550**, 212–229.

Bell, E. F., McIntosh, D. H., Katz, N., & Weinberg, M. D. 2003. A First Estimate of the Baryonic Mass Function of Galaxies. *ApJ*, **585**, L117–L120.

Bender, R. 1988. Velocity anisotropies and isophote shapes in elliptical galaxies. *A&A*, **193**, L7–L10.

Bender, R., & Nieto, J.-L. 1990. Internal kinematics of low-luminosity ellipsoidal galaxies. *A&A*, **239**, 97–112.

Bender, R., Doebereiner, S., & Moellenhoff, C. 1988. Isophote shapes of elliptical galaxies. I - The data. *A&AS*, **74**, 385–426.

Bender, R., Surma, P., Doebereiner, S., Moellenhoff, C., & Madejsky, R. 1989. Isophote shapes of elliptical galaxies. II - Correlations with global optical, radio and X-ray properties. *A&A*, **217**, 35–43.

Bendo, G. J., & Barnes, J. E. 2000. The line-of-sight velocity distributions of simulated merger remnants. *MNRAS*, **316**, 315–325.

Benson, A. J. 2005. Orbital parameters of infalling dark matter substructures. *MNRAS*, **358**, 551–562.

Benson, A. J., Bower, R. G., Frenk, C. S., & White, S. D. M. 2000. Diffuse X-ray emission from late-type galaxy haloes. *MNRAS*, **314**, 557–565.

Benson, A. J., Bower, R. G., Frenk, C. S., Lacey, C. G., Baugh, C. M., & Cole, S. 2003. What Shapes the Luminosity Function of Galaxies? *ApJ*, **599**, 38–49.

Benson, A. J., Lacey, C. G., Frenk, C. S., Baugh, C. M., & Cole, S. 2004. Heating of galactic discs by infalling satellites. *MNRAS*, **351**, 1215–1236.

Bertschinger, E. 2001. Multiscale Gaussian Random Fields and Their Application to Cosmological Simulations. *ApJS*, **137**, 1–20.

Binney, J. 1978. On the rotation of elliptical galaxies. *MNRAS*, **183**, 501–514.

Binney, J., & Tremaine, S. 1987. *Galactic dynamics*. Princeton, NJ, Princeton University Press, 1987, 747 p.

Bizyaev, D., & Kajsin, S. 2004. The Stellar Disk Thickness of Low Surface Brightness Galaxies. *ApJ*, **613**, 886–897.

Blumenthal, G. R., Pagels, H., & Primack, J. R. 1982. Galaxy formation by dissipationless particles heavier than neutrinos. *Nature*, **299**, 37.

Bois, M., *et al.* . 2010. Formation of slowly rotating early-type galaxies via major mergers: a Resolution Study. *ArXiv e-prints*.

Bond, J. R., Cole, S., Efstathiou, G., & Kaiser, N. 1991. Excursion set mass functions for hierarchical Gaussian fluctuations. *ApJ*, **379**, 440–460.

Bournaud, F., Jog, C. J., & Combes, F. 2007. Multiple minor mergers: formation of elliptical galaxies and constraints for the growth of spiral disks. *A&A*, **476**, 1179–1190.

Bower, R. G. 1991. The evolution of groups of galaxies in the Press-Schechter formalism. *MNRAS*, **248**, 332–352.

Bower, R. G., Benson, A. J., Malbon, R., Helly, J. C., Frenk, C. S., Baugh, C. M., Cole, S., & Lacey, C. G. 2006. Breaking the hierarchy of galaxy formation. *MNRAS*, **370**, 645–655.

Boylan-Kolchin, M., Ma, C.-P., & Quataert, E. 2008. Dynamical friction and galaxy merging time-scales. *MNRAS*, **383**, 93–101.

Bruzual, G., & Charlot, S. 2003. Stellar population synthesis at the resolution of 2003. *MNRAS*, **344**, 1000–1028.

Bryan, G. L., & Norman, M. L. 1998. Statistical Properties of X-Ray Clusters: Analytic and Numerical Comparisons. *ApJ*, **495**, 80.

Bullock, J. S., Dekel, A., Kolatt, T. S., Kravtsov, A. V., Klypin, A. A., Porciani, C., & Primack, J. R. 2001. A Universal Angular Momentum Profile for Galactic Halos. *ApJ*, **555**, 240–257.

Burkert, A., Naab, T., Johansson, P. H., & Jesseit, R. 2008. SAURON's Challenge for the Major Merger Scenario of Elliptical Galaxy Formation. *ApJ*, **685**, 897–903.

Carlberg, R. G. 1986. The phase space density in elliptical galaxies. *ApJ*, **310**, 593–596.

Cavaliere, A., & Fusco-Femiano, R. 1976. X-rays from hot plasma in clusters of galaxies. *A&A*, **49**, 137–144.

Chabrier, G. 2003. Galactic Stellar and Substellar Initial Mass Function. *PASP*, **115**, 763–795.

Choi, J.-H., Weinberg, M. D., & Katz, N. 2007. The dynamics of tidal tails from massive satellites. *MNRAS*, **381**, 987–1000.

Cole, S., Aragon-Salamanca, A., Frenk, C. S., Navarro, J. F., & Zepf, S. E. 1994. A Recipe for Galaxy Formation. *MNRAS*, **271**, 781.

Cole, S., Lacey, C. G., Baugh, C. M., & Frenk, C. S. 2000. Hierarchical galaxy formation. *MNRAS*, **319**, 168–204.

Combes, F., Dupraz, C., & Gerin, M. 1990. Gas dynamics in a tidal interaction: formation of rings. *Pages 205–209 of: Dynamics and Interactions of Galaxies.* Wielen, R.

Cox, T. J., Jonsson, P., Primack, J. R., & Somerville, R. S. 2006a. Feedback in simulations of disc-galaxy major mergers. *MNRAS*, **373**, 1013–1038.

Cox, T. J., Dutta, S. N., Di Matteo, T., Hernquist, L., Hopkins, P. F., Robertson, B., & Springel, V. 2006b. The Kinematic Structure of Merger Remnants. *ApJ*, **650**, 791–811.

Cox, T. J., Jonsson, P., Somerville, R. S., Primack, J. R., & Dekel, A. 2008. The effect of galaxy mass ratio on merger-driven starbursts. *MNRAS*, **384**, 386–409.

Croton, D. J., *et al.* . 2006. The many lives of active galactic nuclei: cooling flows, black holes and the luminosities and colours of galaxies. *MNRAS*, **365**, 11–28.

Curtis, H. D. 1920. Modern Theories of the Spiral Nebulae. *JRASC*, **14**, 317.

Davies, R. L., Efstathiou, G., Fall, S. M., Illingworth, G., & Schechter, P. L. 1983. The kinematic properties of faint elliptical galaxies. *ApJ*, **266**, 41–57.

Davis, M., Efstathiou, G., Frenk, C. S., & White, S. D. M. 1985. The evolution of large-scale structure in a universe dominated by cold dark matter. *ApJ*, **292**, 371–394.

de Grijs, R., & van der Kruit, P. C. 1996. Structure analysis of edge-on spiral galaxies. *A&AS*, **117**, 19–37.

de Grijs, R., Peletier, R. F., & van der Kruit, P. C. 1997. The z-structure of disk galaxies towards the galaxy planes. *A&A*, **327**, 966–982.

de Jong, R. S. 1996. Near-infrared and optical broadband surface photometry of 86 face-on disk dominated galaxies. III. The statistics of the disk and bulge parameters. *A&A*, **313**, 45–64.

De Lucia, G., & Blaizot, J. 2007. The hierarchical formation of the brightest cluster galaxies. *MNRAS*, **375**, 2–14.

De Lucia, G., Kauffmann, G., & White, S. D. M. 2004. Chemical enrichment of the intracluster and intergalactic medium in a hierarchical galaxy formation model. *MNRAS*, **349**, 1101–1116.

de Zeeuw, P. T., *et al.* . 2002. The SAURON project - II. Sample and early results. *MNRAS*, **329**, 513–530.

Dehnen, W. 2001. Towards optimal softening in three-dimensional N-body codes - I. Minimizing the force error. *MNRAS*, **324**, 273–291.

Dekel, A., & Birnboim, Y. 2006. Galaxy bimodality due to cold flows and shock heating. *MNRAS*, **368**, 2–20.

Di Matteo, T., Springel, V., & Hernquist, L. 2005. Energy input from quasars regulates the growth and activity of black holes and their host galaxies. *Nature*, **433**, 604–607.

Diemand, J., Kuhlen, M., & Madau, P. 2007. Formation and Evolution of Galaxy Dark Matter Halos and Their Substructure. *ApJ*, **667**, 859–877.

Einstein, A. 1917. Kosmologische Betrachtungen zur allgemeinen Relativitätstheorie. *Sitzungsberichte der Königlich Preußischen Akademie der Wissenschaften (Berlin)*, 142–152.

Eke, V. R., Navarro, J. F., & Frenk, C. S. 1998. The Evolution of X-Ray Clusters in a Low-Density Universe. *ApJ*, **503**, 569.

Ellis, J., Hagelin, J. S., Nanopoulos, D. V., Olive, K., & Srednicki, M. 1984. Supersymmetric relics from the big bang. *Nuclear Physics B*, **238**, 453–476.

Erb, D. K., Steidel, C. C., Shapley, A. E., Pettini, M., Reddy, N. A., & Adelberger, K. L. 2006. The Stellar, Gas, and Dynamical Masses of Star-forming Galaxies at $z \sim 2$. *ApJ*, **646**, 107–132.

Evrard, A. E. 1990. Formation and evolution of X-ray clusters - A hydrodynamic simulation of the intracluster medium. *ApJ*, **363**, 349–366.

Faber, S. M., *et al.* . 1997. The Centers of Early-Type Galaxies with HST. IV. Central Parameter Relations. *AJ*, **114**, 1771.

Fall, S. M., & Efstathiou, G. 1980. Formation and rotation of disc galaxies with haloes. *MNRAS*, **193**, 189–206.

Ferrarese, L., & Merritt, D. 2000. A Fundamental Relation between Supermassive Black Holes and Their Host Galaxies. *ApJ*, **539**, L9–L12.

Ferrarese, L., van den Bosch, F. C., Ford, H. C., Jaffe, W., & O'Connell, R. W. 1994. Hubble Space Telescope photometry of the central regions of Virgo cluster elliptical galaxies. 3: Brightness profiles. *AJ*, **108**, 1598–1609.

Folkes, S., *et al.* . 1999. The 2dF Galaxy Redshift Survey: spectral types and luminosity functions. *MNRAS*, **308**, 459–472.

Font, A. S., Navarro, J. F., Stadel, J., & Quinn, T. 2001. Halo Substructure and Disk Heating in a Λ Cold Dark Matter Universe. *ApJ*, **563**, L1–L4.

Gauthier, J.-R., Dubinski, J., & Widrow, L. M. 2006. Substructure around M31: Evolution and Effects. *ApJ*, **653**, 1180–1193.

Gelb, J. M., & Bertschinger, E. 1994. Cold dark matter. 2: Spatial and velocity statistics. *ApJ*, **436**, 491–508.

Genzel, R., *et al.* . 2008. From Rings to Bulges: Evidence for Rapid Secular Galaxy Evolution at $z \sim 2$ from Integral Field Spectroscopy in the SINS Survey. *ApJ*, **687**, 59–77.

Gerhard, O. E. 1981. N-body simulations of disc-halo galaxies - Isolated systems, tidal interactions and merging. *MNRAS*, **197**, 179–208.

Gnedin, N. Y. 2000. Effect of Reionization on Structure Formation in the Universe. *ApJ*, **542**, 535–541.

Governato, F., Moore, B., Cen, R., Stadel, J., Lake, G., & Quinn, T. 1997. The Local Group as a test of cosmological models. *New Astronomy*, **2**, 91–106.

Governato, F., Mayer, L., Wadsley, J., Gardner, J. P., Willman, B., Hayashi, E., Quinn, T., Stadel, J., & Lake, G. 2004. The Formation of a Realistic Disk Galaxy in Λ-dominated Cosmologies. *ApJ*, **607**, 688–696.

Governato, F., Willman, B., Mayer, L., Brooks, A., Stinson, G., Valenzuela, O., Wadsley, J., & Quinn, T. 2007. Forming disc galaxies in ΛCDM simulations. *MNRAS*, **374**, 1479–1494.

Governato, F., *et al.* . 2009. Forming a large disc galaxy from a $z < 1$ major merger. *MNRAS*, **398**, 312–320.

Governato, F., *et al.* . 2010. Bulgeless dwarf galaxies and dark matter cores from supernova-driven outflows. *Nature*, **463**, 203–206.

Graham, A. W., & Worley, C. C. 2008. Inclination- and dust-corrected galaxy parameters: bulge-to-disc ratios and size-luminosity relations. *MNRAS*, **388**, 1708–1728.

Grcevich, J., & Putman, M. E. 2009. H I in Local Group Dwarf Galaxies and Stripping by the Galactic Halo. *ApJ*, **696**, 385–395.

Gunn, J. E., & Gott, III, J. R. 1972. On the Infall of Matter Into Clusters of Galaxies and Some Effects on Their Evolution. *ApJ*, **176**, 1.

Haardt, F., & Madau, P. 1996. Radiative Transfer in a Clumpy Universe. II. The Ultraviolet Extragalactic Background. *ApJ*, **461**, 20.

Hammer, F., Puech, M., Chemin, L., Flores, H., & Lehnert, M. D. 2007. The Milky Way, an Exceptionally Quiet Galaxy: Implications for the Formation of Spiral Galaxies. *ApJ*, **662**, 322–334.

Hansen, S. H., Juncher, D., & Sparre, M. 2010. An attractor for dark matter structures. *ArXiv e-prints*.

Häring, N., & Rix, H.-W. 2004. On the Black Hole Mass-Bulge Mass Relation. *ApJ*, **604**, L89–L92.

Hatton, S., Devriendt, J. E. G., Ninin, S., Bouchet, F. R., Guiderdoni, B., & Vibert, D. 2003. GALICS- I. A hybrid N-body/semi-analytic model of hierarchical galaxy formation. *MNRAS*, **343**, 75–106.

Helmi, A., & de Zeeuw, P. T. 2000. Mapping the substructure in the Galactic halo with the next generation of astrometric satellites. *MNRAS*, **319**, 657–665.

Helmi, A., & White, S. D. M. 1999. Building up the stellar halo of the Galaxy. *MNRAS*, **307**, 495–517.

Hernquist, L. 1989. Tidal triggering of starbursts and nuclear activity in galaxies. *Nature*, **340**, 687–691.

Hernquist, L. 1990. An analytical model for spherical galaxies and bulges. *ApJ*, **356**, 359–364.

Hernquist, L. 1992. Structure of merger remnants. I - Bulgeless progenitors. *ApJ*, **400**, 460–475.

Hernquist, L. 1993. Structure of merger remnants. II - Progenitors with rotating bulges. *ApJ*, **409**, 548–562.

Heyl, J. S., Cole, S., Frenk, C. S., & Navarro, J. F. 1995. Galaxy formation in a variety of hierarchical models. *MNRAS*, **274**, 755–768.

Hirschmann, M., Khochfar, S., Burkert, A., Naab, T., Genel, S., & Somerville, R. 2010. On the evolution of the intrinsic scatter in black hole versus galaxy mass relations. *ArXiv e-prints*.

Hopkins, P. F., Hernquist, L., Cox, T. J., Robertson, B., & Krause, E. 2007. A Theoretical Interpretation of the Black Hole Fundamental Plane. *ApJ*, **669**, 45–66.

Hopkins, P. F., Hernquist, L., Cox, T. J., & Kereš, D. 2008. A Cosmological Framework for the Co-Evolution of Quasars, Supermassive Black Holes, and Elliptical Galaxies. I. Galaxy Mergers and Quasar Activity. *ApJS*, **175**, 356–389.

Hopkins, P. F., Cox, T. J., Younger, J. D., & Hernquist, L. 2009a. How do Disks Survive Mergers? *ApJ*, **691**, 1168–1201.

Hopkins, P. F., *et al.* . 2009b. The effects of gas on morphological transformation in mergers: implications for bulge and disc demographics. *MNRAS*, **397**, 802–814.

Hoyle, F. 1953. On the Fragmentation of Gas Clouds Into Galaxies and Stars. *ApJ*, **118**, 513.

Hubble, E. 1929a. A Relation between Distance and Radial Velocity among Extra-Galactic Nebulae. *Proceedings of the National Academy of Science*, **15**, 168–173.

Hubble, E. P. 1925. NGC 6822, a remote stellar system. *ApJ*, **62**, 409–433.

Hubble, E. P. 1926. Extragalactic nebulae. *ApJ*, **64**, 321–369.

Hubble, E. P. 1929b. A spiral nebula as a stellar system, Messier 31. *ApJ*, **69**, 103–158.

Jedamzik, K. 1995. The Cloud-in-Cloud Problem in the Press-Schechter Formalism of Hierarchical Structure Formation. *ApJ*, **448**, 1.

Jenkins, A., *et al.* . 1998. Evolution of Structure in Cold Dark Matter Universes. *ApJ*, **499**, 20.

Jenkins, A., Frenk, C. S., White, S. D. M., Colberg, J. M., Cole, S., Evrard, A. E., Couchman, H. M. P., & Yoshida, N. 2001. The mass function of dark matter haloes. *MNRAS*, **321**, 372–384.

Jesseit, R., Naab, T., Peletier, R. F., & Burkert, A. 2007. 2D kinematics of simulated disc merger remnants. *MNRAS*, **376**, 997–1020.

Jones, C., & Forman, W. 1984. The structure of clusters of galaxies observed with Einstein. *ApJ*, **276**, 38–55.

Jurić, M., *et al.* . 2008. The Milky Way Tomography with SDSS. I. Stellar Number Density Distribution. *ApJ*, **673**, 864–914.

Kang, X., Jing, Y. P., & Silk, J. 2006. Massive and Red Objects Predicted by a Semianalytical Model of Galaxy Formation. *ApJ*, **648**, 820–825.

Kassin, S. A., *et al.* . 2007. The Stellar Mass Tully-Fisher Relation to z = 1.2 from AEGIS. *ApJ*, **660**, L35–L38.

Katz, N. 1992. Dissipational galaxy formation. II - Effects of star formation. *ApJ*, **391**, 502–517.

Katz, N., & Gunn, J. E. 1991. Dissipational galaxy formation. I - Effects of gasdynamics. *ApJ*, **377**, 365–381.

Katz, N., & White, S. D. M. 1993. Hierarchical galaxy formation - Overmerging and the formation of an X-ray cluster. *ApJ*, **412**, 455–478.

Katz, N., Weinberg, D. H., & Hernquist, L. 1996. Cosmological Simulations with TreeSPH. *ApJS*, **105**, 19.

Kauffmann, G., & Charlot, S. 1998. Chemical enrichment and the origin of the colour-magnitude relation of elliptical galaxies in a hierarchical merger model. *MNRAS*, **294**, 705.

Kauffmann, G., & White, S. D. M. 1993. The merging history of dark matter haloes in a hierarchical universe. *MNRAS*, **261**, 921–928.

Kauffmann, G., White, S. D. M., & Guiderdoni, B. 1993. The Formation and Evolution of Galaxies Within Merging Dark Matter Haloes. *MNRAS*, **264**, 201.

Kauffmann, G., Guiderdoni, B., & White, S. D. M. 1994. Faint Galaxy Counts in a Hierarchical Universe. *MNRAS*, **267**, 981.

Kauffmann, G., Colberg, J. M., Diaferio, A., & White, S. D. M. 1999. Clustering of galaxies in a hierarchical universe - I. Methods and results at $z = 0$. *MNRAS*, **303**, 188–206.

Kaufmann, T., Mayer, L., Wadsley, J., Stadel, J., & Moore, B. 2006. Cooling flows within galactic haloes: the kinematics and properties of infalling multiphase gas. *MNRAS*, **370**, 1612–1622.

Kaufmann, T., Bullock, J. S., Maller, A. H., Fang, T., & Wadsley, J. 2009. Redistributing hot gas around galaxies: do cool clouds signal a solution to the overcooling problem? *MNRAS*, **396**, 191–202.

Kazantzidis, S., Bullock, J. S., Zentner, A. R., Kravtsov, A. V., & Moustakas, L. A. 2008. Cold Dark Matter Substructure and Galactic Disks. I. Morphological Signatures of Hierarchical Satellite Accretion. *ApJ*, **688**, 254–276.

Kazantzidis, S., Zentner, A. R., Kravtsov, A. V., Bullock, J. S., & Debattista, V. P. 2009. Cold Dark Matter Substructure and Galactic Disks. II. Dynamical Effects of Hierarchical Satellite Accretion. *ApJ*, **700**, 1896–1920.

Kennicutt, Jr., R. C. 1998. The Global Schmidt Law in Star-forming Galaxies. *ApJ*, **498**, 541.

Kent, S. M., Dame, T. M., & Fazio, G. 1991. Galactic structure from the Spacelab infrared telescope. II - Luminosity models of the Milky Way. *ApJ*, **378**, 131–138.

Kereš, D., Katz, N., Weinberg, D. H., & Davé, R. 2005. How do galaxies get their gas? *MNRAS*, **363**, 2–28.

Khochfar, S., & Burkert, A. 2006. Orbital parameters of merging dark matter halos. *A&A*, **445**, 403–412.

Klypin, A., & Holtzman, J. 1997. Particle-Mesh code for cosmological simulations. *ArXiv Astrophysics e-prints*.

Klypin, A., Gottlöber, S., Kravtsov, A. V., & Khokhlov, A. M. 1999. Galaxies in N-Body Simulations: Overcoming the Overmerging Problem. *ApJ*, **516**, 530–551.

Klypin, A., Kravtsov, A. V., Bullock, J. S., & Primack, J. R. 2001. Resolving the Structure of Cold Dark Matter Halos. *ApJ*, **554**, 903–915.

Klypin, A., Zhao, H., & Somerville, R. S. 2002. ΛCDM-based Models for the Milky Way and M31. I. Dynamical Models. *ApJ*, **573**, 597–613.

Kormendy, J., & Bender, R. 1996. A Proposed Revision of the Hubble Sequence for Elliptical Galaxies. *ApJ*, **464**, L119.

Kormendy, J., & Fisher, D. B. 2008. Secular Evolution in Disk Galaxies: Pseudobulge Growth and the Formation of Spheroidal Galaxies. *Page 297 of:* J. G. Funes & E. M. Corsini (ed), *Astronomical Society of the Pacific Conference Series*. Astronomical Society of the Pacific Conference Series, vol. 396.

Kowalski, M., *et al.* . 2008. Improved Cosmological Constraints from New, Old, and Combined Supernova Data Sets. *ApJ*, **686**, 749–778.

Kravtsov, A. V. 2003. On the Origin of the Global Schmidt Law of Star Formation. *ApJ*, **590**, L1–L4.

Kravtsov, A. V., Gnedin, O. Y., & Klypin, A. A. 2004. The Tumultuous Lives of Galactic Dwarfs and the Missing Satellites Problem. *ApJ*, **609**, 482–497.

Kregel, M., van der Kruit, P. C., & de Grijs, R. 2002. Flattening and truncation of stellar discs in edge-on spiral galaxies. *MNRAS*, **334**, 646–668.

Kroupa, P. 2001. On the variation of the initial mass function. *MNRAS*, **322**, 231–246.

Lacey, C., & Cole, S. 1993. Merger rates in hierarchical models of galaxy formation. *MNRAS*, **262**, 627–649.

Lacey, C., & Cole, S. 1994. Merger Rates in Hierarchical Models of Galaxy Formation - Part Two - Comparison with N-Body Simulations. *MNRAS*, **271**, 676.

Lake, G. 1989. Phase densities and the merger hypothesis. *AJ*, **97**, 1312–1318.

Larsen, J. A., & Humphreys, R. M. 2003. Fitting a Galactic Model to an All-Sky Survey. *AJ*, **125**, 1958–1979.

Lauer, T. R., *et al.* . 1995. The Centers of Early-Type Galaxies with HST. I. An Observational Survey. *AJ*, **110**, 2622.

Lauer, T. R., *et al.* . 2005. The Centers of Early-Type Galaxies with Hubble Space Telescope. V. New WFPC2 Photometry. *AJ*, **129**, 2138–2185.

Li, Z., Wang, Q. D., & Hameed, S. 2007. Chandra and XMM-Newton detection of large-scale diffuse X-ray emission from the Sombrero galaxy. *MNRAS*, **376**, 960–976.

Lindegren, L., & Perryman, M. A. C. 1996. GAIA: Global astrometric interferometer for astrophysics. *A&AS*, **116**, 579–595.

Macciò, A. V., Dutton, A. A., & van den Bosch, F. C. 2008. Concentration, spin and shape of dark matter haloes as a function of the cosmological model: WMAP1, WMAP3 and WMAP5 results. *MNRAS*, **391**, 1940–1954.

Macciò, A. V., Kang, X., Fontanot, F., Somerville, R. S., Koposov, S., & Monaco, P. 2010. Luminosity function and radial distribution of Milky Way satellites in a ΛCDM Universe. *MNRAS*, **402**, 1995–2008.

Madau, P., Ferguson, H. C., Dickinson, M. E., Giavalisco, M., Steidel, C. C., & Fruchter, A. 1996. High-redshift galaxies in the Hubble Deep Field: colour selection and star formation history to $z \sim 4$. *MNRAS*, **283**, 1388–1404.

Magorrian, J., *et al.* . 1998. The Demography of Massive Dark Objects in Galaxy Centers. *AJ*, **115**, 2285–2305.

Makino, N., Sasaki, S., & Suto, Y. 1998. X-Ray Gas Density Profile of Clusters of Galaxies from the Universal Dark Matter Halo. *ApJ*, **497**, 555.

Maller, A. H., & Bullock, J. S. 2004. Multiphase galaxy formation: high-velocity clouds and the missing baryon problem. *MNRAS*, **355**, 694–712.

Martin, C. L. 1999. Properties of Galactic Outflows: Measurements of the Feedback from Star Formation. *ApJ*, **513**, 156–160.

Martin, C. L. 2005. Mapping Large-Scale Gaseous Outflows in Ultraluminous Galaxies with Keck II ESI Spectra: Variations in Outflow Velocity with Galactic Mass. *ApJ*, **621**, 227–245.

Mastropietro, C., Moore, B., Mayer, L., Wadsley, J., & Stadel, J. 2005. The gravitational and hydrodynamical interaction between the Large Magellanic Cloud and the Galaxy. *MNRAS*, **363**, 509–520.

Mastropietro, C., Burkert, A., & Moore, B. 2009. Effects of ram pressure on the gas distribution and star formation in the Large Magellanic Cloud. *MNRAS*, **399**, 2004–2020.

Mathews, W. G., & Brighenti, F. 2003. Hot Gas in and around Elliptical Galaxies. *ARA&A*, **41**, 191–239.

Maulbetsch, C., Avila-Reese, V., Colín, P., Gottlöber, S., Khalatyan, A., & Steinmetz, M. 2007. The Dependence of the Mass Assembly History of Cold Dark Matter Halos on Environment. *ApJ*, **654**, 53–65.

McGaugh, S. S. 2005. The Baryonic Tully-Fisher Relation of Galaxies with Extended Rotation Curves and the Stellar Mass of Rotating Galaxies. *ApJ*, **632**, 859–871.

McKee, C. F., & Ostriker, J. P. 1977. A theory of the interstellar medium - Three components regulated by supernova explosions in an inhomogeneous substrate. *ApJ*, **218**, 148–169.

Mestel, L. 1963. On the galactic law of rotation. *MNRAS*, **126**, 553.

Mihos, J. C., & Hernquist, L. 1994. Triggering of starbursts in galaxies by minor mergers. *ApJ*, **425**, L13–L16.

Mihos, J. C., & Hernquist, L. 1996. Gasdynamics and Starbursts in Major Mergers. *ApJ*, **464**, 641.

Mo, H. J., & White, S. D. M. 1996. An analytic model for the spatial clustering of dark matter haloes. *MNRAS*, **282**, 347–361.

Mo, H. J., Mao, S., & White, S. D. M. 1998. The formation of galactic discs. *MNRAS*, **295**, 319–336.

Monaco, P., Fontanot, F., & Taffoni, G. 2007. The MORGANA model for the rise of galaxies and active nuclei. *MNRAS*, **375**, 1189–1219.

Moore, B., Governato, F., Quinn, T., Stadel, J., & Lake, G. 1998. Resolving the Structure of Cold Dark Matter Halos. *ApJ*, **499**, L5.

Moore, B., Ghigna, S., Governato, F., Lake, G., Quinn, T., Stadel, J., & Tozzi, P. 1999. Dark Matter Substructure within Galactic Halos. *ApJ*, **524**, L19–L22.

Moster, B. P., Somerville, R. S., Maulbetsch, C., van den Bosch, F. C., Macciò, A. V., Naab, T., & Oser, L. 2010. Constraints on the Relationship between Stellar Mass and Halo Mass at Low and High Redshift. *ApJ*, **710**, 903–923.

Naab, T., & Burkert, A. 2003. Statistical Properties of Collisionless Equal- and Unequal-Mass Merger Remnants of Disk Galaxies. *ApJ*, **597**, 893–906.

Naab, T., Jesseit, R., & Burkert, A. 2006. The influence of gas on the structure of merger remnants. *MNRAS*, **372**, 839–852.

Nagashima, M. 2001. A Solution to the Missing Link in the Press-Schechter Formalism. *ApJ*, **562**, 7–23.

Navarro, J. F., & Benz, W. 1991. Dynamics of cooling gas in galactic dark halos. *ApJ*, **380**, 320–329.

Navarro, J. F., & White, S. D. M. 1994. Simulations of dissipative galaxy formation in hierarchically clustering universes-2. Dynamics of the baryonic component in galactic haloes. *MNRAS*, **267**, 401–412.

Navarro, J. F., Frenk, C. S., & White, S. D. M. 1995. Simulations of X-ray clusters. *MNRAS*, **275**, 720–740.

Navarro, J. F., Frenk, C. S., & White, S. D. M. 1997. A Universal Density Profile from Hierarchical Clustering. *ApJ*, **490**, 493.

Negroponte, J., & White, S. D. M. 1983. Simulations of mergers between disc-halo galaxies. *MNRAS*, **205**, 1009–1029.

Noguchi, M. 1988. Gas dynamics in interacting disc galaxies - Fuelling of nuclei by induced bars. *A&A*, **203**, 259–272.

Okamoto, T., Eke, V. R., Frenk, C. S., & Jenkins, A. 2005. Effects of feedback on the morphology of galaxy discs. *MNRAS*, **363**, 1299–1314.

Oppenheimer, B. D., & Davé, R. 2006. Cosmological simulations of intergalactic medium enrichment from galactic outflows. *MNRAS*, **373**, 1265–1292.

Park, C., Choi, Y.-Y., Vogeley, M. S., Gott, J. R. I., & Blanton, M. R. 2007. Environmental Dependence of Properties of Galaxies in the Sloan Digital Sky Survey. *ApJ*, **658**, 898–916.

Peebles, P. J. E. 1969. Origin of the Angular Momentum of Galaxies. *ApJ*, **155**, 393.

Peek, J. E. G. 2009. Hitting the Bull's-Eye: The Radial Profile of Accretion and Star Formation in the Milky Way. *ApJ*, **698**, 1429–1436.

Perlmutter, S., *et al.* . 1999. Measurements of Omega and Lambda from 42 High-Redshift Supernovae. *ApJ*, **517**, 565–586.

Pohlen, M., Dettmar, R.-J., Lütticke, R., & Schwarzkopf, U. 2000. Three-dimensional modelling of edge-on disk galaxies. *A&AS*, **144**, 405–428.

Press, W. H., & Schechter, P. 1974. Formation of Galaxies and Clusters of Galaxies by Self-Similar Gravitational Condensation. *ApJ*, **187**, 425–438.

Puech, M., *et al.* . 2008. IMAGES. III. The evolution of the near-infrared Tully-Fisher relation over the last 6 Gyr. *A&A*, **484**, 173–187.

Purcell, C. W., Bullock, J. S., & Zentner, A. R. 2007. Shredded Galaxies as the Source of Diffuse Intrahalo Light on Varying Scales. *ApJ*, **666**, 20–33.

Purcell, C. W., Kazantzidis, S., & Bullock, J. S. 2009. The Destruction of Thin Stellar Disks Via Cosmologically Common Satellite Accretion Events. *ApJ*, **694**, L98–L102.

Quinn, P. J., Hernquist, L., & Fullagar, D. P. 1993. Heating of galactic disks by mergers. *ApJ*, **403**, 74–93.

Rasmussen, J., Sommer-Larsen, J., Pedersen, K., Toft, S., Benson, A., Bower, R. G., & Grove, L. F. 2009. Hot Gas Halos Around Disk Galaxies: Confronting Cosmological Simulations with Observations. *ApJ*, **697**, 79–93.

Rees, M. J., & Ostriker, J. P. 1977. Cooling, dynamics and fragmentation of massive gas clouds - Clues to the masses and radii of galaxies and clusters. *MNRAS*, **179**, 541–559.

Reid, N., & Majewski, S. R. 1993. Star counts redivivus. I - A new look at the galaxy at faint magnitudes. *ApJ*, **409**, 635–662.

Riess, A. G., *et al.* . 1998. Observational Evidence from Supernovae for an Accelerating Universe and a Cosmological Constant. *AJ*, **116**, 1009–1038.

Rix, H.-W., & White, S. D. M. 1990. Disks in elliptical galaxies. *ApJ*, **362**, 52–58.

Rix, H.-W., Carollo, C. M., & Freeman, K. 1999. Large Stellar Disks in Small Elliptical Galaxies. *ApJ*, **513**, L25–L28.

Robertson, B., Yoshida, N., Springel, V., & Hernquist, L. 2004. Disk Galaxy Formation in a Λ Cold Dark Matter Universe. *ApJ*, **606**, 32–45.

Robertson, B., Bullock, J. S., Cox, T. J., Di Matteo, T., Hernquist, L., Springel, V., & Yoshida, N. 2006a. A Merger-driven Scenario for Cosmological Disk Galaxy Formation. *ApJ*, **645**, 986–1000.

Robertson, B., Cox, T. J., Hernquist, L., Franx, M., Hopkins, P. F., Martini, P., & Springel, V. 2006b. The Fundamental Scaling Relations of Elliptical Galaxies. *ApJ*, **641**, 21–40.

Rothberg, B., & Joseph, R. D. 2006. A Survey of Merger Remnants. III. Are Merger Remnants Supported by Rotation or Anisotropy? *AJ*, **132**, 976–988.

Rubin, V. C., Ford, Jr., W. K., Thonnard, N., & Burstein, D. 1982. Rotational properties of 23 SB galaxies. *ApJ*, **261**, 439–456.

Rupke, D. S., Veilleux, S., & Sanders, D. B. 2005. Outflows in Infrared-Luminous Starbursts at $z < 0.5$. II. Analysis and Discussion. *ApJS*, **160**, 115–148.

Salpeter, E. E. 1955. The Luminosity Function and Stellar Evolution. *ApJ*, **121**, 161.

Scannapieco, C., White, S. D. M., Springel, V., & Tissera, P. B. 2009. The formation and survival of discs in a ΛCDM universe. *MNRAS*, **396**, 696–708.

Schwarzkopf, U., & Dettmar, R.-J. 2000. The influence of interactions and minor mergers on the structure of galactic disks. II. Results and interpretations. *A&A*, **361**, 451–464.

Scorza, C., Bender, R., Winkelmann, C., Capaccioli, M., & Macchetto, D. F. 1998. Stellar disks and embedded bars in early-type galaxies. I. 2-D photometric decomposition of 28 southern early-type galaxies. *A&AS*, **131**, 265–286.

Sembach, K. R., *et al.* . 2003. Highly Ionized High-Velocity Gas in the Vicinity of the Galaxy. *ApJS*, **146**, 165–208.

Shapley, H. 1919. On the Existence of External Galaxies. *PASP*, **31**, 261.

Shaw, M. A., & Gilmore, G. 1989. The luminosity distributions of edge-on spiral galaxies. I - A two-dimensional model and its application to NGC 891 and 4565. *MNRAS*, **237**, 903–927.

Shaw, M. A., & Gilmore, G. 1990. The luminosity distributions of edge-on spiral and lenticular galaxies. II - Modelling the non-thin disc light in a sample of ten galaxies. *MNRAS*, **242**, 59–73.

Shen, S., Mo, H. J., White, S. D. M., Blanton, M. R., Kauffmann, G., Voges, W., Brinkmann, J., & Csabai, I. 2003. The size distribution of galaxies in the Sloan Digital Sky Survey. *MNRAS*, **343**, 978–994.

Silk, J. 1977. On the fragmentation of cosmic gas clouds. I - The formation of galaxies and the first generation of stars. *ApJ*, **211**, 638–648.

Sinha, M., & Holley-Bockelmann, K. 2009. Numerical simulations of hot halo gas in galaxy mergers. *MNRAS*, **397**, 190–207.

Smoot, G. F., *et al.* . 1992. Structure in the COBE differential microwave radiometer first-year maps. *ApJ*, **396**, L1–L5.

Somerville, R. S., & Kolatt, T. S. 1999. How to plant a merger tree. *MNRAS*, **305**, 1–14.

Somerville, R. S., & Primack, J. R. 1999. Semi-analytic modelling of galaxy formation: the local Universe. *MNRAS*, **310**, 1087–1110.

Somerville, R. S., Lemson, G., Kolatt, T. S., & Dekel, A. 2000. Evaluating approximations for halo merging histories. *MNRAS*, **316**, 479–490.

Somerville, R. S., Hopkins, P. F., Cox, T. J., Robertson, B. E., & Hernquist, L. 2008a. A semi-analytic model for the co-evolution of galaxies, black holes and active galactic nuclei. *MNRAS*, **391**, 481–506.

Somerville, R. S., *et al.* . 2008b. An Explanation for the Observed Weak Size Evolution of Disk Galaxies. *ApJ*, **672**, 776–786.

Sommer-Larsen, J., Götz, M., & Portinari, L. 2003. Galaxy Formation: Cold Dark Matter, Feedback, and the Hubble Sequence. *ApJ*, **596**, 47–66.

Spergel, D. N., *et al.* . 2003. First-Year Wilkinson Microwave Anisotropy Probe (WMAP) Observations: Determination of Cosmological Parameters. *ApJS*, **148**, 175–194.

Spergel, D. N., *et al.* . 2007. Three-Year Wilkinson Microwave Anisotropy Probe (WMAP) Observations: Implications for Cosmology. *ApJS*, **170**, 377–408.

Springel, V. 2005. The cosmological simulation code GADGET-2. *MNRAS*, **364**, 1105–1134.

Springel, V., & Hernquist, L. 2003. Cosmological smoothed particle hydrodynamics simulations: a hybrid multiphase model for star formation. *MNRAS*, **339**, 289–311.

Springel, V., & Hernquist, L. 2005. Formation of a Spiral Galaxy in a Major Merger. *ApJ*, **622**, L9–L12.

Springel, V., & White, S. D. M. 1999. Tidal tails in cold dark matter cosmologies. *MNRAS*, **307**, 162–178.

Springel, V., White, S. D. M., Tormen, G., & Kauffmann, G. 2001. Populating a cluster of galaxies - I. Results at [formmu2]z=0. *MNRAS*, **328**, 726–750.

Springel, V., Di Matteo, T., & Hernquist, L. 2005a. Modelling feedback from stars and black holes in galaxy mergers. *MNRAS*, **361**, 776–794.

Springel, V., *et al.* . 2005b. Simulations of the formation, evolution and clustering of galaxies and quasars. *Nature*, **435**, 629–636.

Springel, V., Wang, J., Vogelsberger, M., Ludlow, A., Jenkins, A., Helmi, A., Navarro, J. F., Frenk, C. S., & White, S. D. M. 2008. The Aquarius Project: the subhaloes of galactic haloes. *MNRAS*, **391**, 1685–1711.

Stadel, J., Potter, D., Moore, B., Diemand, J., Madau, P., Zemp, M., Kuhlen, M., & Quilis, V. 2009. Quantifying the heart of darkness with GHALO - a multibillion particle simulation of a galactic halo. *MNRAS*, **398**, L21–L25.

Steinmetz, M., & Navarro, J. F. 1999. The Cosmological Origin of the Tully-Fisher Relation. *ApJ*, **513**, 555–560.

Stewart, K. R., Bullock, J. S., Wechsler, R. H., Maller, A. H., & Zentner, A. R. 2008. Merger Histories of Galaxy Halos and Implications for Disk Survival. *ApJ*, **683**, 597–610.

Stewart, K. R., Bullock, J. S., Wechsler, R. H., & Maller, A. H. 2009. Gas-rich Mergers in LCDM: Disk Survivability and the Baryonic Assembly of Galaxies. *ApJ*, **702**, 307–317.

Stinson, G., Bailin, J., Couchman, H., Wadsley, J., Shen, S., Brook, C., & Quinn, T. 2010. Cosmological Galaxy Formation Simulations Using SPH. *ArXiv e-prints*.

Stoughton, C., *et al.* . 2002. Sloan Digital Sky Survey: Early Data Release. *AJ*, **123**, 485–548.

Strickland, D. K., Heckman, T. M., Colbert, E. J. M., Hoopes, C. G., & Weaver, K. A. 2004. A High Spatial Resolution X-Ray and Hα Study of Hot Gas in the Halos of Star-forming Disk Galaxies. I. Spatial and Spectral Properties of the Diffuse X-Ray Emission. *ApJS*, **151**, 193–236.

Sutherland, R. S., & Dopita, M. A. 1993. Cooling functions for low-density astrophysical plasmas. *ApJS*, **88**, 253–327.

Toomre, A., & Toomre, J. 1972. Galactic Bridges and Tails. *ApJ*, **178**, 623–666.

Tormen, G. 1997. The rise and fall of satellites in galaxy clusters. *MNRAS*, **290**, 411–421.

Toth, G., & Ostriker, J. P. 1992. Galactic disks, infall, and the global value of Omega. *ApJ*, **389**, 5–26.

Tripp, T. M., *et al.* . 2003. Complex C: A Low-Metallicity, High-Velocity Cloud Plunging into the Milky Way. *AJ*, **125**, 3122–3144.

Tüllmann, R., Pietsch, W., Rossa, J., Breitschwerdt, D., & Dettmar, R.-J. 2006. The multi-phase gaseous halos of star forming late-type galaxies. I. XMM-Newton observations of the hot ionized medium. *A&A*, **448**, 43–75.

van den Bosch, F. C., Abel, T., Croft, R. A. C., Hernquist, L., & White, S. D. M. 2002. The Angular Momentum of Gas in Protogalaxies. I. Implications for the Formation of Disk Galaxies. *ApJ*, **576**, 21–35.

van den Bosch, F. C., Yang, X., Mo, H. J., Weinmann, S. M., Macciò, A. V., More, S., Cacciato, M., Skibba, R., & Kang, X. 2007. Towards a concordant model of halo occupation statistics. *MNRAS*, **376**, 841–860.

van Dokkum, P. G., *et al.* . 2004. Stellar Populations and Kinematics of Red Galaxies at z ¿ 2: Implications for the Formation of Massive Galaxies. *ApJ*, **611**, 703–724.

van Kampen, E. 1995. Improved numerical modelling of clusters of galaxies. *MNRAS*, **273**, 295–327.

Velazquez, H., & White, S. D. M. 1999. Sinking satellites and the heating of galaxy discs. *MNRAS*, **304**, 254–270.

Villalobos, Á., & Helmi, A. 2008. Simulations of minor mergers - I. General properties of thick discs. *MNRAS*, **391**, 1806–1827.

Viola, M., Monaco, P., Borgani, S., Murante, G., & Tornatore, L. 2008. How does gas cool in dark matter haloes? *MNRAS*, **383**, 777–790.

Voigt, L. M., & Fabian, A. C. 2004. Thermal conduction and reduced cooling flows in galaxy clusters. *MNRAS*, **347**, 1130–1149.

Walker, I. R., Mihos, J. C., & Hernquist, L. 1996. Quantifying the Fragility of Galactic Disks in Minor Mergers. *ApJ*, **460**, 121.

Wang, B., & Heckman, T. M. 1996. Internal Absorption and the Luminosity of Disk Galaxies. *ApJ*, **457**, 645.

Wang, Q. D., Chaves, T., & Irwin, J. A. 2003. Chandra Observation of the Edge-on Galaxy NGC 3556 (M108): Violent Galactic Disk-Halo Interaction Revealed. *ApJ*, **598**, 969–981.

Weinmann, S. M., van den Bosch, F. C., Yang, X., & Mo, H. J. 2006. Properties of galaxy groups in the Sloan Digital Sky Survey - I. The dependence of colour, star formation and morphology on halo mass. *MNRAS*, **366**, 2–28.

Weinzirl, T., Jogee, S., Khochfar, S., Burkert, A., & Kormendy, J. 2009. Bulge n and B/T in High-Mass Galaxies: Constraints on the Origin of Bulges in Hierarchical Models. *ApJ*, **696**, 411–447.

Wetterich, C. 1988. Cosmology and the fate of dilatation symmetry. *Nuclear Physics B*, **302**, 668–696.

White, S. D. M., & Frenk, C. S. 1991. Galaxy formation through hierarchical clustering. *ApJ*, **379**, 52–79.

White, S. D. M., & Rees, M. J. 1978. Core condensation in heavy halos - A two-stage theory for galaxy formation and clustering. *MNRAS*, **183**, 341–358.

Wyse, R. F. G. 2001. The Merging History of the Milky Way Disk. *Pages 71–80 of:* Funes, J. G., & Corsini, E. M. (eds), *Galaxy Disks and Disk Galaxies*. Astronomical Society of the Pacific Conference Series, vol. 230.

Yoachim, P., & Dalcanton, J. J. 2006. Structural Parameters of Thin and Thick Disks in Edge-on Disk Galaxies. *AJ*, **131**, 226–249.

Zentner, A. R. 2007. The Excursion Set Theory of Halo Mass Functions, Halo Clustering, and Halo Growth. *International Journal of Modern Physics D*, **16**, 763–815.

Zibetti, S., Charlot, S., & Rix, H.-W. 2009. Resolved stellar mass maps of galaxies - I. Method and implications for global mass estimates. *MNRAS*, 1410.

Zwicky, F. 1933. Die Rotverschiebung von extragalaktischen Nebeln. *Helvetica Physica Acta*, **6**, 110–127.

Acknowledgments

Erklärung

Ich versichere, dass ich diese Arbeit selbständig verfasst und keine anderen als die angegebenen Quellen und Hilfsmittel benutzt habe.

Heidelberg, den _____   _____

                                                                    (Benjamin Moster)